Continuous Hydrothermal Flow Synthesis of Functional Oxide Nanomaterials Used in Energy Conversion Devices

Xu, Yu

Publication date:
2017

Document Version
Publisher's PDF, also known as Version of record

Continuous Hydrothermal Flow Synthesis of Functional Oxide Nanomaterials Used in Energy Conversion Devices

Ph.D. Dissertation

By

Yu Xu

In partial fulfillment of the requirements

for the degree of Ph.D.

Department of Energy Conversion and Storage

Technical University of Denmark

June 2017

Preface

The thesis is the result of my Ph.D. study from 1st, July 2014 to 30th, June 2017 in 'Continuous hydrothermal flow synthesis of functional oxides for solid oxide fuel cells' which is one of the three work packages of the project *ProEco* (Green Production of Nanomaterials for Energy Conversion) funded by the Danish Council for Independent Research (Project No. DFF 1335-00138).

The overall aim of the project includes (1) developing a two-stage continuous hydrothermal flow synthesis reactor and applying it to synthesize tailored nanostructured materials for (2) solid oxide fuel cells (SOFCs) and for (3) Lithium-ion batteries (LIBs). The thesis focuses on materials related to the application in SOFCs.

The work presented in the thesis was conducted at two places. Syntheses, characterizations of materials and their applications in SOFC-related fields were conducted at the Section of Mixed Conductors, Department of Energy Conversion and Storage, Technical University of Denmark. The part related to catalysis was conducted at the group of Prof. Dr. Malte Behrens, Faculty of Inorganic Chemistry, University of Duisburg-Essen.

Acknowledgements

First, I would like to express my sincere gratitude to my supervisor Dr. Ragnar Kiebach, and to the great teammate Dr. Philipp Zielke, for their consistent and professional supports during my Ph.D. study. Their supervisions and guidance with patience and immense knowledge are invaluable for me to finish the Ph.D. work and the thesis. Thank you for always being nice and for the enjoyable working environment, which I am sure, will be one of my best memories from the last three years. Also thank you for always being optimistic which encourages me a lot especially in an occasionally hard time during the study. Danke schön.

I would also like to thank my co-supervisors, Prof. Dr. Peter Vang Hendriksen, Prof. Dr. Poul Norby and Dr. Søren Bredmose Simonsen. With their great patience, I was taught and trained in new knowledge and skills from their areas of expertise. I appreciate so much the opportunities to meet and talk with them. Thank you for being such helpful and for your efforts spent on improving my work. Tusind tak.

My thanks and regards shall go to Prof. Dr. Malte Behrens from University of Duisburg-Essen. Thank you for offering me the opportunity to do my external research stay in your group. I had a very good experience from it, both academically and personally. It was a very happy memory of me staying in the group full of young, lovely and friendly people.

Many thanks to Stéven Pirou, Raquel Reolon, Massimo Rosa, Nicholas Farandos, Fatih Özcan, Stefanie Hoffmann, Manuel Heimann and Justus Heese for helping me with my experiments and for expanding my areas of interest. Thank you for fruitful collaborative efforts that account for an important part of the thesis. “All Ph.D. students together do a great job!”

My acknowledgment also goes to colleagues in Risø. I believe Dr. Karen Brodersen has struggled a lot to transfer my ‘magic’ particles to advanced electrodes and I am sure she will make it. Dr. Ngo Vang Nong, Dr. Søren Højgaard Jensen and Dr. Vincenzo Esposito also contributed by commenting and reviewing parts of the thesis. Thank you all for your time and efforts. Mrs. Heidi Adler Berggren,

the secretary in our section, helped making my life much easier with everything being very well organized.

I would like to thank my friends especially the ‘Chinglish’ people, who make my life here colorful and full of happiness. My deepest love to my parents, whose support and love are very precious to me.

In the end, I would like to thank the generous funding from the Danish Council for Independent Research (DFF) within the ProEco project. Thanks to the Department of Energy Conversion and Storage, DTU for providing such a great platform for doing research. My kind regards to Denmark that has a so peaceful and *hyggelig* environment and is full of sweet things and people.

Yu Xu

Roskilde, Denmark, June 2017

Abstract

Continuous hydrothermal flow synthesis (CHFS) was used to prepare functional oxide nanoparticles. Materials synthesized include NiO, Y-doped ZrO_2, Gd-doped CeO_2, $LaCrO_3$ and Ni-substituted $CoFe_2O_4$. These types of oxides can be applied in several energy conversion devices, e.g. as active materials in solid oxide fuel cells (SOFCs), oxygen transport membranes (OTMs), and water electrolysis processes. Compared with other chemical synthesis methods, CHFS is advantageous for preparing nanosized materials with a narrow size distribution and a high phase purity. Moreover, CHFS has a high throughput as materials are continuously produced, and the technology can be scaled-up to an industrial-relevant production capacity.

The thesis starts with investigating the most appropriate mixer design for a novel two-stage reactor by computational fluid dynamics modelling. On basis of the modelling results, a two-stage CHFS reactor was constructed, and proof-of-concept syntheses of NiO and Y-doped ZrO_2 (YSZ), in both one-stage and two-stage modes, were conducted.

Secondly, Gd-doped CeO_2 (GDC) nanoparticles (6 – 40 nm) were synthesized, and the effect of the pH on their size, morphology and composition was studied. An up-scaled synthesis of $Gd_{0.2}Ce_{0.8}O_{2-\delta}$ nanoparticles was made, and the as-synthesized particles were processed into inks that displayed a good printability in inkjet printing of electrolytes on both green NiO-GDC and pre-sintered NiO-YSZ substrates. Particularly on the pre-sintered NiO-YSZ substrate, dense continuous layers (< 2 µm in thickness) composed of GDC and YSZ that fully covered the substrate were obtained after firing at 1300 °C.

In addition, $(La_{0.6}Sr_{0.4})_{0.99}CoO_3$ – $Gd_{0.2}Ce_{0.8}O_{2-\delta}$ (LSC-GDC) core-shell type particles were prepared and their high-temperature microstructural evolution was studied in two different sintering processes, i.e. spark plasma sintering and conventional sintering. By conventional hydrothermal batch-type synthesis, a core-shell structure was realized by precipitating ~6 nm large GDC particles on the surface of LSC particles under a mild hydrothermal condition of 100 °C resulting in an integral GDC

shell around the LSC core. It was found that by spark plasma sintering, a fine microstructure containing nanograins could be obtained and the graded core-shell architecture could be partially maintained.

For the first time, phase-pure $LaCrO_3$ was obtained by CHFS without any post treatments. A continuous production of cube-shaped $LaCrO_3$ particles (639 nm) was achieved. Processing parameters (temperature and alkali concentration) were found to affect the phase purity of the obtained particles significantly. The synthesized $LaCrO_3$ particles were used to prepare 10Sc1YSZ – $LaCrO_3$ dual-phase oxygen transport membranes. A density of ~90 % was achieved after firing at 1400 °C, which is below normal sintering temperatures for $LaCrO_3$-based ceramics. Oxygen permeation fluxes up to 5×10^{-8} mol cm^{-2} s^{-1} were obtained with a 1 mm thick membrane tested in air/N_2 at 900 °C.

Finally, $CoFe_2O_4$ and Ni-substituted $CoFe_2O_4$ nanoparticles were prepared by CHFS and their catalytic properties were evaluated. The $CoFe_2O_4$ was found to be active for catalytic CO oxidation. A 50 % conversion of CO at 223 °C and a complete conversion at 310 °C was reached. By CHFS, Ni-substituted $CoFe_2O_4$ nanoparticles with controlled Ni contents were synthesized, and their activity as catalysts for the oxygen evolution reaction (the half reaction of water electrolysis) was evaluated. Whereas no simple correlation between the activity and the Ni content was detected, a remarkable improvement of the activity was observed for the sample with 30 at% (in atomic percent) Ni-substituted $CoFe_2O_4$ ($Co_{0.7}Ni_{0.3}Fe_2O_4$) compared to all other investigated compositions.

Overall, the thesis demonstrates the versatility of the CHFS route for preparing functional oxides in nano particulate form, and documents the properties of the synthesized materials in a number of specific applications (fuel cells, membranes and catalysis).

Papers Included in the Thesis

Paper I. Simulation, design and proof-of-concept of a two-stage continuous hydrothermal flow synthesis reactor for synthesis of functionalized nano-sized inorganic composite materials

P. Zielke, **Y. Xu**, S.B. Simonsen, P. Norby, R. Kiebach

J. Supercrit. Fluid, 117, **2016**: 1 – 12.

My work: I conducted the syntheses of NiO and YSZ nanoparticles and their characterization. I wrote the corresponding parts and reviewed the whole paper before submission.

Paper II. Continuous hydrothermal flow synthesis of Gd-doped CeO_2 (GDC) nanoparticles for inkjet printing of SOFC electrolytes

Y. Xu, N.M. Farandos, M. Rosa, P. Zielke, V. Esposito, P.V. Hendriksen, S.H. Jensen, T. Li, G.H. Kelsall, R. Kiebach

Int. J. Appl. Ceram. Tec., ***Submitted***

My work: I did the syntheses of GDC nanoparticles and their characterization, as well as the SEM/EDS investigations of the printed samples on NiO/YSZ substrates. I wrote the paper except the experimental details of the inkjet printing processes. I was responsible for organizing the paper.

Paper III. Hydrothermal synthesis, characterization, and sintering behavior of core-shell particles: a principle study on lanthanum strontium cobaltite coated with nanosized gadolinium doped ceria

Y. Xu, P. Zielke, N.V. Nong, S. Pirou, R. Reolon, S.B. Simonsen, P. Norby, H. Lühmann, W. Bensch, R. Kiebach

J. Solid State. Chem., ***Revised***

My work: I was responsible for experiments and I wrote the paper.

Paper IV. Continuous hydrothermal flow synthesis of $LaCrO_3$ in supercritical water and its application in dual-phase oxygen transport membranes

Y. Xu, S. Pirou, P. Zielke, S.B. Simonsen, P. Norby, P.V. Hendriksen, R. Kiebach

In manuscript

My work: I was responsible for all syntheses and characterization. I wrote the paper except the membrane tests and results. I was responsible for organizing the paper.

Paper V. Continuous hydrothermal flow synthesis of $Co_{1-x}Ni_xFe_2O_4$ (x = 0 – 0.8) ferrite nanoparticles as catalysts for the CO oxidation and the oxygen evolution reaction

Y. Xu, F. Özcan, P. Zielke, S. Hoffmann, M. Heimann, J. Heese, K. Chakrapani, M. Behrens, S.B. Simonsen, P. Norby, P.V. Hendriksen, R. Kiebach

In manuscript

My work: I was responsible for experiments and I wrote the paper.

Papers Not Included in the Thesis

Paper VI. On the properties and long-term stability of infiltrated lanthanum cobalt nickelates (LCN) in solid oxide fuel cell cathodes

R. Kiebach, P. Zielke, S. Veltzé, S. Ovtar, **Y. Xu**, S.B. Simonsen, K. Kwok, H.L. Frandsen, R. Küngas

J. Electrochem. Soc., 164, **2017**: F748-F758

My work: I was responsible for the TEM, STEM and EDS characterization of the samples, and I wrote the corresponding part. I organized and checked the final structure of the paper.

Paper VII. Key elemental interdiffusion mechanism in thin film-based SOFCs degradation

R. Reolon, S. Sanna, **Y. Xu**, C. Bergmann, N. Pryds, V. Esposito

In manuscript

My work: I conducted the TEM, STEM and EDS characterization of the sample. I helped reviewing the corresponding part and the whole paper.

Paper VIII. Study on the tetragonal phase stability and transformation in the low content Y-Ce co-doped zirconia nanocrystalline powders

P. Khajavi, **Y. Xu**, P.V. Hendriksen, R. Kiebach, H. L. Frandsen

In manuscript

My work: I collaborated with the syntheses of $Y_xCe_yZr_{1-x-y}O_{2-\delta}$ nanoparticles and conducted the TEM/EDS characterization. I wrote the corresponding parts and helped reviewing the manuscript.

List of Participating Activities

1. Conferences

(1) Oral presentation 'Continuous Hydrothermal Flow Synthesis of Oxide Nanomaterials in Supercritical H_2O: $CoFe_2O_4$ and Its OER Catalytic Activity' at *21st International Conference on Solid State Ionics*, Padua, Italy, June **2017**.

(2) Oral presentation 'Continuous Hydrothermal Flow Synthesis of $LaCrO_3$' at *5th International Conference from Nanoparticles and Nanomaterials to Nanodevices and Nanosystems*, Porto Heli, Greece, June **2016**.

(3) Oral presentation 'Continuous Hydrothermal Flow Synthesis of Metal Oxide Particles for the Application in Green Energy' at *5th International Solvothermal and Hydrothermal Association Conference*, Tainan City, Taiwan, January **2016**.

2. Posters

(1) 'Continuous Hydrothermal Flow Synthesis of Oxide Nanoparticles and Their Characterization' at *1st and 2nd DTU Energy's Annual PhD Symposium with Industrial Participation*, Lyngby, Denmark, November, **2015** and **2014**.

(2) 'Continuous Hydrothermal Synthesis of LSC-CGO Nanocomposite Powders in Supercritical Water' at *2nd International PhD Summer School: IMAGINE: Methods in Imaging of Energy Material Microstructure*, Hundested, Denmark, August, **2014**.

Table of Contents

Chapter I. Introduction

1.1 Solvothermal and hydrothermal synthesis

Solvothermal synthesis terms the process that is used to synthesize materials in the presence of aqueous/non-aqueous solvents under an increased temperature and pressure. When aqueous solvents are used, it is usually called hydrothermal synthesis. Solvothermal/hydrothermal synthesis is advantageous for getting a precise control over the chemical composition, phase purity, size and morphology of products by tuning processing parameters, such as the solvent, pH, reaction duration, temperature and pressure [1]. Particularly for nanotechnology, the solvothermal/hydrothermal method is appealing for its wide applicability to process monodispersed homogeneous nanomaterials, hybrid nanomaterials and nanocomposites, for instance, metals, oxides, nitrides, sulphides, organic-inorganic hybrid nanostructures, and core-shell nanostructures, etc [2,3]. Moreover, consistent with the philosophy of the *green chemistry*, solvothermal/hydrothermal synthesis has a relatively low impact on both the environment and energy consumption, compared with other advanced techniques for processing materials (**Fig. 1.1**) [4].

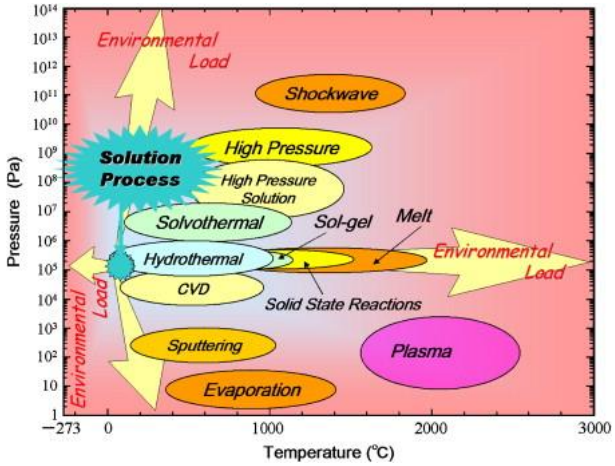

Figure 1.1 Pressure-temperature map of several material processing techniques. Reprinted from ref. [4].

According to the definition [5], a hydrothermal process usually is conducted in a closed heterogeneous system under a temperature higher than 100 °C and a pressure higher than 1 atm. Thanks to techniques [6], such as in-situ X-ray total scattering and neutron diffraction, it is possible

to monitor the nucleation and growth of crystals under hydrothermal conditions. Alternatively, by modelling, it is possible to compute the dependence of the thermodynamic equilibria on the hydrothermal conditions prior to synthesis in order to choose suitable experimental conditions for desired phases [7], and to understand the kinetic process from nucleation to growth of crystals [8]. In principle, two fundamental steps are involved in a hydrothermal reaction, including (1) hydration of metal cations to hydroxides, and (2) dehydration/condensation of these hydroxides to metal oxides that nucleate from the supersaturated solutions. The hydroxide ions presented in the reaction are either from the self-ionization of water or from the addition of mineralizers (e.g. alkalis).

$$M^{x+} + x\ OH^- \rightarrow M(OH)_x$$

$$M(OH)_x \rightarrow MO_{x/2} + (x/2)\ H_2O$$

In last two decades, a remarkable progress has been made on hydrothermal synthesis to push it forward towards the synthesis of nanomaterials in an industrial level. Instead of only being accommodated in a fixed-volume autoclave, the hydrothermal process is now also operated in a continuous flow-type apparatus, known as continuous hydrothermal flow synthesis (CHFS) [9]. Supercritical water (scH_2O) is usually used to heat reactants solutions, and the residence time of the process is short within seconds to minutes. The continuous operation makes it very efficient to do a high-throughput synthesis of a series of nanoparticles to conduct a screening analysis and rapid optimization. For instance, this method has been used to map out the phase and sintering behavior of $Ce_xZr_yY_zO_{2-\delta}$ [10,11], to optimize the performance of transparent conductive oxides (ZnO [12,13], indium tin oxide [14]), to analyze photocatalytic activity of series TiO_2 nanoparticles [15], and to correlate the structure-composition-property relationship of cathode materials for lithium ion batteries [16]. Moreover, the large-scale production of nanopowders by CHFS in an industrial level has already been tested [17–19].

1.2 Continuous hydrothermal flow synthesis by using the supercritical water

1.2.1 Supercritical water (scH$_2$O)

In a typical *T* – *p* phase diagram of a fluid (**Fig. 1.2**), the gas and liquid are separated by the gas – liquid boundary that is composed of (*T*, *p*) coordinate points under which conditions the two phases are in equilibrium. However, the boundary terminates at the critical point. Above the critical point, macroscopically only one homogeneous phase can be found in the system, which is termed as the supercritical fluid. More recently, a deep understanding of the supercritical fluid by inelastic X-ray scattering and molecular dynamic modelling however suggests that atomic fluctuations exist in the supercritical fluid resulting in dynamic heterogeneities. The occurrence of the maximum specific heat, and correspondingly the thermal expansion and compressibility of the supercritical fluid as temperature or pressure is described by the Widom line that extends from the critical point to the supercritical region [20].

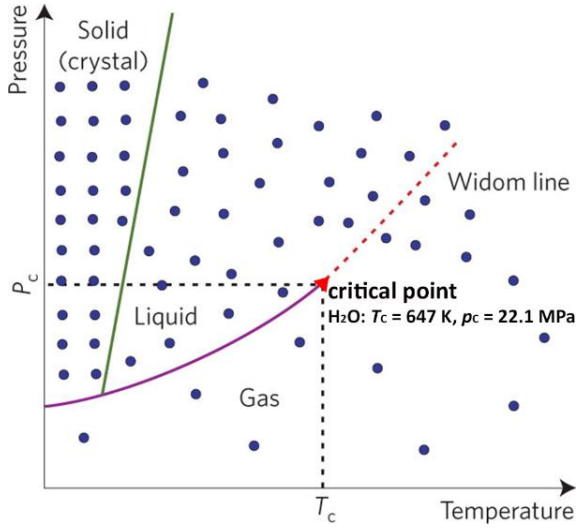

Figure 1.2 *T* – *p* phase diagram of a fluid, where the gas-liquid boundary ends at the critical point, above which the system becomes homogeneous (the supercritical fluid). Reproduced with the original figure from ref. [20].

Among all fluids, CO_2 and H_2O are mostly studied with respect to their applications as solvents in the green chemical processes [21,22]. H_2O goes into the supercritical state when the temperature and pressure exceed 647 K and 22.1 MPa respectively. The scH_2O behaves very differently

compared with H_2O at ambient conditions, and is regarded by many researchers as an intermediate state between the liquid and gaseous phase since the physicochemical properties of the scH_2O are generally in-between of those of the two phases. Evolutions of several physicochemical properties of H_2O as the temperature and pressure, including the density, the dielectric constant, the viscosity and the ionic product are summarized in the following.

(1) Density. When H_2O moves to conditions close to the supercritical state, its density drops remarkably, as shown in **Fig. 1.3**. The density of H_2O at the critical point (T_C = 647 K, p_C = 22.1 MPa) is 322 kg m^{-3}. It is worth to notice that in states near the critical point (600 – 700 K), the density of H_2O varies largely by slightly changing the temperature and/or pressure. The density significantly affects the solvent power of H_2O. Therefore, the scH_2O has a wide applicability as a solvent, thanks to the highly changeable solubility properties in the (near-) supercritical state controlled by the temperature and pressure [22].

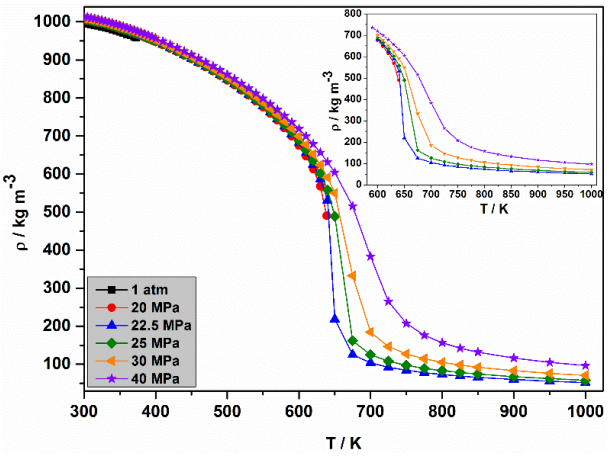

Figure 1.3 Dependence of the density of H_2O on the temperature and pressure; under all pressures, data of either the liquid phase or the supercritical phase are plotted whereas the density of vapor is excluded; the inset provides a zoom-in of the density of H_2O in the (near-) supercritical state. Replotted with data from ref. [23].

(2) Dielectric constant. At ambient conditions, the dielectric constant of H_2O is ~78. The species of compounds that can dissolve in H_2O are highly dependent on the dielectric constant of H_2O. The H_2O is polar and it is therefore a good solvent for ionic compounds such as inorganic salts. However, the polarity of H_2O is remarkably reduced in the (near-) supercritical state, as the dielectric constant

of the scH_2O drops below 20 (**Fig. 1.4**), a value that is comparable with the dielectric constant of organic solvents at ambient conditions. The scH_2O therefore turns out as a good solvent for non-polar compounds (e.g. hydrocarbons) and is miscible with gases (e.g. oxygen and hydrogen).

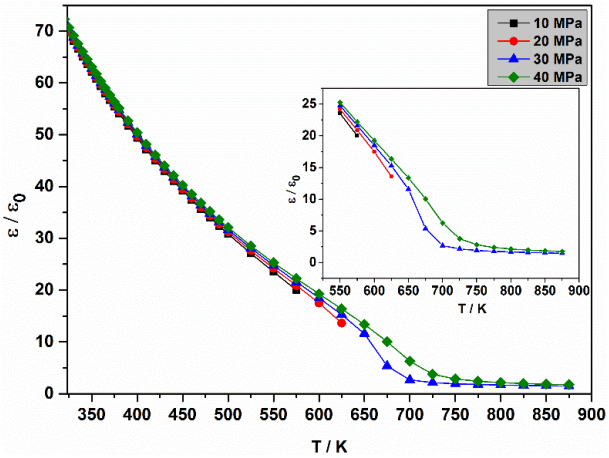

Figure 1.4 Dependence of the dielectric constant of H_2O on the temperature and pressure; the inset provides a zoom-in of the dielectric constant of H_2O in the (near-) supercritical state. Replotted with data from ref. [24].

(3) Viscosity. As shown in **Fig. 1.5**, the viscosity of H_2O remarkably drops as the temperature increases, and reaches the lowest near the supercritical point. The gas-like viscosity of the scH_2O enables it to act as a good reaction medium since the low viscosity as well as the high diffusivity are advantageous to a fast reaction rate [25].

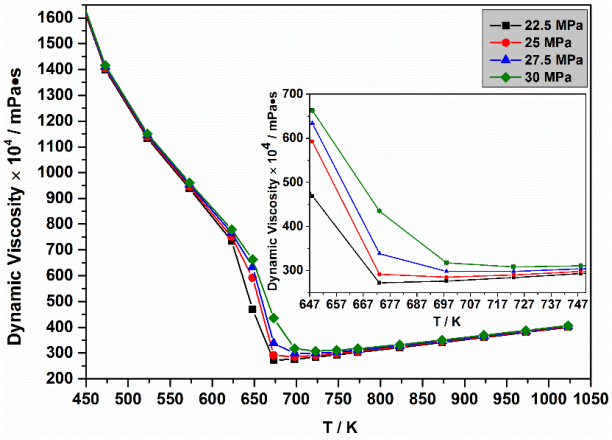

Figure 1.5 Dependence of the dynamic viscosity of H_2O on the temperature and pressure; the inset provides a zoom-in of the dynamic viscosity of H_2O in the supercritical state. Replotted with data from ref. [26].

(4) Ionic product. In the subcritical range, the ionic product of H_2O increases with the temperature and peaks at around 500 – 600 K (**Fig. 1.6**). However, the ionic product drops in orders of magnitude when H_2O goes to the supercritical state. This is because the low density as well the low dielectric constant reduce the solvation and stabilization power of H_2O for the ionic species. Nonetheless, the self-ionization process of H_2O provides H_3O^+ and OH^- ions that can act as acid or base catalyst precursors [25].

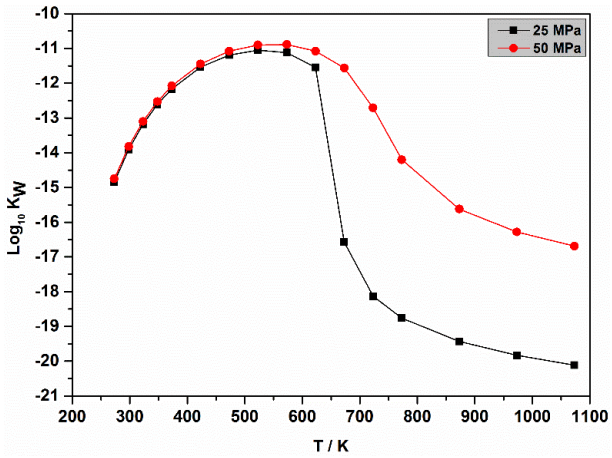

Figure 1.6 Dependence of the ionic product of H_2O on the temperature and pressure. Replotted with data from ref. [27].

To summarize, the scH_2O possesses properties and advantages from both the liquid and gaseous phase, such as a liquid-comparable density (correspondingly solvent power) and a gas-comparable viscosity. Moreover, it is relatively easy to tune these properties of the scH_2O efficiently by slightly changing the temperature and pressure. Organic compounds can be processed in the scH_2O, as they are highly soluble in the scH_2O due to the reduced dielectric constant of the scH_2O. This has resulted in wide applications, such as the supercritical water biomass valorization to process biomass into biogas and biofuels and supercritical water oxidation process for the organic waste treatment [28]. Meanwhile, a high miscibility between organics or gases and the scH_2O also contributes to forming a homogeneous reaction environment for chemical processes proceeding in the scH_2O.

1.2.2 Fundamentals of continuous hydrothermal flow synthesis (CHFS) using the scH_2O

The properties of H_2O acting either solely as solvent or as one of the reactants have a large influence on hydrothermal synthesis in an aqueous system. The drastic changes in the properties of H_2O near its critical point, as reviewed above, offer great opportunities to control the hydrothermal process and therefore to control the properties of the synthesized materials in terms of their phase, composition, size and morphology, etc. Especially, hydrothermal synthesis operated at (near-) supercritical conditions is attractive to the synthesis of nanomaterials.

The hydrothermal reaction rate is remarkably increased at supercritical conditions, due to the low dielectric constant of the scH_2O. According to the theory of Born [29,30], the hydrolysis reaction in principle can be regarded as an electrostatic reaction between metal ions and hydroxyl ions. The impact of the dielectric constant ε on the reaction rate k can be described by the **Eq. 1.1**,

$$\ln(k) = \ln(k_0) - (\omega / RT) \bullet (1/\varepsilon - 1/\varepsilon_0) \qquad (\mathbf{1.1}),$$

where ω is a constant determined by the reaction system, k_0 is the reaction rate at the dielectric constant ε_0, R is the gas constant and T is the absolute temperature.

Adschiri et al. [30] plotted the dielectric factor [$-(1/\varepsilon - 1/\varepsilon_0)$] vs. the temperature and pressure, as shown in **Fig. 1.7a**. It can be seen that under all pressures, the dielectric factor is almost negligible in the subcritical range whereas becomes pronounced in the supercritical range. This was examined by experimental kinetic studies (**Fig. 1.7b**) on the hydrothermal system using $Al(NO_3)_3$ as the precursor, and the results showed that above the critical temperature the reaction rate is greatly increased. The high hydrothermal reaction rate in the (near-) supercritical range has several advantages. Firstly, during CHFS, a high degree of supersaturation can be generated in a very short time, which is preferred for the synthesis of nanomaterials. Secondly, rapid nucleation of materials in a continuous (near-) supercritical flow can be accomplished, which makes a continuous operation possible. Thirdly, a long-term high-temperature treatment usually applied in a conventional

hydrothermal process can be avoided since the nucleation and crystallization of products can be achieved fast.

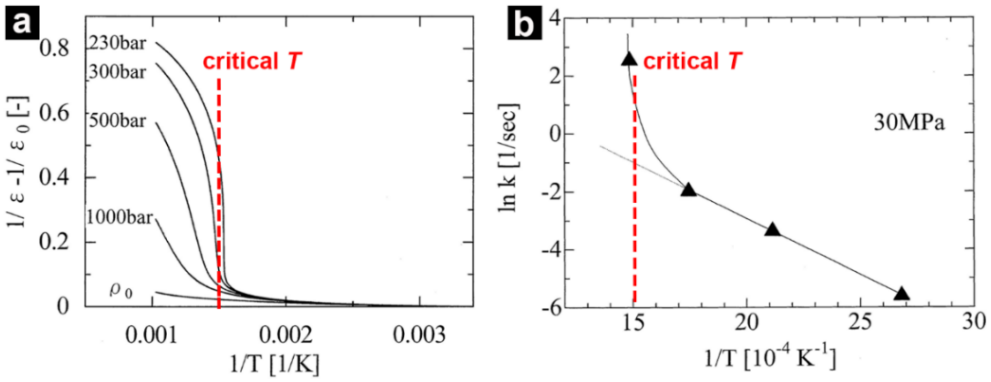

Figure 1.7 (**a**) The dielectric factor [– (1/ε – 1/ε_0)] vs. the temperature and pressure. (**b**) The Arrhenius plot of the first-order rate constant *k* evaluated at different reaction temperatures, in a hydrothermal system using $Al(NO_3)_3$ as the precursor. Reproduced with original figures adopted from ref. [30].

As reviewed above, the thermodynamic properties of H_2O drastically change with minor variations of the temperature and pressure in the (near-) supercritical state. According to the classical nucleation theory, the driving force of nucleation and the following crystallite growth highly depends on the degree of supersaturation. The solubility of materials (or products) in the scH_2O during CHFS therefore plays an important role in the nucleation and growth of products and has to be carefully controlled. Sue et al. [31] built a setup to measure the solubilities of PbO and CuO in the subcritical and supercritical H_2O. The dependence of the solubility of CuO on the temperature is presented in **Fig. 1.8**. In the subcritical range, CuO dissolves more as the temperature increases. When going to the (near-) supercritical range, the solubility of CuO sharply drops. The sharp decrease of the solubility near the critical point together with the remarkably increased reaction rate in the (near-) supercritical state result in a high degree of supersaturation generated in a very short period. The high degree of supersaturation is favored to the formation of a large amount of nuclei in a short time, which is beneficial to the formation of nanoparticles according to the balance of population.

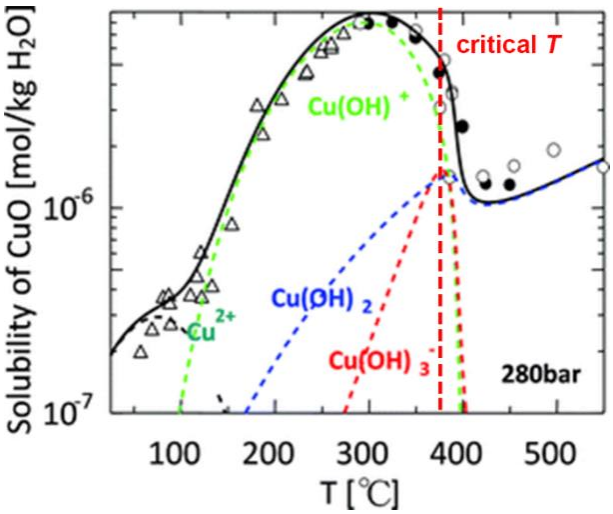

Figure 1.8 Solubilities vs. the *T* of H_2O at 280 bar. The solubility of CuO is presented by the experimental data in the scattered points (△○●). The calculation of the solubility presented by the black curve was obtained from a hydration model based on the relationship between the equilibrium constant and the temperature [31]. Reproduced with the original figure from ref. [19]; details found in ref. [31].

CHFS in principle takes advantage of the drastic equilibrium and kinetic shifts when the temperature and pressure condition of a precursor mixture is suddenly brought to the (near-) supercritical range. In a typical CHFS process, the scH_2O is used to heat the precursor rapidly to (near-) supercritical conditions in a flow-type apparatus, thus reducing the reaction period required for crystallization and growth of materials. Pioneered by Adschiri et al. [9,32], the CHFS technique has sparked a broad and active research field covering the modelling, design and optimization of flow-type apparatuses to conduct the CHFS process, modelling and *in situ* monitoring of the nanomaterial formation process, synthesis of various types of nanomaterials and evaluation of their performance in specific applications. A schematic overview of activities related to the CHFS technique is presented in **Fig. 1.9**.

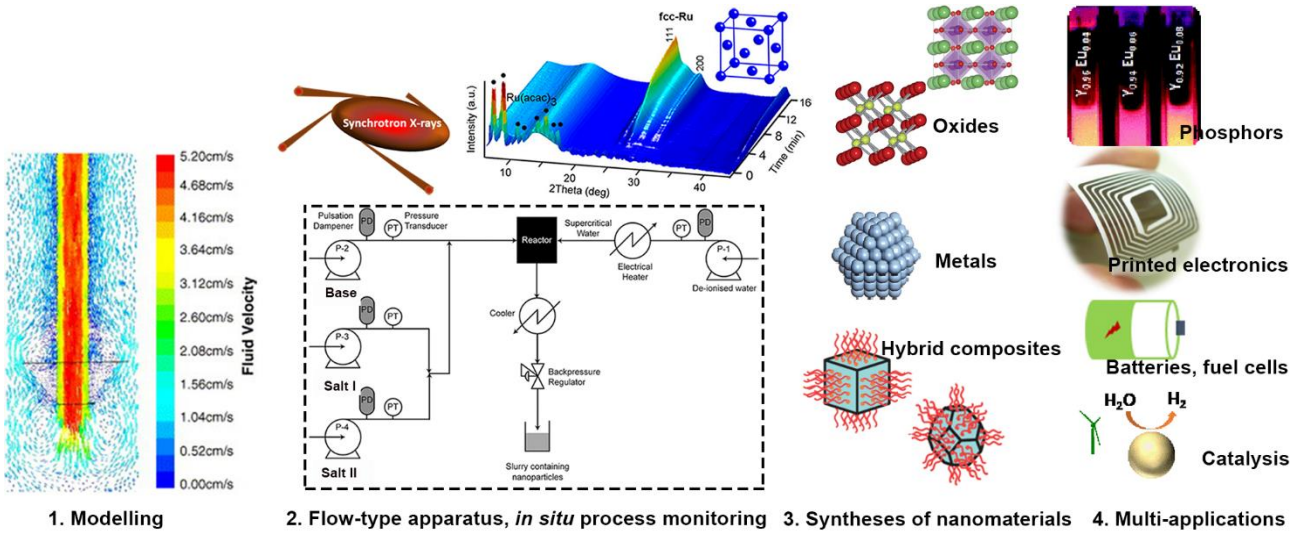

Figure 1.9 A schematic description of activities related to the CHFS technique. Reproduced with figures adopted from or inspired by ref. [33–41].

1.2.3 Design of flow-type apparatuses for CHFS using the scH_2O

Unlike the conventional hydrothermal synthesis under either subcritical or supercritical conditions that is usually accommodated in an autoclave, CHFS requires a flow-type apparatus within which the scH_2O and reactants flows are brought to mix with each other. Given differences between the scH_2O and the reactants in terms of their flow rate, temperature, viscosity, concentration and density, it is important to get an accurate understanding of the mixing behavior. It is commonly acknowledged that the mixer geometry of a flow-type apparatus has a primary impact on the mixing regime, of which the heating rate and the temperature distribution for instance significantly affect the size and size distribution of particles, process stability and reproducibility [42–44]. Accordingly, design and optimization of the mixer geometry is a major task when constructing a flow-type apparatus for CHFS.

A direct observation of the mixing regime in operando during the CHFS process however is rather challenging. Numerical calculation mostly by computational fluid dynamics (CFD) modelling has been used as a powerful tool to evaluate the mixing performance and to find the possible flaws of a mixer geometry. Quantitative studies are conducted to understand the effects of the mixer geometry, diameter and fluid properties (e.g., density, *Re* number, and flow rate) on the mixing behavior.

The T-shaped tee mixer, described in the first CHFS study [9], is often used partly due to its simple geometry. In this mixer, there are different ways to configure the direction of the scH_2O and reactants flows [45]. Some of these will lead to significant 'back mixing' (**Fig. 1.10a**) where scH_2O penetrates against the cold reactants flow resulting in a pre-heating of the reactants, inhomogeneous mixing and temperature distribution, as well as possible pre-formation of particles before the mixing point. Back mixing can therefore lead to a relatively wide size distribution. By numerical simulation, it was found that the density gradient is the main driving force for mixing. However, when the buoyancy forces derived from the density gradient overcome the inertial forces of the downward-flowing aqueous reactants fluid, it will result in 'back mixing' [46]. In order to find the most appropriate flow configuration with the minimized temperature gradient in the mixing regime, CFD modelling has been applied to determine the influence on the temperature distribution within the mixing regime from the inner diameter [45] and from the mixer geometry [47].

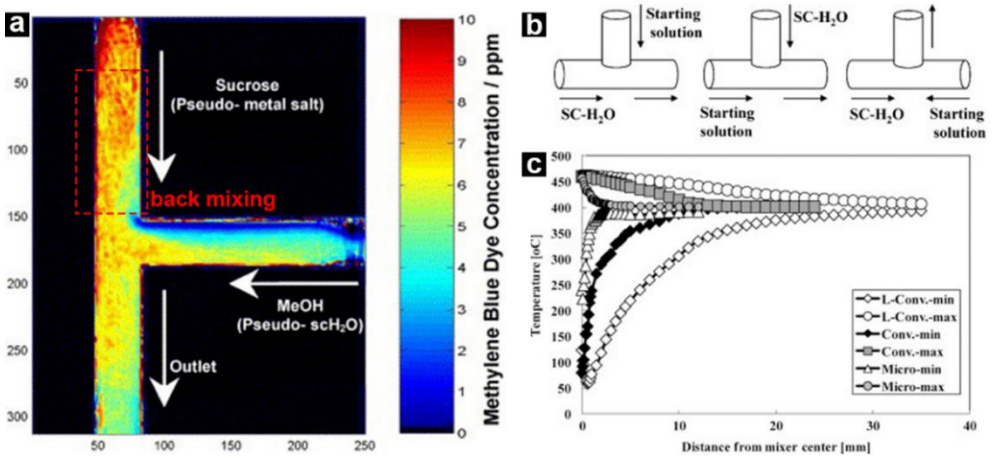

Figure 1.10 (**a**) 'Back mixing' observed by the light imaging absorption (500 W spotlight; digital video camera) within a T-shaped mixer ('bending stream', the second in **b**, rotating 90° clockwise); methanol and 40 % w/w aqueous sucrose solution (saturated with methylene blue dye 12 ppm) were used to mimic the scH_2O flow and the reactants solution flow separately. (**b**) Three configurations of flow directions in a T-shaped mixer: straight stream, bending stream and counter stream (left to right). (**c**) Maximum and minimum temperature distributions within a mixer of three different geometries (L-Conv, Conv and Micro); a good mixing is by minimizing the temperature gradient within the mixing regime in which the maximum and minimum temperatures rapidly reach the same (i.e. in minimized distance from mixer center) to realize a homogeneous temperature distribution. Reproduced with original figures adopted from ref. [45,46].

The CFD modelling also contributes to designs of novel types of mixers. For instance, to address the shortcomings of the T-shaped tee mixer such as the 'back mixing' and the particle accumulation and agglomeration within the reactor, a 'nozzle'-shaped mixer was designed [39]. Ma et al. [48] compared the mixing behaviors between the counter-current mixer and the confined jet mixer by modelling the velocity and temperature fields at various process conditions including the temperatures and flow rates of the scH_2O and precursor. The fluid dynamics with respect to the velocity, temperature and *Re* number were also calculated with an X-shaped mixer [49,50].

It is obviously interesting to scale up the flow-type reactor in order to transfer a laboratory-developed flow-type apparatus to an industrial-level synthesis of a large capacity [18]. The CFD modelling can be used for simulating the mixing behavior after volumetric scale-up before a real construction. For instance, the temperature and fluid velocity fields were calculated for a volumetrically scaled confined jet mixer and were compared with those of a lab-scale system [51].

The efforts to get an *in situ* observation of the mixing behavior within a mixer between the scH_2O and reactants flows are described in literatures. For example, a cell was developed for a direct observation of the mixing behavior by assembling a transparent T-shaped trench tee mixer with two more transparent sapphire windows [52]. Mixing patterns were recorded optically for evaluation at various processing conditions. Alternatively, light absorption imaging (LAI) based on the absorption of light by dyed fluids was used to study the mixing behavior [46]. Methanol and 40 % w/w aqueous sucrose solution (saturated with methylene blue dye, 12 ppm) at ambient conditions were used to mimic the scH_2O and the aqueous reactants respectively. They were chosen because the density and viscosity ratios between them are very close to those between the scH_2O and the aqueous reactants in a CHFS process. The concentration maps obtained from the LAI were used to visualize the mixing behavior, which together with modelling could be used to optimize the mixer. More recently, the neutron radiography was used to visualize the temperature and density profiles of the mixing regime within a T-shaped tee mixer [53]. The neutron radiography was recorded by measuring the intensity of scattered neutrons that are mostly caused by interactions with hydrogen

atoms. It is suitable for visualizing the change in the density of water in a CHFS process. The neutron radiography was successfully used to compare the mixing behavior within a T-shaped tee mixer working with different configurations of the flows' feeding directions.

Lester et al. [39] proposed the criteria for an 'ideal' design of a mixer. (1) Rapid and uniform mixing of the scH_2O and reactants flows in order to homogenize the condition for particle nucleation and narrow down the size distribution of the as-prepared particles. (2) Minimal heating convection/conduction on the reactants fluid prior to the mixer in order to avoid premature precipitation/deposition of metal salts in pipes. (3) Forming a strong net downstream flow to prevent particles accumulating within the apparatus that might result in blockage. However, it seems that there is not a 'perfect'-fit mixer design of a flow-type apparatus for CHFS in all cases. Nonetheless, as reviewed above, the CFD modelling as well as the development of visualization techniques for an *in situ* observation of the mixing behavior are valuable for designing and optimizing new mixers [54].

1.2.4 Nanomaterials synthesized by CHFS

Nanomaterials possess special physicochemical properties relative to materials of larger dimensions because of the so-called size effect originated from the large surface-to-body-atom ratios [55]. The size, morphology and composition have rather high impacts on the exhibited properties of nanomaterials. In the following, the application of CHFS to a highly efficient synthesis of various types of nanomaterials is reviewed with respect to highlighting the effects of the processing parameters including the reaction temperature, pressure, residence time, and pH on the properties of the as-synthesized nanomaterials in terms of their size distribution, composition and morphology. The review focusses on materials prepared by CHFS in a flow-type apparatus and with H_2O (and/or aqueous solvents) under (near-) supercritical conditions (**Table 1.1**).

Ce-Zr-O oxides. Cubic-phase fluorite-type oxides especially ZrO_2 and CeO_2 based oxides are attractive for their good oxygen ionic conductivity and oxygen buffering ability. For example, the ionic

conductivities in air at 800 °C of $(Y_2O_3)_{0.08}(ZrO_2)_{0.92}$ and $Gd_{0.2}Ce_{0.8}O_2$ are 0.03 S cm^{-1} and 0.053 S cm^{-1} respectively [56], and they are widely used as electrolyte materials in solid oxide fuel/electrolysis cells (SOFC/SOECs).

ZrO_2 has three primary polymorphs that are monoclinic, tetragonal and cubic, of which the stabilization temperatures are < 1173 °C, 1173 – 2370 °C and 2370 – 2690 °C separately. It seems that the precursor affects the phase of ZrO_2 obtained by CHFS, since cubic-ZrO_2 [9] and mixture of monoclinic- and orthorhombic-ZrO_2 [57] nanoparticles were obtained separately starting from $ZrOCl_2$ and $ZrO(NO_3)_2$ under similar conditions (673 K, 30 MPa). $Zr(ac)_4$ was also used to prepare ZrO_2 by CHFS under near- and supercritical conditions (573 – 723 K, 10 – 45 MPa) [58]. However, a composite of monoclinic- and tetragonal-ZrO_2 nanoparticles was obtained in all cases. It was found that the temperature has the largest effect on the size distribution and phase composition of the ZrO_2 nanoparticles. An increase of the temperature leads to a higher content of the monoclinic phase and a larger particle size.

In principle, the tetragonal and cubic phases of ZrO_2 are thermodynamically metastable, and stabilizing ZrO_2 especially of the cubic polymorph by substituting Zr cations over a wide temperature range is of more interests to applications. Y-doped ZrO_2 is a good example as an appropriate level of Y_2O_3 dopant (e.g. 8 mol%) into the ZrO_2 crystal lattice can stabilize the cubic polymorph ranging from the room temperature until nearly 1000 °C. Under hydrothermal conditions, the hydrolysis of Zr and Y cations, however, have different preferred pH conditions. CHFS of Y-doped ZrO_2 nanoparticles was studied with respect to the effect of pH on the conversion rates of Y and Zr cations and the corresponding stoichiometric compositions of $Y_xZr_{1-x}O_2$ [59,60]. It was found that a complete conversion of Zr cations is reached irrespective of pH and temperature whereas the conversion of Y cations increases with pH and temperature. The pH has to be higher than 8 in order to get a stoichiometric composition of $Y_xZr_{1-x}O_2$.

Due to their relatively high ionic conductivity at low temperatures, CeO_2 based oxides have been regarded as promising alternatives to ZrO_2 based oxides for the use as electrolyte materials

particularly in medium/low-temperature SOFC/SOECs [61]. Phase-pure CeO_2 nanoparticles were prepared by CHFS with a very short time (< 1 s) when the temperature was higher than 573 K [62]. The precursor was found to have an impact on the agglomeration state of the formed CeO_2 nanoparticles, as that the CeO_2 nanoparticles tended to precipitate within the reactor when $Ce(NO_3)_3$ was used as the precursor. However a continuous recovery of well-dispersed CeO_2 nanoparticles could be achieved when $(NH_4)_2Ce(NO_3)_6$ was used thanks to the stabilization effect originated from NH_4^+ cations [63].

The substitution of Ce cations within the CeO_2 crystal lattice by trivalent cations has arisen as an effective way to increase the concentration of oxygen vacancies and correspondingly the ionic conductivity. Zr-, La- and/or Pr-doped CeO_2 nanoparticles were prepared by CHFS with respect to studying the effects of the reaction temperature as well as the residence time on the composition of doped CeO_2 [63]. The difference in the reactivity of the dopant precursors, however, requires different reaction temperatures (≥ 573 K for $ZrO(NO_3)_2$, ≥ 673 K for both $La(NO_3)_3$ and $Pr(NO_3)_3$) in order to get a complete conversion of dopants from salts to oxides. Besides, adding an excessive dopant precursor in the starting precursor solution also can be used to offset the influence from the different reactivity to get a desired stoichiometric composition. Therefore, by adjusting the temperature it is difficult, but possible, to get a precise control on the composition of the doped CeO_2 nanoparticles. Residence time of 10 s was sufficient to get a full conversion of both the Ce and dopant cations during CHFS. Compared with the conventional hydrothermal synthesis conducted in an autoclave, CHFS was found suitable to get phase-pure doped CeO_2 nanoparticles with a higher dopant level. For instance, the Bi dopant level (x) of $Bi_xCe_{1-x}O_2$ obtained by CHFS was increased to 0.7, in comparison to 0.6 in $Bi_xCe_{1-x}O_2$ synthesized by the conventional hydrothermal method [64]. Phase-pure Zn-doped CeO_2 nanoparticles of an unprecedented Zn level up to 30 mol% were also prepared by CHFS [40,65].

$Zr_xCe_{1-x}O_2$ based oxides are used as oxygen buffers in the three way catalysts for treatments of automotive exhausts due to their high oxygen storage capacity and improved thermal stability. By

CHFS, highly crystallized homogeneous $Zr_xCe_{1-x}O_2$ nanoparticles of 3 – 7 nm were rapidly prepared at ~573 K and 25 MPa in a single step [66]. Compared with $Zr_xCe_{1-x}O_2$ prepared by the coprecipitation method, the CHFS-synthesized $Zr_xCe_{1-x}O_2$ nanoparticles with the same composition and the similar crystallite size had less agglomerations and exhibited higher thermal stability as well as oxygen storage capacity [67]. Moreover, the CHFS-synthesized $Zr_xCe_{1-x}O_2$ nanoparticles were further used as supports for Rh nanoparticles, which displayed a better catalytic performance towards NO reduction [68,69]. The concentration of oxygen vacancies within the crystal lattice of $Zr_xCe_{1-x}O_2$ solid solutions can in principle be further increased by introducing more dopant cations. It was shown that a precise control on the chemical composition of the doped $Zr_xCe_{1-x}O_2$ nanoparticles could be achieved by CHFS [70].

ZnO. ZnO is a wide-band-gap semi-conductive material with a direct band gap of 3.4 eV and exciton binding energy of 60 meV at room temperature. Its optical and electric properties result in applications in such as UV/blue emitter, optoelectric transducers, and photocatalysts and so on. First attempts on CHFS of ZnO nanoparticles in the scH_2O started almost at the same time in several groups [71–73]. However, rather different morphologies and particle sizes were reported. This suggested that a close look on the nucleation and growth process of ZnO by CHFS was necessary. The morphology and size evolutions of the ZnO nanoparticles were mapped with the pH during the CHFS process (**Fig. 1.11**) [74]. It was found that by increasing the concentration of KOH (thus increasing pH), the growth of ZnO was limited, and the morphology proceeded from nanorods to spherical nanoparticles. Søndergaard et al. [75] studied the dependence of size and morphology of ZnO on the temperature of a wide range from 293 – 673 K. It was found that at the neutral pH condition, the ZnO particles became more and more isotropic as the temperature increased. Moreover, in the high temperature range (513 – 673 K), the particles did not grow much as the temperature increased while the morphology was unchanged. It was explained that at (near-) supercritical conditions, a rapid nucleation resulted in a large amount of nucleation sites and a fast depletion of the precursor, thus hindering the particle growth. At ~573 K, varying pH resulted in

different morphologies of the as-prepared ZnO, as rods, isotropic particles and plates were obtained separately at the acidic, neutral and alkaline conditions. The results are different from the observations in [74] as ZnO plates were obtained in alkaline conditions, which might be because that different temperatures were applied (683 K, [74]; 573 K, [75]). The formation of the nanorods was explained by the fast growth rate of (0001) planes (anisotropic growth) that could be reduced by the shielding effect of OH^- ligands at alkaline conditions (isotropic growth). However, it was found that H_2O_2 can disrupt the OH^- ligands and thus nanorods were obtained at alkaline conditions [76]. The reviewed results show that the temperature and pH need to be carefully adjusted during CHFS in order to control the size and morphology of ZnO.

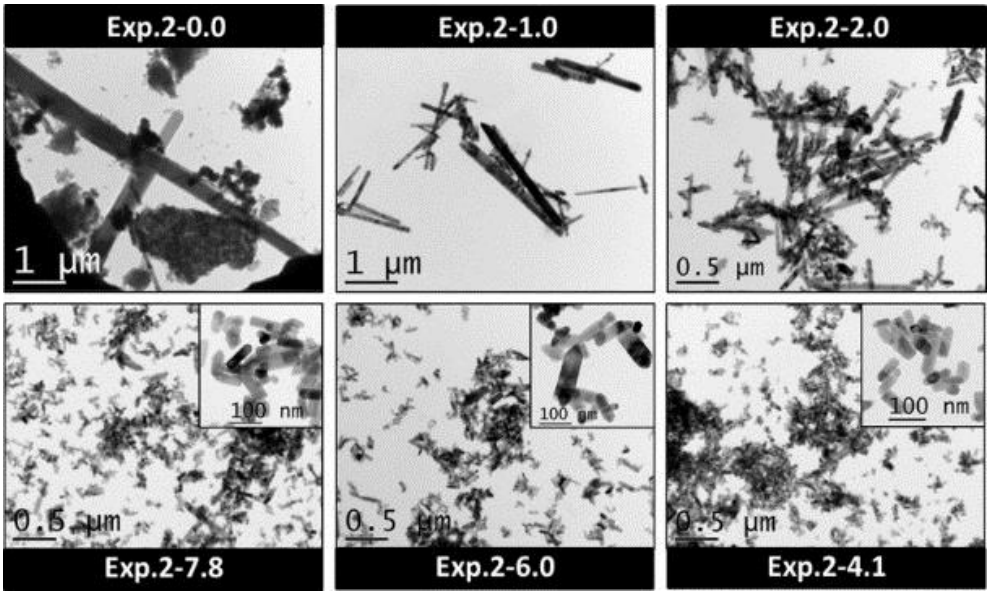

Figure 1.11 TEM images of the ZnO particles prepared by CHFS (683 K, 30.5 MPa) from $Zn(NO_3)_2$ (0.02M) and KOH with different values of [KOH] / [Zn(II)] (molar ratio 0.0 – 7.8). Reprinted from ref. [74].

Doped ZnO, especially the Al- and Ga-doped ZnO have been regarded as promising alternatives to the tin-doped indium oxide (ITO) working as transparent conducting oxides. The dopant level affects the energy levels in the band gap of the doped ZnO, which determines the semiconductivity and transparency. CHFS displayed advantages in synthesizing the Al- and Ga-doped or Al/Ga co-doped ZnO nanoparticles, since it was able to control the dopant content precisely and to prepare a library of doped ZnO of series compositions rapidly [12,13]. This enabled mapping the electric conductivity

and transparency of the doped ZnO with their compositions. Further, various dopants including transitional metals (Ti, V, Cr, Mn, Fe, Co, Ni and Y), lanthanides (La, Ce, Pr, Nd, Gd and Er), Ag, Ga and S were also used to dope ZnO with respect to studying their effects on the photocatalytic activity [76].

TiO_2. As one of the most well-known semiconductors, anatase (TiO_2 with a direct band gap of 3.2 eV) is employed widely as photocatalyst and the electric conducting material in dye-sensitized solar cells [77]. The applicability of CHFS to a highly efficient synthesis of TiO_2 has been demonstrated in [78,79]. Crystallized anatase TiO_2 nanoparticles of 13 – 30 nm were obtained by mixing the precursor solution with the supercritical alkali solution (premixing the scH_2O and alkali solution) in a flow-type apparatus [79]. At supercritical conditions, the average size of TiO_2 increased when an alkali solution of a higher concentration was used. In comparison, the temperature (673, 723, and 773 K) seemed not to affect the average particle size (~16 nm) since in their study [79] the residence time was reduced simultaneously as the temperature increased. However, the degree of crystallinity of the anatase TiO_2 nanoparticles was increased with the temperature [80].

Sn-doped TiO_2 nanoparticles [81] were prepared by CHFS, for the application as an anode material in Li-ion batteries. Anatase TiO_2 nanoparticles with Sn dopants up to 15 mol% were obtained. The average size of the Sn-doped TiO_2 nanoparticles increased with the content of dopants.

In-Sn-O oxide. In_2O_3 is also a wide band gap semiconductor with a direct band gap of 3.7 eV, and Sn-doped In_2O_3 (ITO) is better known as a transparent conducting oxide. Phase-pure In_2O_3 nanoparticles with an average size of 14 nm were prepared by CHFS [82]. The nanoparticles were made into a gas sensor that displayed a significantly selective response to ethanol gas. The attempt to apply CHFS to the synthesis of ITO, however, initially failed due to the different hydrolysis rates of In and Sn cations that in principal could be controlled by the pH [83]. In another work [84], the precursor with a neutralized pH (7) was used instead of lower pHs (1.2 – 1.9) in [83] and phase-pure Sn-doped In_2O_3 nanoparticles of ~30 nm size were obtained at supercritical conditions (673 – 723 K, 30 MPa). The average size of the obtained nanoparticles could be further reduced to 18 nm when

hexanoic acid was used as a surfactant. The reaction temperature was found important for getting a phase-pure Sn-doped In_2O_3, since InOOH was left as an impurity that was independent of pH when the reaction temperature was lower than 673 K [14].

V_xO_y, Mn_xO_y, Fe_xO_y, Co_xO_y, NiO and CuO. The first transition metal oxides listed here are attractive particularly with respect to their magnetic properties and applications as catalysts, magnetic and semiconductive materials. The presence of unpaired *d*-orbital electrons and correspondingly inherent reversible valence variations of the metal atoms in these transition metal oxides result in various oxidation states of the metal elements. The oxides exist in many polymorphs. For instance, iron oxides have 16 polymorphs [85] while manganese oxides display 30 different crystal structures [86].

CHFS was applied to prepare VO_2 in a single step at temperatures of 608 – 648 K and 24.1 MPa [87,88]. The synthesized VO_2 nanoparticles were in a composite of two polymorphs: metastable VO_2 (B) and monoclinic VO_2 (M). The reaction temperature affected the phase composition such that a higher reaction temperature resulted in an increase of the composition of VO_2 (M). VO_2 exhibits semiconductivity at low temperatures, however, becomes semi-metallic at high temperatures. The semiconductor-to-metal phase transition proceeds at 68 °C, and VO_2 changes from being highly transmissive to the long-wave thermal radiation to being reflective [89]. From the viewpoint of applying VO_2 as a coating for windows to reduce the loss of building interior heat, for instance, it would be preferred to reduce the transition temperature to be below the ambient temperature. Nb-doped VO_2 nanoparticles of several compositions were prepared by CHFS using the scH_2O (723 K, 24.1 MPa) [90]. The Nb dopant content not only affected the particle size but also the morphology of the as-synthesized particles. Increasing the content of Nb in the doped nanoparticles reduced the average particle size, while the particles became more isotropic. The transition temperature was brought down to ~46 °C with an appropriate level of Nb dopant.

Lee et al. [91] reported the one-step synthesis of Mn_xO_y by CHFS starting from $Mn(NO_3)_2$ at supercritical conditions (653 K and 703 K, 30 MPa). The synthesized particles were composites of

Mn_2O_3 and MnO_2. The reaction temperature largely influenced the phase composition, average particle size and particle morphology. MnO_2 was the predominant phase in the particles synthesized at 703 K whereas Mn_2O_3 was the predominant one in the particles synthesized at 653 K. The high reaction temperature (703 K) resulted in much smaller, more homogeneous and spherical particles. This was possibly because of the rapid formation of a large amount of nuclei in the supercritical state (703 K) in comparison to the case in the near-supercritical state (the temperature of the feeding scH_2O was 653 K whereas the real reaction temperature could be even lower), which depleted the precursor in the solution and limited the growth of formed particles. The pH was also found to affect the phase of Mn_xO_y crystallized from the CHFS process [92]. At 637 K, MnO_2 crystallized from the acidic condition (no addition alkaline) generated after cations hydrolysis, whereas Mn_3O_4 crystallized from the alkaline condition (with extra alkaline).

Among all polymorphs of Fe_xO_y, three of them are often observed: Fe_3O_4 (magnetite, cubic, spinel structure), α-Fe_2O_3 (hematite, rhombohedral/hexagonal), and γ-Fe_2O_3 (maghemite, cubic/tetragonal). Magnetite (Fe_3O_4) and maghemite (γ-Fe_2O_3) are magnetically responsive and thus are widely used particularly in biomedical imaging [85]. Cote et al. obtained phase-pure α-Fe_2O_3 nanoparticles by CHFS starting from $Fe(NO_3)_3$. It was found that by mixing the supercritical alkali solution with the precursor the α-Fe_2O_3 displayed a more homogeneous and smaller average particle size in comparison with those obtained by mixing the precursor and alkali solution with the scH_2O [93]. However, a mixture of α-Fe_2O_3 and γ-Fe_2O_3 was obtained by CHFS, as reported by Sue et al [94]. A direct comparison of the results is difficult, since the apparatus and the reaction conditions were rather different. The conversion rate of Fe cations during CHFS was very high, as a nearly complete conversion could be achieved with a residence time less than 2 s [94] at the supercritical condition. A continuous production of phase-pure Fe_3O_4 starting from Fe^{2+} and Fe^{3+} at 425 K and 25 MPa however required the addition of citrates as anti-oxidants, as shown in [95]. Hematite (α-Fe_2O_3) was formed as an impurity that could be avoided when a sufficient amount of citrate was added.

The one-step synthesis of Co_3O_4 cube-shaped nanoparticles by CHFS was reported by several groups. The pH during the synthesis was found to have an influence on the phase purity of the cobalt oxide particles. Under the supercritical condition (673 K, 30 MPa), as the pH increased with the addition of KOH, the phase of the crystallized cobalt oxides changed from Co_3O_4 (low pH, KOH / Co^{2+} molar ratio = 0 – 4) to CoO (high pH, KOH / Co^{2+} molar ratio = 4 – 20) [92]. The reaction temperature affected the crystallinity of the synthesized Co_3O_4 particles. The formation of highly crystallized Co_3O_4 without impurities (e.g., CoOOH) preferred a high reaction temperature (> 673 K, [93,96,97]). Moreover, the reaction temperature influenced the conversion rate of Co cations during the reaction (~99 % within 2 s at 703 K), as a longer residence time was necessary under low reaction temperatures (473, 523 and 573 K, [96]) in order to increase the degree of conversion (however, < 80 %). Besides the Co_3O_4 nanocubes obtained directly by CHFS, Chowdhury et al. [98] presented a way to synthesize Co_3O_4 octahedrons by CHFS. When urea was used to precipitate Co cations by CHFS, $Co(OH)_2$ of an octahedron morphology could be obtained in a single step at 553 K and 20 MPa. These octahedrons were further annealed at 573 K and were converted to Co_3O_4 displaying the reserved octahedron morphology.

A continuous production of NiO and CuO by CHFS was also reported. During CHFS of NiO, the residence time significantly affected the average size of the NiO particles. By increasing the total flow rates, the residence time was decreased that resulted in a reduction of the average particle size [45,94]. However, one should be careful when reducing the residence time, as the conversion rate of Ni cations to oxides was reduced simultaneously [45,94]. This could be offsetted by increasing the pH during the synthesis, as a high conversion rate (~90 %) was reached at high pH values (KOH / Ni^{2+} molar ratio ≥ 1.75) [57]. Highly crystallized CuO was prepared by CHFS rapidly, although the conversion rate of Cu cations to CuO was rather low (< 50 %) [43,57,94] because of the relatively high solubility of CuO in the scH_2O [57].

Perovskite oxides. Perovskite-structure oxides with a chemical formula ABO_3 (A, B are cations) are widely used as solid conductors (e.g. $LaCoO_3$), ferroelectric materials (e.g. $BaTiO_3$) and piezoelectric

materials (e.g. $PbZrO_3$, $PbTiO_3$). A typical synthesis of perovskite oxides is by solid-state reactions among compounds containing the corresponding A and B cations that are usually conducted at > 1000 °C. By this method, it is rather challenging to obtain nanoparticles that would display some special physicochemical properties derived from the size effect. CHFS with a high productivity is advantageous if applied to the synthesis of perovskite oxides nanoparticles especially when large amounts of nanoparticles are required.

The tetragonal and cubic phases are the two most known polymorphs of $BaTiO_3$. CHFS was applied to rapidly synthesize $BaTiO_3$ nanoparticles in a single step [99–102]. The density of water during CHFS that could be tuned by the temperature and/or pressure was found to influence the phase of the as-synthesized $BaTiO_3$. In the water with a high density (> 0.5 g cm^{-3}), the cubic phase was obtained whereas the tetragonal phase was obtained in the water with a low density (< 0.5 g cm^{-3}) [99]. When TiO_2 sol was used as one of the reactants, extending the residence time was preferred to convert more TiO_2 to $BaTiO_3$ and thus to get rid of TiO_2 left as impurities [100,101]. Increasing the reaction temperature was also helpful to the conversion of TiO_2 [100]. However, the average size of the $BaTiO_3$ particles became larger as either the residence time or the reaction temperature or both were increased.

CHFS was also used to prepare phase-pure Sr-doped $BaTiO_3$ ($Sr_xBa_{1-x}TiO_3$) nanoparticles in a single step [17,103]. At the supercritical condition (663 K, 25 MPa), $Sr_xBa_{1-x}TiO_3$ nanoparticles with an average size between 8 and 18 nm were produced in a continuous way. The average size of the nanoparticles decreased with an increase of the Sr dopant content. The one-step synthesis of doped $CaTiO_3$ ($Sr_xCa_{1-x}TiO_3$, $Sr_{0.2}Ca_{0.8}Ti_{1-x}Fe_xO_3$) nanoparticles by CHFS at supercritical conditions was also studied [104,105]. In all cases, pH had a rather large effect on the phase purity of the nanoparticles. In general, a high conversion rate of Ca and Sr required a high alkaline condition [104]. Moreover, during the synthesis, the solubilities of both the TiO_2 and Fe species were increased when a high alkaline condition (pH > 13, [105]) was used. Therefore, the pH during CHFS should be carefully controlled and a high pH was preferred in order to get single-phase doped oxides.

CHFS of other types of perovskite oxides including $BaZrO_3$ [106] and $Na_xK_{1-x}NbO_3$ [107] at supercritical conditions were also reported. The water density affected the phase purity of the as-synthesized $KNbO_3$ at the supercritical condition. Single-phase $KNbO_3$ nanoparticles were only obtained when the temperature was over 753 K and the corresponding density of the scH_2O was lower than 100 kg m^{-3}.

Spinel oxide. Homogeneous spinel-type oxides are attractive for their magnetic and electric properties that can be used in magnetic storage (e.g. ferrites) and catalytic processes (e.g. manganites). The chemical formula of a spinel-type oxide is AB_2O_4 (A, B are metal cations). One can expect that a feasible synthesis method should be able to form a homogeneous solid solution of the A and B mono-oxides without leaving impurities.

$MeFe_2O_4$ (Me = Co, Ni, Cu and Zn) nanoparticles were synthesized by CHFS at supercritical conditions. CHFS of $CoFe_2O_4$ at supercritical conditions (653 K, 24 MPa [108]; 713 K, 30 MPa [109]) resulted in single-phase nanoparticles of which the average size was as small as 3 nm. However, α-Fe_2O_3 often came as an impurity because the solubility of the Fe-hydrated species at supercritical conditions was lower in comparison to that of the Co-hydrated species [108] and α-Fe_2O_3 nucleated from the supersaturated solution prior to the reaction with Co-hydrated species. Introducing alkali to the system was necessary to get the spinel phase. The processing conditions such as the temperature, pH and residence time had to be carefully controlled in order to get a single-phase homogeneous $MeFe_2O_4$ by adjusting solubilities of Me- and Fe-hydrates to a similar order [110,111]. As shown in **Fig. 1.12** (reproduced with the original figure from [57], ZnO is not presented), the solubility decreases in the order ZnO > CuO > NiO > Fe_2O_3, which means the driving force for the nucleation of Fe_2O_3 from the supersaturated solution would be the largest [110]. This explains the presence of (α/γ)-Fe_2O_3 often observed as byproducts [108,110]. Taking CHFS of $NiFe_2O_4$ [111] as an example, a high reaction temperature (> 647 K) was required to obtain the phase-pure nanoparticles. Moreover, by increasing the pH with addition of NaOH, the conversion rate of Ni could

be increased and thus a stoichiometric $NiFe_2O_4$ (Ni/Fe molar ratio = 0.5) could be obtained since the difference between the solubility of NiO and Fe_2O_3 was significantly narrowed (**Fig. 1.12**).

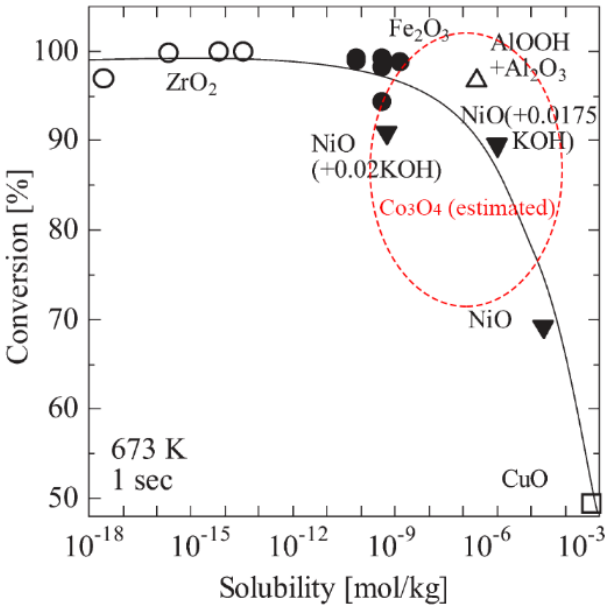

Figure 1.12 Solubilities of metal oxides in the scH_2O (673 K, 30 MPa); the solubility of Co_3O_4 was estimated to be within the region based on results from ref. [93,108,112]. Reproduced with the original figure adopted from ref. [57].

In addition to a careful control of the reaction temperature and pH, CHFS of phase-pure $NiCo_2O_4$ required the addition of H_2O_2 as an oxidant when Co(II) precursor was used [112]. To obtain phase-pure spinel-type oxides ($CuMn_2O_4$ [113], $MgFe_2O_4$ [114], and $CoAl_2O_4$ [115]) of two metals of which the oxides have rather different solubilities was rather challenging by CHFS, as very often a second phase was found in the products.

Electrode materials for Li-ion batteries. The Li-ion batteries (LIBs) are one of the most popular rechargeable batteries that have found wide applications in portable electronics, electric vehicles, etc. Since its beginning, CHFS has been used to develop materials for LIBs. Its high productivity makes it possible to bridge a laboratory research to a large-scale industrial production.

$LiCoO_2$ is used as the prevalent cathode material for LIBs. Starting from LiOH and $Co(NO_3)_2$, fine $LiCoO_2$ particles (< 1 µm) were prepared by CHFS with a residence time short as 7 s [116,117]. The phase-pure $LiCoO_2$ could be obtained only at supercritical conditions (> 663 K). H_2O_2 was used as

an oxidant for Co(II) as the released O_2 is miscible with the scH_2O providing a homogeneous oxidative environment. A sufficient amount of H_2O_2 was necessary to avoid the formation of $CoO/Co(OH)_2$ as byproducts. Either a subcritical reaction temperature or a low LiOH/Co molar ratio (< 10) should be avoided in order to get a phase-pure $LiCoO_2$. [117].

$LiFePO_4$ can be synthesized by CHFS at both the subcritical (573 K) and supercritical conditions (658 K) [118]. The average size of the synthesized particles was increased from 44 nm to 117 nm as the reaction temperature was increased. Meanwhile, the morphology of the $LiFePO_4$ particles became more spherical at the high reaction temperature. Carbon-coated $LiV_xFe_{1-x}PO_4$ nanoparticles with a core-shell structure were also prepared by CHFS [119]. The V dopant level affected both the particle size and morphology, as an increase in the content of V resulted in larger particles (> 100 nm) and change of the morphology from the spherical to the platelet.

As an alternative to the conventionally used graphite, $Li_4Ti_5O_{12}$ is developed for an anode material of LIBs that is known for its safety, good Li-ion mobility, long cycle life and low volume change during the charge/discharge process [120]. A rapid single-step synthesis of $Li_4Ti_5O_{12}$ by CHFS was conducted at the near- and supercritical condition (623 – 773 K, 25 MPa). Cube-shaped nanoparticles were obtained of which the average particle size (2 – 20 nm) was highly dependent on the reaction temperature and residence time [121]. Increasing the reaction temperature resulted in an increase of the average size as well as the crystallinity of the as-synthesized particles. However, extending the residence time (> 30 s) not only increased the average particle size but also brought more anatase TiO_2 as an impurity.

Nanophosphor. Inorganic phosphors are fundamental materials in applications such as lighting devices and displays. The desired phosphors should have a high luminescence efficiency and a high chemical and physical stability. The study on the synthesis and properties of nanophosphors is active due to the known size quantum effects of nanoparticles [122].

ZrO_2:Eu^{3+} with a tetragonal [123] and cubic [124] phase nanoparticles (5 – 6 nm) were separately obtained by CHFS (the two phases show nearly identical XRD patterns so the two reported results might be in fact the same). ZrO_2:Eu^{3+} nanoparticles were obtained at both the subcritical and supercritical conditions (573 – 673 K). The reaction temperature affected the average size of the nanoparticles as a higher reaction temperature resulted in a larger average particle size (~10 nm at 573 K to ~25 nm at 673 K) [124]. Moreover, a high reaction temperature (> 623 K) was favored to get a full conversion of metal cations from the precursors to the oxides.

YAG ($Y_3Al_5O_{12}$) based oxides also account for a fraction of the inorganic phosphors. CHFS was applied to a continuous production of YAG [125], YAG:Tb^{3+} [126], and YAG:Eu^{3+} [127] nanoparticles. A high temperature (> 658 K [125]) within the supercritical condition was necessary to obtain nanoparticles with a small size (50 nm) and narrow size distribution. A relatively long reaction time (≥ 20 s) was optimal to get phase-pure YAG-based oxides over a wide range of pHs without impurities such as AlOOH and YOOH [126,127].

The green-emitting (α-Zn_2SiO_4:Mn^{2+} [128]), yellow-emitting (β-Zn_2SiO_4:Mn^{2+} [128]), blue-emitting ($ZnGa_2O_4$:Mn^{2+} [129]) and red-emitting (Pr-doped $CaTiO_3$ [130]) nanophosphors were also prepared by CHFS in a single step. Zn_2SiO_4:Mn^{2+} sub-micrometer particles in a composite of α and β phases were obtained with a residence time as short as 0.1 s at supercritical conditions (≥ 673 K, ≥ 30 MPa). The type of precursors for the synthesis together with the pH affected the relative solubilities of Zn, Si and Mn, which therefore should be carefully controlled in order to get the particles in the desired phase crystallized from solutions. Increasing the reaction temperature (673 – 773 K) resulted in a higher crystallinity, a larger average size (270 – 450 nm) and change of the morphology from round to rod-shaped of the Zn_2SiO_4:Mn^{2+} particles [128]. Similarly, due to the rather different solubilities of Zn, Ga and Mn, a very narrow pH range (7 – 10) was optimal for the precipitation of phase-pure $ZnGa_2O_4$:Mn^{2+} without ZnO as a by-product [129]. In the case of Pr-doped $CaTiO_3$, the use of a high pH (KOH/NO^{3-} molar ratio ≥ 1) and a relatively long residence time (≥ 5 s) was necessary in order to get phase-pure Pr-doped $CaTiO_3$ nanoparticles of stoichiometric compositions [130].

Mineral compounds. CHFS of mineral compounds has also attracted a wide attention. Boehmite (γ-AlOOH) can act as a catalyst support or as a precursor for the production of Al_2O_3. It was prepared in a single step by CHFS at both subcritical and supercritical conditions [32,131,132]. In addition to the pressure, the reaction temperature (≥ 523 K [32], > 503 K [131]) was important for a successful crystallization, and affected the highly anisotropic morphology of the as-synthesized boehmite particles. The morphology evolution with the temperature and pressure was studied in [32,131] in detail.

Hydroxyapatite [$Ca_{10}(OH)_2(PO_4)_6$] is a synthetic apatite that is chemically compatible with the biological apatite in bones, and it is widely used as a bioceramic in biomedical areas. A continuous production of hydroxyapatite by CHFS was conducted at both subcritical and supercritical conditions (573 – 673 K). The hydroxyapatite particles displayed a nanorod morphology and the average particle size increased with the reaction temperature [133]. During the CHFS process, the reaction temperature, pH and the type of alkali could be used to change the size and morphology (nanorod, nanotube and nanosheets) of the synthesized hydroxyapatite, although the correlations were not fully understood [134]. To improve the mechanical properties, the preparation of cation-substituted and anion-substituted hydroxyapatite by CHFS was also reported [134–136]. Single-phase $Mg_xCa_{10-x}(OH)_2(PO_4)_6$ nanorods were prepared of which the stoichiometric composition was controlled and the Mg level could be as high as $x = 0.2$ [135]. CHFS was applied to the preparation of phase-pure carbonate-substituted and silicate-substituted hydroxyapatite [$Ca_{10}(OH)_2(CO_3)_x(PO_4)_{6-x}$ and $Ca_{10}(OH)_2(SiO_4)_x(PO_4)_{6-x}$] nanorods with the highest dopant levels up to 5 wt% carbonate and 1.1 wt% silicate at the applied conditions. The incorporation of carbonate into the structure was found to reduce the average size of the nanorods [136].

Continuous productions of layered double hydroxides (LDHs) of $[Ca_2Al(OH)_6]NO_3$ and $[Mg_3Al(OH)_8](CO_3)_2$ [137] and of tobermorite [138] by CHFS were also reported. The reaction temperature during CHFS was lower than 523 K to avoid the decomposition of the formed LDHs. Moreover, an increase in the reaction temperature drove the growth of hydroxides and

simultaneously changed the morphology. However, the influence of the pressure was less pronounced [137].

Metal nanoparticles. The broad applicability of CHFS was also highlighted by being applied in a continuous production of metal nanoparticles. The synthesis takes advantage of the property that H_2 or reductive organics are highly miscible with the H_2O at the near- or supercritical state. As a result, a homogeneous reductive atmosphere is formed.

Fine Ni particles (< 600 nm) were precipitated on the surface of Fe_3O_4 by CHFS at subcritical conditions (593 – 633 K) and with the presence of H_2 decomposed from formic acid [139]. 1,10-phenanthroline was used to complex the Ni^{2+} cations to prevent the hydrolysis of Ni^{2+} in water, which otherwise would favor the formation of NiO at a hydrothermal condition. Moreover, the reaction temperature should be set lower than 633 K as NiO was found at higher reaction temperatures. Similarly, in the CHFS process of preparing Ni nanoparticles starting from Ni^{2+}-hydrazine complex, the reaction temperature should be lower than 623 K to avoid the decomposition of hydrazine prior to reducing Ni^{2+} [140]. It seems that during CHFS of metal nanoparticles, the hydrolysis of metal cations (Ni^{2+}) should be prevented and in general, a relatively low reaction temperature is favored. However, a different pathway of the formation of metal nanoparticles by CHFS was proposed in the case of synthesizing Cu nanoparticles [141]. The Cu^{2+} hydrated first, which was followed by dehydration to oxides and reduction to Cu with the presence of H_2 formed by the decomposition of formic acid. Therefore, a relative long residence time (> 0.4 s) and a sufficient amount of formic acid (HCOOH / $Cu(HCOO)_2$ molar ratio ≥ 5) were required to get phase-pure Cu nanoparticles without impurities such as CuO and Cu_2O. The average size of the Cu nanoparticles significantly decreased when the reaction temperature (673 K) exceeded the critical point because a highly supersaturated solution rapidly formed above the critical point that resulted in large amounts of nuclei. A similar result was also observed in CHFS of Ag nanoparticles. At supercritical conditions a higher reaction temperature resulted in Ag nanoparticles with a smaller average size [142]. CHFS was also applied to the synthesis of Bi_2Te_3, an alloy known as a thermoelectric material [143]. It was found that the

reductive ability of glucose used as the reductant during the synthesis was dependent on the concentration of the added NaOH, which affected the phase and composition of the alloy obtained from the CHFS system.

Organic-inorganic hybrid nanoparticles. The fact that non-polar organics are highly miscible with H_2O at the near- and supercritical conditions due to the reduced dielectric constant also provides a homogeneous environment for reactions between the organics and inorganics. *In situ* modification by organics on the surface of the as-synthesized inorganic nanoparticles, as well as the synthesis of organic-inorganic hybrid nanocomposites therefore can be realized by CHFS with the (near-) supercritical water as the reaction medium.

During CHFS, organics can be introduced to tune the size and morphology of nanoparticles. For instance, oleic acid was introduced in the CHFS process at the near- and supercritical hydrothermal conditions (623 – 653 K) to tune the morphology and size of the as-synthesized $BaFe_2O_4$ nanoparticles [144]. With the oleic acid acting as the capping agent, it was possible to tune the morphology from spherical-shaped to cube- and octahedral-shaped depending on the amount of oleic acid. The average particle size was also reduced from 20 nm (no capping agent) to 9 nm.

The stability of the as-prepared inorganic nanoparticles dispersed in aqueous or organic solvents also can be adjusted by surface modification. In CHFS, organic surfactants could be introduced shortly after the synthesis of nanoparticles, and the colloidal properties of the organic-modified nanoparticles could be controlled due to the presence of organic chains on the surface [115,145–147]. For example, magnetite (Fe_3O_4) nanoparticles used for magnetic resonance imaging in the biomedical area should be highly dispersible in water and blood without agglomeration. The inherently hydrophobic Fe_3O_4 nanoparticles could be made hydrophilic by surface functionization with citric acid or 3,4-dihydroxyhydrocinnamic acid that were introduced during the CHFS process [145,146]. Reversely, by introducing hydrophobic organic capping agents such as hexanoic acid [115] and dodecyl succinic acid [147] during CHFS, the surface-functioned nanoparticles could be easily extracted from an aqueous solvent and well dispersed in an organic solvent. Further, the

surface-functionalized nanoparticles prepared by CHFS could also be used for '*click reactions*', as the presence of organic chains on the surface could act as clickable anchors. This enables CHFS to be used for a highly efficient and potentially large-scale synthesis of wide types of organic-inorganic functional nanomaterials [148].

Sulphides. Aside from metal oxides and metals, synthesis of metal sulphides by CHFS has also been reported [149]. Thiourea provided the only source of S and therefore its decomposition at different conditions significantly affected the phase of the synthesized metal sulphides by CHFS. For instance, in the synthesis of ZnS, when the thiourea was premixed with the metal salt at the room temperature and were then heated by the (near-) scH_2O, a high temperature (≥ 673 K) was required to obtain ZnS. This was because the decomposition of the thiourea to HS^- was limited by the short residence time, one of the inherent characteristics of the CHFS process. In comparison, if the thiourea was premixed with H_2O and was heated together to the (near-) supercritical state, the reaction temperature required to get ZnS could be lowered down to 523 K, as the time for thiourea decomposition was much longer. Moreover, it was found that separating the two processes, i.e. formation of HS^- and the precipitation of metal sulphides, by feeding the thiourea with the (near-)scH_2O to the CHFS system was favored since uniform and monodisperse metal sulphides particles could be obtained in this case.

Metal organic frameworks. Metal organic frameworks (MOFs) are hybrid materials in which metal ions or metal clusters are connected by polydentate organic ligands. The MOFs display an architecture of a large porosity with pore size ranging from 2 to 50 nm. They are thus attractive for applications such as gas adsorption, storage and sensing, catalysis and drug delivery [150,151]. Synthesis of MOFs by CHFS with the potential to scale up to an industrial level has been reported [151,152]. A continuous production of the phase-pure copper (II) carboxylate (HKUST-1) by CHFS was conducted at subcritical conditions (≤ 573 K), as the synthesis at the supercritical condition (673 K) resulted in Cu_2O [151]. The concentration of the Cu(II) precursor affected the size of the as-prepared HKUST-1, and smaller crystals were found when a higher concentration of the Cu(II)

precursor was used. The observation is similar to those found in the synthesis of metal oxides by CHFS, which is related to the sudden decrease of solubilities when the metal precursors are heated rapidly by the (near-) scH_2O. A higher degree of supersaturation is achieved when a precursor of a higher concentration is used, which according to the nucleation theory resulted in forming larger amounts of nuclei however smaller size of each nuclei. A similar dependence of the crystal size of Ni(II) carboxylate (CPO-27) [151] and zeolitic-imidazolate framework (ZIF-8) [152] on the concentration of the Ni(II) and Zn(II) precursors was also found.

Table 1.1. Representative samples of nanomaterials prepared by CHFS in scH_2O

Sample	**Precursor**	**T (K); P (MPa); τ (s)**	**Morphology; Size (nm)**	**Ref.**
(cubic)ZrO_2	$ZrOCl_2$	673 – 763; 30; ~120	spherical; ~10	[9]
(orthorhombic + monoclinic)ZrO_2	$ZrO(NO_3)_2$	673; 30	4.3 – 4.7	[57]
(tetragonal + monoclinic) ZrO_2	Zr $(ac)_4$	573 – 723; 10 – 45; 1 – 65	3.8 – 6.8	[58]
$Y_xZr_{1-x}O_2$	$ZrO(NO_3)_2$, $Y(NO_3)_3$	573 – 673; 30; 0.17 – 0.35	4 – 6	[59]
$Y_xZr_{1-x}O_2$	$ZrO(NO_3)_2$, $Y(NO_3)_3$	623 – 673; 25 – 35; 30 – 60	≤ 5	[60]
CeO_2	$Ce(NO_3)_3$	573 – 673; 30; 0.3 – 43	octahedral; 20 – 300	[62]
$Zr_xLa_yPr_zCe_{1-x-y-z}O_2$	$(NH_4)_2Ce(NO_3)_6$, $ZrO(NO_3)_2$, $La(NO_3)_3$, $Pr(NO_3)_3$	673; 24.5; 10 – 60	6 – 7.7	[63]
$Bi_xCe_{1-x}O_2$ ($0 \leq x \leq 0.07$)	$Bi(NO_3)_3$, $(NH_4)_2Ce(NO_3)_6$	648; 25; 15	spherical; 2.5 – 4.5	[64]
$Zn_xCe_{1-x}O_2$ ($0 \leq x \leq 0.3$)	$Zn(NO_3)_2$, $(NH_4)_2Ce(NO_3)_6$	673 – 723; 24.1	faceted; 3.2 – 4.8	[40,65]
$ZrxCe_{1-x}O_2$	$Zr(ac)_4$, $(NH_4)_2Ce(NO_3)_6$	573; 25	3 – 7	[66]
$ZrxCe_{1-x}O_2$	$ZrO(NO_3)_2$, $Ce(NO_3)_3$	673; 25; 6	6.8 – 16.2	[67–69]
$Zr_xLa_yY_zCe_{1-x-y-z}O_2$	$ZrO(NO_3)_2$, $La(NO_3)_3$, $Y(NO_3)_3$, $(NH_4)_2Ce(NO_3)_6$	723; 24.1	near-spherical; 2.8 – 6	[70]

ZnO	$Zn(NO_3)_2$	573 – 673; 30; 0.5 – 1	spherical; 23 – 57	[71]
ZnO	$Zn(OAc)_2$	673; 24.5; 8.9 – 16.3	spherical; 120 – 320	[72]
ZnO	$Zn(NO_3)_2$	673; 30; 10	nanorod; 150 (Ø), 600 (H)	[73]
ZnO	$Zn(NO_3)_2$	683; 30.5; 11	nanorod, spherical; 19 – 331 (Ø), 22 – 166 (H)	[74]
ZnO	$Zn(NO_3)_2$	513 – 673; 26	near-spherical; 20 – 25	[75]
ZnO	$Zn(NO_3)_2$	673 – 723; 24.1	polygonal (near-spherical); 53(22)	[76]
ZnO	$Zn(NO_3)_2$, H_2O_2	673 – 723; 24.1	nanorod; 59(24) (Ø), 15(5) (H)	[76]
$Al_xZn_{1-x}O$	$Al(NO_3)_3$, $Zn(NO_3)_2$	608; 24.1	nanorod; 38(17) – 43(14) (Ø), 132(83) – 187(92) (H)	[12]
$Ga_xZn_{1-x}O$	$Ga(NO_3)_3$, $Zn(NO_3)_2$	608; 24.1	near-spherical; 36(9) – 44(8)	[12]
$Al_xGa_yZn_{1-x-y}O$	$Al(NO_3)_3$, $Ga(NO_3)_3$, $Zn(NO_3)_2$	608; 24.1	nanorod; 23.2 – 26.3; 19.3 – 21.9	[13]
TiO_2	$TiCl_4$, $TiSO_4$	673 – 723; 30 – 35	prismatic; ~20	[9]
TiO_2	$TiCl_4$	508 – 703; 0.58 – 50 (water – propanol)	disk-shaped; 10.6 – 17.2	[78]
TiO_2	$Ti(SO_4)_2$	673 – 773; 30; 0.6 – 5.5	disk-shaped; 13 – 30	[79]
TiO_2	$Ti[OCH(CH_3)_2]_4$	523 – 673; 25; ~10 (water – isopropanol)	near-spherical; 8.2 – 19.2	[80]
TiO_2	$TiOSO_4$	641; 24.1; ~5	near-spherical; ~4	[81]
$Sn_xTi_{1-x}O_2$	$SnSO_4$, $TiOSO_4$	641; 24.1; ~5	near-spherical; ~5.4	[81]
In_2O_3	$In(NO_3)_3$	580; 24.1	spherical; 14	[82]

Sn-doped In_2O_3	SnO_2 sol, $In(NO_3)_3$	723; 30; 7	spherical; ~30	[84]
Sn-doped In_2O_3	K_2SnO_3, $In(NO_3)_3$	623 (heat treated at 873); 24.1	spherical, cube; 11(5)	[14]
VO_2	NH_4VO_3	608 – 648; 24.1; 20 – 27	nanosheets; 40	[87,88]
Nb-doped VO_2	$C_4H_4NNbO_9$, NH_4VO_3	608; 24.1; 10	plate-like microcrystals, round nanocrystals; 20 - 200	[90]
MnO_2, Mn_2O_3	$Mn(NO_3)_2$	653 – 703; 30	micro-rods, spherical micro particles	[91]
MnO_2, Mn_2O_3	$Mn(NO_3)_2$	673; 30; 38	(MnO_2) rod; 1 – 2 µm; (Mn_3O_4) spherical particles; 10 – 200 nm	[92]
α-Fe_2O_3	$Fe(NO_3)_3$	469 – 659; 24.5	near-cube; 27 – 97	[93]
(α, γ)-Fe_2O_3	$Fe(NO_3)_3$	673; 30; 0.002 – 2.028	4 – 6.7	[94]
Fe_3O_4	Fe^{2+}, Fe^{3+}; citrates	423; 25; 4	near-cube; 3.8 – 17.8	[95]
Co_3O_4, CoO	$Co(NO_3)_2$	673; 30; 21	faceted cube (Co_3O_4); 100 – 400; irregular-shaped (CoO); 20 – 200	[92]
Co_3O_4	$Co(NO_3)_2$	473 – 659; 24	cube; 20 – 37	[93]
Co_3O_4	$Co(OAc)_2$, H_2O_2	473 – 603; 24; 0.5 – 7	cube; 9 – 20	[96]
Co_3O_4	$Co(OAc)_2$, H_2O_2	673; 24	cube; 2 – 10	[97]
Co_3O_4	$CoCl_2$, urea	553 (annealed at 573); 20	octahedron; 1300	[98]
NiO	$Ni(NO_3)_2$	673; 30; 1.3 – 2.7	nano-plate; 20.1 – 54.3	[45]

NiO	$Ni(NO_3)_2$	673; 30; 0.002 – 2.008	nano-plate; 15.4 – 18.7	[94]
NiO	$Ni(NO_3)_2$	673; 30	nano-plate; 3.4 – 16.7	[57]
CuO	$Cu(NO_3)_2$	673; 30	near-cube; 31	[57]
CuO	$Cu(NO_3)_2$	673; 30; 0.002 – 2.008	near-cube; 23.7 – 34.3	[94]
CuO	$CuSO_4$	673; 30	near-cube; 29.8 – 63.8	[43]
$BaTiO_3$	TiO_2 sol, $Ba(OH)_2$	573 – 693; 20 – 40; 0.69 – 5.11	spherical; 30; cube; 50 – 100	[99]
$BaTiO_3$	TiO_2 sol, $Ba(OH)_2$	573 – 693; 30; 0.1 – 40	spherical; 36 – 46; cube; 50	[100]
$BaTiO_3$	TiO_2 sol, $Ba(OH)_2$	673; 30; 0.007 – 2	spherical; 8.9 – 32.3	[101]
$BaTiO_3$	TiO_2 sol, $TiCl_4$, $Ba(NO_3)_2$	673; 30; 0.008	spherical; 5.6 – 12.7	[102]
$Sr_xBa_{1-x}TiO_3$	$Ba[OCH(CH_3)_2]_2$, $Sr[OCH(CH_3)_2]_2$, $Ti[OCH(CH_3)_2]_4$ dissolved in ethanol	673; 23; 50 (water – ethanol)	cube; 16 – 20	[103]
$Sr_xBa_{1-x}TiO_3$	$[CH_3CH(O-)CO_2NH_4]_2Ti(OH)_2$, $Ba(NO_3)_2$, $Sr(NO_3)_2$	663; 25	7.9 – 17.3	[17]
$Sr_xCa_{1-x}TiO_3$	$Ca(NO_3)_2$,$Sr(NO_3)_2$, TiO_2 sol	673; 30; 5	cube; 22 – 36	[104]
$Sr_{0.2}Ca_{0.8}Fe_xTi_{1-x}O_3$ ($0.1 \leq x \leq 0.3$)	$Ca(NO_3)_2$, $Sr(NO_3)_2$, $Fe(NO_3)_3$, TiO_2 sol	673; 30; 10	cube; 20 – 27	[105]
$BaZrO_3$	$ZrO(NO_3)_2$, $Ba(NO_3)_2$, $Ba(OAc)_2$	723 – 758; 30; 15 – 31	spherical; 67 – 134	[106]
$Na_xK_{1-x}NbO_3$	Nb_2O_5 sol, KOH, NaOH	673 – 753; 25 – 30; 0.1 – 8.3	cube; ~200 ($KNbO_3$); 50 – 100($NaNbO_3$); 55.1 ($Na_xK_{1-x}NbO_3$)	[107]
$CoFe_2O_4$	$Co(NO_3)_2$, $Fe(NO_3)_3$	467 – 653; 23 – 25; 11 – 23	12 – 15	[108]
$CoFe_2O_4$	$Co(NO_3)_2$, $Fe(NO_3)_3$	713; 30; 10	3	[109]

$MeFe_2O_4$ (Me = Ni, Cu, Zn)	$Ni(NO_3)_2$, $Cu(NO_3)_2$, $Zn(NO_3)_2$, $Fe(NO_3)_3$	673; 30; 0.002 – 4	8.8 (Ni); 21.6 (Cu); 13.8 (Zn)	[110]
$NiFe_2O_4$	$Ni(NO_3)_2$, $Fe(NO_3)_3$	673; 30; 1	cube-shaped; 4.9	[111]
$NiCo_2O_4$	$Ni(NO_3)_2$, $Co(NO_3)_2$, H_2O_2	583 – 723; 24.1	cube-shaped; 3 – 15	[112]
$CuMn_2O_4$	$CuMn(OH)_3$ sol	673; 30	spherical, cube; 20 – 25	[113]
$MgFe_2O_4$	$Fe(OH)_3$ + $Mg(OH)_2$ suspension	733; 30; 0.9	spherical; 17(3)	[114]
$CoAl_2O_4$	$Co(OH)_2$ + $Al(OH)_3$ sol	523; 30; 2	15	[115]
$LiCoO_2$	LiOH, $Co(NO_3)_2$, H_2O_2	673; 30	dodecahedron; 600 – 1000	[116]
$LiCoO_2$	LiOH, $Co(NO_3)_2$, H_2O_2	663 – 684; 30; 7 – 58	plate; 550	[117]
$LiFePO_4$	$FeSO_4$, H_3PO_4, LiOH	573, 658; 25	spherical; 110 (658 K)	[118]
C-coated $LiV_xFe_{1-x}PO_4$	fructose, $FeSO_4$, $VOSO_4$, LiOH	608; 24.1; ~6.5	spherical; < 100 platelet; > 100	[119]
$Li_4Ti_5O_{12}$	$Li[OCH_2CH_3]$, $Ti[OCH(CH_3)_2]_4$	623 – 773; 25; 30 – 300	cube; 2 – 20	[121]
$ZrO_2:Eu^{3+}$	$ZrO(NO_3)_2$, $Eu(NO_3)_3$	573 – 673; 30	spherical; 5	[123]
$ZrO_2:Eu^{3+}$	$Zr(ac)_4$, $Eu(ac)_3$, H_2O_2	573 – 673; 24; 4	spherical; 5.7	[124]
YAG ($Y_3Al_5O_{12}$)	$Al(acac)_3$, $Y(ac)_3$ (solvent: ethanol and water)	533 – 658; 24; 3 – 13	cube-shaped; 50 – 150	[125]
$YAG:Tb^{3+}$	$Al(NO_3)_3$, $Y(NO_3)_3$, $Tb(NO_3)_3$	673; 30; 2.5	cube-shaped; 40 – 140	[126]
$YAG:Eu^{3+}$	$Al(NO_3)_3$, $Y(NO_3)_3$, $Eu(NO_3)_3$	673; 28; 5 – 20	spherical; 65 – 94	[127]
$Zn_2SiO_4:Mn^{2+}$	$Zn(NO_3)_2$, $ZnSO_4$, $Zn(OAc)_2$; $Mn(NO_3)_2$, $MnSO_4$, $Mn(OAc)_2$; $NaSiO_3$, SiO_2 sol	673; 30; 0.13	spherical, rod; 270 – 450	[128]
$ZnGa_2O_4:Mn^{2+}$	$Zn(NO_3)_2$, $Mn(NO_3)_2$, $Ga(NO_3)_3$	573 – 773; 25 – 35; 0.13 – 1.13	octahedron; 11.5 – 19.6	[129]
Pr-doped $CaTiO_3$	$Ca(NO_3)_2$, $Pr(NO_3)_3$, TiO_2 sol	673; 30; 5	cube; 11 – 24	[130]

γ-AlOOH (boehmite)	$Al(NO_3)_3$	523 – 763; 25 – 45	needle-shaped, rhombic plate-shaped, hexagonal plate-shaped; 100 – 1500	[32]
γ-AlOOH (boehmite)	$Al(NO_3)_3$	603 – 693; 20 – 40	needle-shaped; plate-shaped, bar-shaped; 200 – 1200	[131]
γ-AlOOH (boehmite)	$Al(NO_3)_3$	623 – 673; 25 – 40	plate-shaped; 70 – 470	[132]
$Ca_{10}(OH)_2(PO_4)_6$	$Ca(NO_3)_2$, $(NH_4)_2HPO_4$	573 – 673; 24	nanorods; 15 – 40 (Ø), 65 – 140 (H)	[133]
$Mg_xCa_{10-x}(OH)_2(PO_4)_6$	$Mg(NO_3)_2$, $Ca(NO_3)_2$, $(NH_4)_2HPO_4$	548; 24	nanorods; 57 (Ø), 234 (H)	[135]
$Ca_{10}(OH)_2(CO_3)_x(PO_4)_{6-x}$, $Ca_{10}(OH)_2(SiO_4)_x(PO_4)_{6-x}$	$Ca(NO_3)_2$, $(NH_4)_2HPO_4$, urea, $Si(OAc)_4$	637; 24	(CO_3-substituted) nanorods; 27 – 50 (Ø), 64 – 146 (H); (SiO_4-substituted) nanorods; 40 (Ø), 140 – 184 (H)	[136]
$[Ca_2Al(OH)_6]NO_3$, $[Mg_3Al(OH)_8](CO_3)_2$	$Ca(NO_3)_2$, $Mg(NO_3)_2$, $Al(NO_3)_3$	348 – 523; 5, 24; 4	nanoplate; 25 – 62 (L), 10 (H) (CaAl-NO3); 30 – 40 (L), 4 – 5 (H) (MgAl-CO3)	[137]
Ni precipitated on Fe_3O_4	$Ni(OAc)_2$, 1,10-phenanthroline, K(OAc), AcOH complex; $FeSO_4$, 1,10-phenanthroline, K(OAc), AcOH complex; formic acid (providing H_2)	593 – 653; 30; 19 – 26	22 – 98	[139]
Ni	$NiSO_4$, hydrazine hydrate	423 – 623; 30; 60	40 – 60	[140]

Cu	$Cu(HCOO)_2$, PVP; formic acid (providing H_2)	623 – 673; 25 – 30; 1.1 – 2.7	spherical; 17.3 – 42.3	[141]
Ag	Ag(OAc)	688; 23; < 2	spherical; 14 - 27	[142]
Bi_2Te_3	$BiCl_3$, $Te(OH)_6$, glucose	673; 30; < 60	granular; 70	[143]
oleic acid modified $BaFe_2O_4$	$Fe(NO_3)_3$, $Ba(OH)_2$, oleic acid	723 – 773; 30; 20	round, cube, octahedral; 28, 9, 8	[144]
ZnS, CdS, PbS, CuS, $Fe_{1-x}S$, Bi_2S_3	$Zn(NO_3)_2$, $Cd(NO_3)_2$, $Pb(NO_3)_2$, $Cu(NO_3)_2$, $FeSO_4$, $Bi(NO_3)_3$, thiourea	523 – 673; 25	varying among metal sulphides	[149]
Copper carboxylate (HKUST-1)	$Cu(NO_3)_2$, benzene-1,3,5-tricarboxylic acid	573; 25; < 1	< 10 µm	[151]
Nickel carboxylate (CPO-27)	$Ni(OAc)_2$, 2,5-dihydroxyterephthalic acid	573; 25	12 – 15	[151]
Zeolitic-imidazolate framework (ZIF-8)	$Zn(OAc)_2$, 2-methylimidazole, ammonium hydroxide	298 – 673; 24	cube; < 2 µm	[152]

1.2.5 *In situ* monitoring, thermodynamic and kinetic modelling of the process in CHFS

As reviewed above, the experimentation results of CHFS have made a magnificent contribution to the synthesis of various types of nanomaterials. In addition, a substantial effort has been made in order to identify the dependence of properties of the synthesized nanomaterials (e.g. phase, size, morphology, composition, etc.) on the processing parameters (e.g. temperature, pressure, flow rate, residence time, etc.). However, to link the properties to the reaction parameters is not straightforward. Firstly, during the CHFS process, altering one specific parameter can change other parameters, which makes it difficult to isolate the effect of a specific parameter [96]. For example, the change in the reaction temperature can alter the residence time of the process [79]. Secondly, CHFS appears like a ‘black box’ where the input and output are known whereas the process in-between is hidden. Therefore, advanced techniques for an *in situ* observation on the material formation process during

CHFS are highly desired. Alternatively, modelling of the process can be helpful to understand the process.

X-rays with a high energy and penetration capability are often used to study dynamic processes including crystallization and growth of nanoparticles at the subcritical and supercritical conditions within a capillary reactor simulating the conditions of CHFS (**Fig. 1.13**). For instance, time-resolved diffraction patterns of $Ce_xZr_{1-x}O_2$ [153], TiO_2 [154], and YAG [155] were obtained by the *in situ* synchrotron X-ray diffraction technique. Analyzing the diffraction data provides information on such as the phase transition and crystallite growth as the CHFS process proceeds. Moreover, by comparing the data obtained when varying the processing parameters, the effects can be clarified [154,155]. Aside from the diffraction, coupled *in situ* small angle X-ray scattering and wide angle X-ray scattering (SAXS/WAXS) were also used to study the nucleation and growth proceeding during the CHFS process [156,157]. Nucleation of CeO_2 nanoparticles occurring in the mixing zone where the scH_2O met and heated the Ce precursor was observed by the *in situ* X-ray tomography using the angle-dispersive and energy-dispersive X-ray radiations [158,159]. 2D maps of the diffraction peak intensity (indicating crystallinity) and of the FWHM of peaks (indicating crystallite size) within the mixing zone were obtained to reveal the formation process of CeO_2 by CHFS.

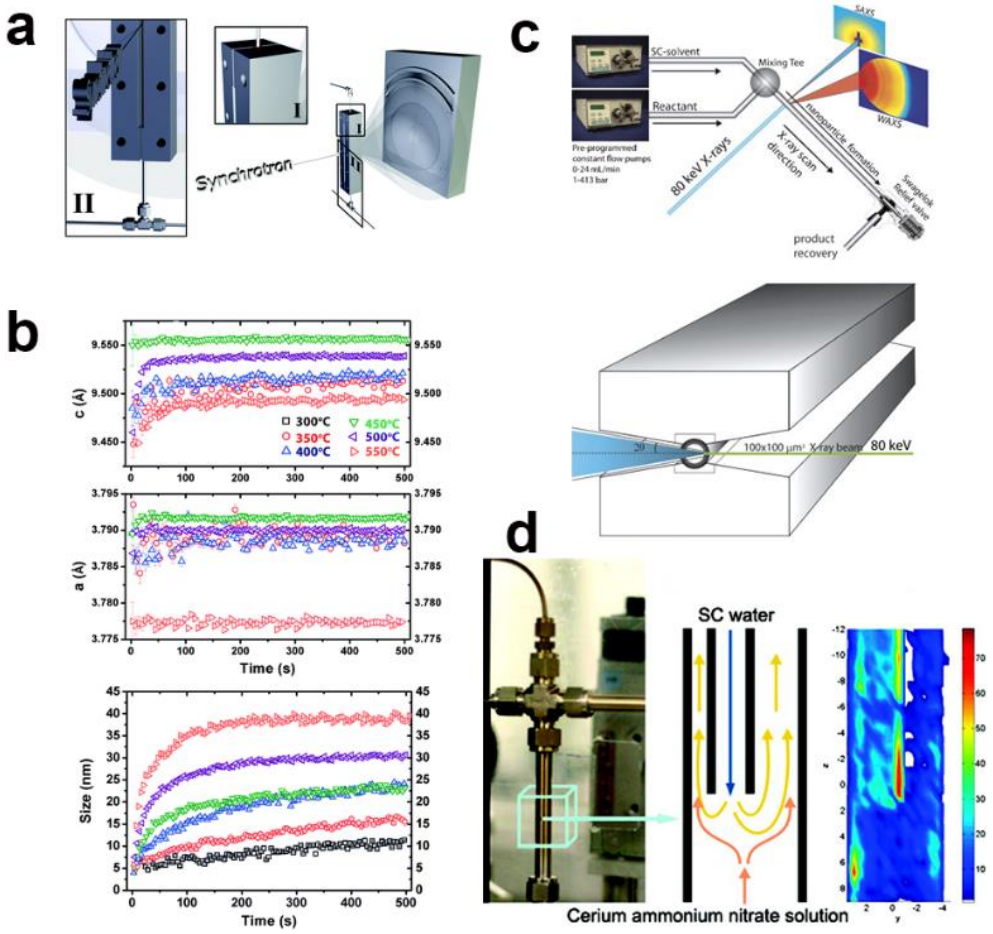

Figure 1.13 (**a**) Setup designed for *in situ* synchrotron X-ray diffraction; (**b**) time-resolved unit cell parameters and crystal size of anatase TiO_2 based on sequential Rietveld refinements of *in situ* synchrotron X-ray diffraction data. Reprinted from ref. [154]. (**c**) Continuous flow reactor for simultaneous *in situ* SAXS/WAXS measurement. Reprinted from ref. [156]. (**d**) Counter-current mixer of a continuous flow reactor; *in situ* X-ray tomography energy-dispersive diffraction image based on intensities from the ceria (113) reflection. Reprinted from ref. [158].

Numerical calculations have been used to predict the size distribution of the synthesized particles by CHFS [160–162]. The modelling was conducted based on the understanding that the CHFS process was divided into steps, including solution mixing, chemical reaction and crystallization (generation of supersaturation, nucleation and crystal growth). Therefore, a reaction model solving the reaction rate, a thermodynamic model solving the equilibrium, and a nucleation model solving the nucleation process were developed independently, and were further integrated with the population balance model solving the crystal growth to predict the particle size distribution. Effects

of the key processing parameters such as the reaction temperature and the residence time on the particle size distribution therefore could be quantitatively determined [160,161].

1.3 Overview of the PhD dissertation

Nowadays, the needs to develop clean and renewable energy cannot be overemphasized. SOFCs (an efficient use of fuels), Li-ion batteries (reliable energy storage), and catalytic hydrogen production (zero-emission fuel) represent three of the main ways towards a clean energy society. Oxide nanomaterials are particularly attractive to the above-mentioned applications, and are under focus of research with respect to their syntheses and properties.

The dissertation summarizes the work on continuous hydrothermal flow synthesis of several types of oxide (simple, doped and complex) nanomaterials, focusing on synthesis processes, characterizations and whenever possible primary applications. Divided by the type of material under focus, the dissertation is composed of chapters as following.

(1) Based on the results of CFD modelling, a two-stage flow-type apparatus (CHFS reactor) was built. Proof syntheses of NiO and Y-doped ZrO_2 (YSZ) nanoparticles were conducted with the newly built CHFS reactor. This part of work is presented in **Chapter III**.

(2) Gd-doped CeO_2, known for its good ionic conductivity and as a potential alternative to Y-doped ZrO_2, was another cubic fluorite-type oxide of interest. Syntheses of $Gd_xCe_{1-x}O_{2-\delta}$ (GDC) nanoparticles were studied. Further studies on applying wet as-synthesized nanoparticles to prepare inks available for inkjet printing of GDC electrolytes were conducted. Results are presented in **Chapter IV**.

(3) Composites of $Gd_xCe_{1-x}O_{2-\delta}$ (GDC) and $La_{1-x}Sr_xCoO_3$ (LSC) are attractive for many applications particularly in electrochemical processes, since the interface between them provides electrochemically active sites. Core-shell LSC-GDC particles were prepared by the conventional batch-type hydrothermal route. Spark plasma sintering and conventional sintering were applied to

compare the microstructural evolution of core-shell particles at different sintering conditions. Results are presented in **Chapter V**.

(4) Perovskite-type $LaCrO_3$ particles were synthesized by CHFS. The as-synthesized particles were applied to make dual-phase oxygen transport membranes. Results are presented in **Chapter VI**.

(5) Spinel-type $CoFe_2O_4$ and Ni-substituted $CoFe_2O_4$ ($Co_{1-x}Ni_xFe_2O_4$) nanoparticles were synthesized by CHFS. Catalytic activity of the nanoparticles were investigated in reactions including CO oxidation and oxygen evolution reaction. Results are presented in **Chapter VII**.

Table 1.2 presents an overview of the work included in the thesis.

Table 1.2. Overview of the materials and applications under focus in the thesis

Materials	**Applications**	**Chapters**
NiO	Advanced anode for SOFCs	Chapter III, Outlook
$Y_xZr_{1-x}O_{2-\delta}$		
$Gd_xCe_{1-x}O_{2-\delta}$	Electrolyte for SOFCs	Chapter IV
$(La_{0.6}Sr_{0.4})_{0.99}CoO_3$-$Gd_{0.2}Ce_{0.8}O_{2-\delta}$ core-shell structures		Chapter V
$LaCrO_3$	Oxygen transport membranes	Chapter VI
$Co_{1-x}Ni_xFe_2O_4$	Catalysts in CO oxidation and oxygen evolution reaction	Chapter VII
precursor of $La_{0.6}Sr_{0.4}CoO_3$	Cathode for SOFCs	Outlook
Mn_xO_y		Outlook

References

[1] M. Yoshimura, K. Byrappa, Hydrothermal processing of materials: past, present and future, J. Mater. Sci. 43 (2008) 2085–2103. doi:10.1007/s10853-007-1853-x.

[2] W. Shi, S. Song, H. Zhang, Hydrothermal synthetic strategies of inorganic semiconducting nanostructures, Chem. Soc. Rev. 42 (2013) 5714–5743. doi:10.1039/c3cs60012b.

[3] B.L. Cushing, V.L. Kolesnichenko, C.J. O'Connor, Recent advances in the liquid-phase syntheses of inorganic nanoparticles, Chem. Rev. 104 (2004) 3893–3946. doi:10.1021/cr030027b.

[4] K. Byrappa, T. Adschiri, Hydrothermal technology for nanotechnology, Prog. Cryst. Growth Charact. Mater. 53 (2007) 117–166. doi:10.1016/j.pcrysgrow.2007.04.001.

[5] K. Byrappa, M. Yoshimura, History of Hydrothermal Technology, in: Handb. Hydrothermal Technol. A Technol. Cryst. Growth Mater. Process., Noyes Publications, 2001: pp. 53–81. doi:10.1016/B978-081551445-9.50003-9.

[6] K.M.Ø. Jensen, C. Tyrsted, M. Bremholm, B.B. Iversen, In situ studies of solvothermal synthesis of energy materials, ChemSusChem. 7 (2014) 1594–1611. doi:10.1002/cssc.201301042.

[7] R.E. Riman, W.L. Suchanek, K. Byrappa, C.W. Chen, P. Shuk, C.S. Oakes, Solution synthesis of hydroxyapatite designer particulates, Solid State Ionics. 151 (2002) 393–402. doi:10.1016/S0167-2738(02)00545-3.

[8] B.T. Batio, A. Testino, V. Buscaglia, M.T. Buscaglia, M. Viviani, P. Nanni, Kinetic modeling of aqueous and hydrothermal synthesis of barium titanate (BaTiO3), Chem. Mater. 17 (2005) 5346–5356. doi:10.1021/cm051119f.

[9] T. Adschiri, K. Kanazawa, K. Arai, Rapid and continuous hydrothermal crystallization of metal oxide particles in supercritical water, J. Am. Ceram. Soc. 75 (1992) 1019–1022. doi:10.1111/j.1151-2916.1992.tb04179.x.

[10] X. Weng, J.K. Cockcroft, G. Hyett, M. Vickers, P. Boldrin, C.C. Tang, S.P. Thompson, J.E. Parker, J.C. Knowles, I. Rehman, I. Parkin, J.R.G. Evans, J.A. Darr, High-throughput continuous hydrothermal synthesis of an entire nanoceramic phase diagram, J. Comb. Chem. 11 (2009) 829–834. doi:10.1021/cc900041a.

[11] R. Quesada-Cabrera, X. Weng, G. Hyett, R.J.H. Clark, X.Z. Wang, J.A. Darr, High-throughput continuous hydrothermal synthesis of nanomaterials (part II): unveiling the as-prepared CexZryYzO2-ð phase diagram., ACS Comb. Sci. 15 (2013) 458–463. doi:10.1021/co3001346.

[12] D.P. Howard, P. Marchand, I.D. Johnson, C.J. Carmalt, I.P. Parkin, J.A. Darr, Conducting Al and Ga-

doped zinc oxides; rapid optimisation and scale-up, J. Mater. Chem. A. 4 (2016) 12774–12780. doi:10.1039/C6TA03364D.

[13] D.P. Howard, P. Marchand, L. McCafferty, C.J. Carmalt, I.P. Parkin, J.A. Darr, High-throughput continuous hydrothermal synthesis of transparent conducting aluminum and gallium co-doped zinc oxides, ACS Comb. Sci. 19 (2017) 239–245. doi:10.1021/acscombsci.6b00118.

[14] P. Marchand, N.M. Makwana, C.J. Tighe, I. Gruar, I.P. Parkin, C.J. Carmalt, J.A. Darr, High-throughput synthesis, screening, and scale-up of optimized conducting indium tin oxides, ACS Comb. Sci. 18 (2016) 130–137. doi:10.1021/acscombsci.5b00166.

[15] N.M. Makwana, C.J. Tighe, R.I. Gruar, P.F. McMillan, J.A. Darr, Pilot plant scale continuous hydrothermal synthesis of nano-titania; effect of size on photocatalytic activity, Mater. Sci. Semicond. Process. 42 (2016) 131–137. doi:10.1016/j.mssp.2015.08.043.

[16] I.D. Johnson, M. Loveridge, R. Bhagat, J.A. Darr, Mapping structure-composition-property relationships in V- and Fe- doped LiMnPO4 cathodes for Lithium-ion batteries, ACS Comb. Sci. 18 (2016) 665–672. doi:10.1021/acscombsci.6b00035.

[17] P.W. Dunne, C.L. Starkey, A.S. Munn, S.V.Y. Tang, O. Luebben, I. Shvets, A.G. Ryder, Y. Casamayou-Boucau, L. Morrison, E.H. Lester, Bench- and pilot-scale continuous-flow hydrothermal production of barium strontium titanate nanopowders, Chem. Eng. J. 289 (2015) 433–441. doi:10.1016/j.cej.2015.12.056.

[18] R.I. Gruar, C.J. Tighe, J.A. Darr, Scaling-up a confined jet reactor for the continuous hydrothermal manufacture of nanomaterials, Ind. Eng. Chem. Res. 52 (2013) 5270–5281. doi:10.1021/ie302567d.

[19] T. Adschiri, Y.-W. Lee, M. Goto, S. Takami, Green materials synthesis with supercritical water, Green Chem. 13 (2011) 1380–1390. doi:10.1039/c1gc15158d.

[20] P.F. McMillan, H.E. Stanley, Fluid phases: going supercritical, Nat. Phys. 6 (2010) 479–480. doi:10.1038/nphys1711.

[21] C.A. Eckert, B.L. Knutson, P.G. Debenedetti, Supercritical fluids as solvents for chemical and materials processing, Nature. 383 (1996) 313–318. doi:10.1038/383313a0.

[22] H. Machida, M. Takesue, R.L. Jr. Smith, Green chemical processes with supercritical fluids: properties, materials, separations and energy, J. Supercrit. Fluids. 60 (2011) 2–15. doi:10.1016/j.supflu.2011.04.016.

[23] W. Wagner, A. Pruß, The IAPWS formulation 1995 for the thermodynamic properties of ordinary water substance for general and scientific use, J. Phys. Chem. Ref. Data. 31 (2002) 387–535. doi:10.1063/1.1461829.

[24] D.P. Fernández, A.R.H. Goodwin, E.W. Lemmon, J.M.H. Levelt Sengers, R.C. Williams, A formulation

for the static permittivity of water and steam at temperatures from 238 K to 873 K at pressures up to 1200 MPa, including derivatives and Debye–Hückel coefficients, J. Phys. Chem. Ref. Data. 26 (1997) 1125–1166. doi:10.1063/1.555997.

[25] A. Kruse, E. Dinjus, Hot compressed water as reaction medium and reactant, J. Supercrit. Fluids. 39 (2007) 362–380. doi:10.1016/j.supflu.2006.03.016.

[26] A. Nagashima, I. Tanishita, Viscosity measurement of water and steam at high temperatures and high pressures, Bull. JSME. 54 (1969) 1467–1478. doi:10.1299/jsme1958.12.1467.

[27] A. V. Bandura, S.N. Lvov, The ionization constant of water over wide ranges of temperature and density, J. Phys. Chem. Ref. Data. 35 (2006) 15–30. doi:10.1063/1.1928231.

[28] A. Loppinet-Serani, C. Aymonier, F. Cansell, Current and foreseeable applications of supercritical water for energy and the environment, ChemSusChem. 1 (2008) 486–503. doi:10.1002/cssc.200700167.

[29] H. Hayashi, Y. Hakuta, Hydrothermal synthesis of metal oxide nanoparticles in supercritical water, Materials (Basel). 3 (2010) 3794–3817. doi:10.3390/ma3073794.

[30] T. Adschiri, Y. Hakuta, K. Arai, Hydrothermal synthesis of metal oxide fine particles at supercritical conditions, Ind. Eng. Chem. Res. 39 (2000) 4901–4907. doi:10.1021/ie0003279.

[31] K. Sue, Y. Hakuta, R.L. Jr. Smith, T. Adschiri, K. Arai, Solubility of lead(II) oxide and copper(II) oxide in subcritical and supercritical water, J. Chem. Eng. Data. 44 (1999) 1422–1426. doi:10.1021/je9901029.

[32] T. Adschiri, K. Kanazawa, K. Arai, Rapid and continuous hydrothermal synthesis of boehmite particles in subcritical and supercritical water, J. Am. Ceram. Soc. 75 (1992) 2615–2618. doi:10.1111/j.1151-2916.1992.tb05625.x.

[33] J. Zhang, S. Ohara, M. Umetsu, T. Naka, Y. Hatakeyama, T. Adschiri, Colloidal ceria nanocrystals: a tailor-made crystal morphology in supercritical water, Adv. Mater. 19 (2007) 203–206. doi:10.1002/adma.200600964.

[34] R.I. Gruar, C.J. Tighe, J. Muir, J.T. Kittler, M. Wodjak, A.J. Kenyon, J.A. Darr, Continuous hydrothermal synthesis of surface-functionalised nanophosphors for biological imaging, RSC Adv. 2 (2012) 10037–10047. doi:10.1039/c2ra21798h.

[35] J.-L. Mi, Y. Shen, J. Becker, M. Bremholm, B.B. Iversen, Controlling allotropism in ruthenium nanoparticles: a pulsed-flow supercritical synthesis and in situ synchrotron X-ray diffraction study, J. Phys. Chem. C. 118 (2014) 11104–11110. doi:10.1021/jp501229p.

[36] S. Magdassi, M. Grouchko, A. Kamyshny, Copper nanoparticles for printed electronics: routes towards achieving oxidation stability, Materials (Basel). 3 (2010) 4626–4638. doi:10.3390/ma3094626.

[37] N. Shirato, M. Cummings, H. Kersell, Y. Li, B. Stripe, D. Rosenmann, S.W. Hla, V. Rose, Elemental fingerprinting of materials with sensitivity at the atomic limit, Nano Lett. 14 (2014) 6499–6504.

doi:10.1021/nl5030613.

[38] A. Chroneos, B. Yildiz, A. Tarancón, D. Parfitt, J.A. Kilner, Oxygen diffusion in solid oxide fuel cell cathode and electrolyte materials: Mechanistic insights from atomistic simulations, Energy Environ. Sci. 4 (2011) 2774–2789. doi:10.1039/c0ee00717j.

[39] E. Lester, P. Blood, J. Denyer, D. Giddings, B. Azzopardi, M. Poliakoff, Reaction engineering: the supercritical water hydrothermal synthesis of nano-particles, J. Supercrit. Fluids. 37 (2006) 209–214. doi:10.1016/j.supflu.2005.08.011.

[40] C.J. Tighe, R.Q. Cabrera, R.I. Gruar, J.A. Darr, Scale up production of nanoparticles: continuous supercritical water synthesis of Ce–Zn oxides, Ind. Eng. Chem. Res. 52 (2013) 5522–5528. doi:10.1021/ie3025642.

[41] J.A. Hammons, J. Ustarroz, T. Muselle, A.A.J. Torriero, H. Terryn, K. Suthar, J. Ilavsky, Supported silver nanoparticle and near-interface solution dynamics in a deep eutectic solvent, J. Phys. Chem. C. 120 (2016) 1534–1545. doi:10.1021/acs.jpcc.5b09836.

[42] E. Lester, P.J. Blood, J.P. Denyer, B.J. Azzopardi, J. Li, M. Poliakoff, Impact of reactor geometry on continuous hydrothermal synthesis mixing, Mater. Res. Innov. 14 (2010) 19–26. doi:10.1179/143307510X12599329343042.

[43] L. Zhou, S. Wang, D. Xu, Y. Guo, Impact of mixing for the production of CuO nanoparticles in supercritical hydrothermal synthesis, Ind. Eng. Chem. Res. 53 (2013) 481–493. doi:10.1021/ie4029413.

[44] J. Sierra-Pallares, D.L. Marchisio, E. Alonso, M.T. Parra-Santos, F. Castro, M. José Cocero, Quantification of mixing efficiency in turbulent supercritical water hydrothermal reactors, Chem. Eng. Sci. 66 (2011) 1576–1589. doi:10.1016/j.ces.2010.12.039.

[45] S.-I. Kawasaki, K. Sue, R. Ookawara, Y. Wakashima, A. Suzuki, Y. Hakuta, K. Arai, Engineering study of continuous supercritical hydrothermal method using a T-shaped mixer: experimental synthesis of NiO nanoparticles and CFD simulation, J. Supercrit. Fluids. 54 (2010) 96–102. doi:10.1016/j.supflu.2010.03.001.

[46] P.J. Blood, J.P. Denyer, B.J. Azzopardi, M. Poliakoff, E. Lester, A versatile flow visualisation technique for quantifying mixing in a binary system: application to continuous supercritical water hydrothermal synthesis (SWHS), Chem. Eng. Sci. 59 (2004) 2853–2861. doi:10.1016/j.ces.2004.04.021.

[47] S.-A. Hong, S.J. Kim, K.Y. Chung, M.-S. Chun, B.G. Lee, J. Kim, Continuous synthesis of lithium iron phosphate (LiFePO4) nanoparticles in supercritical water: effect of mixing tee, J. Supercrit. Fluids. 73 (2013) 70–79. doi:10.1016/j.supflu.2012.11.008.

[48] C.Y. Ma, X.Z. Wang, C.J. Tighe, J.A. Darr, Modelling and simulation of counter-current and confined jet reactors for continuous hydrothermal flow synthesis of nano-materials, IFAC Proc. Vol. 45 (2012) 874–879. doi:10.3182/20120710-4-SG-2026.00073.

[49] A. Aimable, H. Muhr, C. Gentric, F. Bernard, F. Le Cras, D. Aymes, Continuous hydrothermal synthesis of inorganic nanopowders in supercritical water: towards a better control of the process, Powder Technol. 190 (2009) 99–106. doi:10.1016/j.powtec.2008.04.064.

[50] F. Demoisson, M. Ariane, A. Leybros, H. Muhr, F. Bernard, Design of a reactor operating in supercritical water conditions using CFD simulations. Examples of synthesized nanomaterials, J. Supercrit. Fluids. 58 (2011) 371–377. doi:10.1016/j.supflu.2011.07.001.

[51] C.Y. Ma, J.J. Liu, Y. Zhang, X.Z. Wang, Simulation for scale-up of a confined jet mixer for continuous hydrothermal flow synthesis of nanomaterials, J. Supercrit. Fluids. 98 (2015) 211–221. doi:10.1016/j.supflu.2014.12.016.

[52] T. Aizawa, Y. Masuda, K. Minami, M. Kanakubo, H. Nanjo, R.L. Smith, Direct observation of channel-tee mixing of high-temperature and high-pressure water, J. Supercrit. Fluids. 43 (2007) 222–227. doi:10.1016/j.supflu.2007.03.008.

[53] K. Sugioka, K. Ozawa, T. Tsukada, S. Takami, T. Adschiri, K. Sugimoto, N. Takenaka, Y. Saito, Neutron radiography and numerical simulation of mixing behavior in a reactor for supercritical hydrothermal synthesis, AIChE J. 60 (2014) 1168–1175. doi:10.1002/aic.14313.

[54] K. Sue, T. Sato, S. Kawasaki, Y. Takebayashi, S. Yoda, T. Furuya, T. Hiaki, Continuous hydrothermal synthesis of Fe2O3 nanoparticles using a central collision-type micromixer for rapid and homogeneous nucleation at 673 K and 30 MPa, Ind. Eng. Chem. Res. 49 (2010) 8841–8846. doi:10.1021/ie1008597.

[55] E. Roduner, Size matters: why nanomaterials are different, Chem. Soc. Rev. 35 (2006) 583–592. doi:10.1039/b502142c.

[56] C. Sun, R. Hui, J. Roller, Cathode materials for solid oxide fuel cells: a review, J. Solid State Electrochem. 14 (2009) 1125–1144. doi:10.1007/s10008-009-0932-0.

[57] K. Sue, M. Suzuki, K. Arai, T. Ohashi, H. Ura, K. Matsui, Y. Hakuta, H. Hayashi, M. Watanabe, T. Hiaki, Size-controlled synthesis of metal oxide nanoparticles with a flow-through supercritical water method, Green Chem. 8 (2006) 634–638. doi:10.1039/b518291c.

[58] J. Becker, P. Hald, M. Bremholm, J.S. Pedersen, J. Chevallier, S.B. Iversen, B.B. Iversen, Critical size of crystalline ZrO2 nanoparticles synthesized in near- and supercritical water and supercritical isopropyl alcohol, ACS Nano. 2 (2008) 1058–1068. doi:10.1021/nn7002426.

[59] H. Hayashi, A. Ueda, A. Suino, K. Hiro, Y. Hakuta, Hydrothermal synthesis of yttria stabilized ZrO2 nanoparticles in subcritical and supercritical water using a flow reaction system, J. Solid State Chem. 182 (2009) 2985–2990. doi:10.1016/j.jssc.2009.08.013.

[60] I. Gonzalo-Juan, B. Ferrari, M.T. Colomer, M.A. Rodriguez, A.J. Sanchez-Herencia, P.-Y. Koh, A.S. Teja, Synthesis and dispersion of yttria-stabilized zirconia (YSZ) nanoparticles in supercritical water, Mater. Chem. Phys. 134 (2012) 451–458. doi:10.1016/j.matchemphys.2012.03.016.

[61] E.D. Wachsman, K.T. Lee, Lowering the temperature of solid oxide fuel cells, Science. 334 (2011) 935–939. doi:10.1126/science.1204090.

[62] Y. Hakuta, S. Onai, H. Terayama, T. Adschiri, K. Arai, Production of ultra-fine ceria particles by hydrothermal synthesis under supercritical conditions, J. Mater. Sci. Lett. 7 (1998) 1211–1213. doi:10.1023/A:1006597828280.

[63] C. Slostowski, S. Marre, J.-M. Bassat, C. Aymonier, Synthesis of cerium oxide-based nanostructures in near- and supercritical fluids, J. Supercrit. Fluids. 84 (2013) 89–97. doi:10.1016/j.supflu.2013.09.014.

[64] K. Houlberg, E.D. Bøjesen, C. Tyrsted, A. Mamakhel, X. Wang, R. Su, F. Besenbacher, B.B. Iversen, Hydrothermal synthesis and in situ powder X-ray diffraction study of bismuth-substituted ceria nanoparticles, Cryst. Growth Des. 15 (2015) 3628–3636. doi:10.1021/acs.cgd.5b00678.

[65] S. Kellici, K. Gong, T. Lin, S. Brown, R.J.H. Clark, M. Vickers, J.K. Cockcroft, V. Middelkoop, P. Barnes, J.M. Perkins, C.J. Tighe, J.A. Darr, High-throughput continuous hydrothermal flow synthesis of Zn-Ce oxides: unprecedented solubility of Zn in the nanoparticle fluorite lattice, Philos. Trans. A. Math. Phys. Eng. Sci. 368 (2010) 4331–4349. doi:10.1098/rsta.2010.0135.

[66] A. Cabañas, J.A. Darr, E. Lester, M. Poliakoff, Continuous hydrothermal synthesis of inorganic materials in a near-critical water flow reactor; the one-step synthesis of nano-particulate Ce1−xZrxO2 (x = 0–1) solid solutions, J. Mater. Chem. 11 (2001) 561–568. doi:10.1039/b008095k.

[67] J.-R. Kim, W.-J. Myeong, S.-K. Ihm, Characteristics in oxygen storage capacity of ceria–zirconia mixed oxides prepared by continuous hydrothermal synthesis in supercritical water, Appl. Catal. B Environ. 71 (2007) 57–63. doi:10.1016/j.apcatb.2006.08.015.

[68] J.-R. Kim, W.-J. Myeong, S.-K. Ihm, Characteristics of CeO2–ZrO2 mixed oxide prepared by continuous hydrothermal synthesis in supercritical water as support of Rh catalyst for catalytic reduction of NO by CO, J. Catal. 263 (2009) 123–133. doi:10.1016/j.jcat.2009.02.001.

[69] J.-R. Kim, K.-Y. Lee, M.-J. Suh, S.-K. Ihm, Ceria–zirconia mixed oxide prepared by continuous hydrothermal synthesis in supercritical water as catalyst support, Catal. Today. 185 (2012) 25–34. doi:10.1016/j.cattod.2011.08.018.

[70] X. Weng, B. Perston, X.Z. Wang, I. Abrahams, T. Lin, S. Yang, J.R.G. Evans, D.J. Morgan, A.F. Carley, M. Bowker, J.C. Knowles, I. Rehman, J.A. Darr, Synthesis and characterization of doped nano-sized ceria–zirconia solid solutions, Appl. Catal. B Environ. 90 (2009) 405–415. doi:10.1016/j.apcatb.2009.03.031.

[71] K. Sue, K. Murata, K. Kimura, K. Arai, Continuous synthesis of zinc oxide nanoparticles in supercritical water, Green Chem. 5 (2003) 659–662. doi:10.1039/b306544h.

[72] R. Viswanathan, R.B. Gupta, Formation of zinc oxide nanoparticles in supercritical water, J. Supercrit. Fluids. 27 (2003) 187–193. doi:10.1016/S0896-8446(02)00236-X.

[73] S. Ohara, T. Mousavand, T. Sasaki, M. Umetsu, T. Naka, T. Adschiri, Continuous production of fine zinc oxide nanorods by hydrothermal synthesis in supercritical water, J. Mater. Sci. 43 (2007) 2393–2396. doi:10.1007/s10853-007-1823-3.

[74] F. Demoisson, R. Piolet, M. Ariane, A. Leybros, F. Bernard, Influence of the pH on the ZnO nanoparticle growth in supercritical water: experimental and simulation approaches, J. Supercrit. Fluids. 95 (2014) 75–83. doi:10.1016/j.supflu.2014.08.007.

[75] M. Søndergaard, E.D. Bøjesen, M. Christensen, B.B. Iversen, Size and morphology dependence of ZnO nanoparticles synthesized by a fast continuous flow hydrothermal method, Cryst. Growth Des. 11 (2011) 4027–4033. doi:10.1021/cg200596c.

[76] J.B.M. Goodall, D. Illsley, R. Lines, N.M. Makwana, J.A. Darr, Structure–property–composition relationships in doped zinc oxides: enhanced photocatalytic activity with rare earth dopants, ACS Comb. Sci. 17 (2015) 100–112. doi:10.1021/co500109f.

[77] J.B.M. Goodall, S. Kellici, D. Illsley, R. Lines, J.C. Knowles, J.A. Darr, Optical and photocatalytic behaviours of nanoparticles in the Ti–Zn–O binary system, RSC Adv. 4 (2014) 31799–31809. doi:10.1039/C3RA48030E.

[78] P. Hald, J. Becker, M. Bremholm, J.S. Pedersen, J. Chevallier, S.B. Iversen, B.B. Iversen, Supercritical propanol–water synthesis and comprehensive size characterisation of highly crystalline anatase TiO2 nanoparticles, J. Solid State Chem. 179 (2006) 2674–2680. doi:10.1016/j.jssc.2006.05.012.

[79] S. Kawasaki, X. Yan, K. Sue, Y. Hakuta, A. Suzuki, K. Arai, Continuous supercritical hydrothermal synthesis of controlled size and highly crystalline anatase TiO2 nanoparticles, J. Supercrit. Fluids. 50 (2009) 276–282. doi:10.1016/j.supflu.2009.06.009.

[80] J.-L. Mi, S. Johnsen, C. Clausen, P. Hald, N. Lock, L. Sø, B.B. Iversen, Highly controlled crystallite size and crystallinity of pure and iron-doped anatase-TiO2 nanocrystals by continuous flow supercritical synthesis, J. Mater. Res. 28 (2012) 333–339. doi:10.1557/jmr.2012.234.

[81] M. Lübke, I. Johnson, N.M. Makwana, D. Brett, P. Shearing, Z. Liu, J.A. Darr, High power TiO2 and high capacity Sn-doped TiO2 nanomaterial anodes for lithium-ion batteries, J. Power Sources. 294 (2015) 94–102. doi:10.1016/j.jpowsour.2015.06.039.

[82] S. Elouali, L.G. Bloor, R. Binions, I.P. Parkin, C.J. Carmalt, J.A. Darr, Gas sensing with nano-indium oxides (In2O3) prepared via continuous hydrothermal flow synthesis, Langmuir. 28 (2012) 1879–1885. doi:10.1021/la203565h.

[83] Z. Fang, H. Assaaoudi, R.I.L. Guthrie, J.A. Kozinski, I.S. Butler, Continuous synthesis of tin and indium oxide nanoparticles in sub- and supercritical water, J. Am. Ceram. Soc. 90 (2007) 2367–2371. doi:10.1111/j.1551-2916.2007.01773.x.

[84] J. Lu, K. Minami, S. Takami, M. Shibata, Y. Kaneko, T. Adschiri, Supercritical hydrothermal synthesis

and in situ organic modification of indium tin oxide nanoparticles using continuous-flow reaction system, ACS Appl. Mater. Interfaces. 4 (2012) 351–354. doi:10.1021/am2014234.

[85] U.T. Lam, R. Mammucari, K. Suzuki, N.R. Foster, Processing of iron oxide nanoparticles by supercritical fluids, Ind. Eng. Chem. Res. 47 (2008) 599–614. doi:10.1021/ie070494+.

[86] D.M. Robinson, Y.B. Go, M. Mui, G. Gardner, Z. Zhang, D. Mastrogiovanni, E. Garfunkel, J. Li, M. Greenblatt, G.C. Dismukes, Photochemical water oxidation by crystalline polymorphs of manganese oxides: structural requirements for catalysis, J. Am. Chem. Soc. 135 (2013) 3494–3501. doi:10.1021/ja310286h.

[87] M.J. Powell, P. Marchand, C.J. Denis, J.C. Bear, J.A. Darr, I.P. Parkin, Direct and continuous synthesis of VO2 nanoparticles, Nanoscale. 7 (2015) 18686–18693. doi:10.1039/C5NR04444H.

[88] M. Lübke, N. Ding, M. Powell, D.J.L. Brett, P.R. Shearing, Z. Liu, J.A. Darr, VO2 nano-sheet negative electrodes for lithium-ion batteries, Electrochem. Commun. 64 (2016) 56–60. doi:10.1016/j.elecom.2016.01.013.

[89] C.G. Granqvist, P.C. Lansåker, N.R. Mlyuka, G.A. Niklasson, E. Avendaño, Progress in chromogenics: new results for electrochromic and thermochromic materials and devices, Sol. Energy Mater. Sol. Cells. 93 (2009) 2032–2039. doi:10.1016/j.solmat.2009.02.026.

[90] R. Quesada-Cabrera, M.J. Powell, P. Marchand, C.J. Denis, F. Di Maggio, J.A. Darr, I.P. Parkin, Scalable production of thermochromic Nb-doped VO2 nanomaterials using continuous hydrothermal flow synthesis, J. Nanosci. Nanotechnol. 16 (2016) 10104–10111. doi:10.1166/jnn.2016.12842.

[91] J.-H. Lee, J.-Y. Ham, Synthesis of manganese oxide particles in supercritical water, Korean J. Chem. Eng. 23 (2006) 714–719. doi:10.1007/BF02705916.

[92] A. Nugroho, J. Kim, Effect of KOH on the continuous synthesis of cobalt oxide and manganese oxide nanoparticles in supercritical water, J. Ind. Eng. Chem. 20 (2014) 4443–4446. doi:10.1016/j.jiec.2014.02.014.

[93] L.J. Cote, A.S. Teja, A.P. Wilkinson, Z.J. Zhang, Continuous hydrothermal synthesis and crystallization of magnetic oxide nanoparticles, J. Mater. Res. 17 (2002) 2410–2416. doi:10.1557/JMR.2002.0352.

[94] K. Sue, S. Kawasaki, M. Suzuki, Y. Hakuta, H. Hayashi, K. Arai, Y. Takebayashi, S. Yoda, T. Furuya, Continuous hydrothermal synthesis of Fe2O3, NiO, and CuO nanoparticles by superrapid heating using a T-type micro mixer at 673K and 30MPa, Chem. Eng. J. 166 (2011) 947–953. doi:10.1016/j.cej.2010.11.080.

[95] L. Maurizi, F. Bouyer, J. Paris, F. Demoisson, L. Saviot, N. Millot, One step continuous hydrothermal synthesis of very fine stabilized superparamagnetic nanoparticles of magnetite, Chem. Commun. 47 (2011) 11706–11708. doi:10.1039/c1cc15470b.

[96] E. Lester, G. Aksomaityte, J. Li, S. Gomez, J. Gonzalez-Gonzalez, M. Poliakoff, Controlled continuous hydrothermal synthesis of cobalt oxide (Co3O4) nanoparticles, Prog. Cryst. Growth Charact. Mater. 58 (2012) 3–13. doi:10.1016/j.pcrysgrow.2011.10.008.

[97] F. Moro, S.V. Yu Tang, F. Tuna, E. Lester, Magnetic properties of cobalt oxide nanoparticles synthesised by a continuous hydrothermal method, J. Magn. Magn. Mater. 348 (2013) 1–7. doi:10.1016/j.jmmm.2013.07.064.

[98] M. Chowdhury, O. Oghenochuko, M. Kebede, F. Cummings, O. Cespedes, M. Aliwa, V. Fester, Rapid and large-scale synthesis of Co3O4 octahedron particles with very high catalytic activity, good supercapacitance and unique magnetic property, RSC Adv. 5 (2015) 104991–105002. doi:10.1039/C5RA20763K.

[99] Y. Hakuta, H. Ura, H. Hayashi, K. Arai, Effect of water density on polymorph of BaTiO3 nanoparticles synthesized under sub and supercritical water conditions, Mater. Lett. 59 (2005) 1387–1390. doi:10.1016/j.matlet.2004.11.063.

[100] Y. Hakuta, H. Ura, H. Hayashi, K. Arai, Continuous production of BaTiO3 nanoparticles by hydrothermal synthesis, Ind. Eng. Chem. Res. 44 (2005) 840–846. doi:10.1021/ie049424i.

[101] K. Matsui, T. Noguchi, N.M. Islam, Y. Hakuta, H. Hayashi, Rapid synthesis of BaTiO3 nanoparticles in supercritical water by continuous hydrothermal flow reaction system, J. Supercrit. Fluids. 46 (2008) 129–136. doi:10.1016/j.supflu.2008.04.011.

[102] H. Hayashi, T. Noguchi, N.M. Islam, Y. Hakuta, Y. Imai, N. Ueno, Hydrothermal synthesis of BaTiO3 nanoparticles using a supercritical continuous flow reaction system, J. Cryst. Growth. 312 (2010) 1968–1972. doi:10.1016/j.jcrysgro.2010.03.034.

[103] G. Philippot, K.M.Ø. Jensen, M. Christensen, C. Elissalde, M. Maglione, B.B. Iversen, C. Aymonier, Coupling in situ synchrotron radiation with ex situ spectroscopy characterizations to study the formation of Ba1−xSrxTiO3 nanoparticles in supercritical fluids, J. Supercrit. Fluids. 87 (2014) 111–117. doi:10.1016/j.supflu.2013.12.009.

[104] T. Ono, K. Sue, D. Furuta, M. Aoki, Y. Hakuta, Y. Takebayashi, S. Yoda, T. Furuya, T. Sato, T. Hiaki, Continuous hydrothermal synthesis of Ca1−xSrxTiO3 solid-solution nanoparticles using a T-type micromixer, J. Supercrit. Fluids. 85 (2014) 159–164. doi:10.1016/j.supflu.2013.11.010.

[105] J. Lu, Y. Hakuta, H. Hayashi, T. Ohashi, T. Nagase, Y. Hoshi, K. Sato, M. Nishioka, T. Inoue, S. Hamakawa, Preparation of Ca0.8Sr0.2Ti1−xFexO3−δ (x=0.1–0.3) nanoparticles using a flow supercritical reaction system, J. Supercrit. Fluids. 46 (2008) 77–82. doi:10.1016/j.supflu.2008.02.010.

[106] A. Aimable, B. Xin, N. Millot, D. Aymes, Continuous hydrothermal synthesis of nanometric BaZrO3 in supercritical water, J. Solid State Chem. 181 (2008) 183–189. doi:10.1016/j.jssc.2007.11.015.

[107] S. Toyama, H. Hayashi, M. Takesue, M. Watanabe, R.L. Jr. Smith, Synthesis of alkali niobate

K1−xNaxNbO3 nanoparticles using a supercritical water flow system, J. Supercrit. Fluids. 107 (2016) 1–8. doi:10.1016/j.supflu.2015.08.008.

[108] L.J. Cote, A.S. Teja, A.P. Wilkinson, Z.J. Zhang, Continuous hydrothermal synthesis of CoFe2O4 nanoparticles, Fluid Phase Equilib. 210 (2003) 307–317. doi:10.1016/S0378-3812(03)00168-7.

[109] N. Millot, B. Xin, C. Pighini, D. Aymes, Hydrothermal synthesis of nanostructured inorganic powders by a continuous process under supercritical conditions, J. Eur. Ceram. Soc. 25 (2005) 2013–2016. doi:10.1016/j.jeurceramsoc.2005.03.202.

[110] T. Sato, K. Sue, W. Suzuki, M. Suzuki, K. Matsui, Y. Hakuta, H. Hayashi, K. Arai, S. Kawasaki, A. Kawai-Nakamura, T. Hiaki, Rapid and continuous production of ferrite nanoparticles by hydrothermal synthesis at 673 K and 30 MPa, Ind. Eng. Chem. Res. 47 (2008) 1855–1860. doi:10.1021/ie071168x.

[111] K. Sue, M. Aoki, T. Sato, D. Nishio-Hamane, S. Kawasaki, Y. Hakuta, Y. Takebayashi, S. Yoda, T. Furuya, T. Sato, T. Hiaki, Continuous hydrothermal synthesis of nickel ferrite nanoparticles using a central collision-type micromixer: effects of temperature, residence time, metal salt molality, and NaOH addition on conversion, particle size, and crystal phase, Ind. Eng. Chem. Res. 50 (2011) 9625–9631. doi:10.1021/ie200036m.

[112] P. Boldrin, A.K. Hebb, A.A. Chaudhry, L. Otley, B. Thiebaut, P. Bishop, J.A. Darr, Direct synthesis of nanosized NiCo2O4 spinel and related compounds via continuous hydrothermal synthesis methods, Ind. Eng. Chem. Res. 46 (2007) 4830–4838. doi:10.1021/ie061396b.

[113] D. Rangappa, S. Ohara, M. Umetsu, T. Naka, T. Adschiri, Synthesis, characterization and organic modification of copper manganese oxide nanocrystals under supercritical water, J. Supercrit. Fluids. 44 (2008) 441–445. doi:10.1016/j.supflu.2007.09.022.

[114] T. Sasaki, S. Ohara, T. Naka, J. Vejpravova, V. Sechovsky, M. Umetsu, S. Takami, B. Jeyadevan, T. Adschiri, Continuous synthesis of fine MgFe2O4 nanoparticles by supercritical hydrothermal reaction, J. Supercrit. Fluids. 53 (2010) 92–94. doi:10.1016/j.supflu.2009.11.005.

[115] J. Lu, K. Minami, S. Takami, T. Adschiri, Rapid and continuous synthesis of cobalt aluminate nanoparticles under subcritical hydrothermal conditions with in-situ surface modification, Chem. Eng. Sci. 85 (2013) 50–54. doi:10.1016/j.ces.2012.01.061.

[116] T. Adschirib, Y. Hakuta, K. Kanamura, K. Arai, Continuous production of LiCoO2 fine crystals for lithium batteries by hydrothermal synthesis under supercritical condition, High Press. Res. 20 (2001) 373–384. doi:10.1080/08957950108206185.

[117] Y.H. Shin, S.-M. Koo, D.S. Kim, Y.-H. Lee, B. Veriansyah, J. Kim, Y.-W. Lee, Continuous hydrothermal synthesis of HT-LiCoO2 in supercritical water, J. Supercrit. Fluids. 50 (2009) 250–256. doi:10.1016/j.supflu.2009.06.012.

[118] C. Xu, J. Lee, A.S. Teja, Continuous hydrothermal synthesis of lithium iron phosphate particles in

subcritical and supercritical water, J. Supercrit. Fluids. 44 (2008) 92–97. doi:10.1016/j.supflu.2007.09.001.

[119] I.D. Johnson, M. Lübke, O.Y. Wu, N.M. Makwana, G.J. Smales, H.U. Islam, R.Y. Dedigama, R.I. Gruar, C.J. Tighe, D.O. Scanlon, F. Corà, D.J.L. Brett, P.R. Shearing, J.A. Darr, Pilot-scale continuous synthesis of a vanadium-doped LiFePO4/C nanocomposite high-rate cathodes for lithium-ion batteries, J. Power Sources. 302 (2016) 410–418. doi:10.1016/j.jpowsour.2015.10.068.

[120] A. Laumann, M. Bremholm, P. Hald, M. Holzapfel, K. Thomas Fehr, B.B. Iversen, Rapid green continuous flow supercritical synthesis of high performance Li4Ti5O12 nanocrystals for Li ion battery applications, J. Electrochem. Soc. 159 (2012) A166–A171. doi:10.1149/2.084202jes.

[121] Y. Shen, J.R. Eltzholtz, B.B. Iversen, Controlling size, crystallinity, and electrochemical performance of Li4Ti5O12 nanocrystals, Chem. Mater. 25 (2013) 5023–5030. doi:10.1021/cm402366y.

[122] H. Chander, Development of nanophosphors - A review, Mater. Sci. Eng. R Reports. 49 (2005) 113–155. doi:10.1016/j.mser.2005.06.001.

[123] Y. Hakuta, K. Sue, Y. Takebayashi, S. Yoda, T. Furuya, H. Takashima, Preparation of rare-earth doped zirconia nanoparticles via supercritical hydrothermal method for luminescence properties, Key Eng. Mater. 512–515 (2012) 59–64. doi:10.4028/www.scientific.net/KEM.512-515.59.

[124] H. Hobbs, S. Briddon, E. Lester, The synthesis and fluorescent properties of nanoparticulate ZrO2 doped with Eu using continuous hydrothermal synthesis, Green Chem. 11 (2009) 484–491. doi:10.1039/b812149d.

[125] A. Cabañas, J. Li, P. Blood, T. Chudoba, W. Lojkowski, M. Poliakoff, E. Lester, Synthesis of nanoparticulate yttrium aluminum garnet in supercritical water–ethanol mixtures, J. Supercrit. Fluids. 40 (2007) 284–292. doi:10.1016/j.supflu.2006.06.006.

[126] Y. Hakuta, T. Haganuma, K. Sue, T. Adschiri, K. Arai, Continuous production of phosphor YAG:Tb nanoparticles by hydrothermal synthesis in supercritical water, Mater. Res. Bull. 38 (2003) 1257–1265. doi:10.1016/S0025-5408(03)00088-6.

[127] J.H. In, H.C. Lee, M.J. Yoon, K.K. Lee, J.W. Lee, C.H. Lee, Synthesis of nano-sized YAG:Eu3+ phosphor in continuous supercritical water system, J. Supercrit. Fluids. 40 (2007) 389–396. doi:10.1016/j.supflu.2006.08.006.

[128] K. Shibuki, M. Takesue, T.M. Aida, M. Watanabe, H. Hayashi, R.L. Smith, Continuous synthesis of Zn2SiO4:Mn2+ fine particles in supercritical water at temperatures of 400–500°C and pressures of 30–35MPa, J. Supercrit. Fluids. 54 (2010) 266–271. doi:10.1016/j.supflu.2010.05.007.

[129] H. Hayashi, A. Suino, K. Shimoyama, M. Takesue, S. Tooyama, R.L. Smith, Continuous hydrothermal synthesis of ZnGa2O4:Mn2+ nanoparticles at temperatures of 300–500°C and pressures of 25–35MPa, J. Supercrit. Fluids. 77 (2013) 1–6. doi:10.1016/j.supflu.2013.02.004.

[130] K. Sue, S. Kawasaki, T. Sato, D. Nishio-Hamane, Y. Hakuta, T. Furuya, Continuous hydrothermal synthesis of Pr-doped CaTiO3 nanoparticles from a TiO2 sol, Ind. Eng. Chem. Res. 55 (2016) 7628–7634. doi:10.1021/acs.iecr.6b00833.

[131] N. Lock, P. Hald, M. Christensen, H. Birkedal, B.B. Iversen, Continuous flow supercritical water synthesis and crystallographic characterization of anisotropic boehmite nanoparticles, J. Appl. Crystallogr. 43 (2010) 858–866. doi:10.1107/S0021889810019187.

[132] Y. Hakuta, H. Ura, H. Hayashi, K. Arai, Effects of hydrothermal synthetic conditions on the particle size of γ-AlO(OH) in sub and supercritical water using a flow reaction system, Mater. Chem. Phys. 93 (2005) 466–472. doi:10.1016/j.matchemphys.2005.03.047.

[133] A.A. Chaudhry, S. Haque, S. Kellici, P. Boldrin, I. Rehman, F.A. Khalid, J.A. Darr, Instant nano-hydroxyapatite: a continuous and rapid hydrothermal synthesis, Chem. Commun. (2006) 2286–2288. doi:10.1039/b518102j.

[134] E. Lester, S.V.Y. Tang, A. Khlobystov, V.L. Rose, L. Buttery, C.J. Roberts, Producing nanotubes of biocompatible hydroxyapatite by continuous hydrothermal synthesis, CrystEngComm. 15 (2013) 3256–3260. doi:10.1039/c3ce26798a.

[135] A.A. Chaudhry, J. Goodall, M. Vickers, J.K. Cockcroft, I. Rehman, J.C. Knowles, J.A. Darr, Synthesis and characterisation of magnesium substituted calcium phosphate bioceramic nanoparticles made via continuous hydrothermal flow synthesis, J. Mater. Chem. 18 (2008) 5900–5908. doi:10.1039/b807920j.

[136] A.A. Chaudhry, J.C. Knowles, I. Rehman, J.A. Darr, Rapid hydrothermal flow synthesis and characterisation of carbonate- and silicate-substituted calcium phosphates, J. Biomater. Appl. 28 (2013) 448–461. doi:10.1177/0885328212460289.

[137] Q. Wang, S.V.Y. Tang, E. Lester, D. O'Hare, Synthesis of ultrafine layered double hydroxide (LDHs) nanoplates using a continuous-flow hydrothermal reactor, Nanoscale. 5 (2013) 114–117. doi:10.1039/c2nr32568c.

[138] M. Diez-Garcia, J.J. Gaitero, J.S. Dolado, C. Aymonier, Ultra-fast supercritical hydrothermal synthesis of tobermorite under thermodynamically metastable conditions, Angew. Chemie. 129 (2017) 3210–3215. doi:10.1002/ange.201611858.

[139] K. Sue, N. Kakinuma, T. Adschiri, K. Arai, Continuous production of nickel fine particles by hydrogen reduction in near-critical water, Ind. Eng. Chem. Res. 43 (2004) 2073–2078. doi:10.1021/ie030638u.

[140] P. Hald, M. Bremholm, S.B. Iversen, B.B. Iversen, Surfactant-free synthesis of nickel nanoparticles in near-critical water, J. Solid State Chem. 181 (2008) 2681–2683. doi:10.1016/j.jssc.2008.06.041.

[141] S. Kubota, T. Morioka, M. Takesue, H. Hayashi, M. Watanabe, R.L. Jr. Smith, Continuous supercritical hydrothermal synthesis of dispersible zero-valent copper nanoparticles for ink applications in printed electronics, J. Supercrit. Fluids. 86 (2014) 33–40. doi:10.1016/j.supflu.2013.11.013.

[142] G. Aksomaityte, M. Poliakoff, E. Lester, The production and formulation of silver nanoparticles using continuous hydrothermal synthesis, Chem. Eng. Sci. 85 (2013) 2–10. doi:10.1016/j.ces.2012.05.035.

[143] J.-L. Mi, T.N. Jensen, P. Hald, J. Overgaard, M. Christensen, B.B. Iversen, Glucose-assisted continuous flow synthesis of Bi2Te3 nanoparticles in supercritical/near-critical water, J. Supercrit. Fluids. 67 (2012) 84–88. doi:10.1016/j.supflu.2012.03.009.

[144] D. Rangappa, T. Naka, S. Ohara, T. Adschiri, Preparation of Ba-hexaferrite nanocrystals by an organic ligand-assisted supercritical water process, Cryst. Growth Des. 10 (2010) 11–15. doi:10.1021/cg900941p.

[145] T. Togashi, S. Takami, K. Kawakami, H. Yamamoto, T. Naka, K. Sato, K. Abe, T. Adschiri, Continuous hydrothermal synthesis of 3,4-dihydroxyhydrocinnamic acid-modified magnetite nanoparticles with stealth-functionality against immunological response, J. Mater. Chem. 22 (2012) 9041–9045. doi:10.1039/c2jm30325f.

[146] R.I. Gruar, C.J. Tighe, P. Southern, Q.A. Pankhurst, J.A. Darr, A direct and continuous supercritical water process for the synthesis of surface-functionalized nanoparticles, Ind. Eng. Chem. Res. 54 (2015) 7436–7451. doi:10.1021/acs.iecr.5b01817.

[147] M. Gimeno-Fabra, F. Hild, P.W. Dunne, K. Walton, D.M. Grant, D.J. Irvine, E.H. Lester, Continuous synthesis of dispersant-coated hydroxyapatite plates, CrystEngComm. 17 (2015) 6175–6182. doi:10.1039/C5CE00628G.

[148] M.D. de Tercero, M. Bruns, I.G. Martínez, M. Türk, U. Fehrenbacher, S. Jennewein, L. Barner, Continuous hydrothermal synthesis of in situ functionalized iron oxide nanoparticles: a general strategy to produce metal oxide nanoparticles with clickable anchors, Part. Part. Syst. Charact. 30 (2013) 229–234. doi:10.1002/ppsc.201200109.

[149] P.W. Dunne, C.L. Starkey, M. Gimeno-Fabra, E.H. Lester, The rapid size- and shape-controlled continuous hydrothermal synthesis of metal sulphide nanomaterials, Nanoscale. 6 (2014) 2406–2418. doi:10.1039/c3nr05749f.

[150] P.W. Dunne, E. Lester, R.I. Walton, Towards scalable and controlled synthesis of metal–organic framework materials using continuous flow reactors, React. Chem. Eng. 1 (2016) 352–360. doi:10.1039/C6RE00107F.

[151] M. Gimeno-Fabra, A.S. Munn, L.A. Stevens, T.C. Drage, D.M. Grant, R.J. Kashtiban, J. Sloan, E. Lester, R.I. Walton, Instant MOFs: continuous synthesis of metal-organic frameworks by rapid solvent mixing, Chem. Commun. 48 (2012) 10642–10644. doi:10.1039/c2cc34493a.

[152] A.S. Munn, P.W. Dunne, S.V.Y. Tang, E.H. Lester, Large-scale continuous hydrothermal production and activation of ZIF-8, Chem. Commun. 51 (2015) 12811–12814. doi:10.1039/C5CC04636J.

[153] C. Tyrsted, J. Becker, P. Hald, M. Bremholm, J.S. Pedersen, J. Chevallier, Y. Cerenius, S.B. Iversen,

B.B. Iversen, In-situ synchrotron radiation study of formation and growth of crystalline CexZr1−xO2 nanoparticles synthesized in supercritical water, Chem. Mater. 22 (2010) 1814–1820. doi:10.1021/cm903316s.

[154] J.E. Rostgaard, C. Tyrsted, K.M.Ø. Jensen, M. Bremholm, M. Christensen, J. Becker-Christensen, B.B. Iversen, Pulsed supercritical synthesis of anatase TiO2 nanoparticles in a water-isopropanol mixture studied by in situ powder X-ray diffraction, Nanoscale. 5 (2013) 2372–2378. doi:10.1039/c3nr33127j.

[155] P. Nørby, K.M.Ø. Jensen, N. Lock, M. Christensen, B.B. Iversen, In situ synchrotron powder X-ray diffraction study of formation and growth of yttrium and ytterbium aluminum garnet nanoparticles in sub- and supercritical water, RSC Adv. 3 (2013) 15368–15374. doi:10.1039/c3ra41854e.

[156] M. Bremholm, H. Jensen, S.B. Iversen, B.B. Iversen, Reactor design for in situ X-ray scattering studies of nanoparticle formation in supercritical water syntheses, J. Supercrit. Fluids. 44 (2008) 385–390. doi:10.1016/j.supflu.2007.09.029.

[157] M. Bremholm, M. Felicissimo, B.B. Iversen, Time-resolved in situ synchrotron X-ray study and large-scale production of magnetite nanoparticles in supercritical water, Angew. Chemie. 121 (2009) 4882–4885. doi:10.1002/ange.200901048.

[158] V. Middelkoop, P. Boldrin, M. Peel, T. Buslaps, P. Barnes, J.A. Darr, S.D.M. Jacques, Imaging the inside of a continuous nanoceramic synthesizer under supercritical water conditions using high-energy synchrotron X-radiation, Chem. Mater. 21 (2009) 2430–2435. doi:10.1021/cm900118z.

[159] V. Middelkoop, C.J. Tighe, S. Kellici, R.I. Gruar, J.M. Perkins, S.D.M. Jacques, P. Barnes, J.A. Darr, Imaging the continuous hydrothermal flow synthesis of nanoparticulate CeO2 at different supercritical water temperatures using in situ angle-dispersive diffraction, J. Supercrit. Fluids. 87 (2014) 118–128. doi:10.1016/j.supflu.2013.12.022.

[160] M. Chen, C.Y. Ma, T. Mahmud, J.A. Darr, X.Z. Wang, Modelling and simulation of continuous hydrothermal flow synthesis process for nano-materials manufacture, J. Supercrit. Fluids. 59 (2011) 131–139. doi:10.1016/j.supflu.2011.07.002.

[161] A. Erriguible, F. Marias, F. Cansell, C. Aymonier, Monodisperse model to predict the growth of inorganic nanostructured particles in supercritical fluids through a coalescence and aggregation mechanism, J. Supercrit. Fluids. 48 (2009) 79–84. doi:10.1016/j.supflu.2008.09.014.

[162] A. Leybros, R. Piolet, M. Ariane, H. Muhr, F. Bernard, F. Demoisson, CFD simulation of ZnO nanoparticle precipitation in a supercritical water synthesis reactor, J. Supercrit. Fluids. 70 (2012) 17–26. doi:10.1016/j.supflu.2012.06.001.

Chapter II. Experimental

One may notice that in following chapters, the experimental details are included separately for the materials under focus. This chapter is to provide an overview of the experimental work involved in the thesis, including material syntheses, processing of the synthesized materials for application purposes, and characterization techniques.

2.1 Material synthesis

Continuous hydrothermal flow synthesis (CHFS) was used to prepare materials using supercritical water (scH_2O) in an in-house developed two-stage flow-type apparatus (hereafter termed as CHFS reactor). Prior to building the reactor, computational fluid dynamic (CFD) modelling was applied to study the effects of parameters such as pipe geometries, flow rates and gravity on the mixing behavior, temperature and reactant distribution. Details of the modelling and build-up of the reactor can be found in **Chapter III** and references therein.

Metal nitrates [$Me(NO_3)_n \bullet xH_2O$] were dissolved in deionized water (DI H_2O) to prepare stock solutions. The molarity (mmol g^{-1}) of a stock solution was determined precisely by calcining samples of the stock solution in a furnace using a protocol established in the Chemistry Lab at DTU Energy. For the synthesis of particles, reactant solutions with the desired composition were prepared from stock solutions containing corresponding metal salts. Used as mineralizers to form precursors, KOH pellets (Sigma Aldrich, 85 %) or NaOH pellets (Sigma Aldrich, ≥98 %) were dissolved in DI H_2O for solutions with various defined concentrations.

In the CHFS process, all liquids were fed to the reactor at ambient conditions by metering pumps (Milton Roy). In total, five pumps were connected to the reactor. One of them was used to feed DI H_2O to the reactor, which was heated by a preheater to supercritical conditions (scH_2O). Two of them were used to feed separately reactant solutions and KOH/NaOH solutions (in the cases when no alkali was involved in the synthesis, DI H_2O was fed instead) to the first mixer (Stage 1). Prior to the first mixer, these two flows were mixed at a tee-junction, resulting in a precursor flow that was then

fed to the first mixer from its two side arms. The precursor was heated by the scH_2O in the first mixer. The other two pumps were used to feed other flows (e.g. DI H_2O, precursor for a second material and surfactants) to the second mixer (Stage 2) that is integrated in series to the first mixer. The outflow of the second mixer then passed a re-heater (*T* up to 410 °C). Afterwards, the outflow was rapidly cooled down to room temperature by a water-cooled tube-in-tube heat exchanger (Sentry Equipment Corp). After passing by an in-line filter (Swagelok, 90-µm pore size), the product flow was depressurized to atmospheric pressure by a backpressure regulator (Tescom, 26-1700 Series). Synthesized materials were collected in the product slurries at the outlet of the reactor.

The reaction temperatures were monitored by three thermocouples. They are inserted into the reactor at the inlet of the first mixer to read the temperature T_1 of the scH_2O, at the outlet of the second mixer to read the temperature T_2 of the outflow, and at the outlet of the re-heater to read the temperature T_3 of the outflow, respectively. The reaction pressures were controlled by the backpressure regulator.

A schematic description of the CHFS reactor is presented in **Fig. 2.1**. More details of conditions applied in syntheses of a certain material can be found in the corresponding chapter.

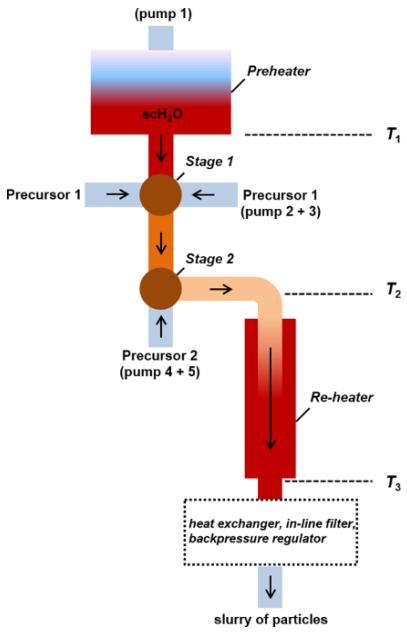

Figure 2.1 A schematic description of the CHFS reactor. The arrows indicate the flow directions.

2.2 Particle processing

Here, the material processing techniques applied for the particles synthesized by CHFS and batch-type hydrothermal synthesis to specific applications are listed.

2.2.1 Spark plasma sintering (SPS)

The SPS system (DR. Sinter Lab 515S, Fuji Electronic Industrial Co., Ltd., Japan) was used, with a pulsed direct current regulated by on-off settings. Powders (6 g) were filled into a Ø16 mm graphite die, which was then pressed under a small pressure of ~5 MPa to ensure a good contact between powders and graphite punches. In the SPS process, a pulsed electric current then passed through the powders under a vacuum of about 10^{-5} atm. The heating rate was 100 °C min^{-1}. In order to remove all gases from the powders, after the temperature reached 800 °C, a uniaxial pressure was slowly applied which reached 50 MPa when the temperature reached 900 °C. The sintering temperature was held at 1000 °C with a constant uniaxial pressure of 50 MPa for 6 min. The cooling rate was set at 100 °C min^{-1} from 1000 °C to 500 °C, and was left cooled down to room temperature. $(La_{0.6}Sr_{0.4})_{0.99}CoO_{3-\delta}$ – $Gd_{0.2}Ce_{0.8}O_{2-\delta}$ core-shell particles were sintered in this way (**Chapter V**).

2.2.2 Conventional sintering in a furnace

The desired amounts of particles were die-pressed into pellets (15 mm diameter) with a weight load of 1000 kg and then isostatically pressed at 65,000 kg load. Afterwards, the pellets were sintered inside a furnace in air at T_{max} for 6 h. Both the heating and cooling rates were set to 100 °C h^{-1}. $(La_{0.6}Sr_{0.4})_{0.99}CoO_{3-\delta}$ – $Gd_{0.2}Ce_{0.8}O_{2-\delta}$ (T_{max} = 1250 °C, **Chapter V**) and $Sc_{0.10}Y_{0.01}Zr_{0.89}O_{2-\delta}$ – $LaCrO_3$ (T_{max} = 1400 °C, **Chapter VI**) were sintered in this way.

2.2.3 Inkjet printing

This work is reported in detail in **Chapter IV**. In brief, $Gd_{0.2}Ce_{0.8}O_{2-\delta}$ nanoparticles with sufficient amounts for making inks were prepared first by CHFS. Afterwards, a primary dispersion of the as-synthesized $Gd_{0.2}Ce_{0.8}O_{2-\delta}$ in a mixture of 50 mL DI H_2O and ~0.6 mL Dispex A40 was made by

using an ultrasonic processor (Hielscher UP200St, Germany). Two inks were formulated from the primary dispersion, and printed separately on green NiO-GDC substrates and on pre-sintered NiO-YSZ substrates.

(1) **Printing on green NiO-GDC substrates**. Polyethylene glycol with a molecular weight 35,000 (PEG 35000) (Sigma Aldrich) was added at a concentration of 10 mg cm^{-3} to raise the viscosity, and Natsurf 265 added at a concentration of 0.2 mg cm^{-3} to reduce the surface tension of the formulated ink to the recommended range for the DMC 10 pL printheads (Fujifilm, USA, [1]). The surface tension was measured using a tensiometer (Model 250-U1, Ramé-hart, USA), and the viscosity was measured using a concentric cylinder viscometer (DV-E Viscometer, Brookhaven, USA). Prior to printing, the ink was first ultrasonicated for 5 min (Q55, QSonica, USA), and then filtered to remove large agglomerates (800 nm syringe filter, Cole Parmer, UK).

Three sets of films with 1, 5, 10, and 20 layers were printed onto a green NiO-GDC substrate to make squares of 7 mm side length with 4 min intervals between each deposition to allow drying. A Ceradrop X-Serie piezoelectric inkjet printer (Ceradrop, France) was used. The voltage profile (amplitude x, time coordinate y) applied to the piezoelectric printhead was (10 V, 0 µs), (0 V, 5 µs), (0 V, 10 µs), (50 V, 15 µs), (50 V, 20 µs), (10 V, 25 µs). With a printhead speed of 100 mm s^{-1} across the substrate, the resulting jetting frequency was 3.48 kHz. This resulted in consistent, spherical, droplet ejection, verified with the in-built camera. The 'splat' diameter was measured using the in-built optical microscope in the printer as 80 µm. The diameter overlap for the printed films was 50 µm with a square droplet deposition lattice (*i.e.* 62.5 %).

The substrate was prepared by mixing the GDC and NiO powders (GDC and NiO powders supplied by Fuel Cell Materials, USA, and Inframat Advanced materials, USA, respectively) with dimethyl sulfoxide (VWR, USA) and polyethersulfone (Ameco Performance, USA) and milled for 48 h (JARMILL, Gladstone Engineering Ltd, UK). Polyethylene glycol 30-dipolyhydroxystearate (Arlacel P135, Uniqema) was added and milling continued for a further 48 h. The final composition contained the above species in the weight ratio of 60 : 90 : 100 : 20 : 2, respectively. The suspension was

degassed under vacuum, cast (height 0.5 mm) onto a plate, and finally submerged in an external coagulant bath to complete the phase inversion process. The substrate was dried and flattened for 24 h before printing. After printing, samples were sintered with the following profiles: 0 – 650 °C at 4 °C min^{-1}; dwell at 650 °C for 4 h (to pyrolyze organics); 650 – 1300 °C at 15 °C min^{-1}; dwell for 8 h; cool to room temperature at 4 °C min^{-1}.

(2) **Printing on pre-sintered NiO-YSZ substrates**. Natsurf 265 was added under magnetic stirring at a concentration of 6 mg cm^{-3} to reduce surface tension of the formulated ink to the recommended range for the DMC 10 pL printheads (Fujifilm, USA, [1]). The surface tension of the ink was assessed using a bubble pressure tensiometer (BP 50, Kruss) and the viscosity was measured with a rheometer (MCR 302, Anton Paar). The rheological measurements were carried out in rotational mode with a plate-plate configuration up to a shear rate of 1000 s^{-1}.

A Pixdro LP50 printer equipped with a DMC 10-pL printhead was used for depositing the ink. Before printing, the ink was filtered using a syringe filter with a 700 nm mesh. Each sample consisted of 10 layers printed only after complete drying of the material previously printed. The substrate coverage and the optimal splat overlap was achieved by printing with a resolution of 700 DPI (dots per inch). The jetting pulse was optimized in order to jet single spherical droplets and the resulting voltage profile was (0 V, 0 µs), (50 V, 6 µs), (50 V, 16 µs). A jetting frequency of 1 kHz was used.

The substrate [2] was a pre-sintered NiO-YSZ cermet anode on a NiO-YSZ support. The green NiO-YSZ anode was prepared by tape casting (after reduction of NiO, Ni / YSZ ratio of 40 / 60 vol / vol, 8 mol% Y_2O_3 stabilized ZrO_2). Two layers were co-laminated in the green state at ca. 150 °C, i.e. a 10 – 15 µm thick NiO-YSZ anode on top of a 300 µm thick NiO-YSZ support. The firing of the substrate consisted of a multistep debinding procedure up to 700 °C for 48 h in total. The final sintering temperature, 1300 °C, was kept for 6 h.

The printed samples were sintered in air with the following profile: 0 – 600 °C at 0.25 °C min^{-1}; dwell for 4 h; 600 – T_{max} °C at 1 °C min^{-1}; dwell for 6 h; cool to room temperature at 1.67 °C min^{-1}. Here, three different temperatures T_{max} were used, 800, 1000 and 1300 °C.

2.2.4 Catalytic CO oxidation

Temperature programmed CO oxidation experiments were conducted in a BELCAT-B (BEL Japan, Inc.) catalyst analyzer at a same linear heating rate (3 °C min^{-1}) for all samples between room temperature and 350 °C [3]. The later was maintained for 5 min before cooling down. The $CoFe_2O_4$ particles (by CHFS and the reference) were first mildly pressed and a sieve fraction of the pressed particles ranging from 250 to 355 µm was used, and was mixed with SiC powders (>355 µm) in a weight ratio 1 to 2. Afterwards, the sample (40 mg $CoFe_2O_4$ and 80 mg SiC) was placed on a fixed bed stabilized by quartz wool in a U-shaped cell. Prior to test, the sample was dried at 100 °C for 60 min in He (80 mL min^{-1}). During test, a flow of 3 vol% CO and 6 vol% O_2 in He at 80 mL min^{-1} was passed through the bed. The inlet gas flow was controlled by a mass flow controller while the outlet gas was analyzed by the equipped quadropole mass spectrometer (Pfeiffer Vacuum, Germany). The work is reported in detail in **Chapter VII**.

2.2.5 Electrochemical measurements for oxygen evolution reaction

The activity of $Co_{1-x}Ni_xFe_2O_4$ (x = 0 – 0.8) particles in the oxygen evolution reaction (OER) was evaluated by electrochemical measurements. All measurements were conducted with a conventional three-electrode cell using an Autolab potentiostat/galvanostat (PGSTAT12, Eco Chemie, Utrecht, Netherlands) coupled to a Metrohm RDE rotator [4]. A disc glassy carbon electrode (diameter 0.3 cm, geometric area 0.07069 cm^2) modified with the catalyst inks was used as the working electrode, a silver / silver chloride electrode (Ag/AgCl, 3 mol L^{-1} KCl) as the reference electrode and a platinum foil as the counter electrode. The measured potentials were converted to the reversible hydrogen electrode (RHE) using the following equation $E_{RHE} = E_{Ag/AgCl} + 0.210\ V + 0.059\ pH$. The pH was determined using a pH meter and was 14 for 1 mol L^{-1} KOH.

The glassy carbon electrode was polished on a polishing cloth using alumina paste (0.05 µm) to obtain a mirror-like surface, followed by ultrasonic cleaning in DI H_2O. The Catalyst suspension was prepared by dispersing 2.5 mg particles in 498 µL mixture of ethanol and DI H_2O (1 to 1 in volume ratio) added with 2 µL Nafion 117 solution (Sigma Aldrich), and was sonicated for 20 min. The catalyst suspension of 3 µL was drop-coated onto the polished glassy carbon electrode with a mass loading of 0.21 mg cm^{-2} and was dried in air at room temperature. Before the OER measurements, the prepared electrode was subjected to continuous potential cycling in the potential window of 1 V to 1.45 V vs. RHE until reproducible cyclic voltammogram was obtained. Impedance spectroscopy was recorded in the frequency range from 50 kHz to 1 Hz at the corresponding open circuit potential of the electrode, using an AC perturbation of 10 mV. The resistance of the solution R_s was determined from the resulting Nyquist plot, and later was used for ohmic drop correction to the potential applied on the working electrode, according to the relation $E_c = E_m - i R_s$, where E_c and E_m are the corrected and applied potentials respectively and i is the current. For the OER test, measurements were performed by sweeping the potential from 0 V anodically to 0.8 V at 5 mV s^{-1} with the electrode rotating at 1600 rpm. Current densities were calculated using the geometric surface area of the glassy carbon electrode disk. The work is reported in detail in **Chapter VII**.

2.3 Material characterization

2.3.1 Characterization of particles

Unless specified otherwise, a standard process as following was applied when characterizing the synthesized particles.

Particle separation: Particles were separated from the product slurries by a centrifuge (Sorvall Legend XT with Fiberlite rotor F14s, Thermo Scientific, max. 11000 rpm, 6 × 250 mL), washed by DI H_2O, and dried at ambient conditions.

XRD: X-ray diffraction (XRD) measurements were carried out with drought particles by using a Bruker Robot D8 diffractometer (Cu Kα, 1.54 Å, non-monochromatic, divergent slit size). Usually a

scan range of 10 – 110° in 2θ with a stepsize 0.01° was applied. The Diffrac.Eva Suite (Bruker, Germany) was used to analyze the diffraction data, with respect to identifying phases and estimating crystallite sizes from peak broadening. The FullProf Suite [5] was used to refine diffraction data in the Rietveld method.

Raman: Raman spectra of particles were recorded using a Renishaw inVia Reflex confocal Raman microscope. For the spectra presented, a 532-nm laser and a 50X microscope objective was employed. The spectra were averaged and background-corrected.

TEM: For TEM characterization, samples were prepared by re-dispersing particles in ethanol using an ultrasonic processer (Hielscher UP200St, Germany) and then dropping them on holey carbon/Au or holey carbon/Cu grids. Either a JEOL 3000F transmission electron microscope operating at 300 kV with a field emission gun, or a JEOL 2100 transmission electron microscope operating at 200 kV with a LaB_6 gun was used. The size and morphology of particles were determined with bright-field TEM (BF-TEM) images. High-resolution TEM (HR-TEM) images and selective area electron diffraction (SAED) patterns were also taken with several samples when necessary. The Gatan DigitalMicrograph (Gatan, Inc.) software and the CrystalMatch (Søren B. Simonsen, sobrs@dtu.dk, DTU Energy) software were used to analyze BF-TEM, HR-TEM micrographs and SAED patterns.

STEM and EDS: In addition to the TEM characterization, with the JEOL 3000F equipped with a STEM unit, scanning transmission electron microscopy (STEM) was conducted with several samples. By using a focused beam of electrons to scan over the sample, STEM is able to characterize nanostructures with an atomic resolution, providing information such as imaging, elemental composition and electronic structure [6]. When a high-angle annular dark field (HAADF) detector is used, electrons scattered by atoms, excluding the transmitted, are used for imaging and HAADF-STEM images provide a 'Z'-contrast related to the atomic number. Here, the nominal beam probe size of 0.5 nm and a camera length of 12 cm were used, when doing the HAADF-STEM characterization. In the STEM mode, energy dispersive X-ray spectroscopy (EDS) was carried out by using the equipped Oxford Instruments EDS detector for compositional analysis particularly for

element mapping and line-scan analysis. The INCA software (Oxford Instruments) was used to process the HAADF-STEM images and EDS results.

Standardless EDS quantification: To evaluate chemical compositions of doped oxides and complex oxides, a standardless EDS quantification was applied. Drought particles were loaded on carbon tapes. A Hitachi Tabletop TM3000 scanning electron microscope (SEM) ('Analysis', 15 kV charge-reduction mode) equipped with a silicon drift detector (SDD, energy resolution 154 eV) was used to obtain the EDS spectra.

2.3.2 Characterization of bulk samples

Usually, bulk samples of interest were cut, embedded in epoxy and polished for SEM investigations of cross sections. For SEM investigations of fractured surfaces, bulk samples were broken to expose the fracture, and SEM was conducted on the fresh surfaces. Whenever necessary, surfaces were coated with 10-nm carbon to increase the surface conductivity.

A Zeiss Merlin equipped with a field emission gun operating at 5, 10 or 15 kV was used for SEM investigations. A high-efficiency secondary electron detector (HE-SE2), an on-axis in-lens secondary electron detector (InLens) and an energy-selective backscattered electron detector (ES-BSE) were applied to record micrographs. The micrographs were analyzed by the ThreshAlyzer software (Peter S. Jørgensen, psjq@dtu.dk, DTU Energy). EDS was conducted with a Bruker XFlash 6 EDS detector (energy resolution 129 eV) and data were processed by the Esprit 1.9 software (Bruker, Germany).

References

[1] Fujifilm, Jettable Fluid Formulation Guidelines, 2013.

[2] A. Hauch, M. Mogensen, Ni/YSZ electrode degradation studied by impedance spectroscopy: Effects of gas cleaning and current density, Solid State Ionics. 181 (2010) 745–753. doi:10.1016/j.ssi.2010.04.001.

[3] K.F. Ortega, D. Rein, C. Lüttmann, J. Heese, F. Özcan, M. Heidelmann, J. Folke, K. Kähler, R. Schlögl, M. Behrens, Ammonia decomposition and synthesis over multinary magnesioferrites: Promotional effect of Ga on Fe catalysts for the decomposition reaction, ChemCatChem. 9 (2017) 659–671. doi:10.1002/cctc.201601355.

[4] K. Chakrapani, G. Bendt, H. Hajiyani, I. Schwarzrock, T. Lunkenbein, S. Salamon, J. Landers, H. Wende, R. Schlögl, R. Pentcheva, M. Behrens, S. Schulz, Role of composition and size of cobalt ferrite nanocrystals in the oxygen evolution reaction, ChemCatChem. (2017). doi:10.1002/cctc.201700376.

[5] J. Rodríguez-Carvajal, Recent advances in magnetic structure determination by neutron powder diffraction, Phys. B Condens. Matter. 192 (1993) 55–69. doi:10.1016/0921-4526(93)90108-I.

[6] S.J. Pennycook, A.R. Lupini, M. Varela, A. Borisevich, Y. Peng, M.P. Oxley, K. Benthem, M.F. Chisholm, Scanning Transmission Electron Microscopy for Nanostructure Characterization, in: Scanning Microsc. Nanotechnol., 2007: pp. 152–191. doi:10.1007/978-0-387-39620-0_6.

Chapter III. Simulation, design and proof-of-concept of a two-stage continuous hydrothermal flow synthesis reactor for synthesis of functional nanosized inorganic composite materials

This chapter contains the article 'Simulation, Design and Proof-of-Concept of a Two-Stage Continuous Hydrothermal Flow Synthesis Reactor for Synthesis of Functionalized Nanosized Inorganic Composite Materials' published in *J. Supercrit. Fluids*, **2016**, 117: 1 – 12.

The mixer geometry significantly affects the mixing behavior and therefore plays a very important role in continuous hydrothermal flow synthesis. Computational fluid dynamics simulations were employed to evaluate several mixer geometries for a novel two-stage continuous hydrothermal flow synthesis reactor (CHFS reactor). The novel design was for synthesis of functional nanomaterials, e.g., core-shell or surface-decorated particles. Based on simulation results, a two-stage CHFS reactor was constructed employing a confined jet mixer in the first stage and a counter-flow mixer in the second stage. Simulations were done by the first author of this article. The PhD student assisted building the CHFS reactor.

Afterwards, the two-stage CHFS reactor was applied to synthesize NiO and Y-doped ZrO_2 (YSZ) nanoparticles. The functionality of the CHFS reactor was tested both in syntheses of single-phase nanoparticles and dual-phase nanocomposites, being operated in either the single-stage or two-stage mode. Particularly, in the two-stage synthesis, the ability to tailor the morphology of composite nanoparticles was demonstrated. Moreover, the high productivity of the CHFS technique was employed for providing sufficient amounts of NiO and YSZ nanoparticles for prototyping of energy conversion devices. A detailed characterization of the synthesized materials is also presented in this chapter.

Simulation, design and proof-of-concept of a two-stage continuous hydrothermal flow synthesis reactor for synthesis of functionalized nano-sized inorganic composite materials

Philipp Zielke [*], Yu Xu, Søren Bredmose Simonsen, Poul Norby and Ragnar Kiebach

Department of Energy Conversion and Storage, Technical University of Denmark, P.O. Box 49, DK-4000 Roskilde, Denmark

[*] Corresponding author: P. Zielke, Tel.: +45 40187184. Fax: +45 46775688. Email address: phzi@dtu.dk.

Abstract

Computational fluid dynamics simulations were employed to evaluate several mixer geometries for a novel two-stage continuous hydrothermal flow synthesis reactor. The addition of a second stage holds the promise of allowing the synthesis of functionalized nano-materials as for example core-shell or decorated particles. Based on the simulation results, a reactor system employing a confined jet mixer in the first and a counter-flow mixer in the second stage was designed and built. The two-stage functionality and synthesis capacity is shown on the example of single- and two-stage syntheses of pure and mixed-phase NiO and YSZ particles.

Keywords: supercritical water; hydrothermal; continuous synthesis; nanoparticles; reactor design, computational fluid dynamics

1. Introduction

Nano sized materials with particle sizes below 100 nm are increasingly important of for a large number of applications including healthcare, electronics, cosmetics or energy conversion and storage. Their unique properties make these materials superior, sometimes even indispensable, in many applications, and the need to transfer results from academic research into the industrial sector is growing [1,2]. In this context, the selection of appropriate methods combining synthesis of nanomaterials with required properties as well as scalability is of paramount importance. However,

traditional synthesis methods such as sol–gel, co-precipitation or pyrolysis often require expensive starting materials and can be time consuming. They often are energy intense and can involve the use of organic solvents, which is undesirable from an environmental, green chemistry point of view.

One promising development towards a more environmentally friendly synthesis processes is the use of supercritical fluids such as supercritical carbon dioxide or supercritical water (sc. water). In this context, the continuous hydrothermal flow synthesis (CHFS) technology [3] has recently gained attention as a method capable of producing large quantities of various nanoparticles with good controllability of size, crystallinity and composition, as shown for hydrothermal batch synthesis [4]. In a continuous process a steady inflow of precursor solutions and the supercritical medium are fed to the reactor, resulting in an outflow of the suspended product and therefore eliminating frequent heat-up- and cool-down-periods. The rapid mixing allows for an excellent control of the reaction conditions (e.g. temperature, pressure and flow rates). Employing heat recovery strategies and using water as solvent add to the method's environmental friendliness and its commercial viability. The upscaling of the CHFS process to industrial relevant production rates has been demonstrated by Hanwha Chemical [5] and in the European FP7 project SHYMAN (www.shyman.eu).

The fast and homogeneous mixing of the precursor solution and the sc. water is prerequisite for the synthesis of particle ensembles with narrow size distribution. Stagnant flows and backmixing effects need to be avoided to prevent the clogging of the reactor. Therefore, several mixer geometries have been developed in order to optimize the flow properties. The first reported CHFS system, described by Adschiri, et al. [3], employed a simple T-union mixer, which today is still popular [6,7] because of its simplicity. More complex geometries which promise improved mixing properties are counter-flow [8,9], confined-flow [10–12] and swirl mixers [13] as well as microfluidic systems [14].

Typically, CHFS reactors only have one mixing stage. Extending the reactor design to two mixing stages, which is the content of this work and has been recently presented in the literature [15], could have several advantages: Firstly it offers the possibilities to inject capping agents to prevent agglomeration of the nano particles formed in the first stage. Secondly, the second mixer could

introduce a second salt solution and therefore offer the possibility of synthesizing a second material in the presence of the one formed in the first stage. The second material could not only be obtained in form of isolated nanoparticles, but also could grow as a second phase on the surface of the already existing particles (decorated particles) or even form a complete layer around the particles from the first stage (core-shell structures) [16]. Such advanced nano-structures show promising properties for several applications [17] like catalysis or energy conversion devices, e.g. solid oxide fuel/electrolysis cells, which rely on well mixed composite structures with high surface areas and/or large catalytically active areas.

In the work presented here, a two-stage CHFS reactor was designed and built. In a first step, the mixing geometries for both stages were modeled, optimized using computational fluid dynamics (CFD) simulations. Based on the results, a two-stage reactor capable of operating pressures up to 30 MPa, temperatures up to 450 °C and combined flow rates of precursor solutions and sc. water of up to 250 mL min^{-1} was build. For demonstrating the virtue of the two stage reactor, several successful experiments with NiO-YSZ (12 mol% yttria stabilized zirconia, $Y_{0.22}Zr_{0.78}O_{2-\delta}$), a composite system relevant for anodes used in solid oxide fuel cells, were conducted. Recent studies on optimizing the Ni/YSZ structures show, that size-matched and well-dispersed particles as fine as possible have a beneficial influence on the long-term performance of solid oxide cells [18]. First results show that particles sizes, structures can be tuned to a large degree and that the mixing geometries chosen based on the simulations fully keep up to expectations in real-life operations.

2. Experimental

2.1 Computational details

The three-dimensional model of the mixers were created in Dassault Systèmes SolidWorks 2014 and meshed in ANSYS 14.5 [19]. Whenever possible the symmetry of the model was exploited by using symmetry planes in order to reduce computational time. The flow field, energy transfer and species mixing were calculated using the FLUENT module of ANSYS 14.5. The methodology was

adapted from previous reports in the literature [20–24]. The standard k-ε-model for turbulent flow with the standard model constants implemented into the FLUENT module was used employing standard wall functions and the standard SIMPLE pressure-velocity coupling for a steady-state solution. The inbuilt energy transfer model was used. For the numerical discretization of the governing equations, a second-order upwind scheme was used. In all cases, gravity was taken into account. The density, specific heat, thermal conductivity and viscosity of pure water as a function of the temperature at constant pressure were taken from the 1995 IAPWS formulation [25] and implemented as piece-wise linear fits in the range of 275 K to 705 K with a constant step size of 10 K.

In order to study the mixing behavior the liquid entering the precursor inlet was defined as a mixture of two different species of water with identical properties, as shown by e.g. Ma, et al. [20]. For the temperature dependent self-diffusion constant a piece-wise polynomial fit (two cubic polynomial functions, one above and one below the critical temperature) of the approximation by Macedo and Liu [26] was implemented as described by Sierra-Pallares, et al. [27].

The inlet turbulence intensity was set to 10 % with a length scale of the inlet's diameter. Unless stated otherwise the simulations were run at 240 bar under constant pressure conditions. The temperature of the sc. water was set to 400 °C, the precursor solution to 20 °C.

2.2 Particle synthesis and characterization

Based on the modeling work, a two-stage continuous hydrothermal flow synthesis reactor (CHFS reactor) was built (details see section 3.2) and was tested by applying it to the synthesis of YSZ ($Y_{0.16}Zr_{0.84}O_{2-\delta}$), NiO single-phase nanoparticles and dual-phase mixtures of YSZ and NiO nanoparticles. An scale-up production of the dual-phase mixture was also conducted in order to test the capacity of the CHFS reactor. $Y(NO_3)_3 \cdot 6H_2O$ (99.8 %), $ZrO(NO_3)_2 \cdot 6H_2O$ (99 %) and $Ni(NO_3)_2 \cdot 6H_2O$ (98.5 %) from Sigma Aldrich used as bought were dissolved into DI H_2O to prepare the precursor solutions. The ratio of $Y(NO_3)_3$ to $ZrO(NO_3)_2$ in the solutions was determined by the

stoichiometric molar ratio of YSZ. Aqueous KOH (Sigma Aldrich, 85 %) solution was applied as mineralizer. Details of synthesis conditions are summarized in **Table 1**. The employed flow rates were 10 mL min^{-1} for both the metal salt precursor flows and the KOH flow unless stated otherwise, whereas for the sc. water stream, the flow rate varied from 30 mL min^{-1} for the synthesis of single-phase particles to 35 mL min^{-1} for the synthesis of dual-phase particles as well as the scale-up production. Unless specified otherwise, only the first stage was employed for the particle synthesis, and the precursor flow and the KOH flow were premixed before entering the first stage.

The nanoparticles were separated from the obtained slurry by a centrifuge, then washed and dried. Powder X-ray diffraction measurements were obtained from dried particles on a Bruker Robot diffractometer (Cu Kα, 0.154 nm) at a step size 0.01°. Rietveld refinement was conducted by the FullProf software suite [28] to fit the peaks, determine the unit cell parameters and quantify the compositions. By the Diffrac Eva software suite (Bruker, Germany), the crystallite size was derived from the full width at the half maximum (FWHM) of the (111) and (200) peaks in the XRD patterns of both YSZ and NiO. For TEM characterization, the nanoparticles were re-dispersed in ethanol by means of ultrasonic shaking and dropped onto a Holey carbon film/Au grid. Bright field TEM images were recorded with a JEOL 3000F microscope operating at 300 kV with a field emission gun. Whenever quantifying the size of nanoparticles, the ImageJ software was used to outline the perimeter of the particle projection, and by assuming spherical shape the particle diameter was calculated. Dark-field scanning transmission electron microscopy (DF-STEM) was carried out by using the JEOL 3000F equipped with a STEM unit and a high angle annular dark field (HAADF) detector. The nominal probe size was 0.5 nm and the camera length was 12 cm. For composition analysis, energy dispersive X-ray spectroscopy (EDS) was carried out by using the equipped Oxford Instruments EDS detector and was processed by INCA software. Raman spectra of the dried as-prepared particles were recorded with a Renishaw inVia Reflex confocal Raman microscope. For the spectra presented in this work a 532 nm laser and 50x microscope objective was employed. The spectra are averaged and background-corrected.

Table 1. Summary of reaction conditions

Products		Precursor Solution/(mol L^{-1})	KOH/(mol L^{-1})	T of sc. water /°C	System Pressure/MPa
Single phase	YSZ	$Y(NO_3)_3$ (0.016) $ZrO(NO_3)_2$ (0.057)	1	398	28
	NiO	$Ni(NO_3)_2$ (0.05)	0.5	398	27.8
Dual phase two-stage	YN1 (YSZ+NiO)	St.1: $Ni(NO_3)_2$ (0.05) St.2: $Y(NO_3)_3$ (0.008) $ZrO(NO_3)_2$ (0.029)	1[a]	398	27.5
	YN2 (YSZ+NiO)	St.1: $Ni(NO_3)_2$ (0.05) St.2: $Y(NO_3)_3$ (0.0016) $ZrO(NO_3)_2$ (0.0057)	1[b]	398	28.3
Dual phase single-stage	YNS (YSZ+NiO)	$Ni(NO_3)_2$ (0.1355) $ZrO(NO_3)_2$ (0.0369) $Y(NO_3)_3$ (0.0103)	1	399	28

Notes: T of the sc. water was recorded by the thermocouple before the sc. water stream meets the metal salt precursors flow. System pressure was controlled by the backpressure regulator with a variation ±1 MPa. St.1 and St.2 refer to the first stage and the second stage respectively in the CHFS reactor. a, the KOH solution was pumped into the first stage; b, the KOH solution was pumped into the second stage.

3. Results and discussion

3.1 CFD modelling results

3.1.1 Mixing stage 1

For the design of the first mixing stage several geometries were simulated, including various orientations of T- (introduced by Adschiri, et al. [3]), cross- and Y-junctions (both investigated by e.g. Lester, et al.[29]) as well as confined co- (after Aymonier, et al. [11] and Gruar, et al. [12]) and counter-flow (according to Lester, et al. [8]) geometries. With the assumed typical use-case flow rates of 20 mL min^{-1} for sc. water and precursor solution and dimensions equivalent to 1/4” tubing the simple junction geometries (T, cross, Y) showed poor mixing properties with strong backmixing and were therefore discarded. The results of these simulations are not shown in this publication, but

similar computational [27] and experimental [29–31] studies can be found in the literature. It should be mentioned though, that it has been shown that the mixing using a T-junction geometry can be greatly improved by decreasing the tube diameter [21].

For the counter- and co-flow geometries a 1/16'' capillary (1.59 mm O.D., 0.57 mm I.D.) within a 1/4" tube (6.35 mm O.D., 3.86 mm I.D.) was chosen. Because of the obvious risk of clogging, the inner capillary was not suited for the precursor, but only for the sc. water stream. The meshing was done with similar element sizes to obtain comparable results (co-flow: 63 × 10^3 nodes, 193 × 10^3 elements for 165 mm^3 simulated volume; counter-flow: 106 × 10^3 nodes, 326 × 10^3 elements for 353 mm^3; average element size for both: ~1 × 10^{-3} mm^3). The results of simulations of these two geometries are shown in **Fig. 1** (precursor concentration profiles). The sc. water and precursor flow rates were set to 20 mL min^{-1}. The geometries were oriented vertically with both, an upward (**a**, **d**) and a downward (**b**, **c**) outflow.

The volume in which the mixing occurs was used as a semi-quantitative for the mixing efficiency. Here the mixing volume was defined as the volume in which the precursor concentration was between 5 % and 45 % as well as 55 % to 95 % of the precursor inlet concentration, in other words the volume, which contains neither the pure sc. water nor pure precursor solution nor the complete mixture of those. Given equal flow rates of the sc. water and the precursor solution and similar geometries (here 1/4" tube) the mixing volumes are comparable and a smaller volume points towards a shorter mixing time.

Comparing the different geometries, the co-flow showed a smaller mixing zone (upward outflow, **Fig. 1a**: 13.7 mm^3; downward outflow, **Fig. 1b**: 29.3 mm^3) than the counter-flow (downward outflow, **Fig. 1c**: 109.3 mm^3; upward outflow, **Fig. 1d**: 99.9 mm^3) and can therefore be considered more efficient. The reason for this becomes obvious when looking at the flow field shown in the upper part of **Fig. 2**. The fast outflow from the inner capillary creates a barrel shaped vortex, which pulls the precursor

stream into the sc. water. The mixing occurs almost instantly at the boundary of the vortex (see **Fig. 2** lower part). These findings are in agreement with results from similar simulations by Ma et al. [32].

Because of its more efficient mixing, the co-flow geometry in **Fig. 1b** was chosen for the first mixing stage and investigated further. Since the downward oriented outflow potentially prevents sedimentation of the produced particles into the inlet, it was chosen over the upward oriented geometry, although it showed a roughly twice as big mixing volume. The inherent drawback of the co-flow geometry is, that the precursor solution traveling along the outside of the inner tube (which is heated by the supercritical water stream) is prone to already start precipitating particles before reaching the mixing zone. During the course of this study, a covering of the outside of the inner tube with an oxide layer was observed, which did not lead to a block of the reactor though.

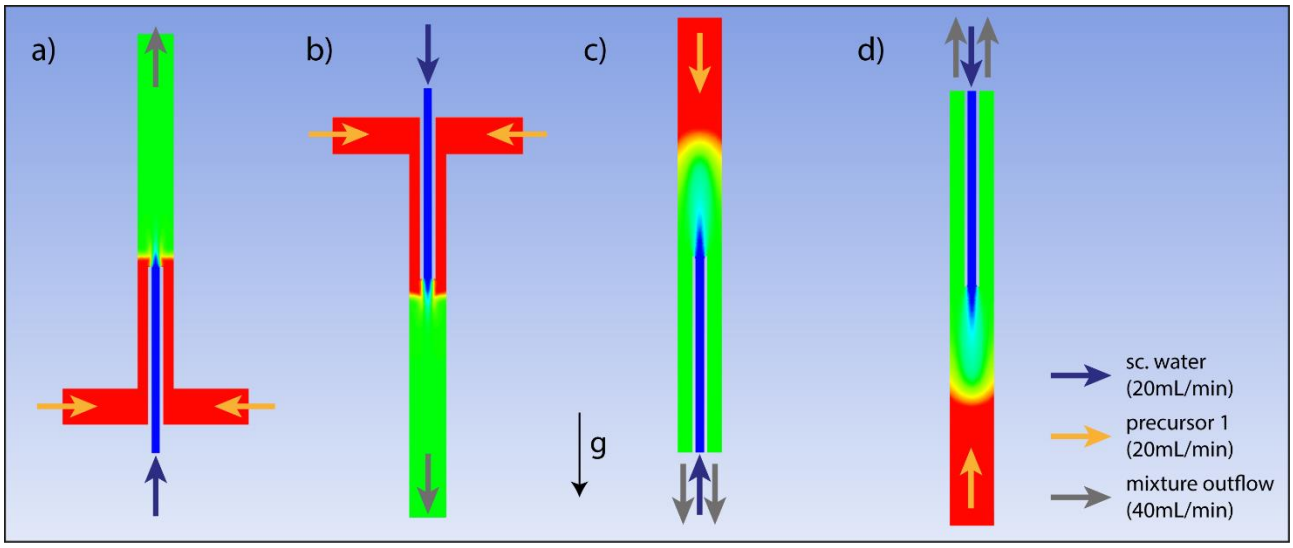

Figure 1. Simulation of (**a, b**) co- and (**c, d**) counter-flow geometries of stage 1. The blue arrows indicate the sc.water inlet (20 mL min^{-1}, 400 °C), the yellow arrows the precursor solution inlet (20 mL min^{-1}, 20 °C) and the gray arrows the mixture outflow. The color code indicates the precursor tracer concentration: red: feed precursor mixture, blue: feed sc.water, other colors indicate degree of mixture between precursor and sc.water. g indicates the direction of the gravitational force; (**a**) upward outflow co-flow; (**b**) downward outflow co-flow; (**c**) downward outflow counter-flow; (**d**) upward outflow counter-flow.

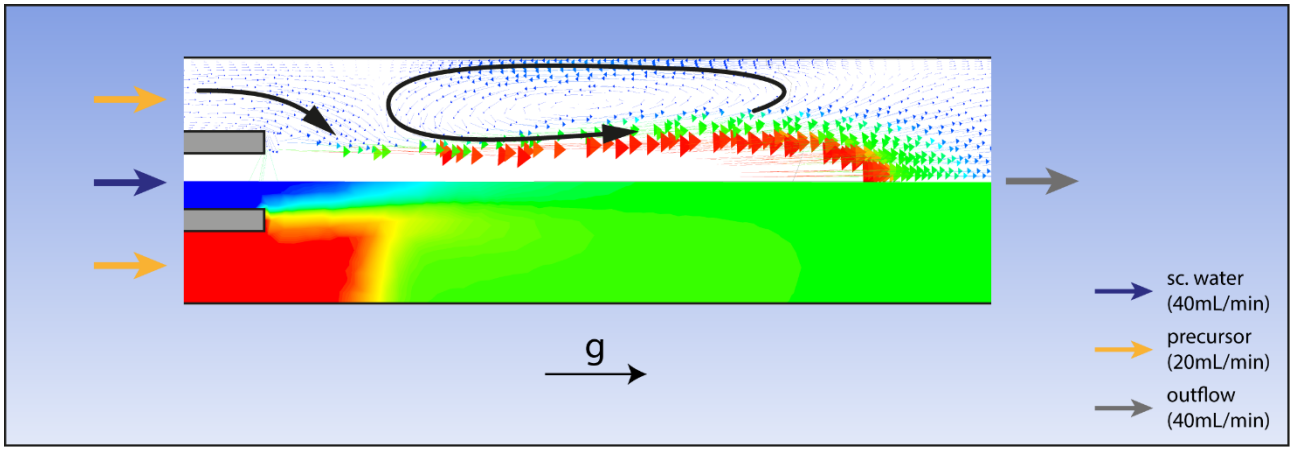

Figure 2. Mixing of stage1, downward outflow co-flow mixer; Top: flow field of the mixer (velocity vectors); bottom: precursor distribution, the color code indicates the precursor tracer concentration: red: feed precursor mixture, blue: feed sc.water, other colors indicate degree of mixture between precursor.

3.1.1.1 Influence of flow rates

The influence of the flow rates of the sc. water and the precursor solution on the vortex-formation in the co-flow mixer that is responsible for the excellent mixing properties was investigated. Flow rates of 5, 20 and 55 mL min^{-1} were chosen for the simulation. These represent the minimum, assumed standard and maximum pumping rates. The values for the mixing volumes are not given, since they are not comparable due to the different flow rates. The results are summarized in **Fig. 3** and **Table 2**.

In cases of identical precursor and sc. water flow rates, a complete mixing within the simulated volume was observed (**Fig. 3d**). Only in the case of the lowest flow rates, a weak backmixing was evident (**Fig. 3a**). Though the simulation still shows a sharp mixing onset and no backflow of sc. water into the precursor solution inlet, these conditions are potentially problematic in reality. A very low sc. water flow combined with higher precursor flows resulted in a very slow mixing (**Fig. 3b**), where no complete mixing was observed in the simulated volume. The simulated flow field (not resented here) did not show the formation of a vortex (as shown in **Fig. 2**). The outer precursor stream sheathed the sc. water stream with a persistent species gradient across the tube within the

simulation volume. When combining a low precursor flow with higher sc. water flow rates strong buoyancy driven backmixing was predicted by the simulation (**Fig. 3e**).

Given that medium to high flow rates (20 – 55 mL min^{-1}) of the sc. water and the precursor solution represent typical synthesis conditions, the simulations showed that the co-flow mixer design provides complete mixing within the simulation volume without the occurrence of backmixing at all relevant flow rates (**Fig. 3c** and **3d**).

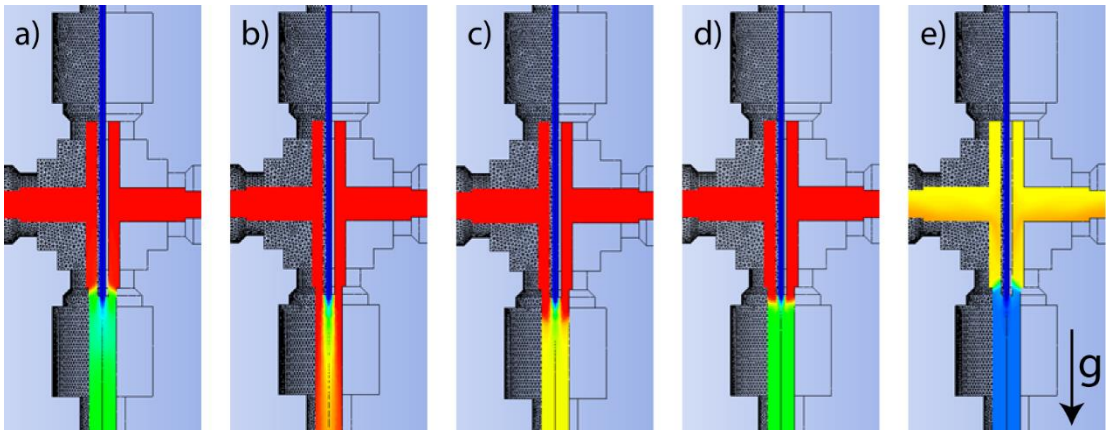

Figure 3. Precursor concentration profiles showing the mixing behavior of stage 1 at different sc. water (SW) and precursor (PC) flow rates, red: high precursor concentration, blue: low precursor concentration. (**a**) SW: 5 mL min^{-1}, PC: 5mL min^{-1}, weak backmixing; (**b**) SW: 5 mL min^{-1}, PC: 55 mL min^{-1}, very slow mixing; (**c**) SW: 20 mL min^{-1}, PC: 55 mL min^{-1}, slightly slow mixing; (**d**) SW: 55 mL min^{-1}, PC: 55 mL min^{-1}, excellent fast mixing; (**e**) SW: 55 mL min^{-1}, PC: 5 mL min^{-1}, strong backmixing.

Table 2. Flow-rate-dependent mixing behavior of stage 1, the letters indicate the corresponding mixing profile in **Fig. 3**

Precursor flow rate / (mL min^{-1})	sc. H_2O flow rate / (mL min^{-1})		
	5	20	55
5	weak backmixing [a)]	backmixing	backmixing [e)]
20	slow mixing	good	good
55	slow mixing [b)]	good [c)]	good [d)]

3.1.1.2 Influence of geometry deviations

Simulations of the co-flow mixer showed a strong influence of small deviations from the ideal geometry on the mixing/flow behavior. **Fig. 4** shows the precursor concentration profiles for (**a**) a perfectly centered, (**b**) 200 µm eccentric and (**c**) 400 µm eccentric supercritical water inlet. The flow rates for the sc. water and the precursor solution were set to 20 mL min^{-1}. The perfect concentric mixer (**Fig. 4a**) showed an excellent mixing with a very small mixing volume and no backmixing. Upon moving the outlet of the sc. water capillary by 200 µm off center (**Fig. 4b**) the mixing profile became asymmetric with still minor backmixing without backflow to the precursor solution inlets. An eccentricity of 400 µm however leads to a completely different result. The precursor concentration profile in **Fig. 4c** shows a massive backmixing comparable to a simple cross mixer. This is suspected caused mainly by the buoyancy of the hot water.

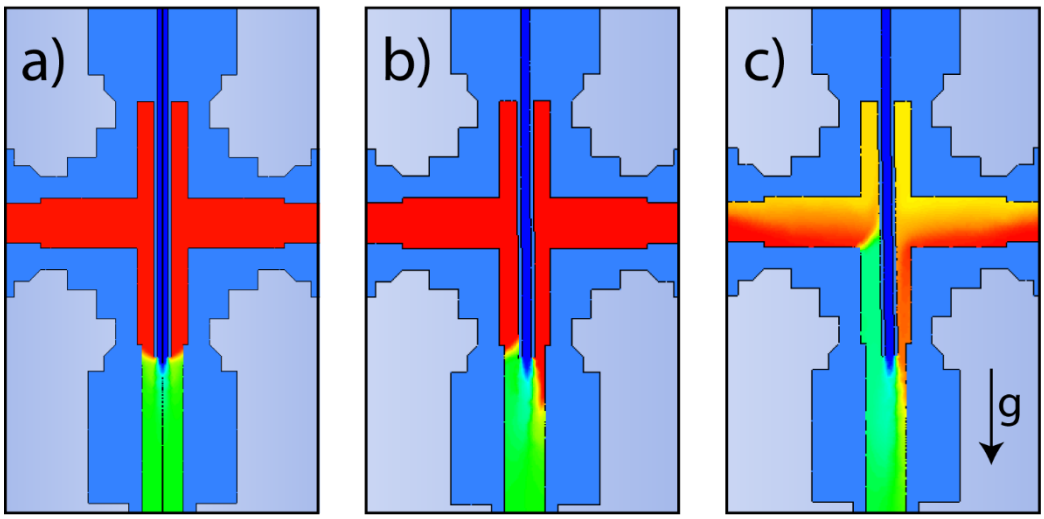

Figure 4. Eccentricity sensitivity of co-flow mixer illustrated by precursor concentration profiles, red: high precursor concentration, blue: low precursor concentration; **a**: inner tube perfectly straight, **b**: inner tube 200 µm bent to the right, **c**: inner tube 400 µm bent to the right.

It should be noted that simulations with an upside-down geometry (not presented here) showed a much smaller influence of eccentricity without backmixing, but were not take into consideration because of the anticipated top-down geometry.

3.1.2 Mixing stage 2

Reducing the diameter of the outflow of the first bears a high risk of clogging of the reactor. Therefore, the diameter was kept (1/4” tubing, 6.35 mm O.D., 3.86 mm I.D.) as the inner capillary of stage two. For the outside, 1/2” tubing (12.70 mm O.D., 8.48 mm I.D.) was chosen.

Fig. 5a shows the simulated mixing behavior of the co-flow mixer under realistic conditions (40 mL min^{-1} from stage 1, 300 °C, 20 mL min^{-1} precursor solution, 20 °C). The very pronounced backmixing precludes this geometry. Only at much higher flow rates close to the maximum output of the pumps which are irrelevant for the anticipated use a satisfactory mixing behavior was observed (not shown) in the simulations. A counter-flow geometry with an upward outflow direction (**Fig. 5b**) presents itself as the much more suitable choice. The relatively small capillary diameter prevents backmixing into the first stage, the buoyancy of the hot and therefore less dens mixture prevents backmixing into the precursor inlet.

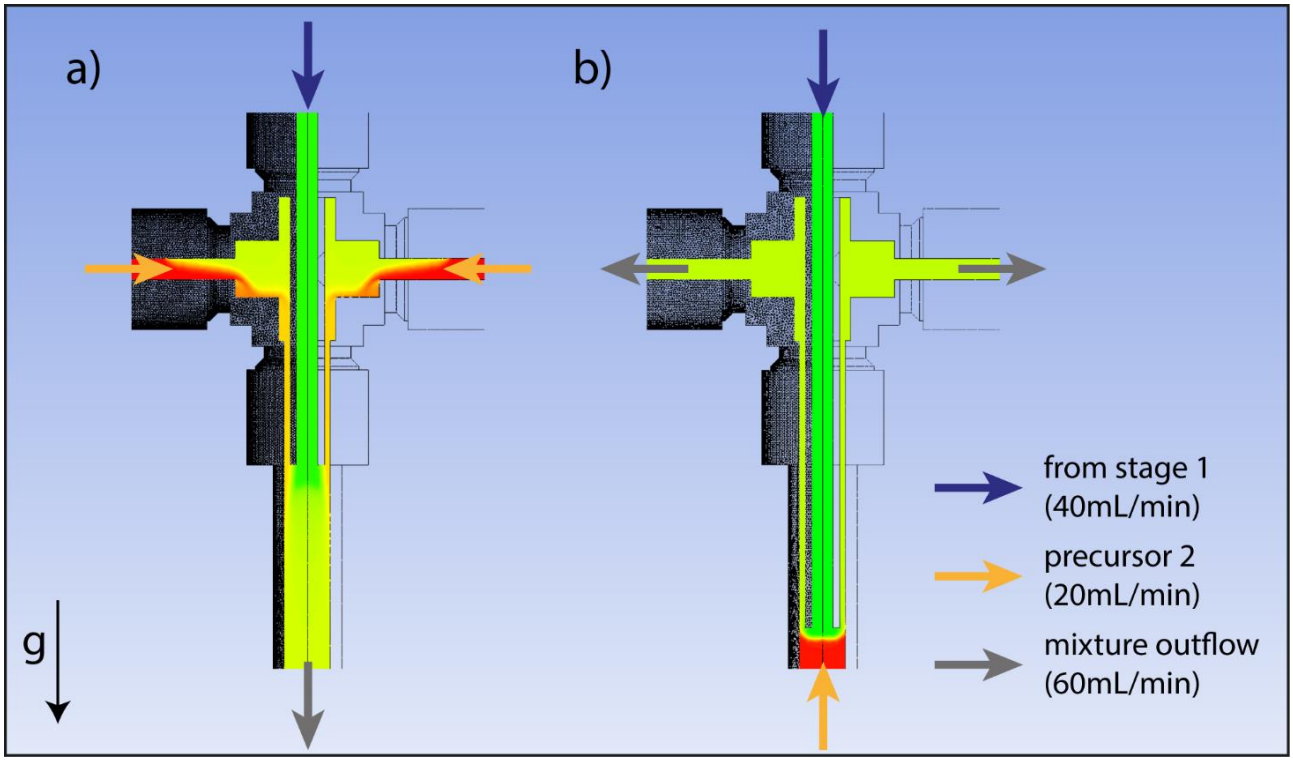

Figure 5. Precursor concentration profiles showing the mixing behavior of co- (**a**) and counter-flow (**b**) design for the second mixing stage.

3.1.2.1 Influence of flow rates

Upon varying the flow rates, no backmixing was observed in the simulations (**Fig. 6**). It mainly influenced the position and shape of the mixing front.

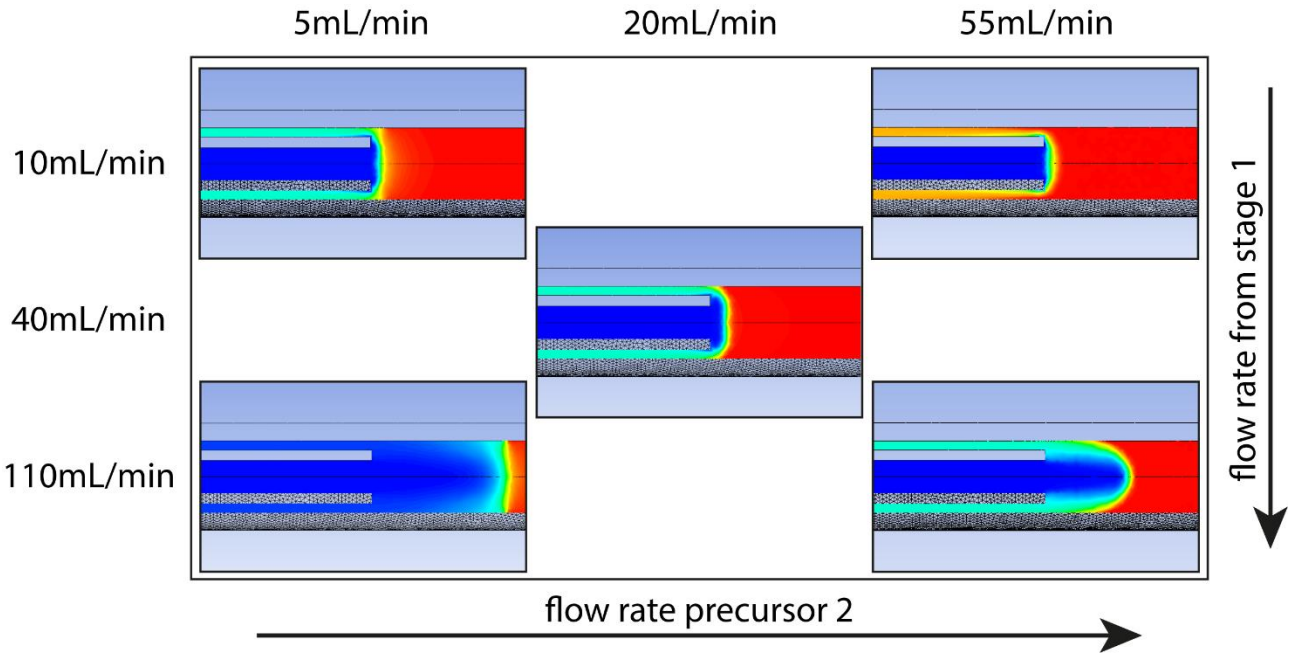

Figure 6. Precursor concentration profiles showing the mixing behavior of stage 2 at different flow rates, red: high precursor concentration, blue: low precursor concentration.

3.1.2.2 Influence of geometry deviations

Fig. 7 shows the eccentricity sensitivity of the counter-flow design of stage 2. Though this geometry completely avoids any kind of backmixing upon bending the inner tube up to 500 µm out of the center, an influence on the mixing efficiency is clearly visible. **Fig. 7b** shows the precursor concentration profile with an eccentricity of 250 µm. 3 cm downstream the mixing point (marked by dashed line) on the left, wider side is approx. 30 % higher than on the right side. Upon 500 µm eccentricity (**Fig. 7c**) the precursor concentration is 60% higher on the wider left side than on the right.

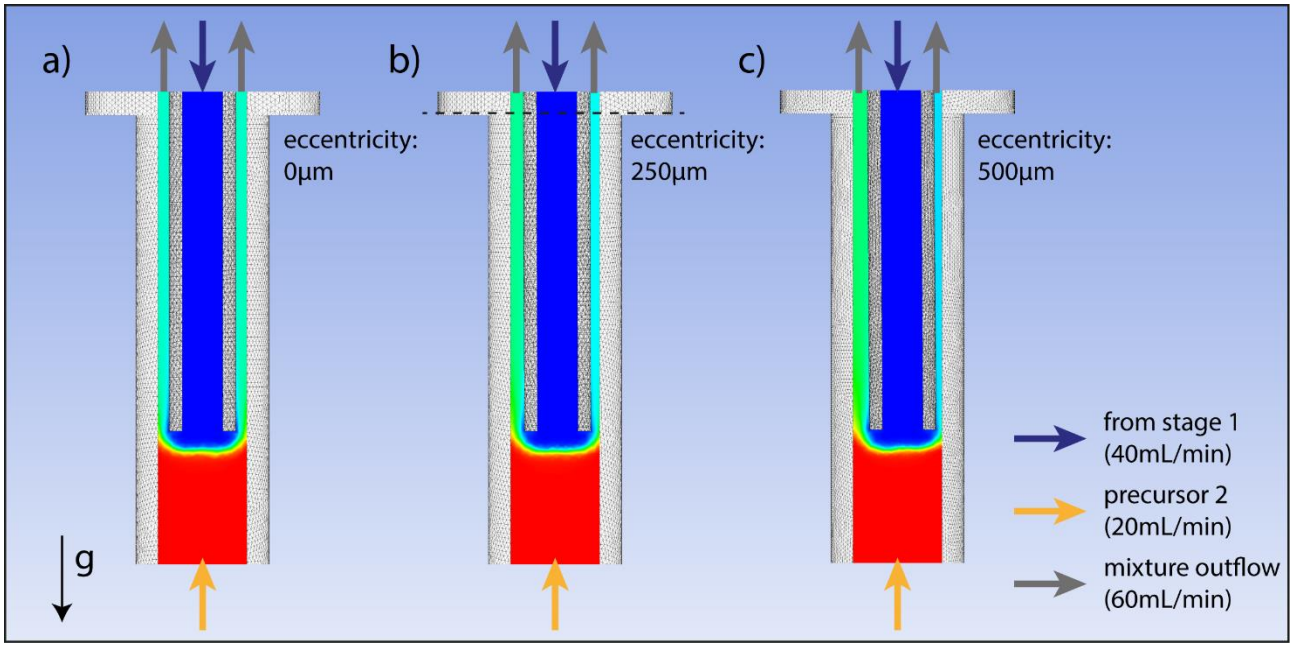

Figure 7. Eccentricity sensitivity of counter-flow mixer (stage 2) illustrated by precursor concentration profiles, red: high precursor concentration, blue: low precursor concentration; **a**: 0 µm eccentricity, **b**: 250 µm eccentricity, **c**: 500 µm eccentricity

3.2 Build-up of the CHFS reactor based on simulation results

A sketch of the continuous hydrothermal reactor that was built based on the results of the CFD simulations presented above is shown in **Fig. 9**. Unless stated otherwise 1/4" stainless steel 316 tubing (6.35 mm O.D., 3.86 mm I.D.) was used. The liquids are supplied by five Milroyal D metering pumps (Milton Roy, 5 - 55 mL min^{-1} capacity, internal relief valves set to 310 bar). Pulsation dampeners installed downstream each pump ensure a more constant flow rate through the reactor. Pump 1 is feeding the to-be-heated medium, typically water, to the preheater. A check-valve between the preheater and pump 1 prevents a backflow of fluid and a depressurization of the system in case of a pump failure. The pressure at the outflow of pump 1 can be monitored by a mechanical pressure gauge and an electronical pressure transducer. The preheater consist of four aluminum plates which were machined to tightly fit approx. 6 meters of 1/4" Inconel 600 tubing (6.35 mm O.D., 3.86 mm I.D .) and 20 1/4" heating cartridges (200 W each, Watlow). The resulting total heating capacity of 4 kW is sufficient to heat the full output of pump 1 to supercritical conditions. The temperature of the

preheater is measured by two independent thermocouples and controlled by a custom-built control system (Elkas Automation). The outflow of the preheater was led past a thermocouple to measure the outflow's temperature and fed to the inner tube of the co-flow mixer as described above. Upstream the mixing stage 1, a rupture disc (Maximator, burst pressure 350 bar @ 400 °C) was installed to depressurize the system in case of an accidental sudden pressure increase. To feed the precursor solution to mixing stage 1 (see **Fig. 8**) two pumps (2 & 3) can be used. This allows for reactant mixtures that can already under normal conditions from precipitates that would harm the pumps, e.g. a mixture of KOH and a metal salt solution that forms hydroxides. The streams of pump 2 und 3 are united and mixed in a simple T-junction. A check valve downstream the T-junction prevents backflow from the reactor in case of a failure of the precursor inlet system. The outflow tube of the first mixing stage forms the inner capillary of the second stage's counter-flow mixer described in the previous section. The precursor for the second stage was fed upwards into the outer tube (1/2", 12.70 mm O.D., 8.48 mm I.D.). The precursor inlet system is identical the one used for the first stage. After mixing the upward streaming mixture is directed horizontally away from the stage 1 outlet by a T-junction (see **Fig. 8**) and then downwards again to avoid sedimentation. Before reaching the reheaters, the temperature of the outflow of stage 2 is measured by a thermocouple. Each of the two reheaters consists of two aluminum half-cylinders that tightly fit the reactor tube on the inside and three barrel heaters (300 W each, Watlow) on the outside. Together those provide a total heating capacity of 1.8 kW. The temperature of each reheater is measured by two independent thermocouples and controlled by a custom-built control system (Elkas Automation). Downstream the reheaters the temperature is measured before the stream is reaching a tube-in-tube heat exchanger (6 m, 1/4" Inconel inner tube, Sentry Equipment Corp.). Here the product stream is cooled down to approx. 20 °C. After passing the two parallel particulate filters (Swagelok), the stream is depressurized to atmospheric pressure. This can be done either by a proportional relief valve (Swagelok) or by a pneumatically driven backpressure regulator (Tescom, 26-1700 Series) with an active feedback control (Tescom, ER5000). Parallel to the backpressure regulator and the process relief valve a safety relief valve is installed to prevent overpressurizing the reactor in case of failure.

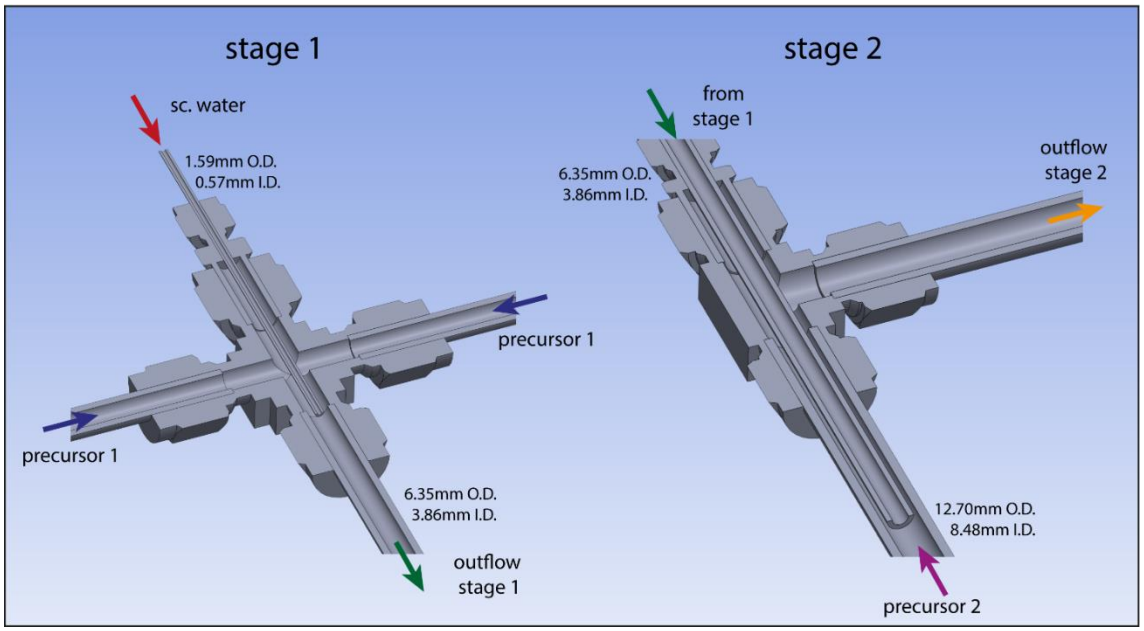

Figure 8. Cross-section of the mixing stage 1 & 2.

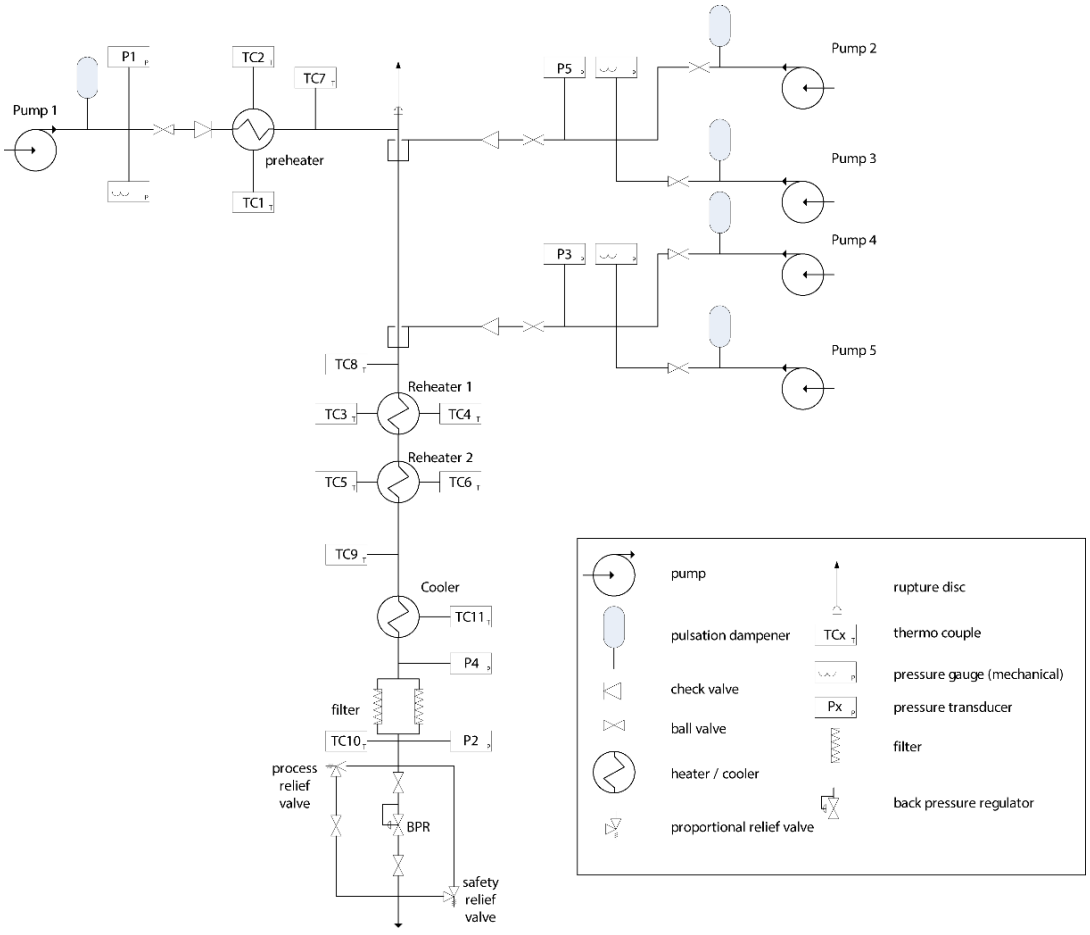

Figure 9. Schematics of the CHFS reactor.

3.3 Single-phase nanoparticles

The syntheses of YSZ and NiO, which have been the subject of CHFS studies in the literature [33–35] and are well-known materials used in solid oxide fuel cells, were used to demonstrate the capabilities of the new CHFS reactor. The reaction conditions are shown in **Table 1**.

3.3.1 YSZ

Fig. 10 sows the characterization results of the as-prepared YSZ particles. The XRD pattern of the obtained powder (**Fig. 10a**) fits the one of cubic $Y_{0.2}Zr_{0.8}O_{1.9}$. To distinguish from the monoclinic phase a Raman spectrum (**Fig. 10b**) was recorded. The single broad feature at ~610 cm^{-1} clearly corresponds to cubic YSZ [36]. The shape and size of the as-prepared particles are shown in the bright field TEM image (**Fig. 10c**). The nanoparticles exhibit a relatively round shape and the result of a particle size distribution based on 141 particles is shown in **Fig. 10d**. The mean particle size was 9.7 nm with a standard deviation of 2.3 nm. The crystallite size derived from the FWHM of the (111) and (220) diffraction peaks was 10 nm which is in good agreement with the TEM result.

The high-resolution TEM (**Fig. 10e**) of the as-prepared particles shows that the nanoparticles are well crystallized. Distances of the lattice spacing were measured to be 2.9 Å and 1.8 Å, which is consistent with the (111)- and the (220)-crystal planes of cubic YSZ. The elemental composition of the obtained nanoparticles was determined by EDS and an average atomic ratio of Y:Zr in the final product was 18:82, which is close to the ratio of the starting precursor solution (22:78). According to Hayashi, et al. [33], the stoichiometric doping of Y into ZrO_2 lattice requires a simultaneous complete conversion of both Zr and Y cations. The Zr^{4+} cation has a very high hydrolysis reaction rate and reaches almost complete conversion even under acidic condition. However, for a complete conversion of Y^{3+} cations high temperatures and pH values (pH > 8) are preferable. Since these conditions were realized in the current work ($T_{sc.\ water}$ = 398 °C, $T_{mixture}$ right after stage 1 = ~ 300 °C, pH~13), the complete conversion of Y^{3+} and stoichiometric YSZ nanoparticles were expected.

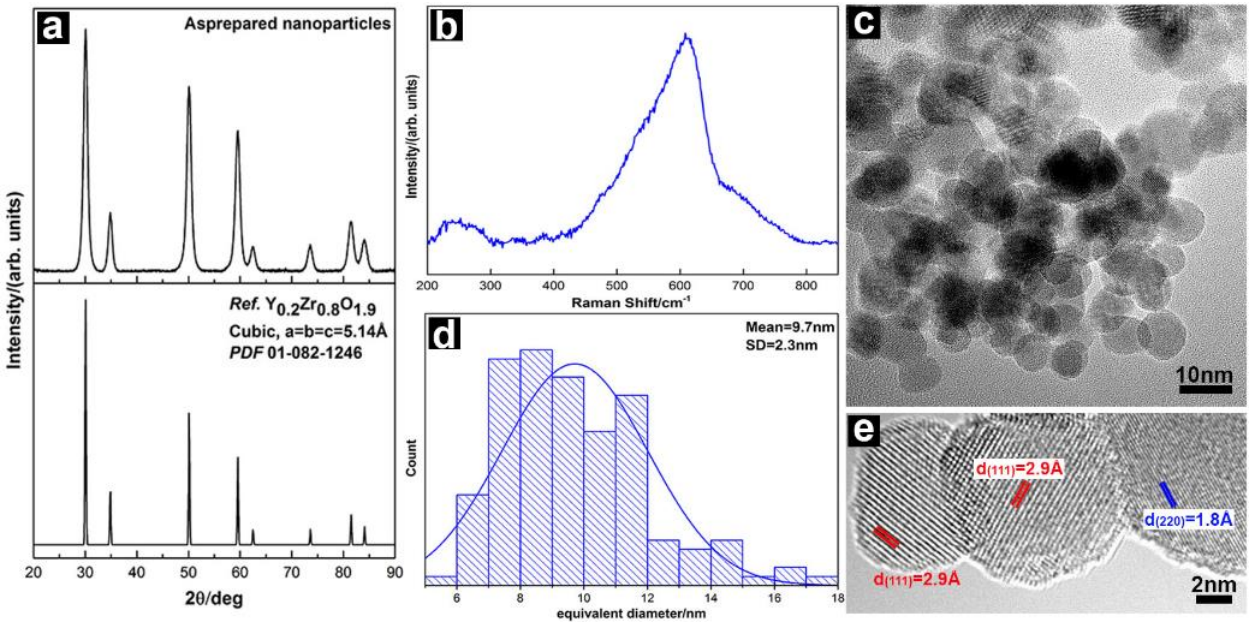

Figure 10. (**a**) Powder X-ray diffraction pattern of the as-prepared particles and comparison with the reference pattern. (**b**) Raman spectrum of the as-prepared nanoparticles. (**c**) Bright field TEM image shows the overview of the as-prepared nanoparticles. (**d**) Particle size distribution of the YSZ particle diameters measured from TEM images like the one presented in (**c**). The total number of particles in the distribution is 141. A Gaussian is fitted to the data and the mean particle size and the standard deviation (SD) is calculated based on the Gaussian fit. (**e**) High-resolution TEM image of the nanoparticles; the marked d-spacings correspond well to those of the (111)- and (220)-planes in cubic YSZ.

3.3.2 NiO

A TEM image and a XRD pattern of the as-prepared NiO particles are presented in **Fig. 11**. The mean size of the particles (bases on 51 particles) long side was 14.2 nm with a standard deviation of 4.6 nm (**Fig. 11c**); the mean short side was 7.4 nm with a standard deviation of 2.9 nm (**Fig. 11d**). The observed Moiré pattern (see for example the marked area in **Fig. 11a**) as well as the XRD diffractogram indicates that the particles were well crystallized. All XRD peaks can be attributed to cubic NiO. The crystallite size derived from the FWHM of the (111) and (220) XRD diffraction peaks was 13 nm and is therefore in good agreement with the TEM values.

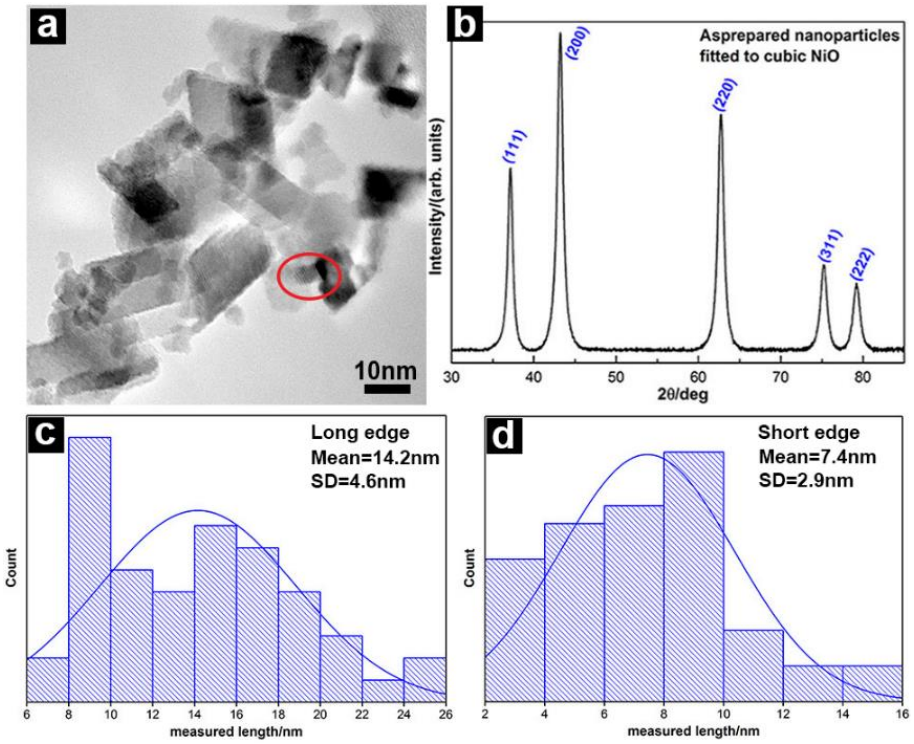

Figure 11. (**a**) Bright field TEM image shows the general overview of the as-prepared nanoparticles in which Moiré pattern can be observed (see area marked in red). (**b**) Powder X-ray diffraction pattern; all peaks can be attributed to the separate crystal planes of cubic NiO. (**c**) Size distribution of the particles' long edge measured from TEM images like the one presented in (**a**). The total number of particles in the distribution is 51. (**d**) Size distribution of the particles' short edge.

3.4 YSZ-NiO dual-phase nanoparticles

The successful application of only the first stage of the CHFS reactor in the separate synthesis of YSZ and NiO nanoparticles was extended to the two-stage synthesis of dual-phase mixtures by additionally applying the second stage into the synthesis process. Two examples (i.e. YN1 and YN2) are being presented in this work. In all cases, $Ni(NO_3)_2$ solution was pumped into the CHFS reactor at the first stage while $Y(NO_3)_3$ and $ZrO(NO_3)_2$ solutions were supplied to the second stage. For YN1 a YSZ precursor feed of 15 mL min^{-1} was used instead of the standard 10 mL min^{-1}.

Since the pure-phase particle sizes derived from the XRD diffraction peaks and for TEM images were in good agreement, the particle sizes of the mixed phases were only calculated from the diffraction peaks.

3.4.1 YN1

Fig. 12 shows the characterization of the as-prepared particles in the synthesis of YN1. Rietveld refinement of the powder X-ray diffraction pattern (**Fig. 12a**) shows that the product is composed of cubic YSZ and cubic NiO. The weight fractions of NiO and YSZ based on the refinement are 34 % and 66 %, which is close to the values assuming a complete conversion of the fed precursor solutions (37.35 mg min^{-1} ≅ 36 wt% and 66.4 mg min^{-1} ≅ 64 wt% for NiO and YSZ respectively). The mean crystallite sizes derived from the XRD diffraction peaks are 9 nm and 16 nm for YSZ (111 and 220 diffraction peak) and NiO (111 and 200 diffraction peak). **Fig. 12b** shows a TEM overview image of the as-prepared YN1 particles. Two types of nanoparticle morphologies are observed: a) a facetted morphology similar to the one observed for the pure NiO sample (**Fig. 11**) and b) a rounded morphology similar to that of the pure YSZ (**Fig. 10**). The particle size is in the order of 10 – 20 nm, which is in accordance with the XRD results. It is further observed from **Fig. 12c**, that the two types of particles are not separated, but well mixed. Measurements of lattice spacings derived from the high-resolution TEM image (**Fig. 12c**) further show that the round particles have lattice distance consistent with cubic YSZ while the faceted ones have lattice distances consistent with cubic NiO.

All this strongly indicate that the rounded particles are cubic YSZ particles and the facetted particles are cubic NiO. The morphologies and sizes of the two phases in the mixture are similar to the ones from the syntheses of single phase, and are very well mixed on a nano scale, which is hard to achieve by simply mixing the pure phases.

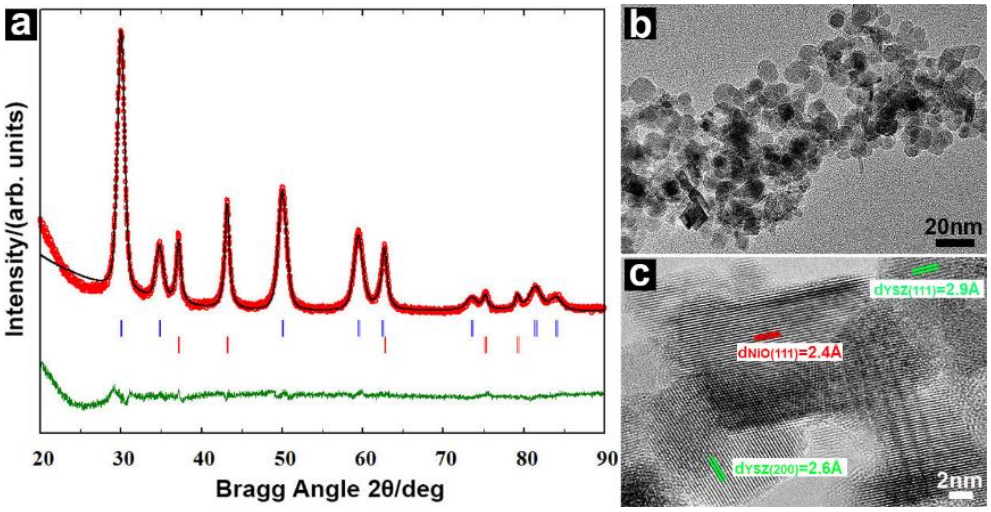

Figure 12. (**a**) Rietveld refinement of powder X-ray diffraction pattern of the as-prepared mixture (YN1) of nanoparticles. The observed pattern (red circles), the calculated pattern (black line), difference profiles between the observed and the calculated (bottom green line) and the Bragg reflection positions (blue and red vertical bars corresponding to YSZ and NiO respectively); R_p 8.13, R_{wp} 7.09, R_e 5.18 and χ^2 1.88. (**b**) Bright field TEM image of the overview of the as-prepared nanoparticles. (**c**) High resolution TEM of the as-prepared nanoparticles; the marked d-spacings correspond well to the lattice spacings in cubic YSZ (green) and NiO (red).

3.4.2 YN2

Results from TEM and XRD characterization of YN2 are shown in **Fig. 13**. Compared to YN1, where the obtained particles were homogenous in size, significant differences in the morphology and size of the obtained crystals were found. TEM characterization (**Fig. 13b**) shows that for YN2 the NiO has a faceted shape as also observed for the pure NiO sample (**Fig. 11**) and for sample YN1 (**Fig. 12**), however the crystal size is significantly larger compared to YN1. Here NiO particles in the range of for example 80 nm (long edge) × 40 nm (short edge) were found, which is about five times larger compared to YN1. Additionally, two types of nano particle accumulations can be observed around the large NiO crystals; the first one is only rounded nanoparticles with diameters around 5 nm (**Fig. 13b** area marked c, same area at higher resolution in **Fig. 13c**). Measurements for lattice distances from HRTEM images of these particles (**Fig. 13c**) show consistency with cubic YSZ. Between the rounded YSZ particles, particle with an elongated plate like morphology (ca. 10 nm × 5 nm) is observed (**Fig. 13b** area marked d, same area at higher resolution in **Fig. 13d**). Measurements of

lattice distances of these particles are consistent with NiO (**Fig. 13d**). The insertion in **Fig. 13b** is an overview image of pure NiO nanoparticles that were sampled before the precursor solution for 8YSZ was pumped into the CHFS reactor. Here only the larger NiO particles were observed. The element mapping (**Fig. 13f**) by combing EDS and DF-STEM indicates that the main phase is NiO (distribution represented by Ni) and YSZ (distribution represented by Zr) distributes around the NiO, supporting the TEM findings described above.

Rietveld refinement of the XRD powder diffractogram (**Fig. 13a**) of YN2 shows that the particles are composed of the same phases found in YN1. However, for YN2, two sets of calculated Bragg reflection positions assigned to NiO must be used to describe the peak shape properly, i.e. two different populations of crystals with different crystallite size (and slightly different unit cell parameters, 4.1967 Å and 4.1802 Å). The weight fractions of NiO and YSZ are calculated to be 84 % and 16 % respectively, which is expected due to the higher weight rate of NiO precursor compared to the YSZ precursor (37.35 mg min^{-1} ≅ 81 wt% and 8.86 mg min^{-1} ≅ 19 wt% for NiO and YSZ respectively, assuming full conversion).

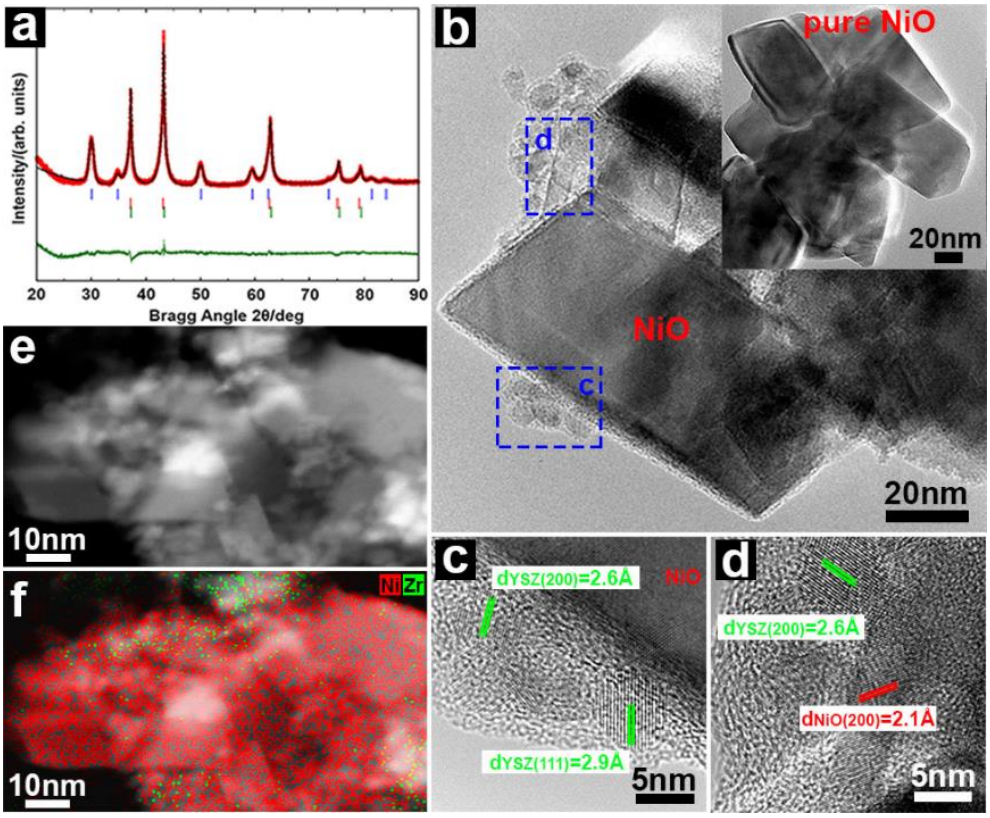

Figure 13. (**a**) Rietveld refinement of powder X-ray diffraction pattern of the as-prepared mixture (YN2) of nanoparticles. The observed pattern (red circles), the calculated pattern (black line), difference profiles between the observed and the calculated (bottom green line) and the Bragg reflection positions (blue vertical bars corresponding to YSZ; red and green vertical bars corresponding to NiO); R_p 9.17, R_{wp} 7.69, R_e 5.18 and χ^2 2.20. (**b**) Bright field TEM image shows the overview of the as-prepared nanoparticles; insertion is the overview of pure NiO nanoparticles that were sampled before the precursor solution for 8YSZ was pumped into the CHFS reactor. (**c**) and (**d**) are high resolution TEM images of the two representative nano-accumulations highlighted in (**b**). (**e**) DF-STEM image of the as-prepared nanoparticles. (**f**) STEM-EDS element mapping of the as-prepared nanoparticles, X-ray photons from Ni Kα and Zr Kα are presented.

The formation of NiO with such different crystal sizes in YN1 compared to YN2 can be explained by the variation of the synthesis conditions. During the synthesis of YN2, the $Ni(NO_3)_2$ solution was mixed with the scH_2O stream in the first stage under neutral pH conditions. It is known from literature [34] that NiO formed under such conditions tends to be larger compared to particles synthesized at high pH values. At the same time the conversion rate of the of Ni^{2+} cations under the neutral pH condition is reported to be less than 70 % [34]. In conclusion, the outflow of the first stage consists of large NiO particles and a significant amount of unconverted Ni^{2+} salt solution. In the second stage

the YSZ-precursor and KOH solution were pumped into the CHFS reactor, mixed with the outflow coming from the first stage (~300 °C), and heated up to ~390 °C by the reheaters. Under these reaction conditions (high pH and high temperature) the agglomerations of YSZ and small NiO particles (**Fig. 13c**) form, indicating that unconverted Ni^{2+} hydrolyzed and converted to NiO after mixing with the alkaline solution in the second stage. In conclusion, the relative positions and structure of the final product can be described as NiO crystals surface decorated with YSZ-NiO.

3.4.3 Dual-phase single-stage NiO-YSZ (YNS)

The TEM images (a representative shown in **Fig. 14a**) of the NiO and YSZ nanoparticles synthesized in a single stage reaction show similar sizes and morphologies to the ones from the two-stage synthesis YN1. Well-crystallized particles of similar sizes around 10 nm were obtained. From the measured crystal plane distances the particles were either identified as cubic NiO or YSZ. Refinement of the XRD pattern gives that the mixture is composed of 27.1 wt% YSZ and 72.9 wt% NiO (assuming full conversion: 57.1 mg min^{-1} ≅ 36.1 wt% YSZ and 101.2 mg min^{-1} ≅ 63.9 wt% NiO). The mean crystallite sizes derived from the XRD diffraction peaks are 9 nm and 7 nm for YSZ (111 and 220 diffraction peak) and NiO (111 and 200 diffraction peak) respectively.

Since NiO-YSZ nanocomposites are used as fuel electrode material in state-of-the-art solid oxide fuel/electrolysis cells and the CHFS synthesis route has been proven to be viable for the production of dense cermets [37], a scaled-up dual-phase single-stage production run was executed. Approx. 140g of nanoparticles were collected in 18 h, proving that the designed synthesis capacity of the CHFS reactor can be reached.

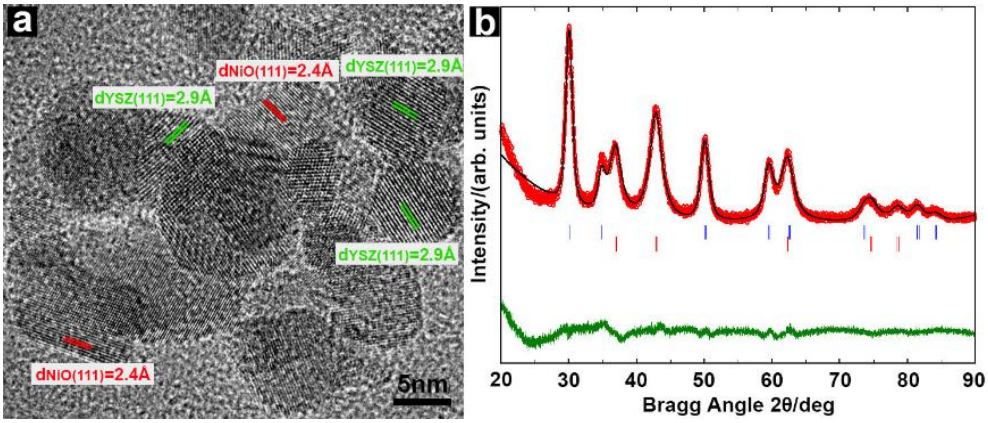

Figure 14. (**a**) High resolution TEM of the as-prepared nanoparticles; the marked d-spacings correspond well to the lattice spacings in cubic YSZ (green) and NiO (red). (**b**) Rietveld refinement of powder X-ray diffraction pattern of the as-prepared mixture (YNS) of nanoparticles. The observed pattern (red circles), the calculated pattern (black line), difference profiles between the observed and the calculated (bottom green line) and the Bragg reflection positions (blue vertical and red vertical bars corresponding to cubic YSZ and NiO respectively); R_p 9.86, R_{wp} 9.55, R_e 6.19 and χ^2 2.38.

4. Conclusion

Computational fluid dynamics simulations were employed to identify the most promising mixer geometries for a two-stage continuous hydrothermal flow reactor. Further simulations were carried out to evaluate the mixing behavior for changes in flow rates and geometry deviations. Based on the results a CHFS system was designed and built. After successful single-stage syntheses of YSZ and NiO the two-stage capabilities were tested. In first test run, the ability to tailor the morphology of composite materials was proven. Lastly a scale-up of a dual-phase single-stage synthesis was performed, providing sufficient amounts of nanoparticles for prototyping of energy conversion devices.

References

[1] Y. Lu, S. Ozcan, Green nanomaterials: On track for a sustainable future, Nano Today. 10 (2015) 417–420. doi:10.1016/j.nantod.2015.04.010.

[2] G.R. Patzke, Y. Zhou, R. Kontic, F. Conrad, Oxide nanomaterials: Synthetic developments, mechanistic studies, and technological innovations, Angew. Chemie - Int. Ed. 50 (2011) 826–859. doi:10.1002/anie.201000235.

[3] T. Adschiri, K. Kanazawa, K. Arai, Rapid and Continuous Hydrothermal Crystallization of Metal Oxide Particles in Supercritical Water, J. Am. Ceram. Soc. 75 (1992) 1019–1022. doi:10.1111/j.1151-2916.1992.tb04179.x.

[4] K. Byrappa, M. Yoshimura, Hydrothermal Technology—Principles and Applications, in: Handb. Hydrothermal Technol., 2013: pp. 1–49. doi:10.1016/B978-0-12-375090-7.00001-3.

[5] T. Adschiri, Y.-W. Lee, M. Goto, S. Takami, Green materials synthesis with supercritical water, Green Chem. 13 (2011) 1380. doi:10.1039/c1gc15158d.

[6] J.J.-D. Kim, Y.-S. Park, B. Veriansyah, Y.-W. Lee, Continuous Synthesis of Surface-Modified Metal Oxide Nanoparticles Using Supercritical Methanol for Highly Stabilized Nanofluids, Chem. Mater. 20 (2008) 6301–6303. doi:10.1021/cm8017314.

[7] P. Hald, J. Becker, M. Bremholm, J.S. Pedersen, J. Chevallier, S.B. Iversen, et al., Supercritical Propanol–Water Synthesis and Comprehensive Size Characterisation of Highly Crystalline anatase TiO2 Nanoparticles, J. Solid State Chem. 179 (2006) 2674–2680. doi:10.1016/j.jssc.2006.05.012.

[8] E. Lester, P. Blood, J. Denyer, D. Giddings, B. Azzopardi, M. Poliakoff, Reaction engineering: The supercritical water hydrothermal synthesis of nano-particles, J. Supercrit. Fluids. 37 (2006) 209–214. doi:10.1016/j.supflu.2005.08.011.

[9] X. Weng, J.K. Cockcroft, G. Hyett, M. Vickers, P. Boldrin, C.C. Tang, et al., High-throughput continuous hydrothermal synthesis of an entire nanoceramic phase diagram., J. Comb. Chem. 11 (2009) 829–34. doi:10.1021/cc900041a.

[10] E.S. Ilin, S. Marre, V. Jubera, C. Aymonier, Continuous supercritical synthesis of high quality UV-emitting ZnO nanocrystals for optochemical applications, J. Mater. Chem. C. 1 (2013) 5058. doi:10.1039/c3tc30737a.

[11] Y. Roig, S. Marre, T. Cardinal, C. Aymonier, Synthesis of Exciton Luminescent ZnO Nanocrystals Using Continuous Supercritical Microfluidics, Angew. Chemie Int. Ed. 50 (2011) 12071–12074. doi:10.1002/anie.201106201.

[12] R.I. Gruar, C.J. Tighe, J.A. Darr, Scaling-up a Confined Jet Reactor for the Continuous Hydrothermal Manufacture of Nanomaterials, Ind. Eng. Chem. Res. 52 (2013) 5270–5281. doi:10.1021/ie302567d.

[13] S. Kawasaki, K. Sue, R. Ookawara, Y. Wakashima, A. Suzuki, Development of novel micro swirl mixer

for producing fine metal oxide nanoparticles by continuous supercritical hydrothermal method., J. Oleo Sci. 59 (2010) 557–562. doi:10.5650/jos.59.557.

[14] S. Marre, A. Adamo, S. Basak, C. Aymonier, K.F. Jensen, Design and Packaging of Microreactors for High Pressure and High Temperature Applications, Ind. Eng. Chem. Res. 49 (2010) 11310–11320. doi:10.1021/ie101346u.

[15] H.L. Hellstern, J. Becker, P. Hald, M. Bremholm, A. Mamakhel, B.B. Iversen, Development of a Dual-Stage Continuous Flow Reactor for Hydrothermal Synthesis of Hybrid Nanoparticles, Ind. Eng. Chem. Res. (2015) 150818144017002. doi:10.1021/acs.iecr.5b02899.

[16] H.L. Hellstern, A. Mamakhel, M. Bremholm, B.B. Iversen, Core-shell nanoparticles by silica coating of metal oxides in a dual-stage hydrothermal flow reactor, Chem. Commun. (2016). doi:10.1039/C5CC09743F.

[17] R. Ghosh Chaudhuri, S. Paria, Core/shell nanoparticles: classes, properties, synthesis mechanisms, characterization, and applications., Chem. Rev. 112 (2012) 2373–433. doi:10.1021/cr100449n.

[18] A. Hauch, K. Brodersen, M. Chen, M.B. Mogensen, Ni/YSZ electrodes structures optimized for increased electrolysis performance and durability, Solid State Ionics. 293 (2016) 27–36. doi:10.1016/j.ssi.2016.06.003.

[19] ANSYS, (2012). www.ansys.com.

[20] C.Y. Ma, J.J. Liu, Y. Zhang, X.Z. Wang, Simulation for scale-up of a confined jet mixer for continuous hydrothermal flow synthesis of nanomaterials, J. Supercrit. Fluids. 98 (2015) 211–221. doi:10.1016/j.supflu.2014.12.016.

[21] S.-I. Kawasaki, K. Sue, R. Ookawara, Y. Wakashima, A. Suzuki, Y. Hakuta, et al., Engineering study of continuous supercritical hydrothermal method using a T-shaped mixer: Experimental synthesis of NiO nanoparticles and CFD simulation, J. Supercrit. Fluids. 54 (2010) 96–102. doi:10.1016/j.supflu.2010.03.001.

[22] A. Leybros, R. Piolet, M. Ariane, H. Muhr, F. Bernard, F. Demoisson, CFD simulation of ZnO nanoparticle precipitation in a supercritical water synthesis reactor, J. Supercrit. Fluids. 70 (2012) 17–26. doi:10.1016/j.supflu.2012.06.001.

[23] L. Zhou, S. Wang, D. Xu, Y. Guo, Impact of Mixing for the Production of CuO Nanoparticles in Supercritical Hydrothermal Synthesis, Ind. Eng. Chem. Res. 53 (2014) 481–493. doi:10.1021/ie4029413.

[24] C.Y. Ma, C.J. Tighe, R.I. Gruar, T. Mahmud, J. a. Darr, X.Z. Wang, Numerical modelling of hydrothermal fluid flow and heat transfer in a tubular heat exchanger under near critical conditions, J. Supercrit. Fluids. 57 (2011) 236–246. doi:10.1016/j.supflu.2011.03.007.

[25] W. Wagner, The IAPWS Formulation 1995 for the Thermodynamic Properties of Ordinary Water Substance for General and Scientific Use, J. Phys. Chem. Ref. Data. 31 (1999) 387.

doi:10.1063/1.1461829.

[26] E.A. Macedo, H. Liu, Accurate correlations for the self-diffusion coefficients of CO2, CH4, C2H4, H2O, and D2O over wide ranges of temperature and pressure, J. Supercrit. Fluids. 8 (1995) 310–317. doi:10.1016/0896-8446(95)90006-3.

[27] J. Sierra-Pallares, D.L. Marchisio, E. Alonso, M.T. Parra-Santos, F. Castro, M. José Cocero, Quantification of mixing efficiency in turbulent supercritical water hydrothermal reactors, Chem. Eng. Sci. 66 (2011) 1576–1589. doi:10.1016/j.ces.2010.12.039.

[28] J. Rodríguez-Carvajal, Recent advances in magnetic structure determination by neutron powder diffraction, Phys. B Condens. Matter. 192 (1993) 55–69. doi:10.1016/0921-4526(93)90108-I.

[29] E. Lester, P.J. Blood, J.P. Denyer, B.J. Azzopardi, J. Li, M. Poliakoff, Impact of reactor geometry on continuous hydrothermal synthesis mixing, Mater. Res. Innov. 14 (2010) 19–26. doi:10.1179/143307510X12599329343042.

[30] K. Sugioka, K. Ozawa, T. Tsukada, S. Takami, T. Adschiri, K. Sugimoto, et al., Neutron radiography and numerical simulation of mixing behavior in a reactor for supercritical hydrothermal synthesis, AIChE J. 60 (2014) 1168–1175. doi:10.1002/aic.14313.

[31] T. Aizawa, Y. Masuda, K. Minami, M. Kanakubo, H. Nanjo, R.L. Smith, Direct observation of channel-tee mixing of high-temperature and high-pressure water, J. Supercrit. Fluids. 43 (2007) 222–227. doi:10.1016/j.supflu.2007.03.008.

[32] C.Y. Ma, M. Chen, X.Z. Wang, Modelling and simulation of counter-current and confined jet reactors for hydrothermal synthesis of nano-materials, Chem. Eng. Sci. 109 (2014) 26–37. doi:10.1016/j.ces.2014.01.006.

[33] H. Hayashi, A. Ueda, A. Suino, K. Hiro, Y. Hakuta, Hydrothermal synthesis of yttria stabilized ZrO2 nanoparticles in subcritical and supercritical water using a flow reaction system, J. Solid State Chem. 182 (2009) 2985–2990. doi:10.1016/j.jssc.2009.08.013.

[34] K. Sue, M. Suzuki, K. Arai, T. Ohashi, H. Ura, K. Matsui, et al., Size-controlled synthesis of metal oxide nanoparticles with a flow-through supercritical water method, Green Chem. 8 (2006) 634. doi:10.1039/b518291c.

[35] X. Weng, D. Brett, V. Yufit, P. Shearing, N. Brandon, M. Reece, et al., Highly conductive low nickel content nano-composite dense cermets from nano-powders made via a continuous hydrothermal synthesis route, Solid State Ionics. 181 (2010) 827–834. doi:10.1016/j.ssi.2010.04.014.

[36] T. Hirata, E. Asari, M. Kitajima, Infrared and Raman Spectroscopic Studies of ZrO2 Polymorphs Doped with Y2O3 or CeO2, J. Solid State Chem. 110 (1994) 201–207. doi:10.1006/jssc.1994.1160.

[37] X. Weng, D. Brett, V. Yufit, P. Shearing, N. Brandon, M. Reece, et al., Highly conductive low nickel content nano-composite dense cermets from nano-powders made via a continuous hydrothermal synthesis route, Solid State Ionics. 181 (2010) 827–834. doi:10.1016/j.ssi.2010.04.014.

Chapter IV. Continuous hydrothermal flow synthesis of Gd-doped CeO_2 (GDC) nanoparticles for inkjet printing of SOFC electrolytes

This chapter contains the manuscript 'Continuous Hydrothermal Flow Synthesis of Gd-doped CeO_2 (GDC) Nanoparticles for Inkjet Printing of SOFC Electrolytes' that is ready for submission.

Gd-doped CeO_2 (GDC) was under focus because it is a good ionic conductor, and it is widely used, e.g. as electrolyte and catalyst material. CHFS was applied to synthesize Gd-doped CeO_2 nanoparticles. The effect of pH on particle size, morphology and composition of the synthesized nanoparticles was investigated. Depending on pH, nanoparticles of 6 to 40 nm size with an octahedral or polyhedral (flat surfaces or 'spherical-like') morphology could be obtained. Similar conversion rates of Ce and Gd cations could be reached only at alkaline conditions.

In addition, results of a collaborative effort between the PhD student and the second and the third author are presented. In an 'all-wet' strategy, the as-synthesized $Gd_{0.2}Ce_{0.8}O_{2-\delta}$ was processed to inks suitable for inkjet printing. The inks showed good jetting behavior. GDC films were printed with the inks on green NiO-GDC substrates and on pre-sintered NiO-YSZ substrates, separately. Particularly, dense continuous layers were observed in the sample with 10-layered films printed on pre-sintered NiO-YSZ substrates after firing at 1300 °C. The thin dense continuous layers consisted of a YSZ layer (0.8 – 1 µm) covered by a GDC layer (0.5 µm) decorated with GDC islands. Such a structure is expected to be attractive for medium/low-temperature solid oxide fuel cells. The thin dense layers fully covering the NiO-YSZ substrate could function as an electrolyte, which would reduce the Ohmic loss due to the significantly reduced thickness. Moreover, the disconnected GDC islands could provide a high number of active sites and a strong bonding to an applied cathode.

Continuous Hydrothermal Flow Synthesis of Gd-doped CeO_2 (GDC) Nanoparticles for Inkjet Printing of SOFC Electrolytes

Yu Xu [1], Nicholas M. Farandos [2], Massimo Rosa [1], Philipp Zielke [1], Vincenzo Esposito [1], Peter Vang Hendriksen [1], Søren Højgaard Jensen [1], Tao Li [2], Geoffrey H. Kelsall [2], Ragnar Kiebach [1,*]

[1] Department of Energy Conversion and Storage, Technical University of Denmark (Risø Campus), Frederiksborgvej 399, 4000 Roskilde, Denmark

[2] Department of Chemical Engineering, Imperial College London, London SW7 2AZ, UK

* Correspondence: R. Kiebach, Email address: woki@dtu.dk, Tel.: + 45 46775624

Abstract

$Gd_xCe_{1-x}O_{2-\delta}$ (GDC) nanoparticles were synthesized using continuous hydrothermal flow synthesis. By varying the synthesis conditions, particle size and morphology could be tailored. Here, particle sizes between 6 to 40 nm with polyhedral or octahedral shape could be obtained. $Gd_{0.2}Ce_{0.8}O_{2-\delta}$ nanoparticles were further processed into inks for inkjet printing. Despite the small particle size/large surface area, inks with excellent printing behavior were formulated. For proof-of-concept, thin GDC layers were printed on a) green NiO-GDC substrates, and on b) pre-sintered NiO-YSZ substrates. While no dense layers could be obtained on the green NiO-GDC substrates, GDC nanoparticles printed on NiO-YSZ substrates formed a dense continuous layer after firing at 1300 °C.

Keywords: continuous flow synthesis; hydrothermal; supercritical water; gadolinium doped ceria; inkjet printing; SOFC; electrolyte; solid oxide fuel cell

1. Introduction

Ceria-based oxides are attractive for several technological applications. For instance, they are applied as electrolytes in solid oxide fuel cells (SOFCs) [1,2] and as ionic conductors in dual-phase

oxygen transport membranes (OTMs) [3,4]. CeO_2 also can be employed as catalyst or catalyst support for noble metals or oxides applied for catalytic gas oxidation reactions [5–7].

Among the possible synthesis routes, the solvothermal/hydrothermal synthesis of CeO_2-based oxides is often used when aiming for nanosized materials [8]. Usually taking place in an aqueous system, hydrothermal synthesis of CeO_2-based oxide nanomaterials proceeds by hydration of metal salts followed by dehydration, crystallization and growth of oxides from a supersaturated solution at an increased temperature and pressure. The size and morphology of CeO_2 nanoparticles can be tailored by adjusting process parameters such as pH value, reaction time, counter anions and addition of surfactants [9–12].

In recent years, remarkable progress has been made in pushing forward the hydrothermal production of nanomaterials to a large industrial scale. This is mainly achieved by applying continuous hydrothermal flow synthesis (CHFS). In CHFS, a flow-type apparatus (CHFS reactor), instead of a fixed-volume batch autoclave found in the conventional hydrothermal synthesis, is used [13,14]. One of the essential parts of a CHFS reactor is a mixer, where a precursor flow constantly fed at ambient temperature is mixed with a supercritical water flow (scH_2O, $T \geq 374$ °C, $p \geq 22.1$ MPa). As a result, the precursor is rapidly heated up by the scH_2O to a (near-) supercritical state, and a solution with a high degree of supersaturation is generated in a short time. As the driving force (*i.e.* the degree of supersaturation) is high, nuclei are formed almost instantly upon mixing. Therefore, the scH_2O provides an ideal environment for hydrothermal synthesis especially of nanomaterials that can be conducted in a continuous flow way [15]. Various types of nanomaterials prepared by CHFS including oxides [16,17], sulfides [18], metals [19] and metal organic frameworks [20] have been reported. Moreover, the scalability of the CHFS to an industrial-level production has been tested in a pilot plant [21], a commercial plant (Hanwha Chemical Corp., Republic of Korea) [22], and in the European FP7 project SHYMAN (www.shyman.eu). The syntheses of CeO_2 nanoparticles, non-doped [23,24] and doped with La, Pr [24], Bi [25] or Zn [26] by CHFS have been reported in literatures. Especially the preparation of $Zr_xCe_{1-x}O_2$ nanoparticles by CHFS with a controlled composition

attracted attention since this material has a high oxygen storage capacity and is used in three-way catalysts for vehicle exhaust treatment [27–29].

Another advantage of CHFS is that the nanoparticles are prepared in an ‘all-wet’ flow process in water, and organic modifiers can be introduced *in situ* shortly after the formation of nanoparticles, which facilitates tuning the colloidal stability of nanoparticle suspensions [30]. The possibility of producing large amounts of nanoparticle suspensions in a sustainable, reproducible manner opens up the opportunity to use these nanoparticle suspensions as feedstock/basis for inks suitable for inkjet printing [31]. This additive manufacturing technique offers the potential to fabricate the functional layers of SOFCs with high reproducibility and high level of customization. Here, the fabrication of thin electrolytes [31], which would increase the cell performance, and of structured electrodes are of particular interest. Inkjet printing is particularly suited to fabricate thin films from colloidal particle dispersions, preferably aqueous dispersions, which are environmentally friendly and suitable for a large-scale industrial deployment.

Here, the one-step continuous production of $Gd_xCe_{1-x}O_{2-\delta}$ nanoparticles is reported. The influence of pH on the morphology, composition and size of the nanoparticles was investigated. Moreover, the combination of CHFS and inkjet printing, two highly scalable techniques, was demonstrated. A scaled-up CHFS of $Gd_{0.2}Ce_{0.8}O_{2-\delta}$ nanoparticles was conducted with increased precursor concentrations to obtain nanoparticles in amounts suitable for inkjet printing. From the as-prepared wet $Gd_{0.2}Ce_{0.8}O_{2-\delta}$ nanoparticles, inks were formulated and used to fabricate printed SOFC electrolytes. Importantly, firing of dense GDC electrolytes typically requires sintering temperatures above approximately 1450 °C [32,33]. As will be shown, by utilizing GDC nanoparticles, it was possible to obtain a dense GDC layer on top of a NiO-YSZ substrate when firing at 1300 °C, i.e. at a firing temperature much more applicable to conventional SOFC manufacturing. A reduction of GDC firing temperature can also be obtained by addition of sintering additives whereas this may be associated with a loss in grain boundary/bulk conductivity [32,34]. Interestingly the formed GDC layer entailed anchoring points for subsequent air electrode deposition (not presented in this paper). This

could improve the adhesion and in turn the strength of the air electrode / electrolyte interface, which is known to be a weak interface of conventional SOFCs [35].

2. Experimental

2.1 Preparation of $Gd_xCe_{1-x}O_{2-\delta}$ by CHFS

$Ce(NO_3)_3 \cdot 6H_2O$ (99 %, Sigma Aldrich) and $Gd(NO_3)_3 \cdot 6H_2O$ (99.9 %, Sigma Aldrich) were dissolved in deionized H_2O (DI H_2O) with concentrations of 0.04 mol L^{-1} for Ce(III) and 0.01 mol L^{-1} for Gd(III). For the up-scaled synthesis, a solution of 0.08 mol L^{-1} Ce(III) and 0.02 mol L^{-1} Gd(III) was used. KOH pellets (≥ 85 %, Sigma Aldrich) were dissolved in DI H_2O to make solutions with varying concentrations of 0.1, 0.15, 0.185, 0.3, 1.0 mol L^{-1}.

An in-house developed two-stage continuous flow-type apparatus (CHFS reactor) was used to conduct the synthesis, details of which were reported previously [36]. Briefly, two mixers (stages) are integrated in series within the reactor. The first mixer with a co-flow pipe-in-pipe geometry was used to mix the scH_2O flow fed by a 1/16″ capillary pipe with the precursor flow fed from two side arms of a 1/4″ encapsulating pipe. The precursor flow was a room-temperature pre-mixture of the Ce, Gd nitrates solution (reactant solution) and the KOH solution. Each solution was fed separately to the reactor, and they were mixed at a T-junction upstream of the first mixer. The outflow of the first mixer was fed subsequently to the second mixer with a counter-current geometry, and was mixed with an upward inlet flow of DI H_2O at room temperature aiming to mitigate sedimentation. The second mixer can for the synthesis of binary systems be used to feed the precursor of a second material [36]. The outflow of the second mixer passed subsequently through a re-heater. In this work, however, the re-heater was not used. The outflow of the re-heater was rapidly cooled down to the room temperature by a water-cooled tube-in-tube heat exchanger. After passing an in-line filter (Swagelok, 90-µm pore size), the product flow was depressurized to atmospheric pressure by a backpressure regulator (Tescom, 26-1700 Series). Three thermocouples were inserted into the reactor, one to measure the temperature (T_1) of the feeding scH_2O flow, one to measure the

temperature (T_2) of the outflow of the second mixer and the other to measure the temperature (T_3) of the outflow after the re-heater. During synthesis, T_1, T_2, and T_3 were maintained at 396 °C, 290 °C and 285 °C, respectively. The estimated residence time (*t)* [37] was ~29 s (see details on the calculation in Supplementary information). The synthesized particles were collected as colloidal slurries at the reactor outlet. A schematic description of the two-stage CHFS reactor is presented in **Fig. 1**. Synthesis conditions are summarized in **Table 1**. The particles were separated from slurries by centrifugation, and then washed by DI H_2O and dried for subsequent characterization.

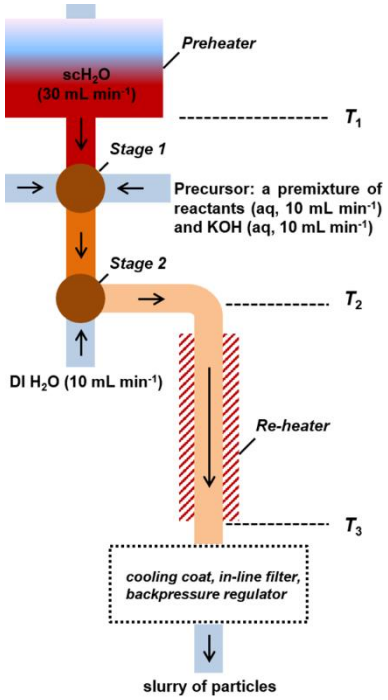

Figure 1. A schematic representation of the two-stage CHFS reactor. Pressure was controlled at 26 MPa. The re-heater was inactive in this study. The flow rate of each DI H_2O/solutions stream is given in parentheses; arrows indicate the flow direction.

Identical conditions as the previous syntheses were applied, except 0.08 mol L^{-1} Ce(III), 0.02 mol L^{-1} Gd(III) nitrates and 1.0 mol L^{-1} KOH solutions were used during the up-scaled CHFS of $Gd_{0.2}Ce_{0.8}O_{2-\delta}$ (CG-s in **Table 1**), to get sufficient amounts of particles for inkjet printing. The conditions were chosen to make sure that $Gd_{0.2}Ce_{0.8}O_{2-\delta}$ nanoparticles with the desired composition

were obtained. The particles were separated from the slurry by centrifugation and washed with DI H_2O.

2.2 Preparation of the primary $Gd_{0.2}Ce_{0.8}O_{2-\delta}$ dispersion; ink formulation, printing and sintering

Primary dispersion

Dispex A40 (Ciba-BASF, UK) was used as dispersant. To prepare the primary dispersion, the wet $Gd_{0.2}Ce_{0.8}O_{2-\delta}$ particles (CG-s in **Table 1**) were re-dispersed in 50 mL DI H_2O and ~0.6 mL Dispex A40 (twelve drops by a 10-mL disposable plastic Pasteur pipette) using an ultrasonic processor (Hielscher UP200St, Germany). The mass fraction of $Gd_{0.2}Ce_{0.8}O_{2-\delta}$ was determined by thermogravimetric analysis (TGA, TG 209 F1 Libra, Netzsch, Germany). The viscosity was measured with a rheometer (MCR 302, Anton Paar). The rheological measurements were carried out in rotational mode with a plate-plate configuration up to a shear rate of 1000 s^{-1}. The primary dispersion was separated to two identical batches.

Printing on green NiO-GDC substrates

To one batch, polyethylene glycol with a molecular weight 35,000 (PEG 35000) (Sigma Aldrich) was added at a concentration of 10 mg cm^{-3} to raise the viscosity, and Natsurf 265 added at a concentration of 0.2 mg cm^{-3} to reduce the surface tension to the recommended range for the DMC 10 pL printhead (Fujifilm, USA, [38]) that was used in this study. The surface tension was measured using a tensiometer (Model 250-U1, Ramé-hart, USA), and the viscosity was measured using a concentric cylinder viscometer (DV-E Viscometer, Brookhaven, USA). Prior to printing, the ink was first sonicated for 5 min (Q55, QSonica, USA), and then filtered to remove large aggregates (800 nm syringe filter, Cole Parmer, UK).

Three sets of films with 1, 5, 10, and 20 layers were printed onto a green NiO-GDC substrate to make squares of 7 mm side length with 4 min intervals between each deposition to allow drying. A Ceradrop X-Serie piezoelectric inkjet printer (Ceradrop, France) was used. The voltage profile

(amplitude x, time coordinate y) applied to the piezoelectric printheads was (10 V, 0 µs), (0 V, 5 µs), (0 V, 10 µs), (50 V, 15 µs), (50 V, 20 µs), (10 V, 25 µs). With a printhead speed of 100 mm s^{-1} across the substrate, the resulting jetting frequency was 3.48 kHz. This resulted in consistent, spherical, droplet ejection, verified with the in-built camera. The 'splat' diameter was measured using the in-built optical microscope in the printer as 80 µm. The diameter overlap for the printed films was 50 µm with a square droplet deposition lattice (*i.e.* 62.5 %).

The substrate was prepared by mixing the GDC and NiO powders (GDC and NiO powders supplied by Fuel Cell Materials, USA, and Inframat Advanced materials, USA, respectively) with dimethyl sulfoxide (VWR, USA) and polyethersulfone (Ameco Performance, USA) and milled for 48 h (JARMILL, Gladstone Engineering Ltd, UK). Polyethylene glycol 30-dipolyhydroxystearate (Arlacel P135, Uniqema) was added and milling continued for a further 48 h. The final composition contained the above species in the weight ratio 60 : 90 : 100 : 20 : 2, respectively. The suspension was degassed under vacuum, cast (height 0.5 mm) onto a plate, and finally submerged in an external coagulant bath to complete the phase inversion process. The substrate was dried and flattened for 24 h before printing. After printing, samples were sintered with the following profiles: 0 – 650 °C at 4 °C min^{-1}; dwell at 650 °C for 4 h (to pyrolyze organics); 650 – 1300 °C at 15 °C min^{-1}; dwell for 8 h; cool to room temperature at 4 °C min^{-1}.

Printing on pre-sintered NiO-YSZ substrates

To the other batch, Natsurf 265 was added under magnetic stirring at a concentration of 6 mg cm^{-3} to reduce surface tension to the recommended range for the DMC 10 pL printhead (Fujifilm, USA, [38]). The surface tension of the ink was assessed using a bubble pressure tensiometer (BP 50, Kruss) and the viscosity was measured with a rheometer (MCR 302, Anton Paar). The rheological measurements were carried out in rotational mode with a plate-plate configuration up to a shear rate of 1000 s^{-1}.

A Pixdro LP50 printer equipped with a DMC 10-pL printhead (Fujifilm, USA, [38]) was used for depositing the ink. Before printing, the ink was filtered using a syringe filter with a 700 nm mesh. Each sample consisted of 10 layers printed only after complete drying of the material previously printed. The substrate coverage and the optimal splat overlap was achieved by printing with a resolution of 700 DPI (dots per inch). The jetting pulse was optimized in order to jet single spherical droplets and the resulting voltage profile was (0 V, 0 µs), (50 V, 6 µs), (50 V, 16 µs). A jetting frequency of 1 kHz was used.

The substrate [39] was a pre-sintered NiO-YSZ cermet anode on a NiO-YSZ support. The green NiO-YSZ anode was prepared by tape casting (after reduction of NiO, Ni / YSZ ratio of 40 / 60 vol / vol, 8 mol% Y_2O_3 stabilized ZrO_2). Two layers were co-laminated in the green state at ca. 150 °C, i.e. a 10 – 15 µm thick NiO-YSZ anode on top of a 300 µm thick NiO-YSZ support. The firing of the substrate consisted of a multistep debinding procedure up to 700 °C for 48 h in total. The final sintering temperature, 1300 °C, was kept for 6 h.

The printed samples were sintered in air with the following profile: 0 – 600 °C at 0.25 °C min^{-1}; dwell for 4 h; 600 – T_{max} °C at 1 °C min^{-1}; dwell for 6 h; cool to room temperature at 1.67 °C min^{-1}. Here, three different temperatures T_{max} were used, 800, 1000 and 1300 °C.

2.3 Characterization

2.3.1 Particle characterization

The pH values of the supernatants of the slurries in **Table 1** were measured by a 781 pH/Ion Meter (Metrohm AG, Switzerland) and pH indicator strips (Sigma Aldrich) after the particles were separated. X-ray diffraction (XRD) analysis was conducted on the dried particles by a Bruker Robot D8 diffractometer (Cu Kα radiation, 0.154 nm; 2θ 10 – 120° with a step size of 0.01°). Using the Diffrac Eva Suite (Bruker, Germany), the volume-weighted crystallite size was estimated from the full width at half maximum (FWHM) of the diffraction peaks in the XRD patterns. For TEM characterization, the particles were re-dispersed in ethanol by means of ultrasonic treatment and dropped onto a holey

carbon film/Cu grid. Bright field TEM (BF-TEM) and high-resolution TEM (HR-TEM) images were recorded with a JEOL 3000F microscope operating at 300 kV with a field emission gun. The images were analyzed by the Gatan DigitalMicrograph software (Gatan Inc., USA) and live fast Fourier transform (FFT) of high-resolution images was performed. To quantify the size of particles, the ImageJ software was used to outline the perimeter of the particles' projections in BF-TEM images, and by assuming a spherical shape, the particle diameters were calculated. To analyze the chemical composition of the particles, they were loaded on carbon tapes and a Hitachi Tabletop TM3000 ('Analysis', 15 kV charge-reduction mode) equipped with a silicon drift detector (SDD, energy resolution 0.154 keV) was used to do a standardless quantification EDS analysis.

The particle surface area (CG-s, particles for making inks) was measured by N_2 adsorption employing the Brauner-Emmett-Teller (BET) theory using a Micrometrics 3Flex BET instrument (Canada) after drying the primary dispersion and degassing at 200 °C.

2.3.2 SEM and EDS investigations of the printed samples

The green printed samples on green NiO-GDC substrates were imaged optically (VHX-900 Digital Microscope, Keyence, UK). Sintered samples were broken, and the fracture surfaces were investigated by using a SEM (TM3030 Tabletop Microscope, Hitachi, Japan) with a 15 kV beam.

The printed samples on pre-sintered NiO-YSZ substrates after firing at 800, 1000 and 1300 °C were cut, embedded in epoxy and polished for SEM investigations of cross sections. Polished surfaces of all samples were coated with 10-nm carbon to increase the surface conductivity. The samples sintered at 800 and 1000 °C were investigated by a Hitachi Tabletop TM3000 SEM (15 kV charge-reduction mode) using the equipped high-sensitivity semiconductor detector.

The sample sintered at 1300 °C was investigated by a Zeiss Merlin SEM with a field emission gun operating at 10 kV. A high-efficiency secondary electron (SE2) detector and an energy selective backscattered detector (BSE) were used simultaneously to record images at each selected area. Besides the polished cross section, the surface of the printed GDC layer (top view) was also

investigated. EDS analysis was conducted on the polished cross section by the equipped Bruker XFlash 6 EDS detector with a standard energy resolution 0.129 keV. An accelerating voltage of 10 kV was used giving a theoretical lateral resolution around 0.5 µm, and a working distance 8 mm was used. The Esprit 1.9 software was used to record and process the spectra by the 'Hyper Map' method. The total spectrum was background subtracted and deconvoluted.

Table 1. CHFS of Gd-doped CeO_2 nanoparticles. Process parameters and microstructural characteristics of the synthesized particles.

Sample	Me^{3+}/mol L^{-1}	KOH/mol L^{-1}	[a] pH of slurry	Crystallite size/nm			[b] Particle size/nm	Morphology
				(111)	(200)	(220)		
CG1	0.05	0	1.9	28.9	30.3	26.1	45(4)[c], 39(8)[d]	octahedral
CG2	0.05	0.1	3.5	8.9	9.5	8.8	8(1)	polyhedral, spherical
CG3	0.05	0.15	5.5	6.0	6.8	5.6	6(1)	polyhedral, spherical
CG4	0.05	0.185	9	7.2	7.5	7.0	7(1)	polyhedral, spherical
CG5	0.05	0.3	11.9	8.2	8.4	8.0	8(2)	spherical, polyhedral
CG6	0.05	1.0	13.1	9.2	9.9	9.0	8(2)	spherical
CG-s	0.1	1.0	12.8	11.9	11.9	11.5	11(2)	spherical

Notes: Me^{3+} are Ce (III) and Gd(III) cations in the reactant solution; a is the pH of the slurry of nanoparticles; b is an average value of sizes of 80 - 100 nanoparticles measured in BF-TEM images; c is the average edge size measured with square projections; d is the average edge size measured with rhombic projections. The numbers in the parentheses represent the associated standard deviations.

3. Results and Discussion

3.1 Continuous hydrothermal flow synthesis (CHFS) of Gd-doped CeO_2 nanoparticles

Fig.2 presents XRD patterns of the synthesized particles. All diffraction peaks of particles synthesized at conditions with various pH values matched to those of CeO_2 (cubic, Fm-3m, ICSD

PDF 01-081-0792). This indicates the presence of cubic CeO_2 phase in all particles, although the shift in 2θ positions of experimental patterns compared with the standard shows the difference in cell parameters arising from Gd^{3+} dopants. The peak broadening suggests that nanoparticles were obtained. The crystallite size was estimated from the FWHM of peaks, and the sizes estimated from the first three peaks corresponding to (111), (200) and (220) planes of a CeO_2 crystal are summarized in **Table 1** (more details in Supporting information). Depending on the experimental conditions, crystallite sizes between 6 – 30 nm can be obtained. The crystallite size first decreased with increasing pH values (pH 1.9 – 5.5) and then increased when more alkali was added (pH 9 – 13.1).

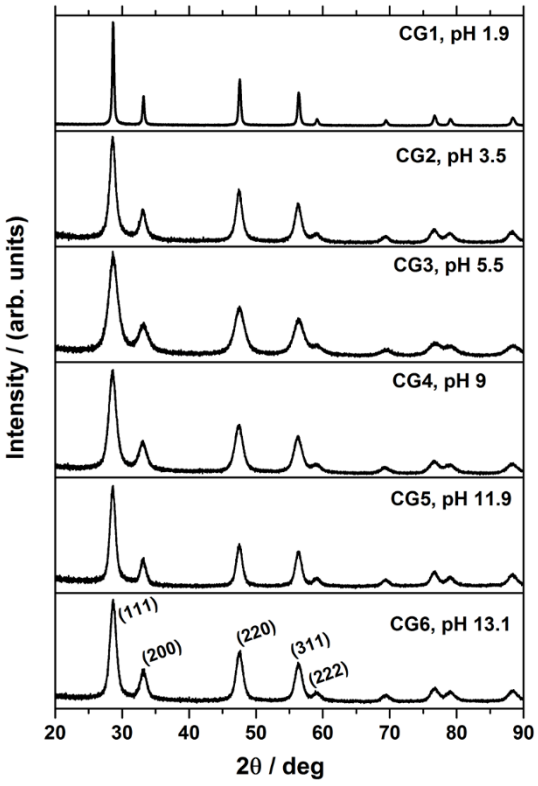

Figure 2. XRD patterns of $Gd_xCe_{1-x}O_{2-\delta}$ particles prepared by CHFS.

The addition of alkali solution (KOH in this study) significantly affected the morphology and size of particles crystallized from the solution in a CHFS process. When the synthesis was conducted in absence of KOH, well-crystallized particles with a fully developed octahedral shape displaying flat surfaces and sharp corners were obtained (**Fig. 3**). Depending on the view direction in the TEM,

projections with different geometries were observed, e.g., square projections viewed in [001] direction (**Fig. 3a**), and rhombohedral projections in [110] direction (**Fig. 3b** and **3c**). FFT (insets in **Fig. 3b and 3c**) conversions show that these octahedra were enclosed by {111} facets (flat surfaces) whereas {002} facets disappeared (sharp corners). As summarized in **Table 1**, the edge length size of these single-crystalline octahedra was 39 – 45 nm measured in TEM. However, crystallite size estimated from XRD was relatively smaller and varied among peaks (**Table 1** and **S1**), indicating a pronounced anisotropic growth of crystallites.

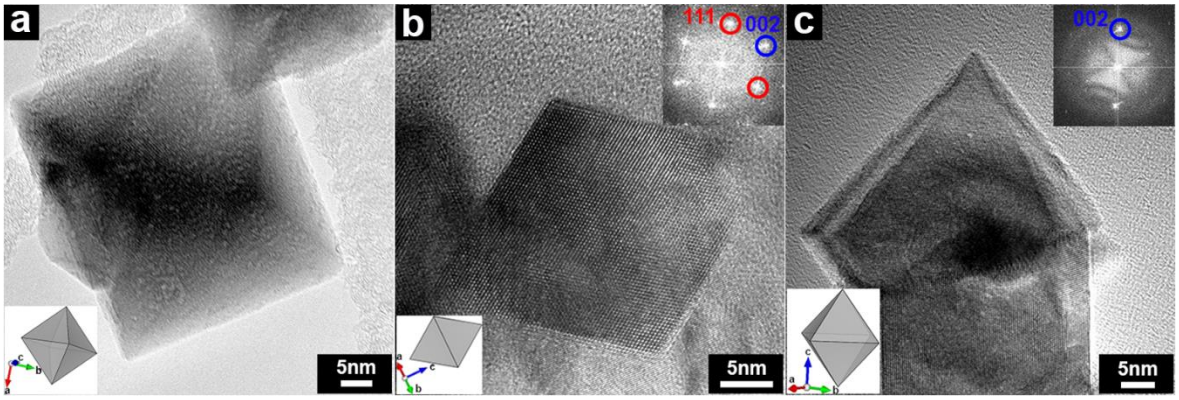

Figure 3. BF-TEM images of CG1 nanoparticles displaying an octahedron morphology with flat surfaces and sharp corners. (**a**) Particle viewed in [001] direction; both (**b**) and (**c**) are particles viewed in [110] direction but oriented in *c*-axis; the insets are live FFT conversions, showing families of {111} and {002} planes.

In comparison, when KOH was introduced to the syntheses (CG2, 3, 4, 5, 6 and CG-s in **Table 1**), the obtained particles were very different with respect to the size and morphology, as presented in **Fig. 4**. KOH was added in order to tune the pH values during the syntheses, which were measured from the final slurries of particles. Firstly, the particle size markedly decreased when alkali was involved in the syntheses for all samples (compared with that of CG1). Moreover, in acidic conditions, the particle size decreased from 8(1) nm (**Fig. 4a**) to 6(1) nm (**Fig. 4b**) as the amount of KOH was increased (pH changed from 3.5 to 5.5). In base conditions, however, the particle size slightly increased from 7(1) nm (**Fig. 4c**) to 8(2) nm (**Fig. 4e**) as the amount of KOH was increased (pH changed from 9 to 11.9). For all samples synthesized with KOH, the crystallite sizes estimated from

different peaks in XRD patterns were relatively close to each other (**Table 1** and **S1**). The particle size statistically quantified with TEM images was also close to the crystallite size for these samples.

In terms of the morphology, all these particles displayed polyhedral shapes (**Fig. 4**), while some of them had relatively flat surfaces (red outlines), others were more spherical-like (blue outlines). As shown in insets, particles displaying flat surfaces were enclosed by {111} and {002} planes, which in some other publications [40,41] have been referred as 'truncated octahedra'. With adding more KOH during syntheses, the amount of particles with flat surfaces decreased while increasing amounts of spherical-like particles were obtained. For instance, a particle (CG6, pH = 13.1) enclosed by {111} and {002} planes (inset in **Fig. 4e**) appeared more spherical-like.

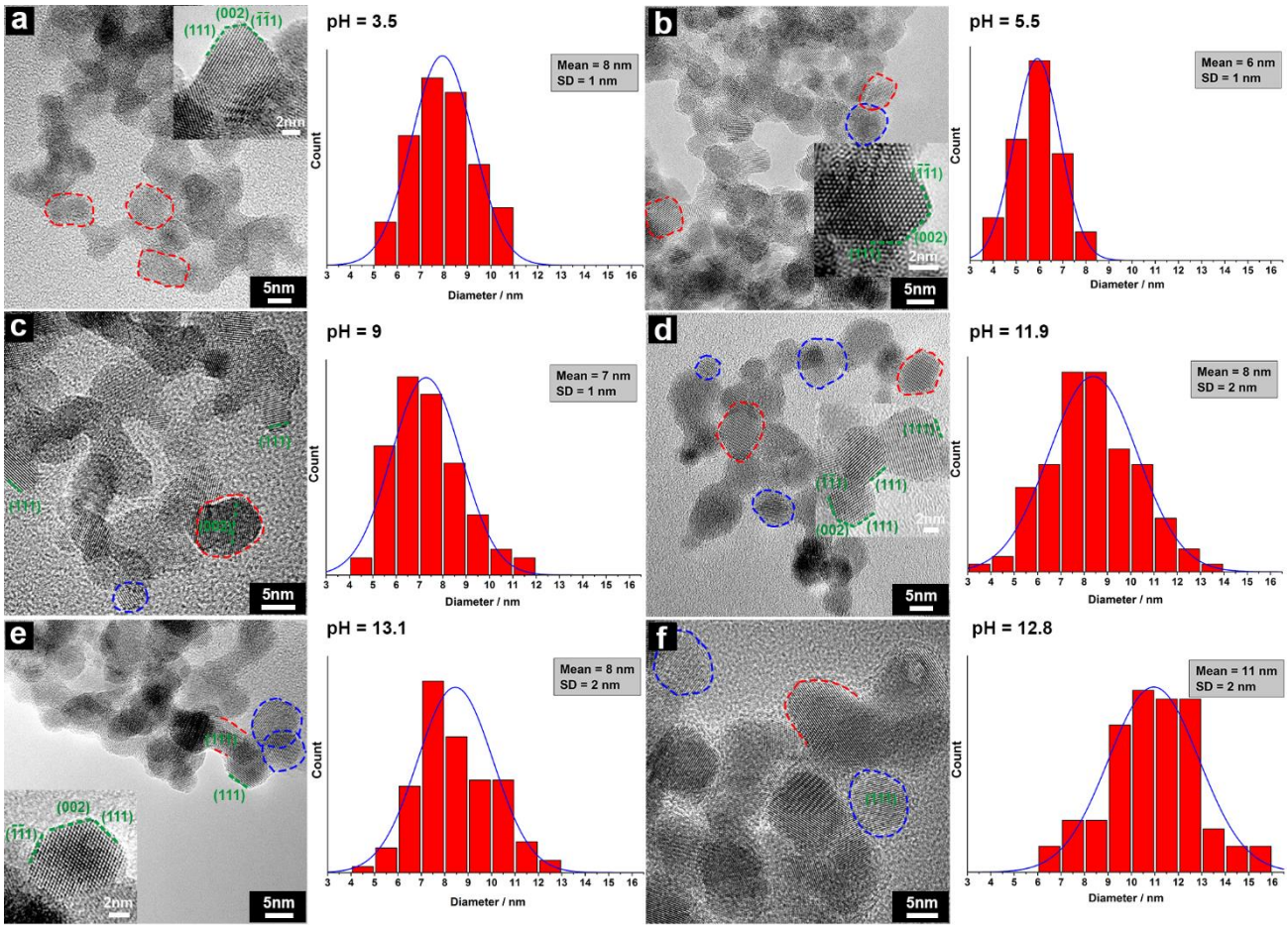

Figure 4. BF-TEM images of GDC nanoparticles and particle size distribution. (**a**) CG2, pH = 3.5; the inset shows a HR-TEM image of a GDC nanoparticle with the truncated octahedron morphology. (**b**) CG3, pH = 5.5; the inset shows a HR-TEM image of a GDC nanoparticle with the truncated octahedron morphology. (**c**) CG4, pH = 9. (**d**) CG5, pH = 11.9; the

inset shows a HR-TEM image of GDC nanoparticles with relatively spherical morphology and with truncated octahedron morphology. (**e**) CG6, pH = 13.1; the inset shows a HR-TEM image of a GDC nanoparticle enclosed by (002) and (111) planes however is spherical-like. (**f**) CG-s, pH = 12.8. The red dashed curves and the blue dashed curves outline the particles with flat surfaces and relatively spherical particles separately.

In absence of surfactants or templates, the morphology of particles mostly depends on crystallographic structures that in turn affect the growth behavior. CeO_2-based oxide has a face-centered cubic (FCC) structure, and the surface energy of low-index planes follows $\gamma_{\{111\}} < \gamma_{\{200\}} < \gamma_{\{110\}}$ [9,40]. Therefore, the growth rate of {111} planes is the lowest and CeO_2 octahedra terminated by {111} planes have the lowest surface energy, i.e. the highest stability. In a typical hydrothermal process, the formation of particles follows a dissolution-nucleation-growth mechanism. CeO_2 particles crystallized from the solution tend to be in an octahedral shape with a minimized surface energy. This was observed in all samples, displaying as fully developed octahedra with flat surfaces and sharp corners (**Fig. 3**) or as polyhedra ('truncated octahedra') either with flat surfaces or with 'spherical-like' appearances (**Fig. 4**). Wang et al. [40] found a 'size effect' that the polyhedra dominated in particles with a size 3 – 10 nm as {002} planes had not disappeared completely. Here the observations are similar, as polyhedra were dominant for particles between 6 – 8 nm (**Fig. 4a – 4e**) while fully developed octahedra dominated in large particles (**Fig. 3**).

The resulting particle size reflects the combined effect of the nucleation and the growth processes. The hydrothermal synthesis of CeO_2 from Ce^{3+} starts from the hydration between Ce^{3+} and OH^- groups either from alkaline addition or self-ionization of water, followed by formation of $Ce(OH)_3$ nuclei, oxidation and growth of CeO_2 crystals [42]. One can expect a high concentration of Ce^{3+} and a high solubility of newly formed $Ce(OH)_3$ intermediates (by reaction between Ce^{3+} and OH^- from water) in the very acidic solution during the synthesis of CG1 where no KOH was added (**Table 1**). Therefore, the amount of nuclei was relatively low whereas a comparatively rapid growth of nuclei was facilitated by the fast mass diffusion in the solution, favoring large crystals [9]. In comparison, during syntheses of CG2 to CG6 (**Table 1**), KOH was introduced and more $Ce(OH)_3$ intermediates were formed in the precursor flow before heating by scH_2O. The solubility of $Ce(OH)_3$ was much

lower in the solution particularly in more alkaline conditions (with more KOH, CG4 to CG6). Compared with the synthesis of CG1, a higher degree of supersaturation was achieved, and as a result the driving force for nucleation was larger, facilitating the formation of more numerous and smaller crystals [9].

The effect of pH on the composition of the synthesized Gd-doped CeO_2 particles is shown in **Fig. 5**. The molar ratio of Ce to Gd was carefully controlled at 80:20 in the reactant solutions, however the ratio of Ce to Gd in particles deviated as Gd deficiency was detected in particles synthesized at acidic conditions (CG1, CG2 and CG3). This suggests that in order to get a stoichiometry composition in Gd-doped CeO_2 particles the pH should be controlled, preferably in the alkaline range. A similar result was observed in CHFS of Y-doped ZrO_2 nanoparticles where the pH value had to be > 8 to achieve a comparable conversion rate of Y and Zr [43].

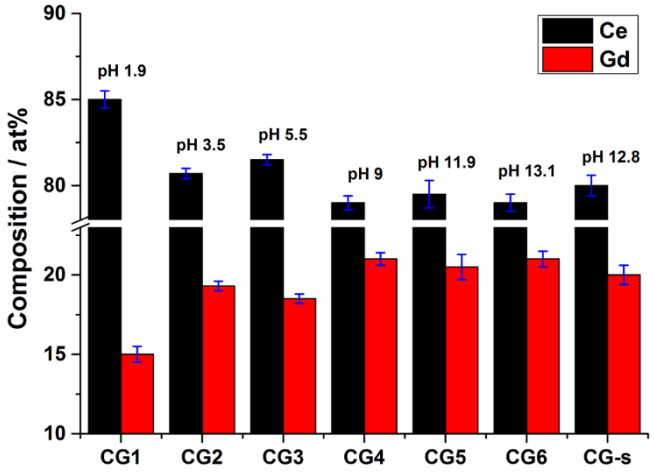

Figure 5. Chemical compositions in atomic percent (at %) of $Gd_xCe_{1-x}O_{2-\delta}$ nanoparticles. Syntheses of all samples started from nitrate precursors composed of 80 % Ce and 20 % Gd in molar percent.

3.2 Properties of the formulated $Gd_{0.2}Ce_{0.8}O_{2-\delta}$ inks

An upscaled synthesis of GDC nanoparticles (CG-s) was conducted to get sufficient amounts of particles for making inks. The BET specific surface area of the particles was measured to be 91.1 $m^2\ g^{-1}$. The particles had a relatively spherical morphology with a narrow size distribution 11 ± 2 nm (**Fig. 4f**). Similar conversion rates of Ce and Gd were achieved, as the elemental composition of the

synthesized particles ($Gd_{0.2}Ce_{0.8}O_{2-\delta}$, **Fig. 5**, CG-s) was the same as the composition (Gd : Ce molar ratio 20 : 80) of the precursor.

The mass fraction of $Gd_{0.2}Ce_{0.8}O_{2-\delta}$ in the primary dispersion was determined by thermogravimetric analysis (TGA) to be 7.2 wt%. The viscosity of the primary dispersion is shown in **Fig. S1**.

Of the ink formulated for printing on green NiO-GDC substrates, the surface tension, viscosity and density were measured to be 27 mN m^{-1}, 2.1 mPa s, and 1.08 g cm^{-3}, respectively (**Fig. S2**). Therefore the calculated Oh^{-1} Number was 12.0, indicating printability [44].

The formulated ink for printing on pre-sintered NiO-YSZ substrates was characterized by measuring surface tension and viscosity and values of 25 mN m^{-1} and 1.0 mPa s (**Fig. S3**) were obtained, respectively. The calculated Oh^{-1} Number was 23.8, which should lead to the formation of satellite droplets according to Jang [44] and Derby [45]. Nonetheless, we observed the generation of stable single droplets during our experiments with a volume between 7 and 8 pL (**Fig. 6**). Thus, probably the presence of nanoparticles influences the jetting behavior of the fluid extending the range of properties at which the ink results printable.

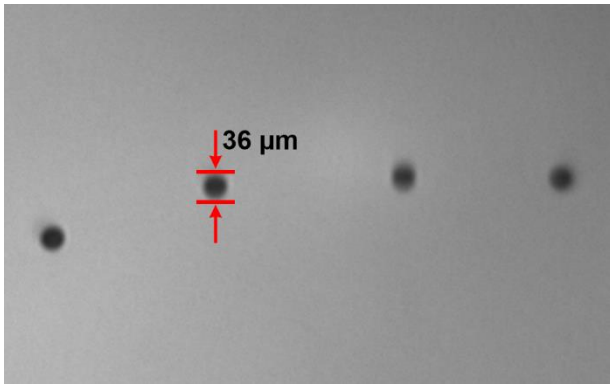

Figure 6. Droplets generated by the printhead. Despite a high value of the Oh^{-1} Number, single round shaped droplets were formed. No satellite droplets were observed.

3.3 Microstructure of the printed GDC films on substrates

3.3.1 Microstructure of GDC printed on green NiO-GDC substrates

Optical images (**Fig. 7**) reveal that cracking was present in the unsintered 10- and 20-layered films, but not in the 1- or 5-layered films. Therefore, it is evident that the cracking occurred during the drying after the printing process, and depended on the thickness of the printed layers, *i.e.* the critical cracking thickness. This is due to the small nominal particle radius (11 ± 2 nm), which affects the critical cracking thickness (proportional by the power 5/3) [46]. The single-layered film sintered at 1300 °C is shown in **Fig. 8**, and micrographs of the 5-layered film are shown in **Fig. S4**. In neither case, the obtained films were continuous, and the NiO-GDC substrate is still visible after sintering in some places (**Fig. 8**). These results indicate that under the conditions applied it was not possible to obtain a dense film completely covering the substrate, which could function as a SOFC electrolyte. Further optimization of the ink formulation, aiming for less particle agglomeration and a crack-free film after printing, and an optimized sintering profile targeting a dense GDC film will be carried out in near future.

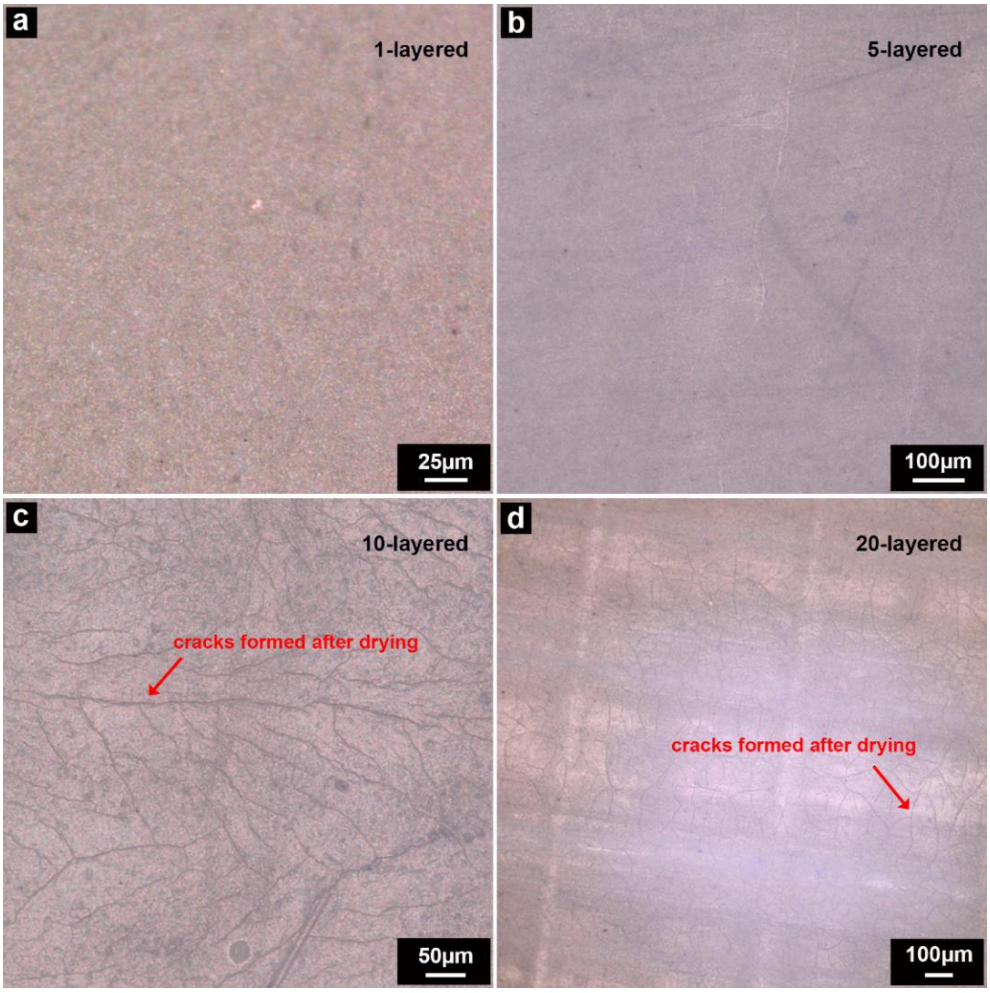

Figure 7. Optical images of the surface (top-down view) of the unsintered GDC films: (**a**) 1 layer, (**b**) 5 layers, (**c**) 10 layers, and (**d**) 20 layers. Cracking can be observed in (**c**) and (**d**). Printed on a green NiO-GDC substrate.

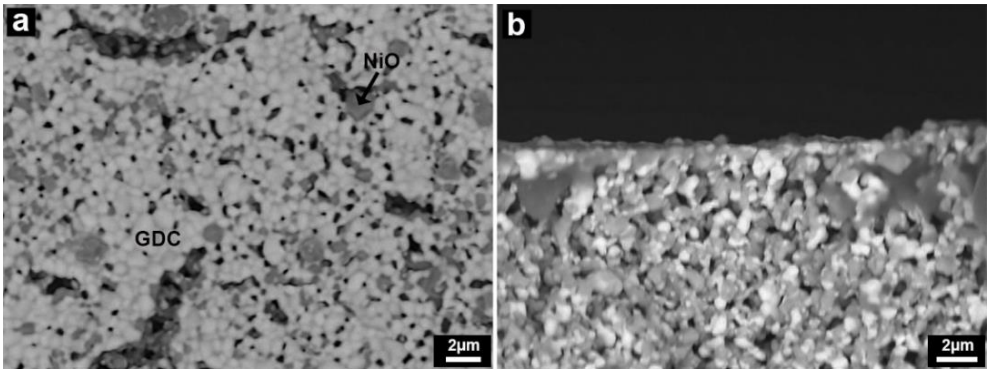

Figure 8. SEM micrographs of (**a**) surface view and (**b**) side view of the single-layered GDC film after sintering at 1300 °C. Printed on a green NiO-GDC substrate.

3.3.2 Microstructure of GDC printed on pre-sintered NiO-YSZ substrates

GDC films were also printed on pre-sintered NiO-YSZ substrates and sintered at 800, 1000 and 1300 °C. **Fig. 9a** presents an overview of the surface (BSE micrographs, top-down view) of the sample sintered at 1300 °C displaying the following regions of interest: i) the inkjet-printed GDC film, ii) the transition area between the inkjet-printed GDC film and the bare substrate, and iii) the uncovered NiO-YSZ substrate. Based on contrast, only one phase (bright grey) was observed in the printed GDC film and in part of the transition area, whereas two phases were present on the uncovered substrate's surface. The SE2 micrograph of the GDC film (**Fig. 9b**) shows that surface structure can be described as islands of GDC grains, which are disconnected by 'trenches'. However, it is worth noticing that inside these trenches no secondary phase was present, as shown by the BSE micrographs (**Fig. 9c** and **Fig. 9d**). For reference, a BSE micrograph (**Fig. 9e**) of the surface of the uncovered substrate shows NiO and YSZ differentiated by the contrast. Considering that GDC was printed on the surface of the substrate, this indicates that GDC completely covered the substrate after sintering although the shrinkage resulted in trenches and disconnected GDC islands on the top.

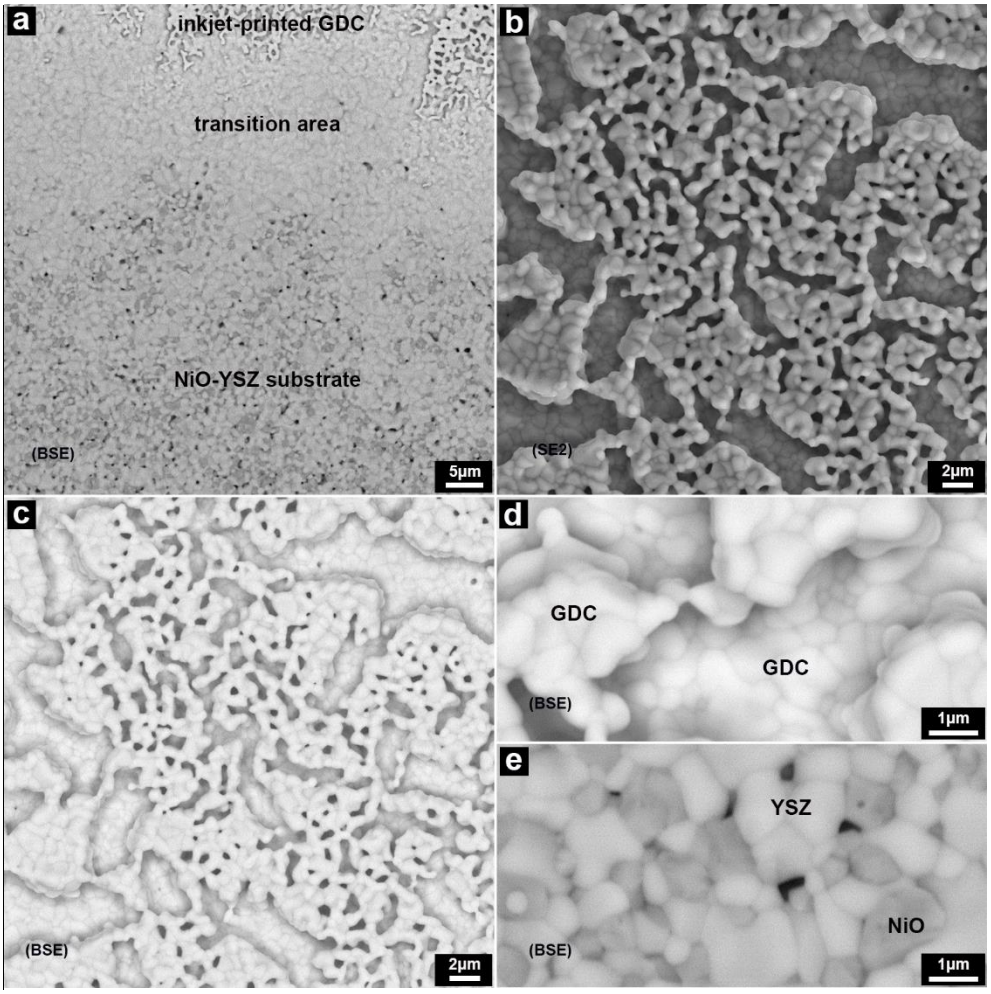

Figure 9. Top-down-view surface BSE micrograph (**a**) of the sample sintered at 1300 °C, including the inkjet-printed GDC film, transition area and NiO-YSZ substrate. SE2 micrograph (**b**) and BSE micrograph (**c**) of the surface of the inkjet-printed GDC film. Zoom-in BSE micrographs of the surface of the GDC film (**d**) and of the substrate (**e**). All images were recorded with an acceleration voltage 15 kV.

For further verification, side-viewed cross section of the part with the printed GDC film was investigated (**Fig. 10, S5, S6**). The SE2 micrograph (**Fig. 10a**) shows the 'trenches' between the islands of GDC grains on top of the printed film after sintering. The BSE micrograph (**Fig. 10b**) shows that at the bottom of the trench as well as below the islands of GDC grains a fully dense, continuous layer was found (**Fig. 10a**). This layer differed significantly in contrast (bright grey) compared to the NiO (dark grey). Element maps (**Fig. 10c – f**) show that the continuous layer could be divided into two parts. The top part was based on GDC (**Fig. 10e**) and was as thin as 0.5 µm (below the trenches), whereas below this part a thin (0.8 – 1 µm) layer of YSZ was formed. This suggests a full coverage

of the substrate by the printed GDC, which is consistent with the top-down-view observation (**Fig. 9d**). Interestingly, the formation of the continuous YSZ layer must have occurred during the sintering at 1300 °C. As shown in **Fig.S7d**, such a layer was not present at the surface of the bare substrate in the unprinted area after sintering. In these uncovered area clearly NiO particles were found at the surface. From an application point of view, this phenomenon is highly advantageous, as the formed dense GDC/YSZ layers can function as a dense electrolyte with a GDC barrier layer. Fast inter-diffusion between ceria and zirconia, with formation of ZrO_2-CeO_2 solid solution, was also expected at the electrolyte/barrier layer interface. However, chemical analysis in **Fig. 10** shows a rather sharp chemical front at the interface. Considering the low thickness of only 1 – 2 µm, better performances of cells with such a microstructure can be expected compared to state-of-the-art cells with electrolyte thicknesses of around 10 µm. Importantly, the corrugated electrolyte surface (disconnected GDC islands, **Fig. 10a**, **10b**) is expected to improve the adhesion between the cathode and electrolyte, while decreasing the interfacial electrolyte/cathode resistance.

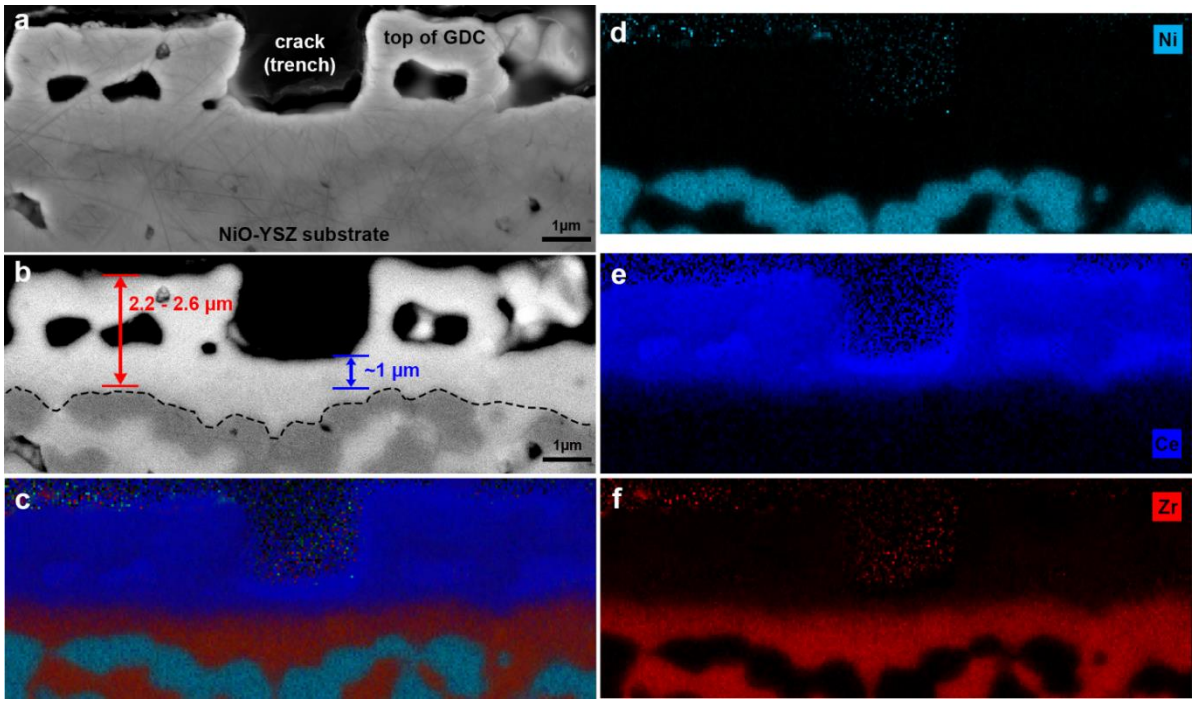

Figure 10. Side-viewed cross-section SE2 (**a**) and BSE (**b**) micrographs of the sample sintered at 1300 °C. EDS element mapping of the area within the image (**b**): map of all elements (**c**), of Ni (**d**), Ce (**e**) and Zr (**f**). Element maps were obtained by deconvoluting the total EDS spectrum of the mapping area, working voltage 10 kV.

For reference, the side-viewed cross-section micrographs of the transition area and of the uncovered substrate are presented in **Fig. S7**. Printed GDC films in samples sintered at 800 °C and 1000 °C were not fully dense. Neither the continuous layer was observed which means that the substrate was not fully covered after sintering (**Fig. S8**).

4. Conclusion

Tailored $Gd_xCe_{1-x}O_{2-\delta}$ (GDC) nanoparticles were synthesized using continuous hydrothermal flow synthesis. By varying the pH, the size, morphology and composition of the GDC particles could be tailored. Here, particle sizes between 6 nm and 40 nm were obtained, while the morphology was polyhedral (flat surfaces and spherical-like) for small particles and octahedral for larger ones. A similar conversion rate of Ce and Gd, and consequently a stoichiometric composition, was achieved when alkaline conditions were applied.

The obtained $Gd_{0.2}Ce_{0.8}O_{2-\delta}$ particles were further processed into inks for inkjet printing. Despite the small particle size/large surface area, inks with the surface tension and the viscosity of 27 mN m^{-1}, 2.1 mPa s and of 25 mN m^{-1}, 1.0 mPa s, separately were obtained. These inks showed excellent printing behavior.

GDC layers were printed on i) green NiO-GDC substrates and, on ii) pre-sintered NiO-YSZ substrates. While for the green NiO-GDC substrates no dense films could be obtained due to cracking of the printed films after drying (10- and 20-layered) and after sintering (1- and 5-layered), the sample with 10-layered GDC film printed on NiO-YSZ substrates formed a dense continuous layer after firing at 1300 °C. This continuous layer was consisted of a thin (0.8 – 1 µm) YSZ layer covered by a GDC layer (0.5 µm) decorated with GDC islands. Such a surface structure is expected to have several advantages over state-of-the-art SOFC cells. Firstly, the thin electrolyte (here 1-2 µm) is expected to cause lower performance losses. Secondly, the disconnected islands of the printed GDC layer could provide a high number of catalytic active sides and could provide a strong

bonding to the applied cathode. The performance of this new type of cells will be investigated in near future.

Supporting Information

1. Estimating crystallite size from the peak broadening in the XRD patterns

By the Diffrac.Eva Suite, the crystallite size of synthesized nanoparticles was estimated from the FWHM of the peaks. Results are summarized in **Table S1**. One may note that the peak broadening from the diffractometer was neglected. The contribution from microstrain to the peak profile deriving from such as non-uniform lattice distortions, dislocations and antiphase domain boundaries was not considered either. To minimize the influence from the background, all diffraction patterns were background-subtracted. The Scherrer equation was used, in which the dimensionless shape factor K = 1 was used.

Table S1. Crystallite size (/ nm) estimated from the FWHM of the peaks in the XRD patterns.

	pH	**(111)**	**(200)**	**(220)**	**(311)**	**(222)**	**(400)**	**(331)**	**(420)**	**(422)**	**(511)**
CG1	1.9	28.9	30.3	26.1	24.3	24.3	23.8	21.6	21.5	20.7	19.2
CG2	3.5	8.9	9.7	8.8						8.8	9.3
CG3	5.5	6.0	6.8	5.6						5.7	5.9
CG4	9	7.2	7.5	7.0			8.1			6.7	6.8
CG5	11.9	8.2	8.4	8.0			7.9			7.8	7.9
CG6	13.1	9.2	9.9	9.0			8.6			8.9	8.9
CG-s	12.8	11.9	11.9	11.5			11.8			11.8	11.2

Note: For the blank cells, no numbers were given because for the corresponding peaks the FWHM could not be determined due to overlapping with neighboring peaks.

2. Estimating residence time *t*

The residence time *t* describes the period starting from the mixing until the end of re-heater. It can be calculated using **Eq. S1**:

$t = V \rho_T / Q$ (**S1**),

where V is the reactor volume (cm^3), Q is the total flow rate ($g\ s^{-1}$), ρ_T is the density of H_2O ($g\ cm^{-3}$) at T K.

In the current case, the hot reaction zone started from the first mixer where the precursor (pre-mixture of the reactant solution and the KOH solution) was heated by the scH_2O, and ended after the re-heater. To simplify the estimation, an average temperature was taken, that was T_a = (396 + 290 + 285) °C / 3 = 324 °C (597 K). The volume of the zone V is 42.4 cm^3, Q is 60 mL min^{-1} (assuming densities of all supplied solutions were 1 $g\ cm^{-3}$, given the supplied solutions were diluted, then the Q equals to 1 $g\ s^{-1}$). At 25 MPa and 597 K, the density of H_2O was 690 × 10^{-3} $g\ cm^{-3}$ (refer to W. Wagner, A. Pruß, *J. Phys. Chem. Ref. Data.* 31 (2002) 387–535. doi:10.1063/1.1461829). The calculations gave a residence time of 29 s.

3. Viscosities of the primary $Gd_{0.2}Ce_{0.8}O_{2-\delta}$ dispersion and of the two formulated inks

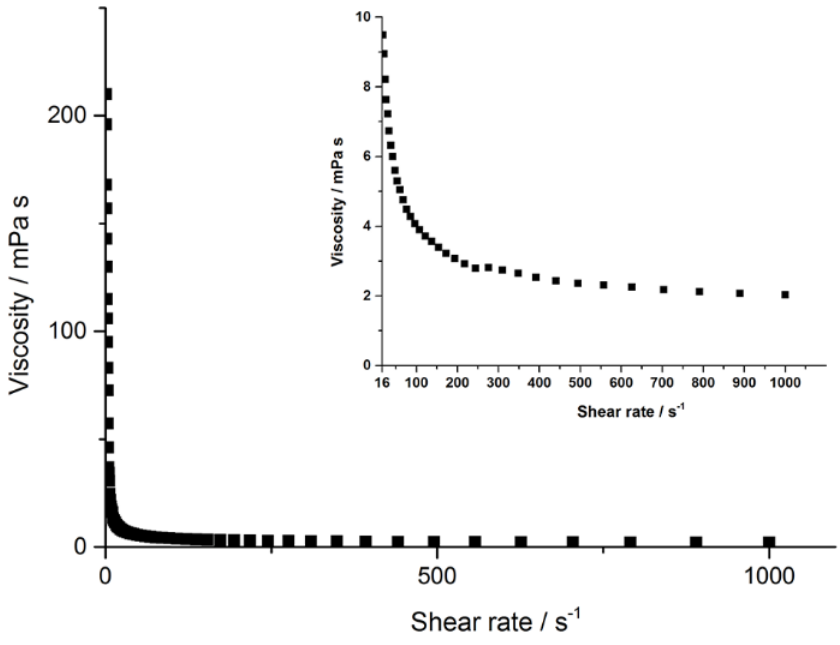

Figure S1. Viscosity of the primary $Gd_{0.2}Ce_{0.8}O_{2-\delta}$ dispersion measured at increasing shear rate.

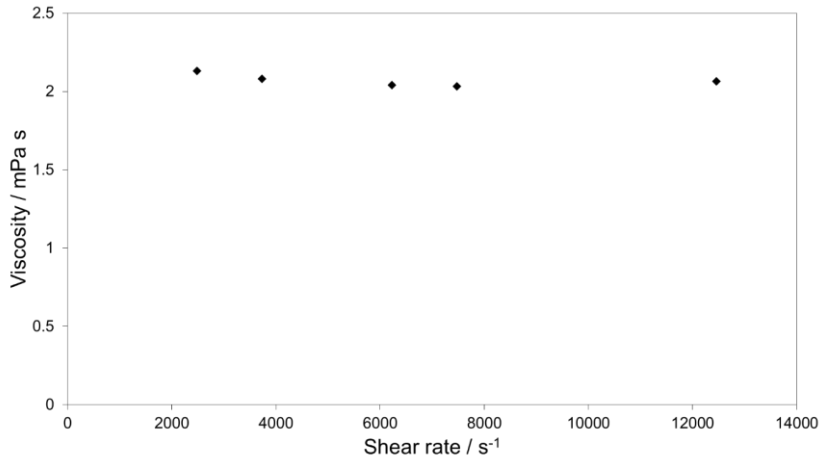

Figure S2. Viscosity of the ink formulated for printing on green NiO-GDC substrates measured at increasing shear rate. As behavior is essentially Newtonian, the average viscosity over shear rates tested may be taken as the ink viscosity during printing.

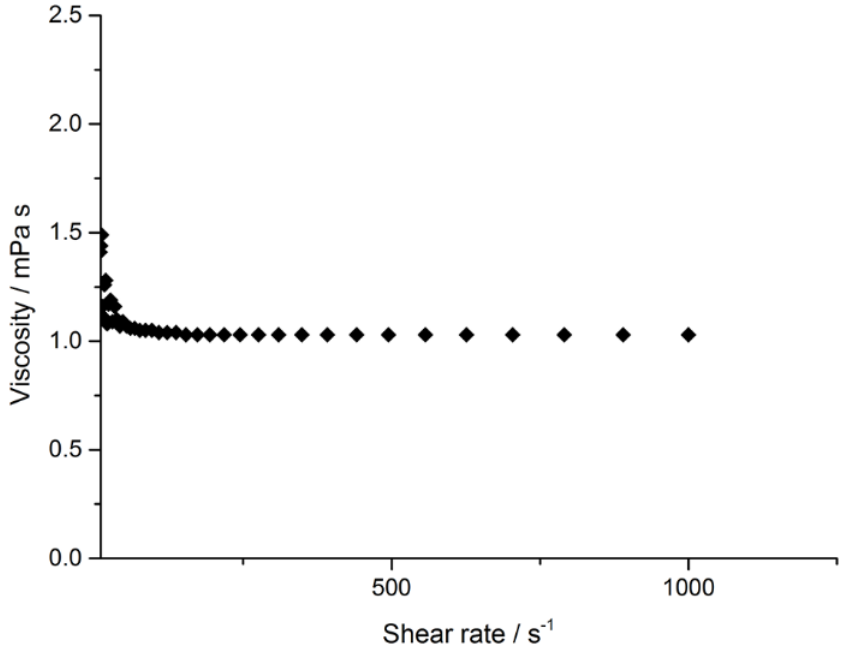

Figure S3. Viscosity of the ink formulated for printing on pre-sintered NiO-YSZ substrates measured at increasing shear rate. The plot shows that the viscosity reaches a plateau at low shear rates, thus 1 mPa s can be considered the viscosity value during inkjet printing.

4. SEM and EDS investigations of the sintered samples

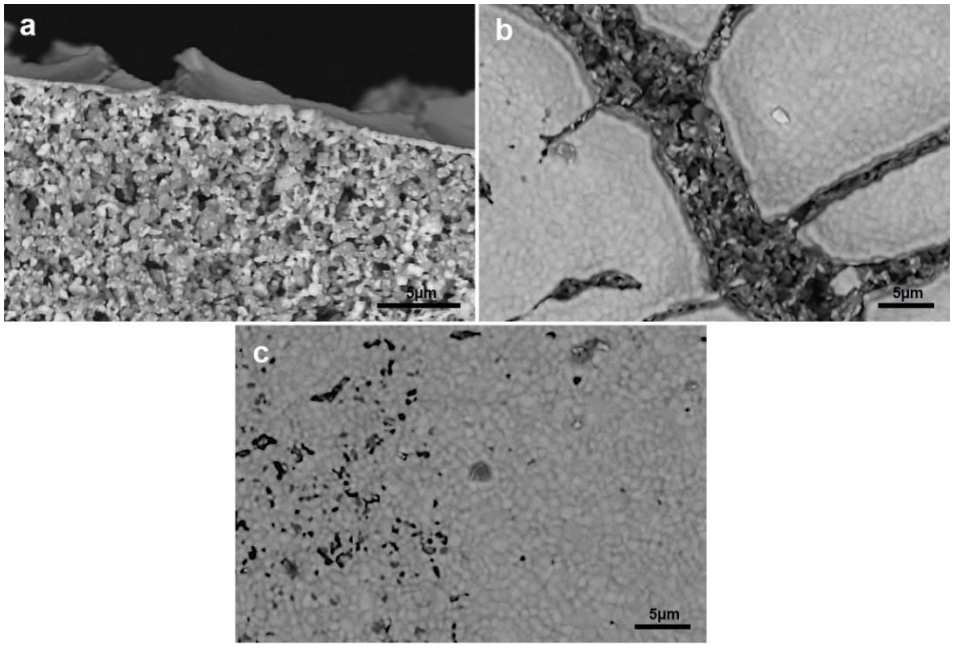

Figure S4. 5-layered GDC film printed on the green NiO-GDC substrate after sintering at 1300 °C; SEM micrographs: (**a**) side view; (**b**) top view showing cracks; and (**c**) top view showing porosity in the printed layers.

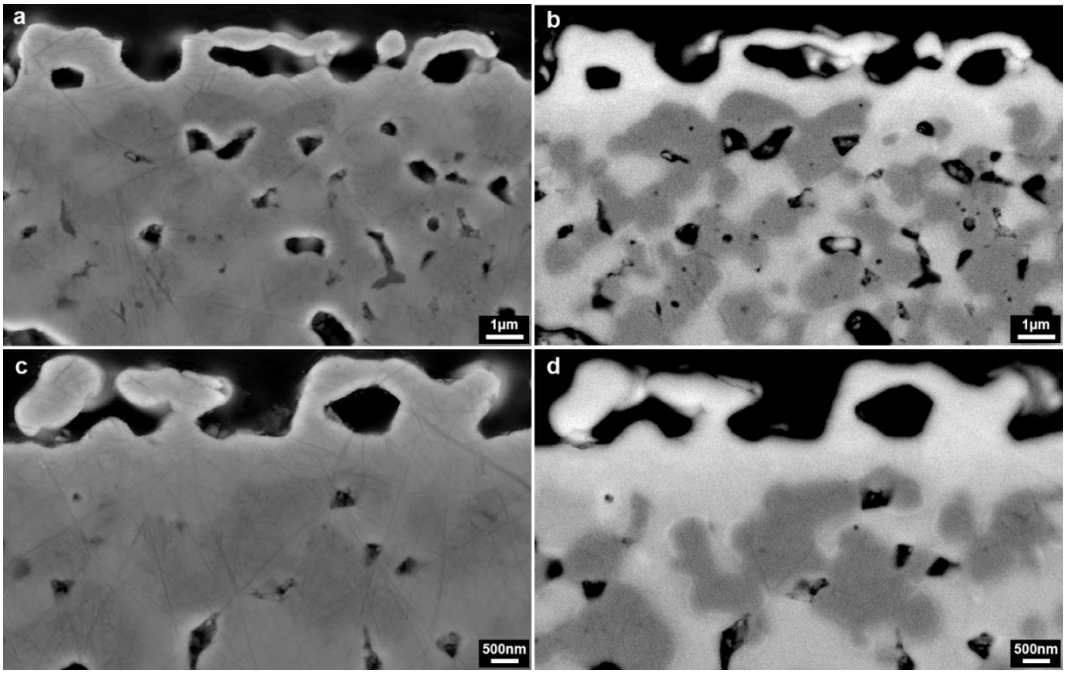

Figure S5. 10-layered GDC film printed on the pre-sintered NiO-YSZ substrate after sintering at 1300°C: two more examples of the side-viewed cross section of the area with the inkjet-printed GDC film. (**a**) and (**c**) are SE2 micrographs and (**b**) and (**d**) are BSE micrographs.

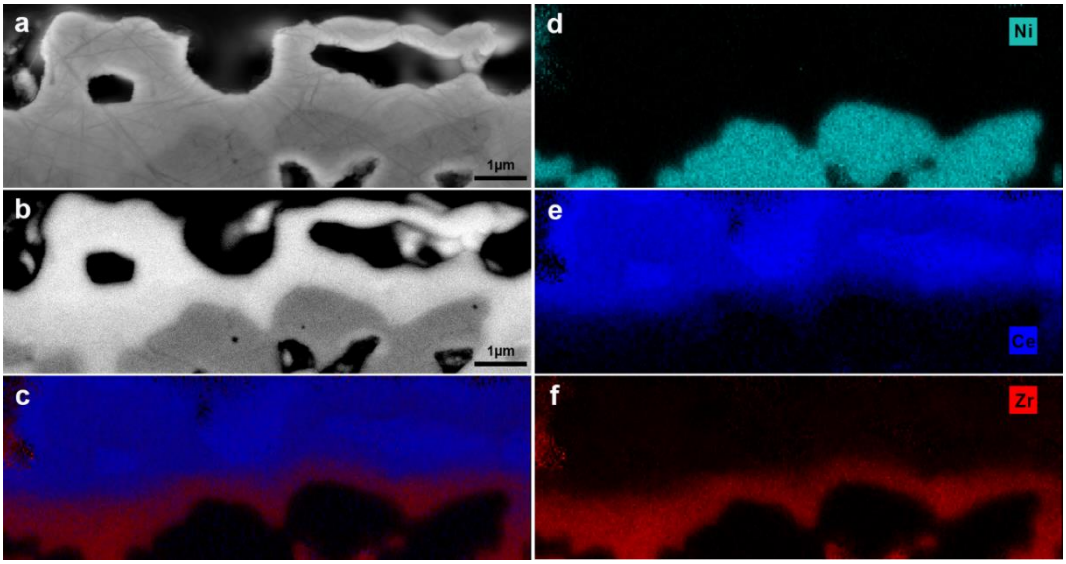

Figure S6. Another example of the GDC film printed on the pre-sintered NiO-YSZ substrate after sintering at 1300°C: EDS mapping of the elements in the cross section of the printed GDC film and substrate.

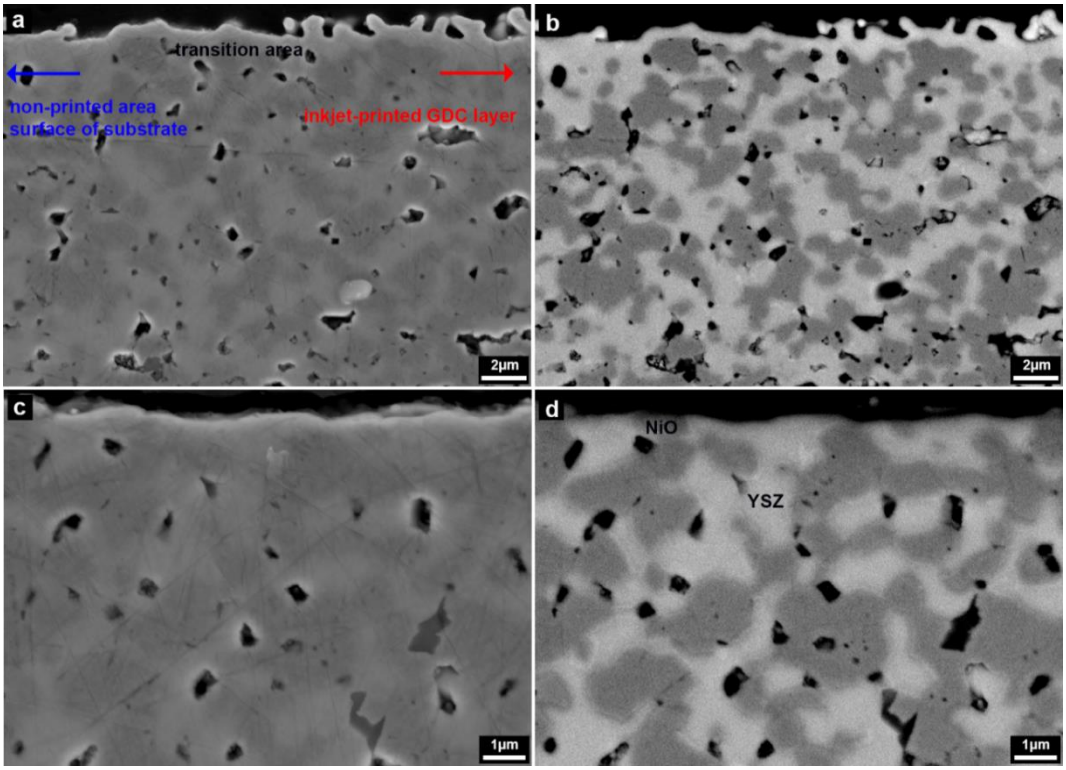

Figure S7. SE2 (**a**) and BSE (**b**) micrographs of the side-viewed cross section of the transition area; right: towards the area with the inkjet-printed GDC film; left: towards the uncovered NiO-YSZ substrate. SE2 (**c**) and BSE (**d**) micrographs of the side-viewed cross section of the uncovered substrate, where NiO exposed on the surface of the substrate is clearly observed.

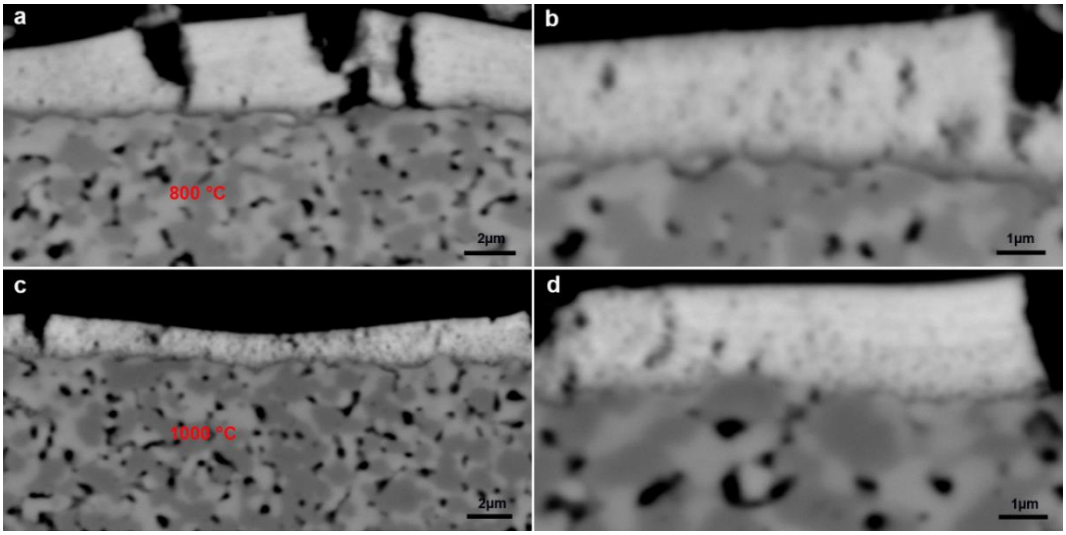

Figure S8. Side-viewed cross sections SE2 micrographs of the samples sintered at 800 °C (**a**, **b**) and at 1000 °C (**c**, **d**). Printed on the pre-sintered NiO-YSZ substrate.

References

[1] V. V. Kharton, F.M. Figueiredo, L. Navarro, E.N. Naumovich, A. V. Kovalevsky, A.A. Yaremchenko, A.P. Viskup, A. Carneiro, F.M.B. Marques, J.R. Frade, Ceria-based materials for solid oxide fuel cells, J. Mater. Sci. 36 (2001) 1105–1117. doi:10.1023/A:1004817506146.

[2] E.D. Wachsman, K.T. Lee, Lowering the temperature of solid oxide fuel cells, Science. 334 (2011) 935–939. doi:10.1126/science.1204090.

[3] W. Fang, F. Liang, Z. Cao, F. Steinbach, A. Feldhoff, A mixed ionic and electronic conducting dual-phase membrane with high oxygen permeability, Angew. Chemie - Int. Ed. 54 (2015) 4847–4850. doi:10.1002/anie.201411963.

[4] S. Cheng, H. Huang, S. Ovtar, S.B. Simonsen, M. Chen, W. Zhang, M. Søgaard, A. Kaiser, P.V. Hendriksen, C. Chen, High-performance microchanneled asymmetric Gd0.1Ce0.9O1.95-δ-La0.6Sr0.4FeO3-δ-based membranes for oxygen separation, ACS Appl. Mater. Interfaces. 8 (2016) 4548–4560. doi:10.1021/acsami.5b10714.

[5] M. Cargnello, V.V.T. Doan-Nguyen, T.R. Gordon, R.E. Diaz, E.A. Stach, R.J. Gorte, P. Fornasiero, C.B. Murray, Control of metal nanocrystal size reveals metal-support interface role for ceria catalysts, Science. 341 (2013) 771–773. doi:10.1126/science.1240148.

[6] Z. Hu, X. Liu, D. Meng, Y. Guo, Y. Guo, G. Lu, Effect of ceria crystal plane on the physicochemical and catalytic properties of Pd/ceria for CO and propane oxidation, ACS Catal. 6 (2016) 2265–2279. doi:10.1021/acscatal.5b02617.

[7] M. Zabilskiy, P. Djinović, E. Tchernychova, O.P. Tkachenko, L.M. Kustov, A. Pintar, Nanoshaped CuO/CeO2 materials: effect of the exposed ceria surfaces on catalytic activity in N2O decomposition reaction, ACS Catal. 5 (2015) 5357–5365. doi:10.1021/acscatal.5b01044.

[8] R.I. Walton, Solvothermal synthesis of cerium oxides, Prog. Cryst. Growth Charact. Mater. 57 (2011) 93–108. doi:10.1016/j.pcrysgrow.2011.10.002.

[9] D. Zhang, X. Du, L. Shi, R. Gao, Shape-controlled synthesis and catalytic application of ceria nanomaterials, Dalt. Trans. 41 (2012) 14455–14475. doi:10.1039/c2dt31759a.

[10] S. Yang, L. Gao, Controlled synthesis and self-assembly of CeO2 nanocubes, J. Am. Chem. Soc. 128 (2006) 9330–9331. doi:10.1021/ja063359h.

[11] L. Yan, R. Yu, J. Chen, X. Xing, Template-free hydrothermal synthesis of CeO2 nano-octahedrons and nanorods: investigation of the morphology evolution, Cryst. Growth Des. 8 (2008) 1474–1477. doi:10.1021/cg800117v.

[12] W. Wang, J.Y. Howe, Y. Li, X. Qiu, D.C. Joy, M.P. Paranthaman, M.J. Doktycz, B. Gu, A surfactant and template-free route for synthesizing ceria nanocrystals with tunable morphologies, J. Mater. Chem. 20

(2010) 7776–7781. doi:10.1039/c0jm00982b.

[13] T. Adschiri, K. Kanazawa, K. Arai, Rapid and continuous hydrothermal crystallization of metal oxide particles in supercritical water, J. Am. Ceram. Soc. 75 (1992) 1019–1022. doi:10.1111/j.1151-2916.1992.tb04179.x.

[14] P.W. Dunne, A.S. Munn, C.L. Starkey, T.A. Huddle, E.H. Lester, Continuous-flow hydrothermal synthesis for the production of inorganic nanomaterials, Philos. Trans. A. 373 (2015) 20150015. doi:10.1098/rsta.2015.0015.

[15] T. Adschiri, Y. Hakuta, K. Arai, Hydrothermal synthesis of metal oxide fine particles at supercritical conditions, Ind. Eng. Chem. Res. 39 (2000) 4901–4907. doi:10.1021/ie0003279.

[16] A. Nugroho, J. Kim, Effect of KOH on the continuous synthesis of cobalt oxide and manganese oxide nanoparticles in supercritical water, J. Ind. Eng. Chem. 20 (2014) 4443–4446. doi:10.1016/j.jiec.2014.02.014.

[17] Y. Shen, J.R. Eltzholtz, B.B. Iversen, Controlling size, crystallinity, and electrochemical performance of Li4Ti5O12 nanocrystals, Chem. Mater. 25 (2013) 5023–5030. doi:10.1021/cm402366y.

[18] P.W. Dunne, C.L. Starkey, M. Gimeno-Fabra, E.H. Lester, The rapid size- and shape-controlled continuous hydrothermal synthesis of metal sulphide nanomaterials, Nanoscale. 6 (2014) 2406–2418. doi:10.1039/c3nr05749f.

[19] S. Kubota, T. Morioka, M. Takesue, H. Hayashi, M. Watanabe, R.L. Jr. Smith, Continuous supercritical hydrothermal synthesis of dispersible zero-valent copper nanoparticles for ink applications in printed electronics, J. Supercrit. Fluids. 86 (2014) 33–40. doi:10.1016/j.supflu.2013.11.013.

[20] P.W. Dunne, E. Lester, R.I. Walton, Towards scalable and controlled synthesis of metal–organic framework materials using continuous flow reactors, React. Chem. Eng. 1 (2016) 352–360. doi:10.1039/C6RE00107F.

[21] R.I. Gruar, C.J. Tighe, J.A. Darr, Scaling-up a confined jet reactor for the continuous hydrothermal manufacture of nanomaterials, Ind. Eng. Chem. Res. 52 (2013) 5270–5281. doi:10.1021/ie302567d.

[22] T. Adschiri, Y.-W. Lee, M. Goto, S. Takami, Green materials synthesis with supercritical water, Green Chem. 13 (2011) 1380–1390. doi:10.1039/c1gc15158d.

[23] Y. Hakuta, S. Onai, H. Terayama, T. Adschiri, K. Arai, Production of ultra-fine ceria particles by hydrothermal synthesis under supercritical conditions, J. Mater. Sci. Lett. 7 (1998) 1211–1213. doi:10.1023/A:1006597828280.

[24] C. Slostowski, S. Marre, J.-M. Bassat, C. Aymonier, Synthesis of cerium oxide-based nanostructures in near- and supercritical fluids, J. Supercrit. Fluids. 84 (2013) 89–97. doi:10.1016/j.supflu.2013.09.014.

[25] K. Houlberg, E.D. Bøjesen, C. Tyrsted, A. Mamakhel, X. Wang, R. Su, F. Besenbacher, B.B. Iversen,

Hydrothermal synthesis and in situ powder X-ray diffraction study of bismuth-substituted ceria nanoparticles, Cryst. Growth Des. 15 (2015) 3628–3636. doi:10.1021/acs.cgd.5b00678.

[26] C.J. Tighe, R.Q. Cabrera, R.I. Gruar, J.A. Darr, Scale up production of nanoparticles: continuous supercritical water synthesis of Ce–Zn oxides, Ind. Eng. Chem. Res. 52 (2013) 5522–5528. doi:10.1021/ie3025642.

[27] J.-R. Kim, K.-Y. Lee, M.-J. Suh, S.-K. Ihm, Ceria–zirconia mixed oxide prepared by continuous hydrothermal synthesis in supercritical water as catalyst support, Catal. Today. 185 (2012) 25–34. doi:10.1016/j.cattod.2011.08.018.

[28] X. Weng, J.K. Cockcroft, G. Hyett, M. Vickers, P. Boldrin, C.C. Tang, S.P. Thompson, J.E. Parker, J.C. Knowles, I. Rehman, I. Parkin, J.R.G. Evans, J.A. Darr, High-throughput continuous hydrothermal synthesis of an entire nanoceramic phase diagram, J. Comb. Chem. 11 (2009) 829–834. doi:10.1021/cc900041a.

[29] J.-R. Kim, W.-J. Myeong, S.-K. Ihm, Characteristics in oxygen storage capacity of ceria–zirconia mixed oxides prepared by continuous hydrothermal synthesis in supercritical water, Appl. Catal. B Environ. 71 (2007) 57–63. doi:10.1016/j.apcatb.2006.08.015.

[30] R.I. Gruar, C.J. Tighe, P. Southern, Q.A. Pankhurst, J.A. Darr, A direct and continuous supercritical water process for the synthesis of surface-functionalized nanoparticles, Ind. Eng. Chem. Res. 54 (2015) 7436–7451. doi:10.1021/acs.iecr.5b01817.

[31] N.M. Farandos, L. Kleiminger, T. Li, A. Hankin, G.H. Kelsall, Three-dimensional inkjet printed solid oxide electrochemical reactors. I. Yttria-stabilized zirconia electrolyte, Electrochim. Acta. 213 (2016) 324–331. doi:10.1016/j.electacta.2016.07.103.

[32] C.J. Fu, Q.L. Liu, S.H. Chan, X.M. Ge, G. Pasciak, Effects of transition metal oxides on the densification of thin-film GDC electrolyte and on the performance of intermediate-temperature SOFC, Int. J. Hydrogen Energy. 35 (2010) 11200–11207. doi:10.1016/j.ijhydene.2010.07.049.

[33] Y.J. Leng, S.H. Chan, S.P. Jiang, K.A. Khor, Low-temperature SOFC with thin film GDC electrolyte prepared in situ by solid-state reaction, Solid State Ionics. 170 (2004) 9–15. doi:10.1016/j.ssi.2004.02.026.

[34] A. Aguadero, L. Fawcett, S. Taub, R. Woolley, K.T. Wu, N. Xu, J.A. Kilner, S.J. Skinner, Materials development for intermediate-temperature solid oxide electrochemical devices, J. Mater. Sci. 47 (2012) 3925–3948. doi:10.1007/s10853-011-6213-1.

[35] G. Delette, J. Laurencin, M. Dupeux, J.B. Doyer, Measurement of the fracture energy at the interface between porous cathode layer and electrolyte in planar solid oxide fuel cells, Scr. Mater. 59 (2008) 31–34. doi:10.1016/j.scriptamat.2008.02.018.

[36] P. Zielke, Y. Xu, S.B. Simonsen, P. Norby, R. Kiebach, Simulation, design and proof-of-concept of a

two-stage continuous hydrothermal flow synthesis reactor for synthesis of functionalized nano-sized inorganic composite materials, J. Supercrit. Fluids. 117 (2016) 1–12. doi:10.1016/j.supflu.2016.06.008.

[37] Y. Hakuta, H. Ura, H. Hayashi, K. Arai, Continuous production of BaTiO3 nanoparticles by hydrothermal synthesis, Ind. Eng. Chem. Res. 44 (2005) 840–846. doi:10.1021/ie049424i.

[38] Fujifilm, Jettable Fluid Formulation Guidelines, 2013.

[39] A. Hauch, M. Mogensen, Ni/YSZ electrode degradation studied by impedance spectroscopy: Effects of gas cleaning and current density, Solid State Ionics. 181 (2010) 745–753. doi:10.1016/j.ssi.2010.04.001.

[40] Z.L. Wang, X. Feng, Polyhedral shapes of CeO2 nanoparticles, J. Phys. Chem. B. 107 (2003) 13563–13566. doi:10.1021/jp036815m.

[41] J.P.Y. Tan, H.R. Tan, C. Boothroyd, Y.L. Foo, C. Bin He, M. Lin, Three-dimensional structure of CeO2 nanocrystals, J. Phys. Chem. C. 115 (2011) 3544–3551. doi:10.1021/jp1122097.

[42] M. Lin, Z.Y. Fu, H.R. Tan, J.P.Y. Tan, S.C. Ng, E. Teo, Hydrothermal synthesis of CeO2 nanocrystals: Ostwald ripening or oriented attachment?, Cryst. Growth Des. 12 (2012) 3296–3303. doi:10.1021/cg300421x.

[43] H. Hayashi, A. Ueda, A. Suino, K. Hiro, Y. Hakuta, Hydrothermal synthesis of yttria stabilized ZrO2 nanoparticles in subcritical and supercritical water using a flow reaction system, J. Solid State Chem. 182 (2009) 2985–2990. doi:10.1016/j.jssc.2009.08.013.

[44] D. Jang, D. Kim, J. Moon, Influence of fluid physical properties on ink-jet printability, Langmuir. 25 (2009) 2629–2635. doi:10.1021/la900059m.

[45] B. Derby, Inkjet printing ceramics: From drops to solid, J. Eur. Ceram. Soc. 31 (2011) 2543–2550. doi:10.1016/j.jeurceramsoc.2011.01.016.

[46] W.B. Russel, N. Wu, W. Man, Generalized Hertzian model for the deformation and cracking of colloidal packings saturated with liquid, Langmuir. 24 (2008) 1721–1730. doi:10.1021/la702633t.

Chapter V. Hydrothermal synthesis, characterization, and sintering behavior of core-shell particles: a principle study on lanthanum strontium cobaltite coated with nanosized gadolinium doped ceria

This chapter contains the revision 'Hydrothermal Synthesis, Characterization, and Sintering Behavior of Core-Shell Particles: a Principle Study on Lanthanum Strontium Cobaltite Coated with Nanosized Gadolinium Doped Ceria' that has been submitted to *J. Solid State Chem*.

$La_{1-x}Sr_xCoO_3$ and $Gd_xCe_{1-x}O_{2-\delta}$ (hereafter called LSC and GDC) are two materials widely investigated in solid oxide fuel cells. Particularly the interface of them in a composite is believed to be the active site of interest. By the conventional batch-type hydrothermal method, LSC-GDC particles with core-shell structure were prepared by precipitating GDC (x = 0.2) nanoparticles on surfaces of LSC (x = 0.4) forming an integral GDC shell in a mild hydrothermal condition.

The microstructural evolution of LSC-GDC core-shell particles was investigated under two different sintering conditions (spark plasma sintering and conventional sintering). It was found that a fine microstructure containing nanograins was obtained by spark plasma sintering, as well as the graded core-shell architecture was partially maintained. Phase transitions of LSC under the low oxygen partial pressure during spark plasma sintering were observed which resulted in the formation of $La_{2-x}SrCoO_4$. In comparison, the grain coarsening process was more pronounced during the conventional sintering process. As a result, coarse grains were found and the core-shell structure was lost.

Hydrothermal Synthesis, Characterization, and Sintering Behavior of Core-Shell Particles: A Principle Study on Lanthanum Strontium Cobaltite Coated with Nanosized Gadolinium Doped Ceria

Yu Xu [1,*], Philipp Zielke [1], Ngo Van Nong [1], Stéven Pirou [1], Raquel Reolon [1], Søren Bredmose Simonsen [1], Poul Norby [1], Henning Lühmann [2], Wolfgang Bensch [2], Ragnar Kiebach [1]

[1] Department of Energy Conversion and Storage, Technical University of Denmark (Risø Campus), Frederiksborgvej 399, 4000 Roskilde, Denmark

[2] Institut für Anorganische Chemie, Christian-Albrechts-Universität zu Kiel, Max-Eyth-Straße 2, D-24118 Kiel, Germany

[*]Correspondence: yuax@dtu.dk, Tel.: +45 93 51 11 48, Fax: +45 46 77 56 88

Abstract

In this work, nanostructured $(La_{0.6}Sr_{0.4})_{0.99}CoO_3$ (LSC)-$Gd_{0.2}Ce_{0.8}O_{2-\delta}$ (GDC) core-shell particles were prepared by precipitating GDC nanoparticles on the surface of LSC particles under hydrothermal conditions. The as-prepared core-shell particles were sintered by spark plasma sintering (SPS) and conventional sintering, and the microstructure evolution and densification behavior were studied. Dense microstructures were obtained by both sintering methods at relatively low temperatures. In case of SPS, the core-shell architecture was partially maintained and nano-structured GDC grains were formed, while conventional sintering led to the formation of larger GDC grains. This work covers a detailed characterization of a) the individual LSC-GDC core-shell particles and b) the composites after densification.

Keywords: hydrothermal; core shell; lanthanum strontium cobaltite; gadolinium-doped ceria; spark plasma sintering

1. Introduction

The search for new functional materials in numerous fields of applications has led to the development of advanced composite materials combining the distinctive behavior of each constituent to obtain tailored properties. Such composite architectures can be controlled down to the nanoscale; especially the core-shell morphology has been used to combine properties of each component in functional materials such as photonic crystals, biomedical compatible systems, catalysts and magnetic structures [1–3].

Composites based on $La_{0.6}Sr_{0.4}CoO_3$ (LSC) and $Gd_{0.2}Ce_{0.8}O_{2-\delta}$ (GDC) are widely used as oxygen electrodes in solid oxide fuel/electrolysis cells (SOFC/SOECs), and are considered in oxygen transport membranes (OTMs) [4–6]. Especially for OTMs, a dense (dual-phase) composite membrane consisting of LSC and GDC is of interest, because the combination of materials with high electronic conductivity (LSC) and high ionic conductivity (GDC) can lead to a high performance in terms of oxygen production. However, obtaining such desired structures in a dense bulk form is challenging, due to the fact that the sintering temperatures for these two materials are different, and especially the high temperature required for densifying GDC of a poor sinterability (1400-1600°C to reach full density of pure GDC) is problematic [7,8]. Moreover, since LSC and GDC have rather different thermal expansion coefficients, it is even more difficult to obtain a fully dense large sample without cracking [9]. Ideally, for OTM applications, the microstructure after sintering should consist of small, but still percolating grain networks in order to maintain both the ionic and electronic percolations. Therefore, it requires a fine control on the phase volume fractions and phase arrangement in the primary powders. Such a microstructure is difficult to obtain with conventional sintering at high temperatures due to severe structural rearrangements [10,11].

One possible way to realize a controlled and designed microstructure in a densified composite is to use core-shell nanostructures of pre-arranged architecture as building blocks for bottom-up manufacturing of functional nanocomposite ceramics. Recent examples realizing this concept are

the use of PbTe-PbS core-shell particles as building blocks for highly homogeneous thermoelectrics [12], ceramics with excellent dielectric properties made of core-shell structured SiO_2-TiO_2 particles synthesized by a solvothermal route [13], and the use of $SrTiO_3$-$NiFe_2O_4$ core-shell particles, prepared by the combination of sol-gel and co-precipitation methods, to obtain structured ceramics [14].

However, densification of the core-shell particles to a ceramic without destroying the original structure by using conventional sintering is challenging, because of the inherent severe structural rearrangement. Even designed core-shell structures do not necessarily lead to core-shell ceramic composites, due to lattice mismatch, different sinterability, interfacial diffusions and/or phase reactions.

An interesting alternative to the conventional sintering is the spark plasma sintering (SPS), which combines a pulsed direct electric current and a uniaxial pressure for the consolidation of powders. Thanks to the very fast densification process as a result of the Joule heating, the applied pressure and the presence of an electric field, SPS can sinter powders to a high density at a lower temperature and in a shorter time than in a conventional sintering process [15,16]. Examples where the use of SPS leads to micro-graded structure have been reported for sintering $BaTiO_3$-$SrTiO_3$ and $BaTiO_3$-$BaZrO_3$ core-shell particles [17] and for producing ZrO_2–ZrB_2 nano-ceramics [18].

Using LSC-GDC core-shell particles as starting material with a designed pre-arrangement of the two phases and accomplishing sintering at a low temperature (1000°C) using SPS are demonstrated in this work. Here, the hydrothermal synthesis and detailed characterizations (by XRD, TEM and STEM-EDS) of the core-shell LSC-GDC particles are described. In addition, the influence of SPS and conventional sintering on the microstructure evolution of as-prepared LSC-GDC core-shell particles is compared.

2. Experimental

2.1 Preparation of LSC-GDC core-shell particles in a hydrothermal autoclave

Commercial $(La_{0.6}Sr_{0.4})_{0.99}CoO_3$ powder (Kusaka Rare Metal Products Co. Ltd., Japan), $Ce(NO_3)_3•6H_2O$, $Gd(NO_3)_3•6H_2O$ salts (Sigma Aldrich, ≥ 99 %) and NaOH (Sigma Aldrich, ≥ 98 %) as purchased were used for the synthesis. The particle size of the LSC measured by a LS 13 320 Laser Diffraction Particle Size Analyzer (using the universal liquid module, measured in the range of 0.04 µm to 2000 µm) displayed a bimodal distribution centered on ~0.3 µm and ~1.0 µm respectively (**Fig. S1** in supporting information). Aimed at a molar ratio of n[LSC core] : n[GDC shell] = 4 : 1 in the core-shell particles, the molar ratio of $Ce(NO_3)_3•6H_2O$: $Gd(NO_3)_3•6H_2O$: NaOH : LSC was kept at 0.44 : 0.11 : 4.50 : 2.20. 0.5 g of LSC powders were first dispersed as much as possible in DI H_2O by an ultrasonic treatment for 20 min, then 0.19 g $Ce(NO_3)_3•6H_2O$ and 0.05 g $Gd(NO_3)_3•6H_2O$ salts were added into the slurry, followed by adding dropwise 4.5 mL 1 mol L^{-1} NaOH aqueous solution. The whole slurry was then transferred into a Teflon liner (230 mL in capacity), and the overall volume was fixed to 45 mL by adding more DI H_2O. Afterwards, the Teflon liner was sealed in a stainless steel autoclave, which was heated to 100 ˚C by a hot plate with a magnetic stirrer. A magnetic bar was stirring inside the slurry in order to reduce the sedimentation and agglomeration of LSC powders. The synthesis at 100 ˚C was conducted for 24 h and then the slurry with particles was left to cool down. The particles were filtered, washed and air-dried for later processing.

2.2 Densification of LSC-GDC particles

2.2.1 Spark plasma sintering (SPS)

The SPS system (DR. Sinter Lab 515S, Fuji Electronic Industrial Co., Ltd., Japan) was used, with a pulsed direct current regulated by on-off settings. As-prepared LSC-GDC particles (6 g) were filled into a Ø16 mm graphite die, which was then pressed under a small pressure of around 5 MPa to ensure a good contact between the powder and graphite punches. In the SPS process, a pulsed electric current then passed through the powders under a vacuum of about 10^{-5} atm. The heating

rate was 100 ˚C min^{-1}. In order to remove all gases from the powders, after the temperature reached 800 ˚C, a uniaxial pressure was slowly applied and it arrived at 50 MPa when the temperature reached 900 ˚C. The sintering temperature was held at 1000 ˚C with a constant uniaxial pressure of 50 MPa for 6 min. The cooling rate was set at 100 ˚C min^{-1} from 1000 °C to 500 °C to avoid cracking. During the sintering process, all parameters such as the electric current, the temperature, the uniaxial pressure, and the sample displacement (shrinkage) were recorded and they are presented in **Fig. S2**.

2.2.2 Conventional sintering in a Muffle furnace in air

LSC-GDC particles with an amount of 1 g were die-pressed into a pellet at 1000 kg load and then isostatically pressed at 65,000 kg load. Afterwards the pellet was sintered inside a muffle furnace in air at 1250 ˚C for 6 h. The heating rate was set to 100 ˚C h^{-1}. Before the temperature reached 1250 ˚C, the pellet was kept at 800 ˚C for 2 h. The cooling rate was also set at 100 ˚C h^{-1}. The temperature profile of the furnace is presented in **Fig. S3**.

2.3 Characterization

For comparison, the raw as-bought LSC particles and the as-prepared LSC-GDC core-shell particles were separately characterized by powder XRD performed on a Bruker D8 Advance diffractometer (Cu K_α radiation) with 2θ = 20-90˚ at a step size of 0.01˚. The diffraction patterns were compared with standard patterns collected in the ICDD *PDF*2 database by the Diffrac.Eva Suite (Bruker), and were further refined by the Rietveld method using the FullProf Suite [19]. Details on the refinement and the refinement residuals are presented in supporting information (**Table S1** and **S2**).

Scanning electron microscopy was carried out by using a Zeiss Merlin SEM equipped with a field emission gun. The sintered pellets were cut, embedded in epoxy and then polished for SEM microstructure investigations. They were also broken for the microscopy observation on the fracture surface. All samples were coated with ca. 20 nm of carbon on the surface in order to increase the surface's electrical conductivity. At each observed area, two images were recorded simultaneously

by processing signals from secondary electrons (SE2) and backscattered electrons (BSE) separately collected by a high efficiency secondary electron (HE-SE2) detector and an incolumn energy selective backscattered electron (ESB) detector. The software ThreshAlyzer was used to do image segmentations and to statistically quantify grain sizes when possible. Details on the analysis can be found in the supplementary material. For the compositional analysis, energy-dispersive X-ray spectroscopy (EDS) was carried out by using a Bruker EDS detector.

For the TEM characterization, the as-prepared LSC-GDC particles were dispersed in ethanol by means of ultrasonic treatment and were dropped onto a holey carbon film/Au grid. Bright field (BF) TEM images were recorded with a JEOL 3000F microscope operating at 300 kV with a field emission gun. Dark-field scanning transmission electron microscopy (DF-STEM) was carried out by using the JEOL 3000F equipped with a STEM unit and a high angle annular dark field (HAADF) detector. The nominal probe size was 0.5 nm and the camera length was 12 cm. For compositional analysis, energy dispersive X-ray spectroscopy (EDS) was carried out by using an Oxford Instruments EDS detector. BF-TEM images were analyzed by using the software Gatan DigitalMicrograph while the DF-STEM images as well as EDS elemental analysis were processed by using the software INCA.

3. Results and Discussion

3.1 Structure and morphology of nano-structured LSC-GDC core-shell particles

Phase purity and morphology of the commercial LSC powder as the starting material were analyzed first by XRD and SEM. The Rietveld refinement in **Fig. 1a** shows a good match between the experimental pattern in both the intensity and Bragg positions and the calculated pattern based on the rhombohedral perovskite structure (*space group*: R-3c). As observed in the SEM image (**Fig. 1b**), LSC particles displayed sharp edges and smooth surfaces. The particle size was not homogeneous, as found by the laser diffraction measurement that the particles displayed a bimodal size distribution (0.04 – 0.45 µm and 0.6 – 1.83 µm). **Fig. 1c** presents the refinement of the XRD pattern of the as-prepared LSC-GDC particles. Although weak, diffraction peaks (Bragg positions

indexed by red vertical bars) corresponding to the newly formed GDC (cubic, *space group*: Fm-3m) were observed in addition to the diffraction peaks of the LSC powders. The significant broadening of GDC diffraction peaks indicates that the GDC phase from the hydrothermal synthesis consisted of small particles relative to the LSC particles. SEM analysis (**Fig. 1d**) shows that the LSC particles in the LSC-GDC sample generally kept the shape and size observed for the raw LSC powders. However, for the LSC-GDC sample, sharp edges were rarely observed. The surfaces of both large and small LSC particles became rough, which can be interpreted as coverage of LSC particles with the new phase determined by XRD to be GDC.

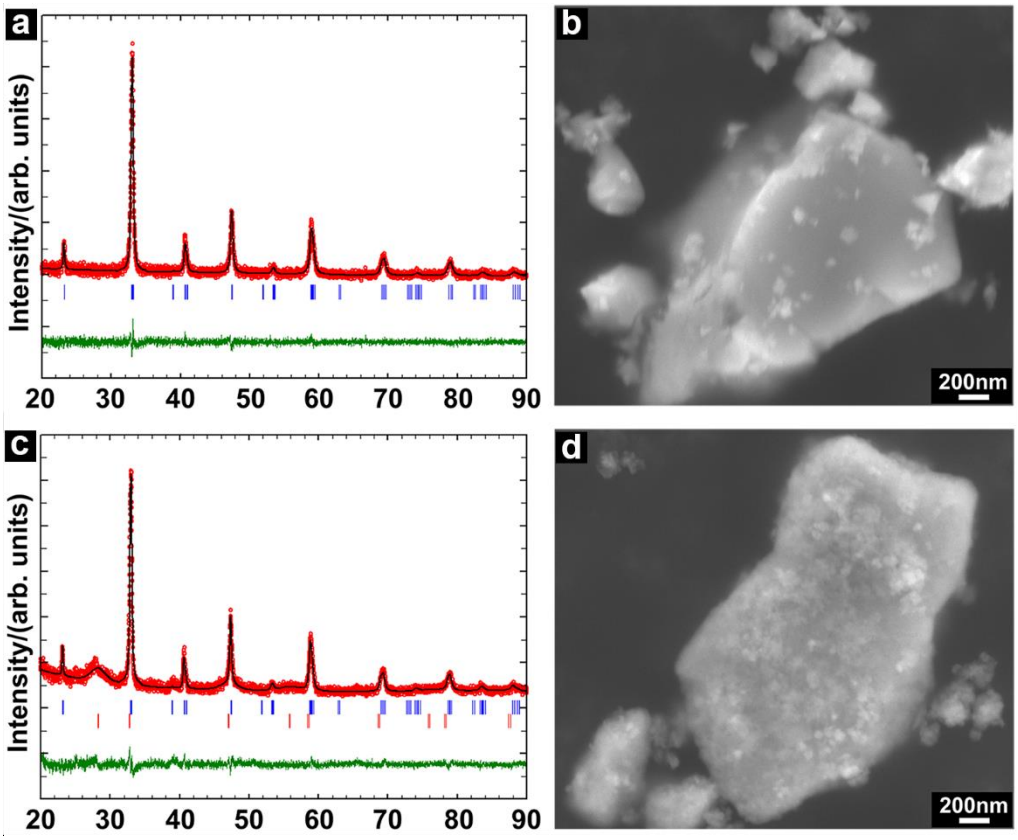

Figure 1. (**a**) Rietveld refinement of the powder X-ray diffraction of the commercial lanthanum strontium cobaltite (LSC) powder. The observed pattern, the calculated pattern, Bragg positions and the differential profile are presented by red circles, the black line, blue vertical bars and the green line, respectively. (**b**) SE2-SEM image of the LSC powders. (**c**) Rietveld refinement of the powder X-ray diffraction of the particle composed of LSC core and the shell of gadolinium-doped ceria (GDC) before sintering; red vertical bars corresponding to Bragg positions of cubic GDC are added. (**d**) SE2-SEM image of the LSC-GDC particles before sintering.

For a more detailed analysis, the LSC-GDC particles were characterized by transmission electron microscopy, and the results are summarized in **Fig. 2**. A BF-TEM image giving a two-dimensional projection of a LSC-GDC particle is presented in **Fig. 2a**. It is clear that the large particles were coated with nanosized crystals. The insets of **Fig. 2a** contain a fast Fourier transform (FFT) and a high-resolution image of the shell. The FFT shows ring patterns indicating that the shell consisted of many small, randomly oriented crystals. Determined by the radius, the rings were separately assigned to the three crystal planes (111), (200) and (220) of a GDC crystal. Details on the FFT conversion, measurement and assignment can be found in **Fig. S5**. In the high-resolution TEM image, two sets of lattice spacings are observed in a single GDC nanoparticle. The measured interplanar spacings were 3.1 Å and 2.7 Å (the angle between them was 55˚) that are consistent with distances of the (111) and (200) planes of a GDC crystal respectively. The mean size of GDC particles was roughly estimated to be 6(±1) nm, by measuring 12 particles. However, it should be noted that the number of distinguishable particles was limited due to overlapping. **Fig. 2b** shows a DF-STEM image of the LSC-GDC particles in which the rough surface is clearly revealed. STEM-EDS maps of all detected metal elements are shown in **Fig. 2c**. X-ray photons emitted from La, Sr and Co were mostly detected in the inner core positions of the LSC-GDC particles. In comparison, the X-ray photons from Ce and Gd were observed over extended areas corresponding to whole areas of the LSC-GDC particles shown in the DF-STEM image. The elemental maps indicate that a core-shell particle was composed of an integral GDC shell covering a LSC core. In addition, the similar distribution of Ce and Gd indicates that Gd was doped into the lattice of CeO_2, i.e., Gd-doped CeO_2. Standardless quantification of the EDS data showed that the ratio of the atomic percent of Ce to that of Gd was 3.6, which is close to the molar ratio (n[Ce]/n[Gd] = 4/1) in the nominal composition of $Gd_{0.2}Ce_{0.8}O_{2-\delta}$. To make it more illustrative, the DF-STEM image, La and Ce element maps are integrated together in **Fig. 2c**, where it can be seen that a GDC shell (represented by Ce) covered a LSC core (represented by La) forming a LSC-GDC core-shell structure.

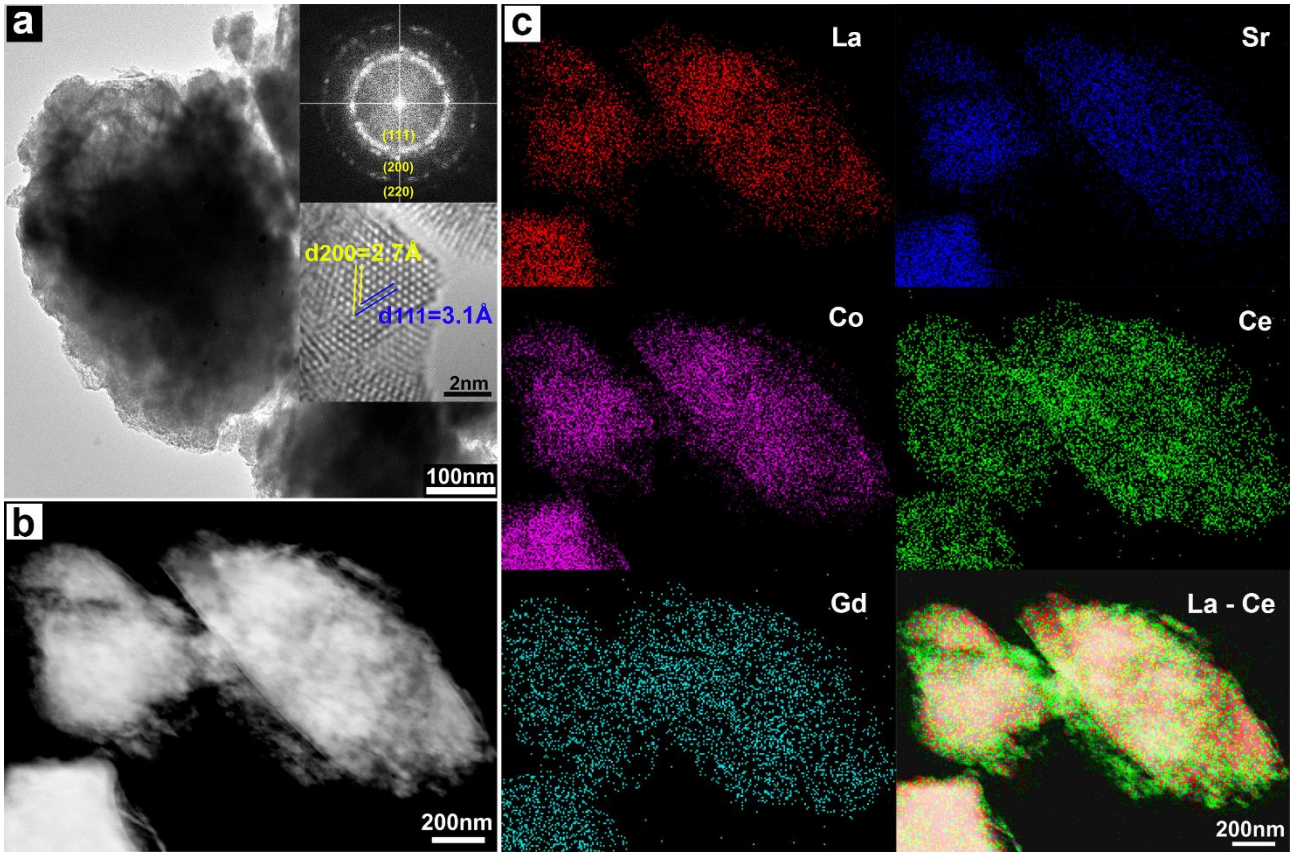

Figure 2. (**a**) BF-TEM image of the LSC-GDC core-shell particles. The first inset is a FFT of the shell composed of nanosized GDC particles randomly oriented; the second inset is a high-resolution image of a GDC nanoparticle in the shell. (**b**) Dark field scanning transmission electron microscopy (DF-STEM) image of LSC-GDC particles. (**c**) Mapping of all involved metallic elements by STEM-EDS; X-ray photons from La Lα, Sr Kα, Co Kα, Ce Lα and Gd Lα.

In the applied hydrothermal condition, the formation of GDC crystals is expected to follow a normal hydrothermal synthesis route that involves steps of hydrolysis of Ce and Gd cations in the alkaline aqueous media and subsequent dehydration and crystallization to metal oxides under the heat treatment at 100°C in the autoclave. For a hydrothermal system containing more than one metallic cation, it is necessary that the applied conditions should be favorable for the simultaneous hydrolysis and dehydration of all cations to a similar degree in order to obtain a mixed oxide of determined composition [20]. These conditions appear to have been realized as Ce and Gd were found to be homogeneously distributed (**Fig. 2c**) and the measured composition of GDC was close to the nominal value. According to the classical nucleation theory, the free energy barrier for the

homogeneous nucleation is higher than that for the heterogeneous nucleation [21,22]. The pre-suspended LSC particles in the autoclave worked as 'impurities' and provided 'crystallization sites' for the GDC phase. Therefore, the crystallization of GDC from the supersaturated solution under the increased temperature might prefer to start by the heterogeneous nucleation of GDC nuclei on LSC surfaces. As the nucleation process continued, an integrated shell composed of GDC crystals was formed on the surfaces of LSC particles. In summary, hydrothermal precipitation is a feasible way of preparing LSC-GDC core-shell particles.

3.2 Behavior of LSC-GDC core-shell particles during SPS and conventional sintering

3.2.1 Phase stability in the sintering processes

To determine phases in the composite after densification of the LSC-GDC core-shell particles by SPS, part of the sintered composite was grinded into powder for XRD characterization. The pattern (**a**) is presented in comparison with that of the LSC-GDC core-shell particles before sintering (**c**) in **Fig. 3**. Both the reflections corresponding to the perovskite-type $La_{1-x}Sr_xCoO_3$ with a rhombohedral crystal (*space group*: R-3c) and fluorite-type cubic $Gd_{0.2}Ce_{0.8}O_{2-\delta}$ (*space group*: Fm-3m) are observed in the pattern of the sintered pellet. However, diffraction peaks from the cubic $Gd_{0.2}Ce_{0.8}O_{2-\delta}$ become sharp compared with those found in the pattern of LSC-GDC particles before sintering. Given that the sintering was conducted at 1000˚C, it is expected that the high temperature drove the growth of GDC nanocrystals. Apart from these two phases that already existed in the core-shell particles, new phases also formed during the SPS process. Diffraction peaks derived from CoO with a cubic crystal (*space group*: Fm-3m) and $La_{2-x}Sr_xCoO_4$ can be identified from the XRD pattern of the sintered pellet. Since $(La_{0.6}Sr_{0.4})_{0.99}CoO_3$ provided the sole source of Co, the newly formed CoO phase must come from the decomposition of $(La_{0.6}Sr_{0.4})_{0.99}CoO_3$. $La_{2-x}Sr_xCoO_4$ was the other decomposition product which is known as a layered perovskite oxide and adopts the K_2NiF_4-type structure composed of [CoO6] corner-shared layers separated by pairs of (La,Sr)O layers [23]. Variation on the levels of Sr doping can cause a structural distortion of $La_{2-x}Sr_xCoO_4$ from the

orthorhombic (x = 0) to the tetragonal (x = 1), and their reflections in XRD are very similar and are thus rather difficult to be distinguished. From the viewpoint of application of the material as an electrode in an SOFC or SOEC, the decomposition is not adverse since the oxygen surface exchange rate would be remarkably increased at the heterogeneous interface between $La_{2-x}Sr_xCoO_4$ and $La_{1-x}Sr_xCoO_3$ [24]. The phase stability of doped lanthanum cobaltites is sensitive to the stoichiometric composition, temperature and partial oxygen pressure [25]. By in-situ X-ray diffraction, previous research [26] determined the influence of oxygen partial pressure on the phase stability and found that in 10^{-4} and 10^{-5} atm oxygen the $La_{0.6}Sr_{0.4}CoO_3$ started to decompose to CoO and $LaSrCoO_4$ at 1000 ˚C and 950 ˚C respectively, and the new phases were kept while cooling down to room temperature. In the current case, the chamber was kept in a constant vacuum condition corresponding to 1.3 x 10^{-5} atm oxygen during the entire SPS process. Under such a low oxygen partial pressure, the $(La_{0.6}Sr_{0.4})_{0.99}CoO_3$ would therefore decompose after the temperature exceeded the critical limit (ca. 950 ˚C [26]). The two new phases were also found stable to persist until the ambient temperature. In addition, peaks corresponding to $SrCO_3$ also can be found in the XRD pattern, which might come from complex reactions during the sintering.

The XRD characterization was also conducted on powders obtained by grinding the pellet densified by conventional sintering in air (see **Fig. 3b**). Only the two phases, rhombohedral LSC and cubic GDC were observed, indicating that they were preserved from the hydrothermally synthesized core-shell particles to the sintered composite. Similar to the case in the SPS, the GDC nanocrystals grew during the sintering process, which results in sharp diffraction peaks in the pattern of the sintered pellet compared with the broad ones in that of LSC-GDC core-shell particles before sintering. In contrast, the LSC seemed phase stable in the applied conditions of the conventional sintering, as no peaks derived from a new crystallite phase appeared in the XRD pattern after conventional sintering. **Fig. S6** in supporting information presents details on fitting peaks to the standard in the database.

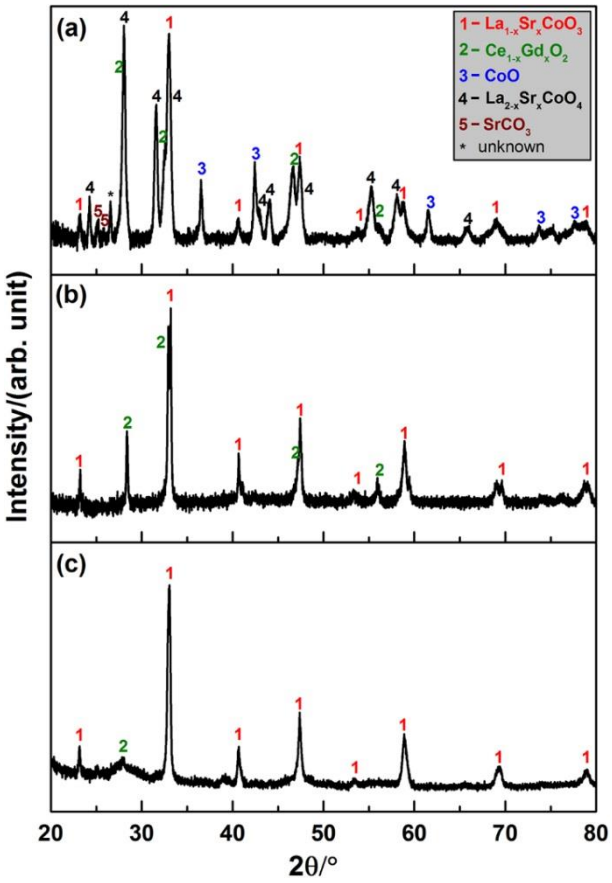

Figure 3. Powder X-ray diffraction patterns of (**a**) LSC-GDC composite densified by SPS of core-shell particles, (**b**) LSC-GDC composite densified by conventional sintering of core-shell particles, and (**c**) LSC-GDC core-shell particles before sintering.

3.2.2 Microstructure

SEM-BSE images on the polished cross sections of the samples densified by SPS and conventional sintering are presented in **Fig. 4a** and **Fig. 4c** respectively. The SPS-densified sample exhibited a much finer microstructure compared with the sample obtained by conventional sintering.

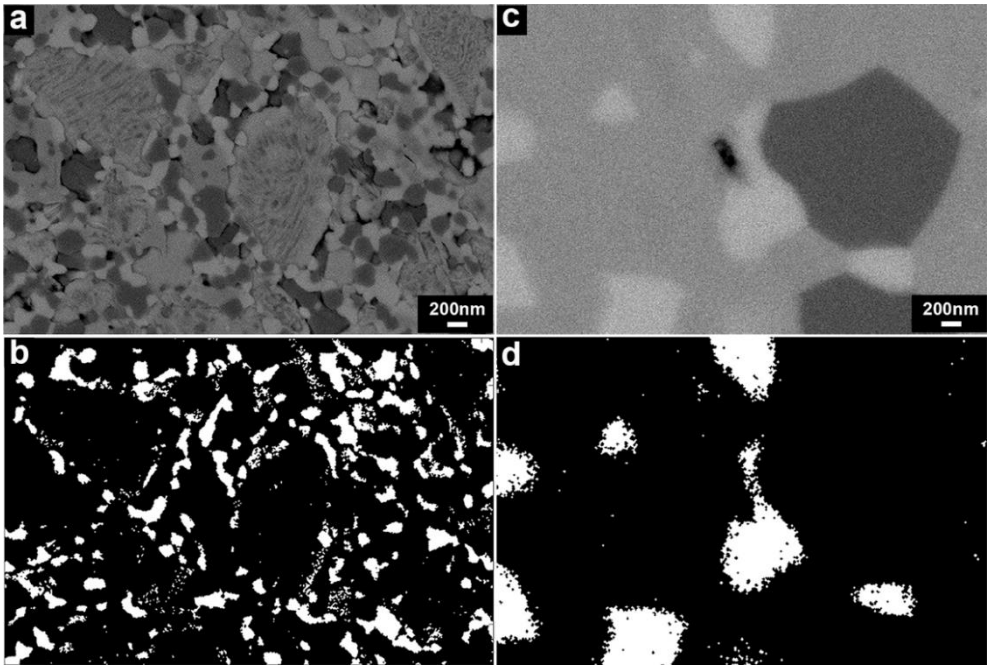

Figure 4. (**a**) An SEM-BSE image of the polished cross section of LSC-GDC densified by spark plasma sintering. (**b**) Segmentation of the GDC phase observed in (**a**). (**c**) An SEM-BSE image of the polished cross section of LSC-GDC densified by conventional sintering. (**d**) Segmentation of the GDC phase observed in (**c**).

The LSC-GDC composite densified by SPS was nearly dense as very few pores could be observed. Three phases of different contrasts (i.e., three scales of grey) could be identified in the SEM-BSE image (**Fig. 4a**). To determine the composition of the three phases EDS was conducted and the distribution of elements was mapped (**Fig.5**). Seen from **Fig. 5**, the brightest phase observed in **Fig. 4a** had high concentrations of Ce and Gd, while high concentrations of La, Sr and Co were found in the slightly darker grey phase. The darkest grey areas appeared to be corresponded to two different compositions, one composed of La, Co and the other enriched in Sr, indicating that Sr was segregated from the others after sintering. When comparing the element maps with the XRD results, it can be concluded that in **Fig. 4a** the brightest grey phase was GDC, while the others that are darker grey were the LSC and its localized decomposition products. In addition, the GDC phase distinguished by the contrast was located in the microstructure (**Fig. 4a**) of the LSC-GDC composite by means of image segmentation, as an example presented in **Fig. 4b**. Analysis of 10 segmentation images showed that the mean grain size of GDC was 87(±7) nm after densification by SPS (the other

images and details on the image segmentation and on the grain size analysis are given in supporting information). Comparing the size of GDC grains in the densified sample (mean diameter = 87(±7) nm) and the size of GDC particles in the shell of initial LSC-GDC core-shell particles (mean diameter = 6(±1) nm) shows that the GDC coarsened during the SPS sintering, as also concluded from the XRD analysis. In the SPS-densified sample, most of the GDC phase was still distributed around the LSC and its decomposition products (**Fig. 4b**), which means that the core-shell structure of the initial powders was partly preserved in the dense sample. However, the connectivity of the GDC phase was decreased which might be due to the shrinkage of the GDC phase during sintering and the consumption of neighboring GDC during the GDC grain coarsening.

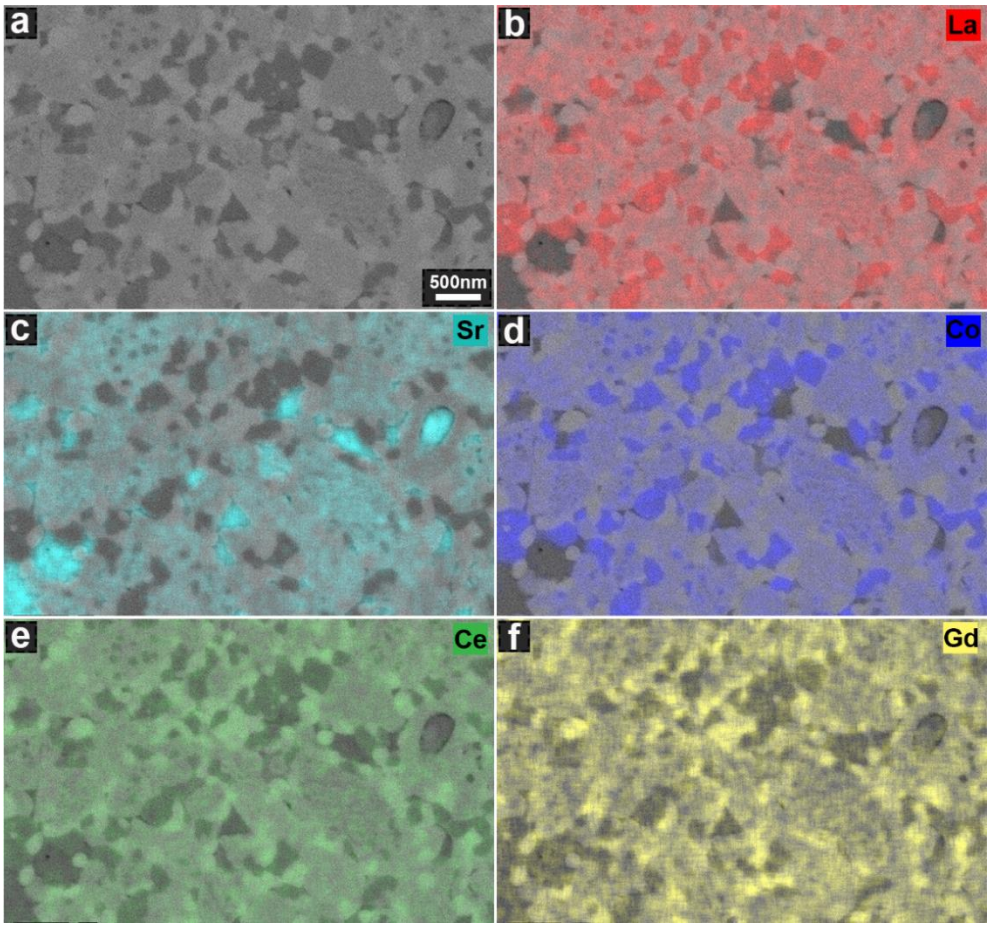

Figure 5. (**a**) SEM-BSE image of the cross section of the LSC-GDC composite densified by SPS recorded with a primary energy of 5 kV. (**b**-**f**) SEM-EDS elemental maps of La L, Sr L, Co L, Ce L and Gd M.

The microstructure of the LSC-GDC sample densified by conventional sintering also exhibited three phases that are distinguishable by the contrast (**Fig. 4c**). Compositional analysis described by the line distribution of elements obtained from SEM-EDS (**Fig. 6**) indicates that compositions of Ce and Gd peaked at the brightest grey phase, similar to the observation in the microstructure of the SPS-densified sample. In comparison, the darker grey phases had relatively high concentrations of La, Sr and Co. Moreover, the darkest grey phase was highly concentrated in Co, indicating that the chemical composition of the LSC varied during the sintering process. The Co-rich phase was also reported for the LSC-GDC composite samples obtained by conventional mixing of LSC and GDC powders and sintering in air [27]. However, the depletion and enrichment of Co from the original LSC perovskite phase possibly did not result in phase transitions, since within the XRD detection limit only diffraction peaks derived from LSC and GDC were observed in the pattern (**Fig. 3c**). A comparison between the XRD and the EDS results therefore indicates that the brightest grey phase was GDC, while the darker grey phases were LSC of different elemental compositions. Similarly, the GDC was located by means of segmentation of the microstructure of the LSC-GDC sample (**Fig. 4c**) sintered conventionally, exemplarily shown in **Fig. 4d**. Analysis of 8 segmented images gave a mean GDC grain size of 384(±78) nm. Compared with those in the microstructure of the SPS-densified sample (mean grain size = 87(±7) nm), the GDC grains were coarser and are more isolated from each other.

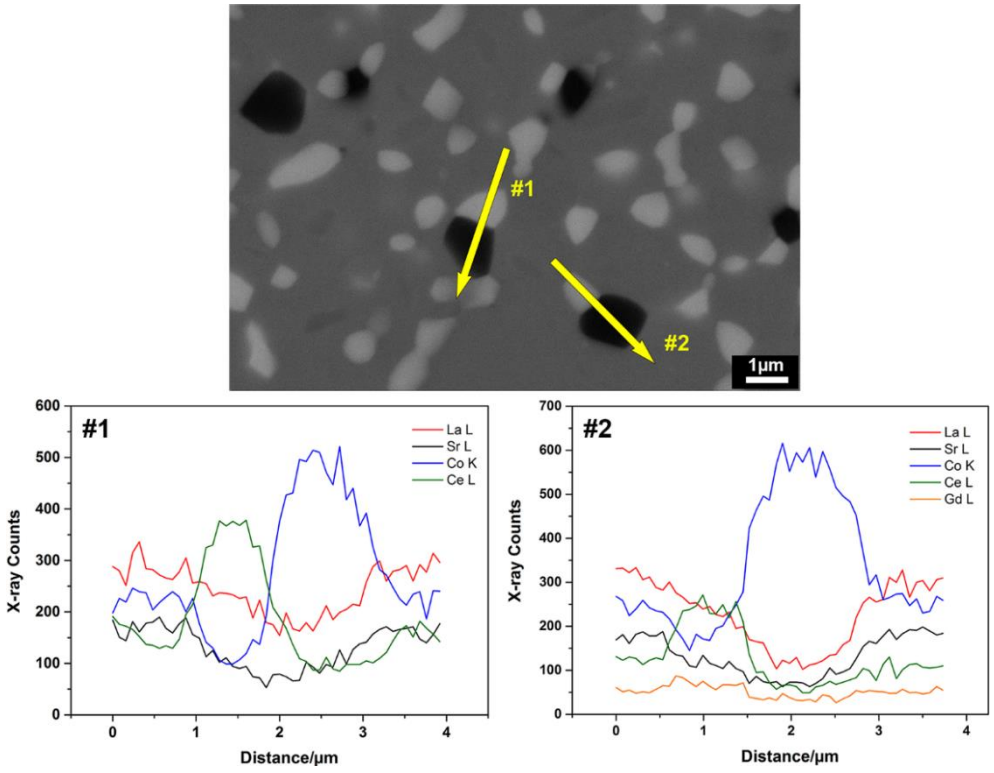

Figure 6. A SEM-BSE image of the polished cross-section of the LSC-GDC sample by conventional sintering recorded with at primary energy of 15 kV, and SEM EDS element line distributions along two selected directions as indicated.

As described above, the two sintered LSC-GDC samples displayed different microstructures. Given that the same LSC-GDC core-shell particles were used as a starting point, possible effects of initial particle morphology, size distribution or agglomeration state on the final microstructure can be excluded. The different sintering conditions alone can explain the differences in the final microstructure. In general, sintering is defined as a process where interparticle pores are removed by thermally activated atomic diffusions. Two competing processes, densification and coarsening, occur in a sintering process [28], and it is known that the coarsening should be suppressed if a ceramic body with a high density is targeted. Both LSC-GDC samples densified by SPS and conventional sintering displayed dense microstructures, indicating that the densification process was completed by both sintering methods. In principle, nanoparticles display a higher sinterability, because the driving force for densification is usually enhanced due to the high surface energy, fast atomic diffusion and large curvature [29]. In the initial stage of sintering LSC-GDC core-shell particles,

the particles contacted with each other by the shell that was composed of large amounts of GDC nanoparticles, which resulted in a large driving force for densification. On the other hand, the grain coarsening commonly observed in powder sintering was also found, especially for GDC grains that derived from GDC nanoparticles of the initial core-shell particles. However, when looking at the GDC grains in the final microstructures, they were finer in the SPS-densified sample than in the conventionally sintered sample. In addition, the size of GDC grains was more homogeneous in the SPS-densified sample (standard deviation of mean grain size = 7 nm) whereas it varied largely in the conventionally sintered sample (standard deviation of mean grain size = 78 nm). This indicates that the coarsening was more pronounced in the conventional sintering process compared with the SPS, which can be due to the higher sintering temperature (1250 °C compared to 1000 °C for SPS) and long stay in the high temperature range (6 h compared to 6 min for SPS) that were applied in the conventional sintering process. The diffusion mechanism of the grain coarsening is by Ostwald ripening [30], meaning that the growth of bigger GDC grains would come at a cost of consuming the neighboring small GDC grains. This possibly explains the reduced percolation of GDC grains after sintering in both cases and that GDC grains were more isolated in the conventionally sintered composite than in the SPS-densified composite.

To summarize, for both sintering methods, the LSC-GDC core-shell particles were sintered into nearly fully dense composites. By using SPS, it was possible to realize a fine structure with GDC nano grains, and to preserve the original prearranged core-shell structure partially in the final densified composite. However, the low oxygen partial pressure during the SPS caused the decomposition of LSC and resulted in formation of new crystallite phases. In comparison, conventional sintering of LSC-GDC core-shell particles conducted at different conditions resulted in a coarse microstructure, where pronounced GDC grain growth was observed.

4. Conclusion

$(La_{0.6}Sr_{0.4})_{0.99}CoO_3$- $Gd_{0.2}Ce_{0.8}O_{2-\delta}$ particles with a core-shell structure were prepared by precipitating $Gd_{0.2}Ce_{0.8}O_{2-\delta}$ nanoparticles on the surface of $(La_{0.6}Sr_{0.4})_{0.99}CoO_3$ particles. The integral shell, composed of ~6 nm large $Gd_{0.2}Ce_{0.8}O_{2-\delta}$ nanoparticles, was prepared under a mild hydrothermal condition at 100 ˚C. The microstructural evolution of core-shell particles was investigated under two different sintering conditions (spark plasma sintering and conventional sintering). In both cases, nearly fully dense composites were obtained. It was found that a fine microstructure containing nanograins was obtained by spark plasma sintering, as well as the graded core-shell architecture was partially maintained. Phase transitions of $(La_{0.6}Sr_{0.4})_{0.99}CoO_3$ under the low oxygen partial pressure during spark plasma sintering resulted in the formation of $La_{2-x}SrCoO_4$, which however is not necessarily adverse for application in oxygen transport membranes or solid oxide cells. In comparison, the grain coarsening process was more pronounced when the core-shell particles were densified by conventional sintering. As a result, coarse grains were found and the core-shell structure was lost in the final microstructure of the composite sintered conventionally.

Supporting Information

1. Details on the commercial $(La_{0.6}Sr_{0.4})_{0.99}CoO_3$ powder used as the core material

According to the information from the provider (Kusaka Rare Metal Products), the commercial $(La_{0.6}Sr_{0.4})_{0.99}CoO_3$ (LSC) powders were produced by the organic acid complex method in following steps (refer to http://www.kc-kusaka.co.jp/works/chemicals/oxides/): (1) dissolve or disperse the metal carbonates or metal hydroxides in water, (2) form precursors by adding organic acids, for instance, citric acid, malic acid etc., (3) dry and calcine the precursors, (4) mill the products into powders of a desired size. Before preparing core-shell particles, the laser diffraction measurement was used to analyze the particle size distribution of the as-obtained commercial LSC powders. The

result is presented in **Fig. S1**. The quantification range was from 0.04 µm to 2000 µm, and D10, D50 and D90 were 0.178 µm, 0.388 µm and 1.255 µm respectively.

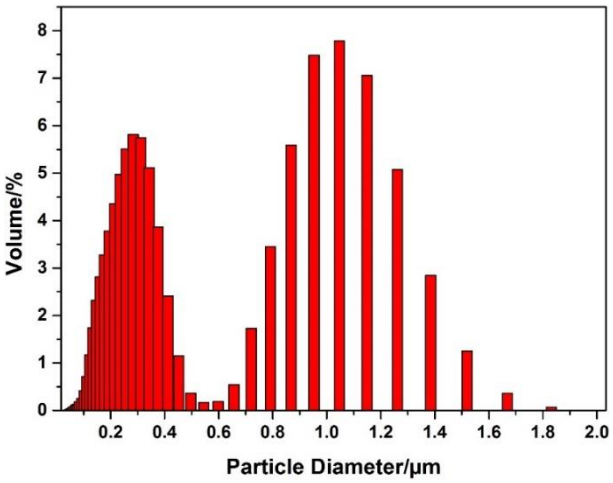

Figure S1. Particle size distribution of the commercial $(La_{0.6}Sr_{0.4})_{0.99}CoO_3$ powder.

2. Details on the densification process by spark plasma sintering and by conventional sintering

Profiles of the spark plasma sintering process are presented in **Fig. S2**. The electric current, the temperature, the applied pressure and the displacement were recorded simultaneously during the sintering process. The programmed temperature profile during the conventional sintering in a muffle furnace is presented in **Fig. S3**.

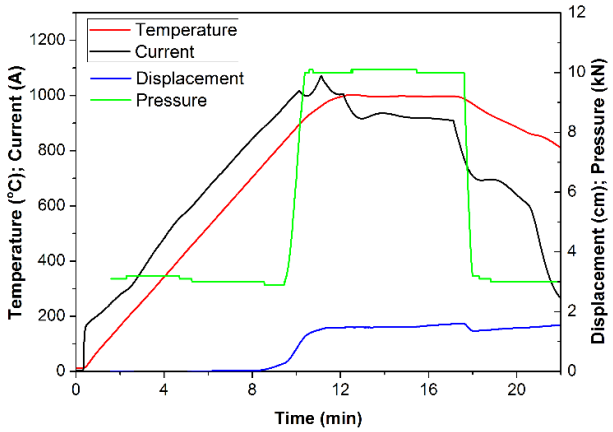

Figure S2. Profiles of the spark plasma sintering of core-shell particles.

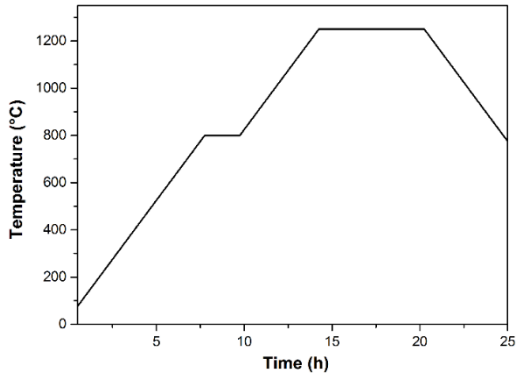

Figure S3. The programmed temperature profile of the conventional sintering of core-shell particles.

3. Rietveld refinement

The refinement was conducted by using the FullProf Suite. The structure of the $(La_{0.6}Sr_{0.4})_{0.99}CoO_3$ in the commercial powder as well as in the LSC-GDC core-shell powder was refined in the R-3c space group. The structure of the $Gd_{0.2}Ce_{0.8}O_{2-\delta}$ in the LSC-GDC core-shell powder was refined in the Fm-3m space group. The peak shape of $(La_{0.6}Sr_{0.4})_{0.99}CoO_3$ in both powder diffraction patterns was described by the Cauchy's integral formulation of the Lorentzian function, while the peak shape of $Gd_{0.2}Ce_{0.8}O_{2-\delta}$ was described by the Thompson-Cox-Hasting formulation of the pseudo-Voigt function. The scale factor, the zero point, and the unit cell parameters were refined. Considering the small size of $Gd_{0.2}Ce_{0.8}O_{2-\delta}$ particles (ca. 6 nm), the peak broadening was assumed to arise purely from the particle size, whereas the strain contribution as well as the instrumental contribution were neglected. The Rietveld refinement residuals are shown in tables below.

Table S1. Rietveld refinement residuals of the diffraction pattern of the raw commercial $(La_{0.6}Sr_{0.4})_{0.99}CoO_3$ powder

Number of Bragg peaks	32
Number of data points	11432
Total number of parameters	13
R_{Bragg}	1.862%
R_F	1.889%
Unit cell	a=b=5.4348Å, c=13.2257Å
χ^2	1.10

Table S2. Rietveld refinement residuals of the diffraction pattern of the $(La_{0.6}Sr_{0.4})_{0.99}CoO_3$-$Gd_{0.2}Ce_{0.8}O_{2-\delta}$ core-shell powder

Phase	$(La_{0.6}Sr_{0.4})_{0.99}CoO_3$	$Gd_{0.2}Ce_{0.8}O_{2-\delta}$
Number of Bragg peaks	32	9
Number of data points	7266	
Total number of parameters	15	
R_{Bragg}	4.153%	8.731%
R_F	4.716%	4.908%
Unit cell	a=b=5.4337Å, c=13.2260Å	a=b=c=5.4466Å
χ^2	1.51	

4. Additional bright-field TEM images of the $(La_{0.6}Sr_{0.4})_{0.99}CoO_3$-$Gd_{0.2}Ce_{0.8}O_{2-\delta}$ core-shell particle

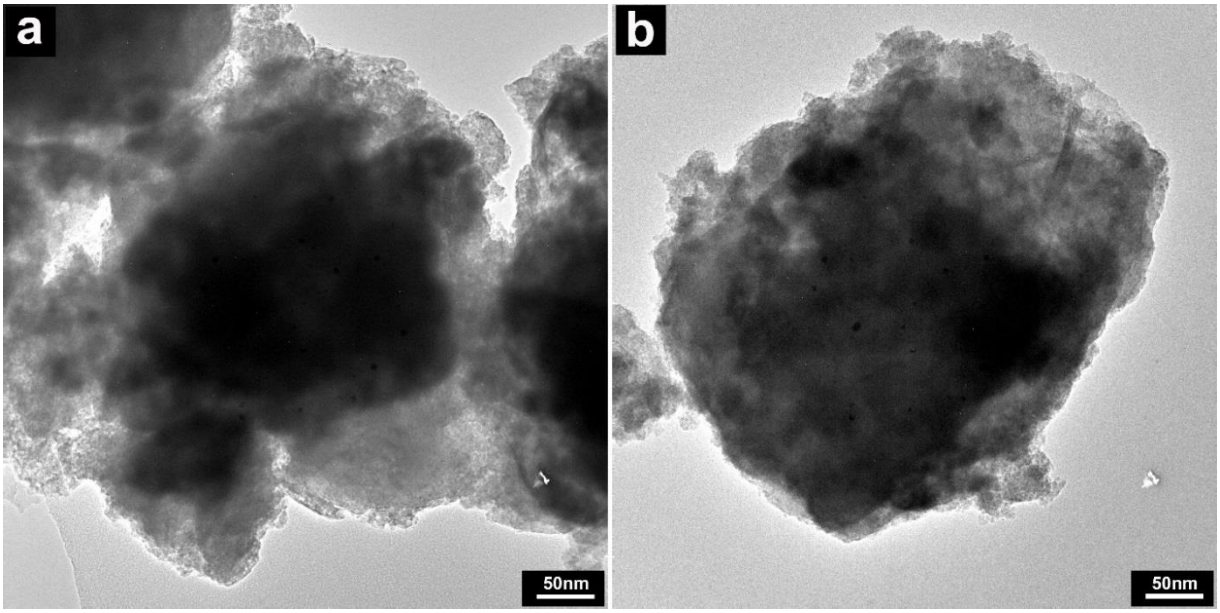

Figure S4. Two additional BF-TEM images of two other core-shell particles.

5. An example on the fast Fourier transform (FFT) of a high-resolution image of the $Gd_{0.2}Ce_{0.8}O_{2-\delta}$ shell

The fast Fourier transform (FFT) of a high-resolution image of the $Gd_{0.2}Ce_{0.8}O_{2-\delta}$ shell was processed by the Digital Micrograph, shown in **Fig. S5**. Then radiuses of three concentric rings were measured separately. By the reciprocal conversion, measured spacings of the corresponding crystal planes were 1/3.17 (= 3.1 Å), 1/3.69 (= 2.7 Å) and 1/5.28 (= 1.9 Å) separately, which can be assigned to (111), (200) and (220) planes of a $Gd_{0.2}Ce_{0.8}O_{2-\delta}$ crystal.

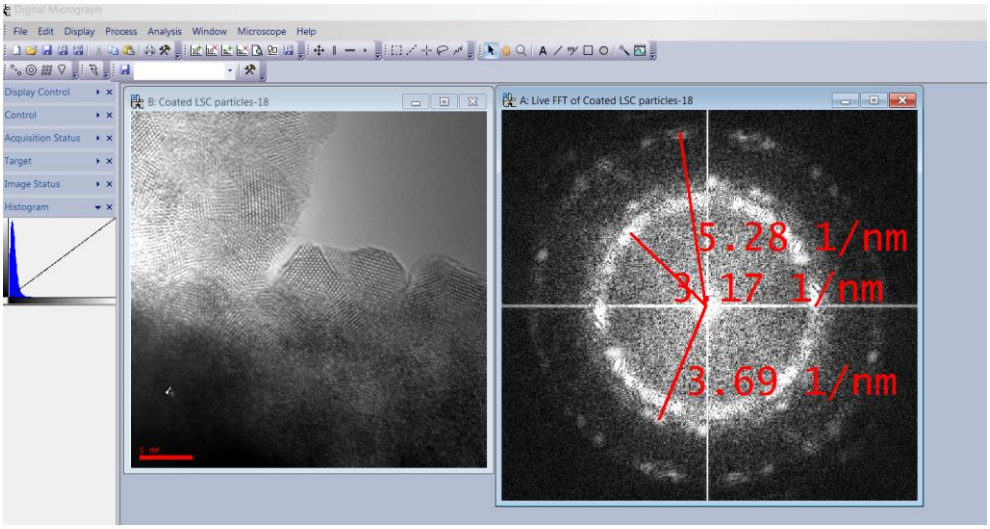

Figure S5. A screenshot presenting the FFT of a high-resolution image of the $Gd_{0.2}Ce_{0.8}O_{2-\delta}$ shell and measurements of distances from rings to the concentric center under the reciprocal space; the FFT was done by the Digital Micrograph; the scale bar in the high-resolution TEM image is 5 nm.

6. Peak fittings of the XRD pattern of the SPS-densified composite

Fig. S6 provides screenshots of the peak fittings of the XRD pattern (using divergent slit size, background subtracted) of the SPS-densified composite to standard patterns in the ICSD database. As observed, all peaks were well fitted to peaks in the stated standard pattern of a certain phase. The two layered double perovskite $La_{2-x}Sr_xCoO_4$ phases (tetragonal and orthorhombic) have similar reflections especially in the low Bragg angle range, and standard patterns of both phases fit well to the experimental pattern, making it is very difficult to separate the two phases barely by XRD.

Nevertheless, the decomposition of $La_{1-x}Sr_xCoO_3$ to the $La_{2-x}Sr_xCoO_4$ during the SPS process was certain, whereas the exact composition of the $La_{2-x}Sr_xCoO_4$ needed to be analyzed by other methods, for example, EDS.

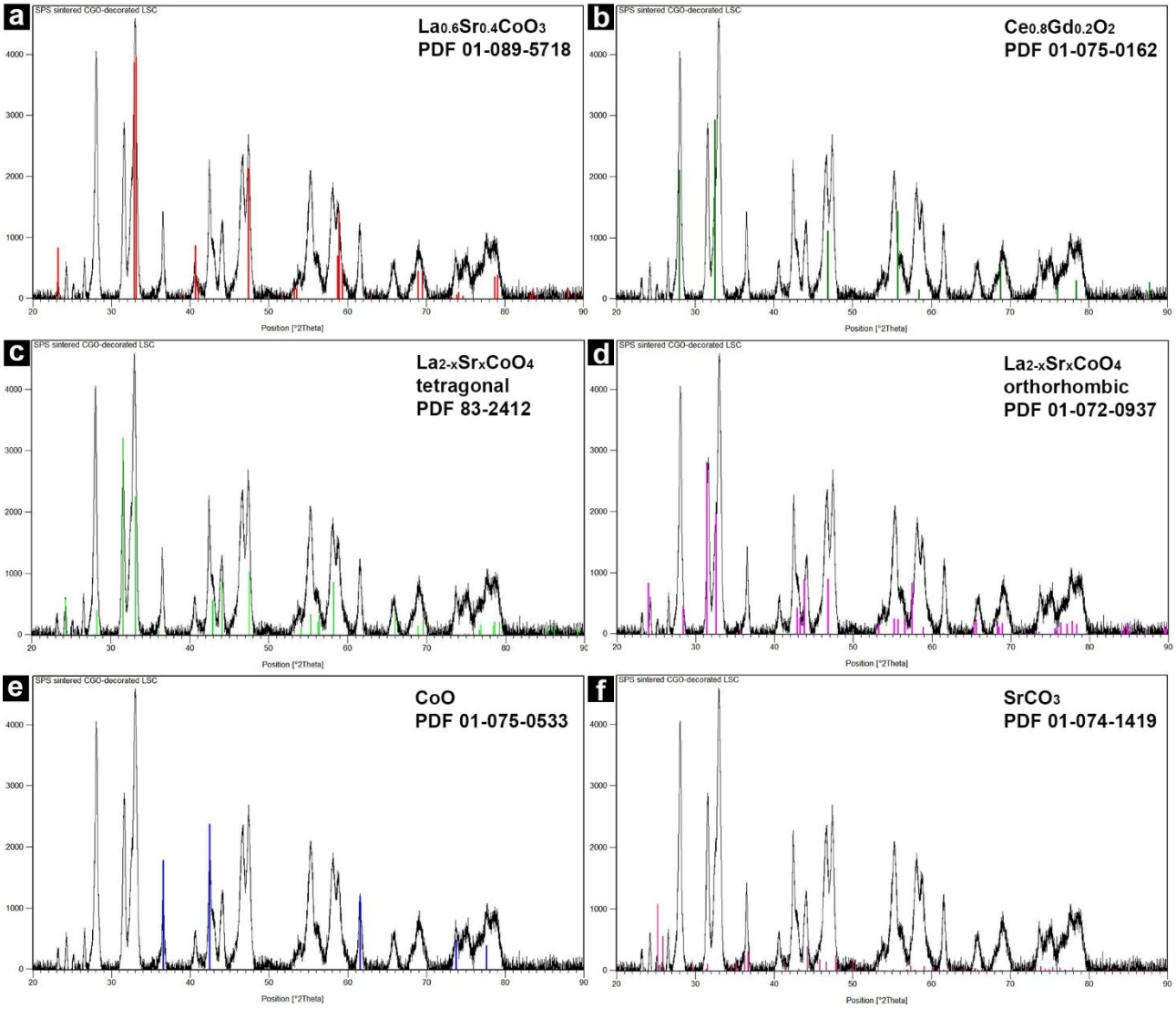

Figure S6. Screenshots of the XRD peak fittings in the software, 2θ = 20-90°. (**a**) $(La_{0.6}Sr_{0.4})CoO_3$ (*space group* R-3c, *PDF* 01-089-5718); (**b**) $Ce_{0.8}Gd_{0.2}O_{1.9}$ (*space group* Fm-3m, *PDF* 01-075-0162); (**c**) and (**d**) correspond to the tetragonal (x=1, *space group* I4/mmm, *PDF* 83-2412) and the orthorhombic (x=0, *space group* Abma, *PDF* 01-072-0937) $La_{2-x}Sr_xCoO_4$; (**e**) CoO (*space group* Fm-3m, *PDF* 01-075-0533) and (**f**) $SrCO_3$ (*space group* Pnma, *PDF* 01-074-1419).

7. Details on analysis of SEM images by the software ThreshAlyzer

ThreshAlyzer is a software based on MATLAB that is designed to analyze the phase distribution in SEM images of polished cross sections. **Fig. S7** presents a screenshot of the window of the software. The input of a SEM image gave a histogram of the intensity. By setting a threshold, the phases displaying a contrast/greyscale higher and lower than the threshold were separated in the final segmentation image (used in the main text). The threshold was adjusted until the final segmentation of phases matched what was seen in images by eyes. The output was the final segmentation image, the phase fractions, the equivalent grain diameter/size and the covered volume ratio of grains with the corresponding size.

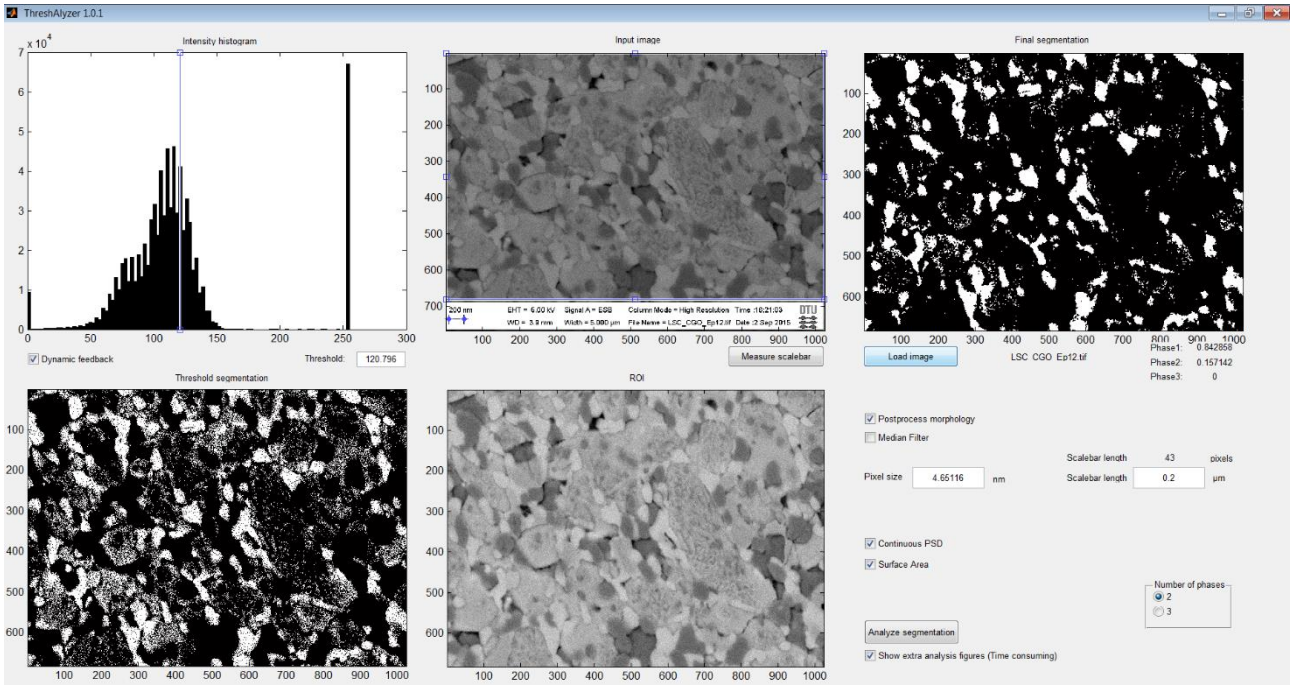

Figure S7. A screenshot of the window of the ThreshAlyzer with an example; from left to right, top: intensity histogram, input image and measure scale bar, and final segmentation; bottom: threshold segmentation, ROI (region of interest) for smaller area analysis, and toggles.

An example on output from analyzing a SEM-BSE image of the SPS-densified LSC-GDC sample by the ThreshAlyzer is presented in **Fig. S8**. By setting a reasonable threshold value, the white GDC phases were isolated from the others (LSC and its decomposition products that displayed in the

darker). The borders were outlined in **Fig. S8b**. The final segmentation highlighting the distribution of GDC grains (in the white) and grains of LSC and its decomposition products (as a whole in the black) is presented in **Fig. S8c**. The grain size and the covered volume ratio of grains at the size were also given in the output, as presented in **Fig. S8d** (GDC grains) and **Fig. S8e** (grains of LSC and its decomposition products).

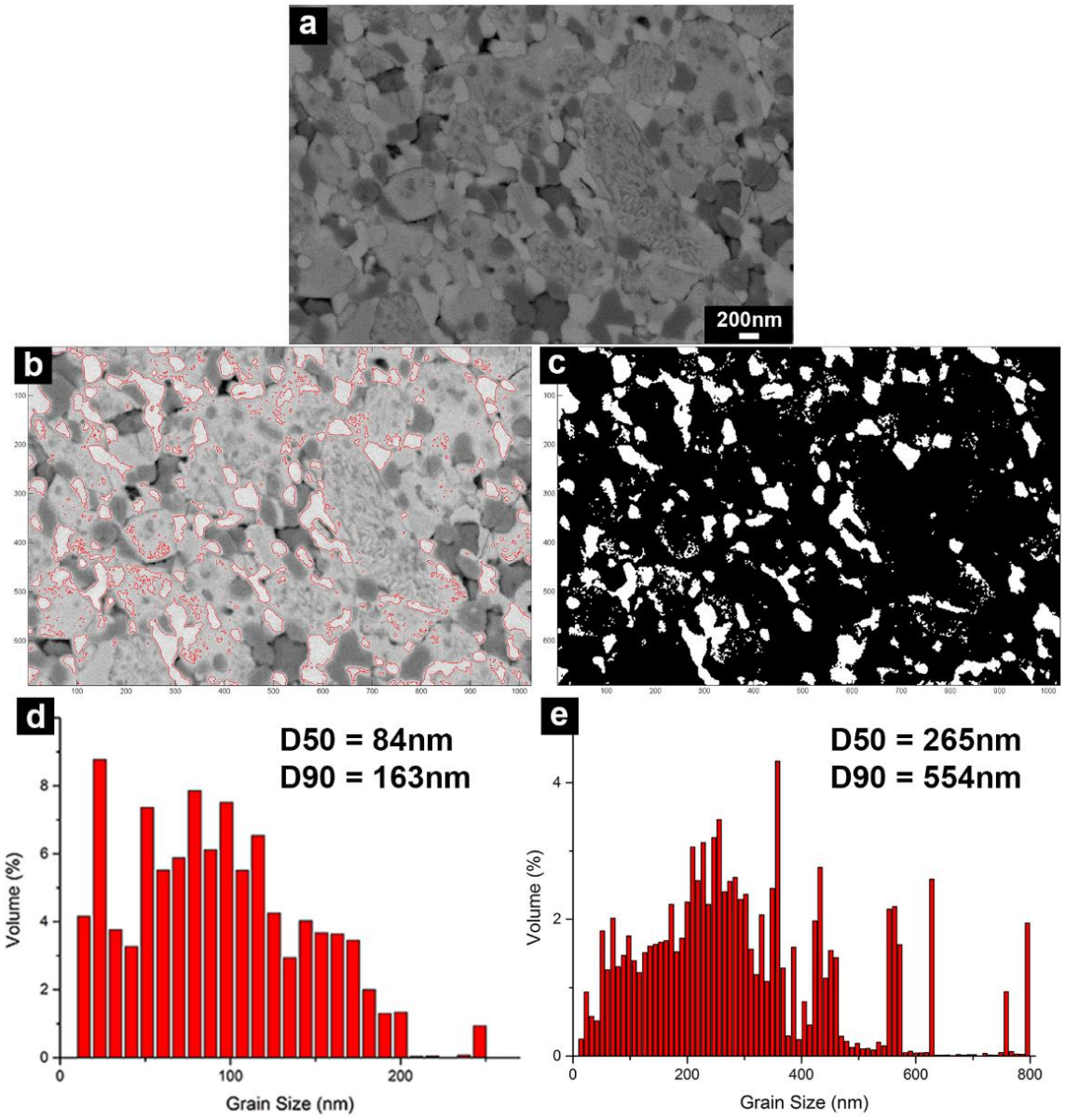

Figure S8. (**a**) A SEM-BSE image of the polished cross section of the sample of spark plasma sintered LSC-GDC core-shell particles. (**b**) The border of the white GDC grains is outlined after setting a threshold in the intensity histogram, which can be used as a guide to evaluate the reasonability of the threshold setting values. (**c**) The final segmentation of the SEM-

BSE image, where the GDC grains are highlighted among the others. (**d**) and (**e**) present the histograms of 'grain size vs. covered volume ratio' for GDC grains and grains of LSC and decomposition products; D50 and D90 mean a cumulative 50 vol% and 90 vol% point of diameter respectively.

10 SEM-BSE images from different places of the polished cross section of the SPS-densified sample were analyzed. Results of D50 and D90 for all grains are presented in **Table S3**. A statistical quantification shows that 50 vol% of GDC grains were below 87(±7) nm, while 50 vol% of grains of LSC and its decomposition products were below 274(±31) nm. It needs to be mentioned that the boundary of grains of LSC and decompositions was not clear in the segmentation, which results in a slightly higher uncertainty in the size quantification of grains. Nevertheless, the D50 (274 nm) of grains of LSC and decompositions in the SPS-densified sample was close to the D50 (388 nm) of the commercial LSC particle measured by the laser diffraction, which supports the argument that the spark plasma sintering is advantageous for maintaining the original metrics of starting powders.

The output also gave an area ratio of the white phase (GDC) and the black phase (LSC and decomposition products), which was used to estimate the volume ratio of the phases in the SPS-densified sample. On average, the quantification gave a volume ratio of two phases at V[GDC]/V[LSC and decompositions] at 17.2/82.8. In comparison, the molar ratio of GDC to LSC in core-shell particles before sintering was 1:4. The density of $La_{0.6}Sr_{0.4}CoO_3$ and $Gd_{0.2}Ce_{0.8}O_{2-\delta}$ is 6.274 g cm^{-3} (N. Orlovskaya, et al., *J. Eur. Ceram. Soc.*, vol20, 2000, p51) and 7.2 g cm^{-3} (https://en.wikipedia.org/wiki/Cerium(IV)_oxide) respectively. Assuming that the sample was fully dense, the theoretical calculation gave a volume ratio of V[GDC]/V[LSC and decompositions] at 14.5/85.5. The measured and the theoretical values match each other well.

Table S3. A summary of the D50 and D90 for all grains by analyzing 10 SEM-BSE images of the polished cross section of the SPS-densified LSC-GDC sample

	grains of GDC		**grains of LSC and decompositions**	
	D50/nm	**D90/nm**	**D50/nm**	**D90/nm**
	103	196	353	547
	93	181	274	554
	84	163	265	554
	88	158	247	470
	81	175	241	414
	88	163	256	479
	82	142	294	482
	88	144	284	442
	84	135	253	428
	79	135	274	526
Average	**87**	**160**	**274**	**489**
SD	7	18	31	50

The same analysis was also conducted for the SEM-BSE images of the polished cross section of the sample densified by conventional sintering of LSC-GDC core-shell particles. In total, 8 SEM-BSE images were analyzed. The results of D50 and D90 of GDC grains are summarized in **Table S4**. The quantification of the size of grains of LSC is not reported here, as the boundary of the grains could not be determined in the image segmentations. 50 vol% of the GDC grains were less than

384(±78) nm, showing a remarkable coarsening of grains during the conventional sintering. The measured volume ratio of V[GDC]/V[LSC and Co-rich phases] was 11.7/88.3.

Table S4. A summary of the D50 and D90 for GDC grains by analyzing 8 SEM-BSE images of the polished cross section of the LSC-GDC sample densified by conventional sintering

	D50/nm	**D90/nm**
	400	758
	217	449
	424	758
	320	680
	403	672
	500	833
	405	730
	404	673
Average	**384**	**694**
SD	78	106

8. Point EDS analysis on the polished cross section of the sample densified by spark plasma sintering

At an accelerating voltage of 10 kV, EDS analysis was conducted on several selected points (**Fig. S9**) on the polished cross section of the SPS-densified sample. It should be noted that the quantification was processed by the embedded ESPRIT Quant Tools for standardless quantitative spectra evaluation and was solely based on data derived from spectra themselves. Nevertheless, the difference of compositions (shown in **Table S5**) at selected points of each greyscale provided a

fingerprint to cross check results obtained from the element mapping. The black phase showed a relatively high concentration of La, Co and especially Sr, whereas the white was highly concentrated in Ce and Gd. The ratio of La, Sr and Co determined in the grey phase was more or less close to the stoichiometric value in the raw LSC powder.

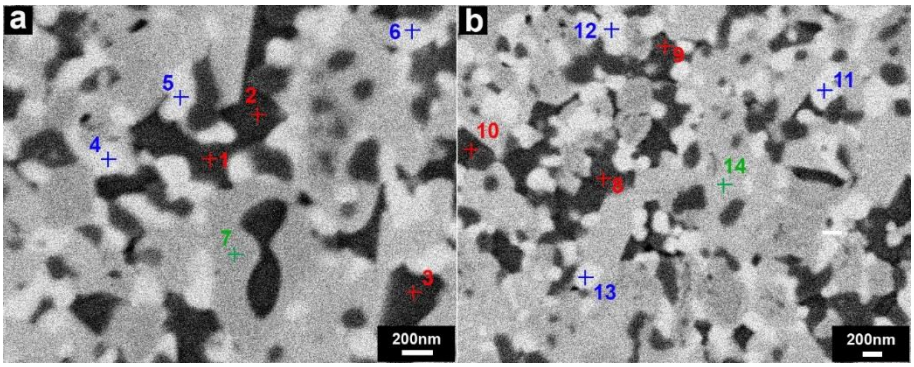

Figure S9. SEM-BSE images of two areas on the polished cross section of the SPS-densified sample; all selected points for EDS analysis are labeled by cross lines.

Table S5. Chemical compositions determined by the point EDS analysis (unit: atomic percent)

	Point	La	Sr	Co	Ce	Gd
Black	#1	20.01	49.36	14.41	16.22	0
	#2	27.99	47.29	14.84	9.57	0.30
	#3	9.40	54.82	17.80	16.85	1.13
	#8	9.44	67.06	11.46	12.04	0
	#9	16.35	40.39	17.78	25.48	0
	#10	11.75	27.62	27.11	14.99	3.42
White	#4	23.61	11.17	7.54	46.82	10.86
	#5	18.50	12.36	11.33	46.38	11.43
	#6	25.12	16.55	10.14	41.67	6.52

	#11	18.53	8.60	8.64	54.50	9.74
	#12	16.07	17.03	11.44	46.21	9.25
	#13	14.80	3.77	28.00	44.10	9.33
Grey	#7	34.67	20.42	25.12	18.11	1.68
	#14	44.33	20.18	19.73	11.85	3.92

9. Element mapping by EDS on the polished cross section of the LSC-GDC sample densified by the conventional sintering

Fig. S10 presents a mapping of La L (**b**), Co K (**c**) and Ce L (**d**) on the polished cross section (**a**) of the sample densified by conventional sintering of LSC-GDC core-shell particles. As observed, the black phase was enriched in Co, while the white phase had a high concentration of Ce. Dopants including Sr and Gd are not presented here, as they were not depleted from the doped phases, as demonstrated by the element line-scan analysis shown in the main text.

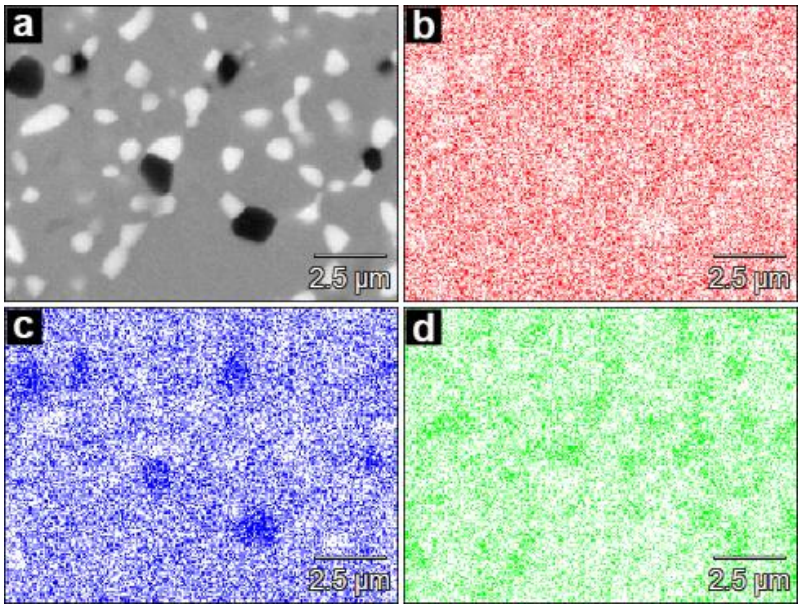

Figure S10. (**a**) A SEM-BSE image of the polished cross section of the LSC-GDC sample densified by conventional sintering. (**b**), (**c**) and (**d**) are element maps of La Lα, Co Kα and Ce Lα, respectively.

9. Additional microscopy images of the samples densified by SPS and conventional sintering

Fig. S11 presents SEM-BSE microscopy images of three additional areas for each sample, **a**-**c** are from the SPS-densified sample and **d**-**e** are from the conventionally sintered sample. A finer structure can be observed in the SPS-densified sample.

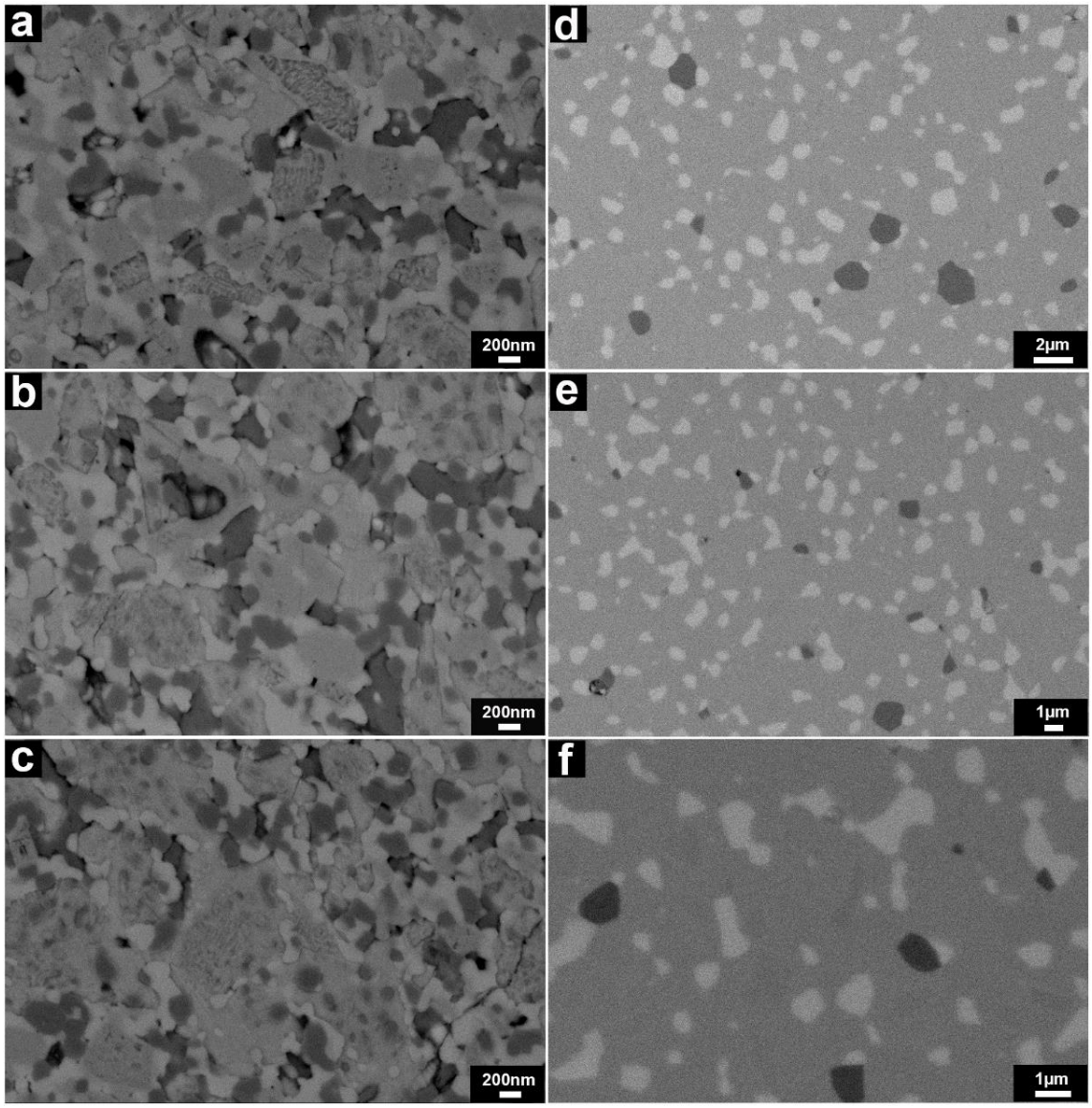

Figure S11. a-**c** (scale bar 200 nm) are three independent areas of the SPS-densified sample, and **d**-**e** (scale bar 1 µm, 1 µm and 2 µm separately) are three independent areas of the sample densified by the conventional sintering. All images were recorded by processing BSEs.

Figure S12 presents microscopy images of the fracture surface of the samples densified by SPS (**a**, **b**) and the conventional sintering (**c**, **d**).

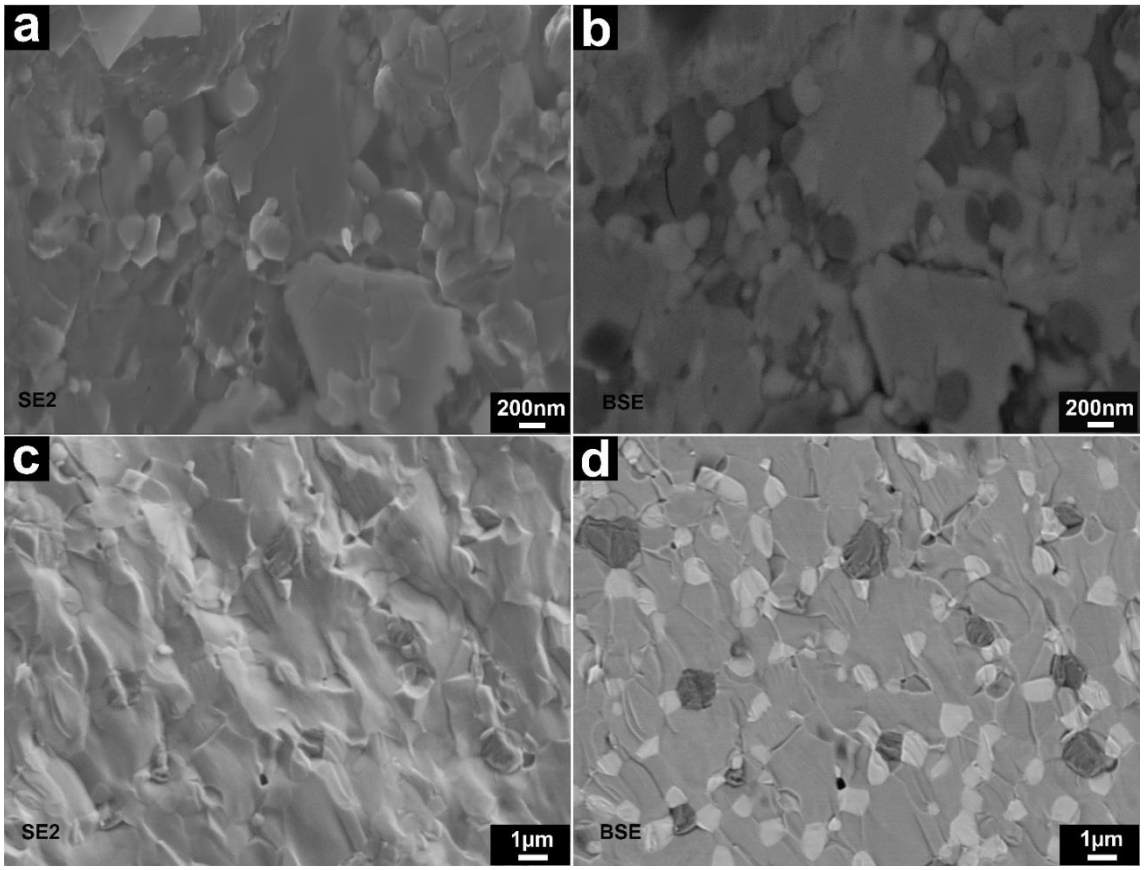

Figure S12. Fracture surface of the samples densified by SPS (**a**, **b**) and by conventional sintering (**c**, **d**). For each selected area, SE2 and BSE images were recorded simultaneously.

References

[1] W. Schärtl, Current directions in core-shell nanoparticle design, Nanoscale. 2 (2010) 829–843. doi:10.1039/c0nr00028k.

[2] S. Wei, Q. Wang, J. Zhu, L. Sun, H. Lin, Z. Guo, Multifunctional composite core-shell nanoparticles, Nanoscale. 3 (2011) 4474–502. doi:10.1039/c1nr11000d.

[3] R. Ghosh Chaudhuri, S. Paria, Core/shell nanoparticles: classes, properties, synthesis mechanisms, characterization, and applications, Chem. Rev. 112 (2012) 2373–433. doi:10.1021/cr100449n.

[4] Z. Jiang, C. Xia, F. Chen, Nano-structured composite cathodes for intermediate-temperature solid oxide fuel cells via an infiltration/impregnation technique, Electrochim. Acta. 55 (2010) 3595–3605. doi:10.1016/j.electacta.2010.02.019.

[5] A. Manthiram, J.-H. Kim, Y.N. Kim, K.-T. Lee, Crystal chemistry and properties of mixed ionic-electronic conductors, J. Electroceramics. 27 (2011) 93–107. doi:10.1007/s10832-011-9635-x.

[6] S.D. Ebbesen, S.H. Jensen, A. Hauch, M.B. Mogensen, High temperature electrolysis in alkaline cells, solid proton conducting cells, and solid oxide cells, Chem. Rev. 114 (2014) 10697–10734. doi:10.1021/cr5000865.

[7] P.-L. Chen, I.-W. Chen, Grain growth in CeO2: Dopant effects, defect mechanism, and solute drag, J. Am. Ceram. Soc. 79 (1996) 1793–1800. doi:10.1111/j.1151-2916.1996.tb07997.x.

[8] P. Datta, Doped ceria based solid oxide fuel cell electrolytes and their sintering aspects: An overview, Mater. Sci. Forum. 835 (2016) 199–236. doi:10.4028/www.scientific.net/MSF.624.109.

[9] C. Sun, R. Hui, J. Roller, Cathode materials for solid oxide fuel cells: A review, J. Solid State Electrochem. 14 (2009) 1125–1144. doi:10.1007/s10008-009-0932-0.

[10] S. Fang, C. Chen, L. Winnubst, Effect of microstructure and catalyst coating on the oxygen permeability of a novel CO2-resistant composite membrane, Solid State Ionics. 190 (2011) 46–52. doi:10.1016/j.ssi.2011.03.009.

[11] J.H. Joo, K.S. Yun, J.H. Kim, Y. Lee, C.Y. Yoo, J.H. Yu, Substantial oxygen flux in dual-phase membrane of ceria and pure electronic conductor by tailoring the surface, ACS Appl. Mater. Interfaces. 7 (2015) 14699–14707. doi:10.1021/acsami.5b03392.

[12] M. Ibáñez, R. Zamani, S. Gorsse, J. Fan, S. Ortega, D. Cadavid, J.R. Morante, J. Arbiol, A. Cabot, Core-shell nanoparticles as building blocks for the bottom-up production of functional nanocomposites: PbTe-PbS thermoelectric properties, ACS Nano. 7 (2013) 2573–2586. doi:10.1021/nn305971v.

[13] C. Hu, Y. Liu, P. Liu, W. Zhang, J. Zhu, Microwave dielectric properties of (1-x)SiO2-xTiO2 composite ceramics derived from core-shell structured microspheres, Mater. Res. Bull. 53 (2014) 54–57. doi:10.1016/j.materresbull.2014.01.016.

[14] B. Mojić-Lanté, J. Vukmirović, K.P. Giannakopoulos, D. Gautam, A. Kukovecz, V. V. Srdić, Influence of synthesis conditions on formation of core-shell titanate-ferrite particles and processing of composite ceramics, Ceram. Int. 41 (2015) 1437–1445. doi:10.1016/j.ceramint.2014.09.076.

[15] M. Suárez, A. Fernández, J.L. Menéndez, R. Torrecillas, H.U. Kessel, J. Hennicke, R. Kirchner, T. Kessel, Challenges and Opportunities for Spark Plasma Sintering : A Key Technology for a New Generation of Materials, in: Sinter. Appl., InTech, 2013: pp. 319–342. doi:10.5772/53706.

[16] Z.A. Munir, U. Anselmi-Tamburini, M. Ohyanagi, The effect of electric field and pressure on the synthesis and consolidation of materials: A review of the spark plasma sintering method, J. Mater. Sci. 41 (2006) 763–777. doi:10.1007/s10853-006-6555-2.

[17] M.T. Buscaglia, M. Viviani, Z. Zhao, V. Buscaglia, P. Nanni, Synthesis of BaTiO3 core-shell particles and fabrication of dielectric ceramics with local graded structure, Chem. Mater. 18 (2006) 4002–4010. doi:10.1021/cm060403j.

[18] B. Basu, T. Venkateswaran, D.Y. Kim, Microstructure and properties of spark plasma-sintered ZrO2-ZrB2 nanoceramic composites, J. Am. Ceram. Soc. 89 (2006) 2405–2412. doi:10.1111/j.1551-2916.2006.01083.x.

[19] J. Rodríguez-Carvajal, Recent advances in magnetic structure determination by neutron powder diffraction, Phys. B Condens. Matter. 192 (1993) 55–69. doi:10.1016/0921-4526(93)90108-I.

[20] L.J. Cote, A.S. Teja, A.P. Wilkinson, Z.J. Zhang, Continuous hydrothermal synthesis of CoFe2O4 nanoparticles, Fluid Phase Equilib. 210 (2003) 307–317. doi:10.1016/S0378-3812(03)00168-7.

[21] R.P. Sear, The non-classical nucleation of crystals: microscopic mechanisms and applications to molecular crystals, ice and calcium carbonate, Int. Mater. Rev. 57 (2012) 328–356. doi:10.1179/1743280411Y.0000000015.

[22] R.P. Sear, Quantitative studies of crystal nucleation at constant supersaturation: experimental data and models, CrystEngComm. 16 (2014) 6506–6522. doi:10.1039/C4CE00344F.

[23] C. Tealdi, C. Ferrara, P. Mustarelli, M.S. Islam, Vacancy and interstitial oxide ion migration in heavily doped La2−xSrxCoO4±δ, J. Mater. Chem. 22 (2012) 8969–8975. doi:10.1039/c2jm30769c.

[24] M. Sase, F. Hermes, K. Yashiro, K. Sato, J. Mizusaki, T. Kawada, N. Sakai, H. Yokokawa, Enhancement of oxygen surface exchange at the hetero-interface of (La,Sr)CoO3/(La,Sr)2CoO4 with PLD-layered films, J Electrochem Soc. 155 (2008) B793--B797. doi:10.1149/1.2928612.

[25] A.N. Petrov, V.A. Cherepanov, A.Y. Zuev, Thermodynamics, defect structure, and charge transfer in doped lanthanum cobaltites: an overview, J. Solid State Electrochem. 10 (2006) 517–537. doi:10.1007/s10008-006-0124-0.

[26] J. Ovenstone, J.S. White, S.T. Misture, Phase transitions and phase decomposition of La1−xSrxCoO3−δ in low oxygen partial pressures, J. Power Sources. 181 (2008) 56–61. doi:10.1016/j.jpowsour.2008.03.033.

[27] A.J. Samson, M. Søgaard, P.V. Hendriksen, (Ce,Gd)O2-δ-based dual phase membranes for oxygen separation, J. Memb. Sci. 470 (2014) 178–188. doi:10.1016/j.memsci.2014.07.028.

[28] I.-W. Chen, X.-H. Wang, Sintering dense nanocrystalline ceramics without final-stage grain growth, Nature. 404 (2000) 168–171. doi:10.1038/35004548.

[29] J. Rufner, D. Anderson, K. Van Benthem, R.H.R. Castro, Synthesis and sintering behavior of ultrafine (<10 nm) magnesium aluminate spinel nanoparticles, J. Am. Ceram. Soc. 96 (2013) 2077–2085. doi:10.1111/jace.12342.

[30] U. Anselmi-Tamburini, J.E. Garay, Z.A. Munir, Fast low-temperature consolidation of bulk nanometric ceramic materials, Scr. Mater. 54 (2006) 823–828. doi:10.1016/j.scriptamat.2005.11.015.

Chapter VI. Continuous hydrothermal flow synthesis of $LaCrO_3$ in supercritical water and its application in dual-phase oxygen transport membranes

This chapter contains the manuscript 'Continuous Hydrothermal Flow Synthesis of $LaCrO_3$ in Supercritical Water and Its Application in Dual-Phase Oxygen Transport Membranes' that is ready for submission.

$LaCrO_3$ sub-micron particles (cube-shaped, 639 nm in edge size) were prepared by CHFS in supercritical water. A continuous production of phase-pure $LaCrO_3$ particles was achieved for the first time, at 410 °C and 28 MPa, with a reaction time as short as 23 s, which remarkably increases the throughput in comparison with conventional hydrothermal batch-type synthesis. On basis of the results obtained by varying reaction conditions, a reaction mechanism for the formation of $LaCrO_3$ in a CHFS process was suggested.

In addition, results of a collaborative effort between the PhD student and the second author are presented. The synthesized $LaCrO_3$ particles were used to prepare $Sc_{0.10}Y_{0.01}Zr_{0.89}O_{2-\delta}$ – $LaCrO_3$ dual-phase oxygen transport membranes. A density of ~ 90 % was achieved after sintering at 1400 °C. Oxygen permeation fluxes of up to 5×10^{-8} mol cm^{-2} s^{-1} were obtained with a 1-mm thick membrane tested in air/N_2 at 900 °C. Given that CHFS is relatively easy to scale up, a rapid, large-scale production of fine $LaCrO_3$ particles can be achieved. To improve membrane performances, it is of interest to prepare doped $LaCrO_3$ with a higher electric conductivity.

Continuous Hydrothermal Flow Synthesis of $LaCrO_3$ in Supercritical Water and Its Application in Dual-Phase Oxygen Transport Membranes

Yu Xu *, Stéven Pirou, Philipp Zielke, Søren Bredmose Simonsen, Poul Norby, Peter Vang Hendriksen, Ragnar Kiebach

Department of Energy Conversion and Storage, Technical University of Denmark (Risø Campus), Frederiksborgvej 399, 4000 Roskilde, Denmark

* Correspondence: Y. Xu, Tel.: +45 93511148, Fax: +45 46775688, Email: yuax@dtu.dk

Abstract

The continuous production of sub-micron $LaCrO_3$ particles (average edge size 639 nm, cube-shaped) by continuous hydrothermal flow synthesis using the supercritical water is reported for the first time. By varying the reaction conditions, it was possible to suggest a reaction mechanism for the formation of this perovskite material. Moreover, dual-phase oxygen transport membranes were manufactured from the synthesized $LaCrO_3$ particles and $(ZrO_2)_{0.89}(Y_2O_3)_{0.01}(Sc_2O_3)_{0.10}$ (10Sc1YSZ). A density of ~90 % was achieved after sintering at 1400 °C. Oxygen permeation fluxes up to 5×10^{-8} mol cm^{-2} s^{-1} were measured on a 1-mm thick membrane.

Keywords: continuous flow synthesis; hydrothermal; supercritical water; perovskite; lanthanum chromite; oxygen transport membrane

1. Introduction

$LaCrO_3$-based oxides have been in the focus of research due to their interesting physicochemical properties, making them suitable for broad range of applications, e.g., as magnetic materials [1,2] or as material for *p*-type transparent conducting oxide films [3]. Utilizing the electrical conductivity [4] deriving from a dynamic valence change of lattice Cr cations or introduced via divalent dopants, $LaCrO_3$-based materials can also be used as catalysts towards CO oxidation and hydrocarbon combustion [5–7], electrochemical gas sensors [8,9], electrodes and interconnect materials [10,11]

in solid oxide fuel cells (SOFCs), and as the electronic conducting phase in dual-phase oxygen transport membranes (OTMs) [12].

Particularly for the last application, in OTMs this class of materials is of interest, because of its chemical stability towards gas impurities (e.g., CO_2 and SO_2) and reducing atmospheres [12,13]. OTMs are able to provide oxygen of high purity (>99 %) for a wide range of applications, such as biomass gasification, oxy-fired cement production and oxy-fuel combustion [14]. With a driving force created by a difference of oxygen partial pressures p_{O2} on the two sides of the membrane, dense ceramic OTMs consisting of ionic and electronic conductors allow simultaneous transports of oxygen ions and electrons in opposite directions, producing a flux of pure oxygen. In dual-phase OTMs, composites of an ionic-conductive material and an electronic-conductive material are used. Doped zirconia, for instance, $(Sc_2O_3)_x(Y_2O_3)_y(ZrO_2)_{1-x-y}$, is a very good ionic conductor (an ionic conductivity 0.12 S cm^{-1} at 850 °C for 10Sc1YSZ, x = 0.10, y = 0.01) [15].

To implement $LaCrO_3$ in the above-mentioned applications, a reliable, controllable and preferably scalable synthesis method is desired to prepare $LaCrO_3$-based oxide particles. Moreover, reducing the size of particles to the submicron- or nano-meter regime will facilitate sintering of $LaCrO_3$, which usually requires high temperatures (~1600 °C for $LaCrO_3$ to get >90 % of the theoretical maximum density [16]). Similar to other lanthanide-transition metal complex oxides, $LaCrO_3$-based oxides can be prepared by conventional high-temperature (typically > 1000 ˚C) solid-state reactions among stoichiometric amounts of simple oxides/carbonates [11]. Although the method is mature, it is a rather timely process and often the as-prepared powders contain impurities, have compositional deviations and display wide size distributions. Among the alternative synthesis approaches, the hydrothermal route is appealing because particles can be obtained directly without any post treatments. Moreover, hydrothermal synthesis is advantageous for controlling the composition, phase and size distribution of particles and is environmentally benign as water is used as the reaction medium. Hydrothermal synthesis of phase-pure $LaCrO_3$ particles was first realized at a temperature higher than 700 ˚C under a pressure of 100 MPa in an autoclave [17]. Later, it was brought to mild

hydrothermal conditions [18–23] in which lower temperatures (425 – 260 ˚C) and autogenous pressures were used. However, the productivity is rather limited by the fixed and usually small capacity of the autoclave accommodating the synthesis, and reaction periods of up to several days to complete the crystallization are required.

To overcome these limitations of batch syntheses routes, continuous hydrothermal flow synthesis (CHFS) [24] is employed in this work. Here, a continuous production of materials is achieved in a flow-type apparatus (CHFS reactor). This type of reactors usually contains a mixer, where a constantly fed room-temperature precursor flow is mixed with a flow of supercritical water (scH_2O, T_C ≥ 374 ˚C, p_C ≥ 22.1 MPa) and is thereby rapidly heated to the (near-) supercritical state. Since the properties of water drastically change near the critical point, the solvent power of water and the hydrothermal reaction rate vary significantly [25]. A high degree of supersaturation is generated in a very short time and nucleation almost starts instantaneously upon mixing. Therefore, the scH_2O provides an ideal reaction environment for hydrothermal synthesis particularly of nanomaterials.

The preparation of several nanomaterials by CHFS has been reported on a laboratory scale, including oxides [26–28], metals [29], sulfides [30] and metal organic frame works (MOFs) [31], and the upscaling ability of CHFS to an industrial scale has been shown for several compounds [32,33]. The here employed reactor is a two-stage CHFS reactor recently designed and installed within the project *ProEco* (www.proeco.dk), to synthesize oxide nanoparticles (such as NiO, $Y_xZr_{1-x}O_{2-\delta}$, $Gd_xCe_{1-x}O_{2-\delta}$, and lanthanide-transition metal perovskites) for applications in electrochemical devices [34]. Compared with the CHFS of simple oxides, there are rather few reports on the one-step continuous synthesis of complex lanthanide-transition metal oxides ($La_{n+1}Ni_nO_{3n+1}$ after post heat treatment [35], $La_{1-x}Sr_xMnO_3$ [36], and La_2CuO_4 [37]).

In this work, the synthesis of $LaCrO_3$ particles by CHFS in scH_2O is reported for the first time, and a mechanism for the formation of the $LaCrO_3$ particles is suggested. The synthesized powders were used to manufacture a set of small planar OTMs. Here, the powders were sintered with 10Sc1YSZ

powders at a temperature as low as 1400 °C, and the resulting dense dual-phase membranes were characterized in terms of microstructure and oxygen permeability.

2. Experimental

2.1 Materials

The 0.1 mol L^{-1} (combined La^{3+} and Cr^{3+} concentration) reactant solution was prepared by dissolving as-bought $La(NO_3)_3 \cdot 6H_2O$ (0.05 mol L^{-1}, Sigma Aldrich, ≥ 99.0 %) and $Cr(NO_3)_3 \cdot 9H_2O$ (0.05 mol L^{-1}, Sigma Aldrich, ≥ 99.0 %) in deionized H_2O (DI H_2O). KOH solutions of various concentrations (0.5, 1, 2, 4 and 6 mol L^{-1}) were prepared by dissolving the corresponding amounts of KOH pellets (Sigma Aldrich, ≥ 85 %) in DI H_2O. Commercial 10Sc1YSZ powder ($(Sc_2O_3)_{0.10}(Y_2O_3)_{0.01}(ZrO_2)_{0.89}$, Daiichi Kigenso Kagaku Kogyo Co. Ldt., Japan) was used as the ionic-conductive material for preparing the dual-phase 10Sc1YSZ – $LaCrO_3$ OTMs.

2.2 Preparation of LaCrO3 by CHFS

The in-house developed two-stage CHFS reactor was used to conduct the synthesis. Details of the reactor can be found elsewhere [34] while a schematic description is presented in **Fig. 1**. Briefly, two mixers (stages) are integrated in series within the reactor. The first mixer with a co-flow pipe-in-pipe geometry was used to mix the scH_2O flow fed by a 1/16'' capillary pipe with the precursor flow fed from two side arms of a 1/4'' encapsulating pipe. The precursor was a pre-mixture of the reactant solution and the KOH solution, which were fed to the reactor by separate pumps, however mixed in a tee-junction prior to the first mixer. The downward outflow of the first mixer then went to the second mixer with a counter-flow geometry. In this work, only a small flow of DI H_2O was fed through the inlet of the second mixer to avoid sedimentation. The outflow of the second mixer then passed through a re-heater. The outflow of the re-heater was rapidly cooled down to the room temperature by a water-cooled tube-in-tube heat exchanger. After passing an in-line filter (Swagelok, 90-µm pore size), the product flow was depressurized to the atmospheric pressure by a backpressure regulator (Tescom, 26-1700 Series). Three thermocouples were inserted into the reactor, i.e. one to measure

the temperature (T_1) of the feeding scH_2O flow, one to measure the temperature (T_2) of the outflow of the second mixer and the third one to measure the temperature (T_3) of the outflow of the re-heater. The synthesized particles were harvested as slurries at the outlet of the reactor. All liquids were separately fed to the reactor by MILROYAL metering pumps. The flow rates of pumps were calibrated with DI H_2O before synthesis, and were kept constant (Q[scH_2O] = 35 mL min^{-1}, Q[reactant (aq)] = 10 mL min^{-1}, Q[KOH (aq)] = 10 mL min^{-1}, and Q[DI H_2O] = 10 mL min^{-1}). The pressure was controlled by the backpressure regulator at 28(±1) MPa throughout the entire synthesis. The variables for the experimental conditions for all syntheses are summarized in **Table 1**.

Table 1. An overview of the variables for the syntheses

Sample	$n[OH^-]$ / $n[Me^{3+}]$	(scH_2O flow) T_1/°C	(outflow of 2nd mixer) T_2/°C	(outflow of re-heater) T_3/°C
LC1	5	400	285	385
LC2	10	400	285	385
LC3	20	410	325	410
LC4	40	410	325	410
LC5	60	410	325	410

Notes: Me^{3+} represents the trivalent La and Cr cations; $n[OH^-]$ / $n[Me^{3+}]$ is the molar ratio between the OH^- and trivalent La and Cr cations when pre-mixing the reactant solution (containing La, Cr cations) and the KOH solution in the tee-junction before the first mixer.

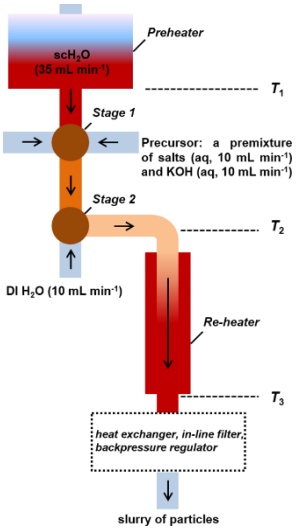

Figure 1. A schematic of the two-stage CHFS reactor. Arrows indicate the flow directions.

2.3 Preparation of 10Sc1YSZ – $LaCrO_3$ OTMs

Symmetrical membranes based on a dual-phase composite consisting of 10Sc1YSZ as the ionic conductor and $LaCrO_3$ as the electronic conductor were prepared and tested by oxygen permeation measurements. For the membranes, $LaCrO_3$ from sample LC5 was used because this was found to contain the purest $LaCrO_3$ as will be described in detail below. The commercial 10Sc1YSZ and the as-prepared $LaCrO_3$ (LC5) powders were blended in a 65 – 35 vol % ratio. A milling process by using an agate mortar was applied to mix the two powders homogeneously. Thereafter, 15 mm-diameter pellets were formed by die pressing at 1000 kg load and then isostatically pressed at 65,000 kg load. The dense membranes were obtained by sintering the green pellets at 1400 °C for 6 h in air (temperature ramp for both heating and cooling steps was 100 °C h^{-1}). The sample intended for the oxygen permeation measurement was polished down to 1-mm thick, and an ink made from $(La_{0.80}Sr_{0.20})MnO_{3-\delta}$ – $(Y_2O_3)_{0.08}(ZrO_2)_{0.92}$ (LSM – YSZ, 50 – 50 vol %) was applied by screen printing on both sides of the membranes to serve as oxygen redox catalyst. Prior to the measurement, the samples were heated to 980 °C for 2 h in air in order to sinter mildly the printed LSM – YSZ layers.

2.4 Characterization

Particles were separated from slurries using a centrifuge, then cleaned with DI H_2O and dried at ambient conditions. Powder X-ray diffraction patterns were obtained from the particles on a Bruker Robot D8 diffractometer (Cu Kα radiation 0.154 nm, 10 – 90° using a stepsize of 0.01°). Patterns were refined in the Rietveld method using the FullProf software suite [38]. Raman spectra of particles were recorded using a Renishaw inVia Reflex confocal Raman microscope. For the spectrum presented in this work, a 532-nm laser and 50X microscope objective was employed. The spectrum was averaged and background-corrected. For the TEM characterization, particles were re-dispersed in ethanol using an ultrasonic processor (Hielscher UP200St, Germany) and dripped onto a holey carbon film/Au grid. Bright field TEM (BF-TEM) imaging and selected area electron diffraction (SAED) were conducted by using a JEOL 3000F microscope operating at 300 kV with a field emission gun. Dark-field scanning transmission electron microscopy (DF-STEM) was carried out using the JEOL

3000F equipped with a STEM unit and a high angle annular dark field (HAADF) detector. The nominal probe size was 0.5 nm and the camera length was 12 cm. For compositional analysis, energy dispersive X-ray spectroscopy (EDS) was carried out using the equipped Oxford Instruments EDS detector and was processed by the INCA EDS analysis software (Oxford instruments). For SEM characterization, particles dispersed on carbon tapes were brought to a Zeiss Merlin equipped with a field emission gun operating at 10 kV. A high-efficiency secondary electron (HE-SE2) detector was used to record microscopy images. The size of particles was measured by the ImageJ software.

The sintered 10Sc1YSZ – $LaCrO_3$ pellet was cut, embedded in epoxy and then polished for SEM microstructure investigation of the cross section. The polished surface was coated by 10-nm carbon to increase the surface conductivity. With the field emission gun operating at 5 kV, a Zeiss Merlin SEM was used to observe the cross section. A high-efficiency secondary electron (HE-SE2) detector and an energy-selective backscattered electron (ES-BSE) detector were used to record images simultaneously at each selected area. The membrane with screen-printed LSM – YSZ catalyst layers heat-treated at 980 °C was cut and polished for SEM investigations of the cross section. The polished surface was coated by 10-nm carbon and was investigated by a Hitachi Tabletop TM3000 SEM (15 kV charge-reduction mode) using the equipped high-sensitivity semiconductor detector. The software ThreshAlyzer was used for image segmentation and statistic quantification of density. Membrane dimensions and $LaCrO_3$ grain sizes were measured by the ImageJ software.

2.5 Oxygen permeation measurements

Oxygen permeation measurements were conducted in an *Oxygen Membrane Rig* built at DTU Energy described elsewhere [39]. The sample was placed in-between two alumina tubes in the center of a height-adjustable tube furnace. Thermocouples were inserted into the alumina tubes and were in contact with the sample in order to monitor the temperature. Before the test, the sample was sealed to alumina tubes by tape-casted sodium aluminosilicate (NAS, Na_2O 17.8 mol %, Al_2O_3 9.4 mol % and SiO_2 72.8 mol% [40]) glass rings/gaskets with an inner diameter of 9 mm. The glass transition temperature of the rings/gaskets is 515 °C [39]. The side walls of the sample were also

coated with a NAS paste to ensure that no oxygen entered from the sweep gas compartment outside of the alumina tubes. The sample was heated to 940 °C in air and afterwards cooled to 750 °C to ensure a gas-tight seal. A gas chromatograph was connected to the outlet of the permeate side to quantify the oxygen leak into the permeate stream. Air was fed to the feed side with a continuous flow rate of 100 $mL_N\ min^{-1}$, while N_2 as a carrier gas was fed to the inlet of the permeate side with various flow rates from 20 $mL_N\ min^{-1}$ to 150 $mL_N\ min^{-1}$. The gas flow was controlled and monitored by a mass flow controller (Brooks). During the measurement, the oxygen flux was permeating across the sample due to the driving force created by the difference of p_{O2} between the feed (high p_{O2}) and permeate (low p_{O2}) side.

In-house built zirconia-based oxygen sensors were used to determine the p_{O2} of the gases at the inlet (prior to the sample) and at the outlet (after passing over the sample) of the permeate side.

The oxygen permeation flux was calculated following the **Eq. 1**,

$$J_{O_2} = (p''_{O_2}\, n'' - p'_{O_2}\, n') / A \qquad (\mathbf{1}),$$

where J_{O2} is the oxygen permeation flux, p_{O2}'' and p_{O2}' are oxygen partial pressures of the outlet and of the inlet gas, n'' and n' are molar flow rates of the outlet and of the inlet gas, respectively, at the permeate side and A (0.64 cm^2) is the net area of the sample exposed to gases.

The **Nernst Eq.** (**2**) was used to calculate the oxygen partial pressure from the measured sensor voltage V,

$$p_{O_2} = p_{O_2,ref} \exp(\frac{4F}{RT}\ V) \qquad (\mathbf{2}),$$

where V is the EMF (electro motive force) measured by the oxygen sensor, T is the temperature of the oxygen sensor and $p_{O2,ref}$ is the oxygen partial pressure at the reference electrode which was maintained at 0.21 atm throughout the measurement.

3. Results and Discussion

3.1 Continuous hydrothermal flow synthesis of $LaCrO_3$

Five groups of $LaCrO_3$ (LC1 – LC5) were synthesized under different synthesis conditions, as summarized in **Table 1**. LC1 and LC2 were prepared under conditions with relatively low pH (in precursors, molar ratios of KOH to [La^{3+}, Cr^{3+}] cations were 0.5/0.1 and 1.0/0.1 respectively) and low temperatures (T_1 = 400 °C, T_2 = 285 °C, T_3 = 385 °C). Characterization by XRD and TEM showed similar crystalline phases and particle morphologies for LC1 and LC2. The XRD pattern of LC1 is presented in **Fig. 2a**, and the diffraction peaks match well to those of the reference pattern of $La(OH)_3$ (ICSD *PDF* 01-075-1900, hexagonal structure). **Fig. 2b** presents a BF-TEM image of particles in LC1. Nanowires with a uniform diameter of around 22 nm and a length ranging from nanometers to submicronmeters were observed. The high-resolution TEM image (**Fig. 2c**) shows that the nanowires were well crystallized. The measured interplanar spacing (3.1 Å) is consistent with the distance of the (101) planes of a hexagonal $La(OH)_3$ crystal. Besides the $La(OH)_3$ nanowires, additional nanosized particulates with an irregular morphology can be found in **Fig. 2b** as agglomerates around the nanowires. The high-resolution TEM image of these irregular-shaped particles (**Fig. 2d**) does not show any periodic crystallographic features, indicating that these particles were amorphous and therefore did not create any diffraction peaks in the XRD pattern. EDS analysis indicated that the irregular-shaped particles were amorphous Cr compounds. In conclusion, $LaCrO_3$ was not formed under synthesis conditions used for LC1 or LC2. Instead, composites of well crystallized $La(OH)_3$ and amorphous Cr compounds were obtained.

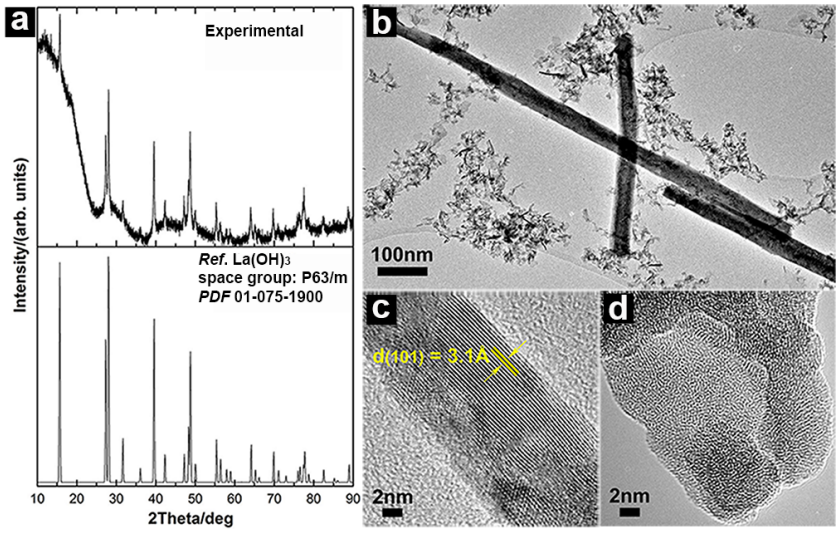

Figure 2. (**a**) XRD pattern and (**b**) BF-TEM image of LC1 particles; HR-TEM images of the nanowire (**c**) and of the irregular-shaped particles (**d**) observed in (**b**).

In principle, the presence of soluble and reactive hydrated complexes of both lanthanide cations Ln^{3+} and transition metal cations Me^{3+} in aqueous solutions is necessary to initiate the formation of $LnMeO_3$ [41] through the hydrothermal route. Aqueous La^{3+} would be readily subject to hydration after being mixed with a strong alkaline solution (KOH in this case), forming $La(OH)_3$. However, $La(OH)_3$ has a nearly negligible solubility similar to other lanthanide trihydroxides [41] and is very stable at an ambient temperature [42]. As temperature increases, however, a more soluble and reactive LaOOH will be formed as a dehydration product. Previous research [43] using high-temperature XRD showed that $La(OH)_3$ is stable below 420 °C while LaOOH is present at temperatures in-between 380 – 580 °C. It is therefore reasonably to assume that by mixing the nitrates solution and KOH solution in the tee-junction before the first mixer, $La(OH)_3$ was formed instantly in the precursor, which further crystallized in the form of nanowires when heated by the scH_2O (at the first mixer/stage) due to the anisotropic crystal growth governed by its inherent crystal structure [44]. In comparison, Cr_2O_3 is known for its amphoteric behavior. The solubility of $Cr(OH)_3$ is pronouncedly enhanced at increased pH values, and can be increased by i) using an alkaline solution of a higher concentration, and ii) increasing the temperature [41,45]. It is known that in a typical hydrothermal process, the crystallization of an oxide usually follows a dissolution-precipitation

mechanism [20]. The presence of amorphous Cr compounds possibly indicates that the solubility of Cr-hydrated complexes was rather low at the applied synthesis conditions of LC1 and LC2. In summary, due to the absence of i) LaOOH (depending on the reaction temperature) and/or ii) soluble Cr-hydrated complexes, i.e. $[Cr(OH)_4]^-$ in alkaline aqueous solutions [45] (depending on the concentration of KOH), $LaCrO_3$ was not formed.

Synthesis conditions were modified by increasing both the reaction temperature and the concentration of KOH solutions (LC3, LC4 and LC5 in **Table 1**). Results of the identified crystalline phases and morphology from the XRD and TEM characterization of LC3 and LC4 particles are summarized in **Fig. 3**. The main peaks in the diffraction patterns of both LC3 (**Fig. 3a**) and LC4 (**Fig. 3c**) match well with the diffraction peaks of $LaCrO_3$ with an orthorhombic structure (ICSD *PDF* 01-070-2694), suggesting the presence of well-crystallized $LaCrO_3$. However, additional diffraction peaks corresponding to $La(OH)_3$ (ICSD *PDF* 01-075-1900) indicate that $La(OH)_3$ was present as a second phase. Refinements on the experimental patterns (see details in Supplementary information) gave phase compositions of 7.1 wt% $La(OH)_3$ and 92.9 wt% $LaCrO_3$ in LC3, and 6.6 wt% $La(OH)_3$ and 93.4 wt% $LaCrO_3$ in LC4. Both LC3 (**Fig. 3b**) and LC4 (**Fig. 3d**) particles exhibited a very different morphology in comparison to the particles found in LC1 and LC2 (**Fig. 2b**). Most particles found in LC3 and LC4 displayed a cube-like shape (square projections in BF-TEM images). The average edge size of these $LaCrO_3$ particles was 652 nm and 770 nm in LC3 (**Fig. 3b**) and LC4 (**Fig. 3d**), respectively. In addition, nanowires and irregular-shaped agglomerates (similar to the observation in **Fig. 2b**), identified as $La(OH)_3$ and amorphous Cr compounds, were also observed around the cube-like particles as minor phases in LC3 and LC4.

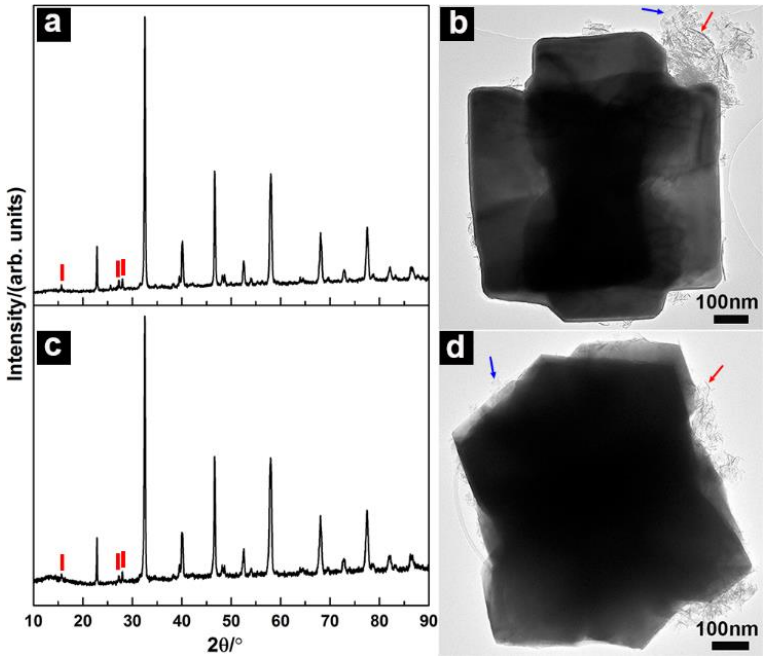

Figure 3. XRD patterns of (**a**) LC3 and (**c**) LC4 particles; the main peaks correspond to $LaCrO_3$ (*space group*: Pnma, ICSD *PDF* 01-070-2694), and the first three diffraction peaks at 15.6°, 27.2° and 28.0° of $La(OH)_3$ (*space group*: P63/m, ICSD *PDF* 01-075-1900) corresponding to the (100), (110) and (101) planes are marked by red vertical bars. BF-TEM images of (**b**) LC3 and (**d**) LC4 particles; the nanowires and irregular-shaped agglomerates are highlighted by the red and blue arrows respectively.

In contrast to LC1 – LC4, in LC5, no secondary phases were found (**Fig. 4**). Rietveld refinement (**Fig. 4a**) of the diffraction pattern showed that only $LaCrO_3$ was present in LC5. Shown in the SEM image (**Fig. 4b**) and the BF-TEM image (**Fig. 4c**), the $LaCrO_3$ particles displayed a cube-like morphology. Measuring the edge size of 10 particles gave an average value of 639(±47) nm. **Fig. 4d** presents an exemplary SAED pattern of a $LaCrO_3$ particle, in which all diffraction dots are assigned to specific planes of an orthorhombic $LaCrO_3$ crystal along the zone axis [011], indicating that particles were single crystals. The phase purity of the LC5 particles was further analyzed by Raman spectroscopy (**Fig. 4e**). All indexed Raman peaks below 600 cm^{-1} were assigned to modes of $LaCrO_3$ of a *Pnma* orthorhombic structure [46–48] (see more details in Supplementary information). The DF-STEM image (**Fig. 4f**) of a $LaCrO_3$ particle also reveals a cube-like shape. STEM-EDS maps of La and Cr are presented in **Fig. 4g** and **4h** respectively. The similar distribution of the two elements in the particle suggests a homogeneous elemental composition.

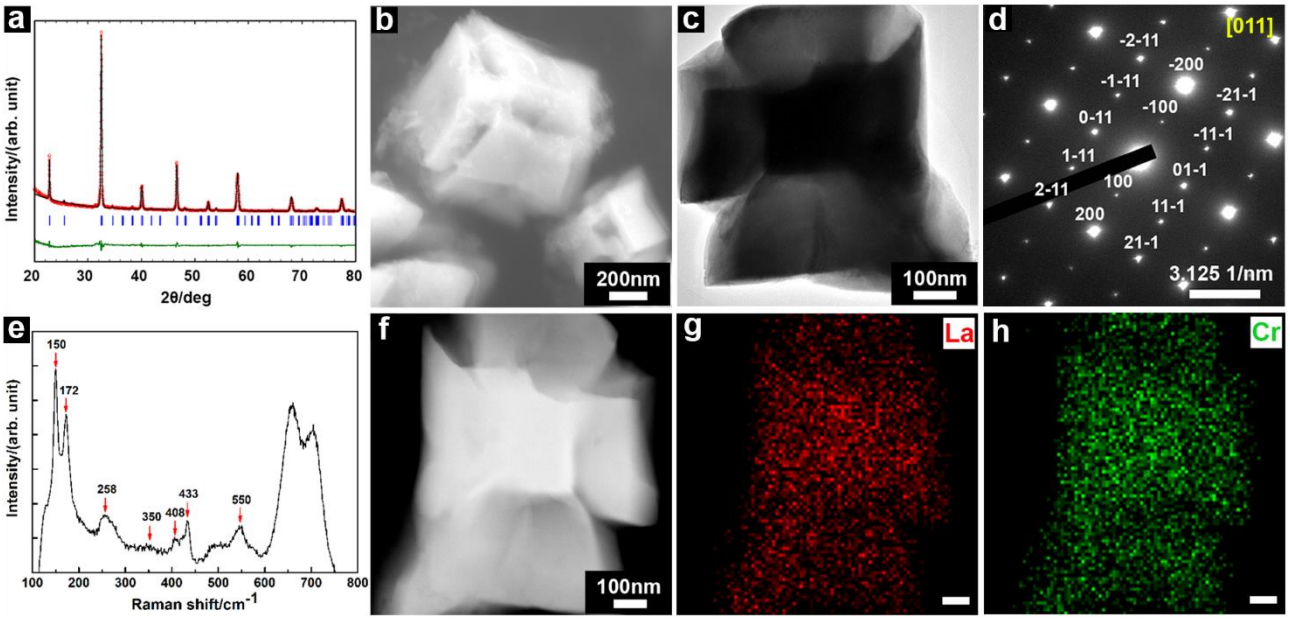

Figure 4. (**a**) Rietveld refinement of the powder XRD of the LC5 particles; the observed pattern (red circles), the calculated pattern (black line), difference profiles between the observed and the calculated pattern (bottom green line) and the Bragg reflection positions (blue vertical bars) of an orthorhombic $LaCrO_3$ crystal. (**b**) SEM image of the LC5 particles. (**c**) BF-TEM image of a $LaCrO_3$ particle. (**d**) SAED of a $LaCrO_3$ particle. (**e**) Raman spectrum of the LC5 particles. (**f**) DF-STEM image of a $LaCrO_3$ particle and STEM-EDS element mapping of the particle, X-ray photons of La Lα (**g**) and Cr Kα (**h**) are presented.

Based on these results, the formation mechanism of $LaCrO_3$ is suggested to follow the mechanism presented in **Fig. 5**. As discussed, the dehydration of $La(OH)_3$ to more soluble and reactive LaOOH is thermally activated. Suggested by the results, it is likely that LaOOH was formed during the synthesis of LC3, LC4 and LC5, due to the increased reaction temperature (325 – 410 °C), which is in the range (380 – 580 °C, [43]) in which LaOOH should be present. For comparison, the reaction temperature in the synthesis of LC1 and LC2 was 285 – 385 °C. Moreover, the dehydration rate of $La(OH)_3$ to LaOOH is also largely dependent on the temperature. An estimation of the dehydration rate (see details in Supplementary information, [49]) shows that the rate in the synthesis of LC3, LC4 and LC5 was nearly two times the rate in the LC1 and LC2 cases. Given the short mean residence time (23.2 – 26.6 s) (see details on the calculation in Supplementary information, [50]) of the CHFS process, a fast conversion from $La(OH)_3$ to LaOOH is important for the yield of $LaCrO_3$. As described

in detail above, the KOH concentration affects the concentration of the soluble $[Cr(OH)_4]^-$. Therefore, one can expect that for LC3 and LC4 synthesized with KOH solutions of lower concentrations than in LC5 (2 mol L^{-1} and 4 mol L^{-1} respectively), the Cr^{3+} was possibly not fully converted. Some LaOOH was therefore left unreacted, since the molar ratio of La to Cr was 1 : 1 in the precursor. After the reaction, when the temperature decreased, the LaOOH was converted to $La(OH)_3$, while the undissolved Cr compounds formed an amorphous phase (no 'dissolution – precipitation' process [20]). On the other hand, the use of a KOH solution of 6 mol L^{-1} ($n[OH^-] / n[Me^{3+}] = 60$) as used for LC5 enabled the formation of $[Cr(OH)_4]^-$ which reacted with the LaOOH to form $LaCrO_3$ particles.

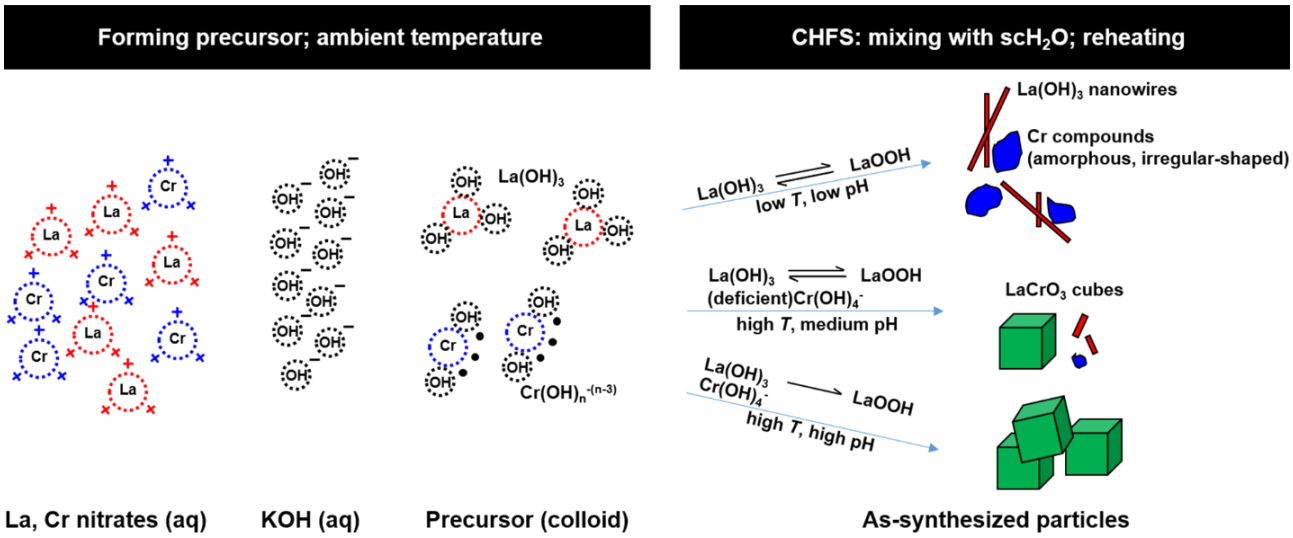

Figure 5. Mechanism suggested for the formation of $LaCrO_3$.

3.2 10Sc1YSZ – $LaCrO_3$ dual-phase oxygen transport membranes

Dual-phase oxygen transport membranes consisting of a stable ionic conductor and a stable electronic conductor can be an alternative to single-phase membranes composed of mixed-ionic-electronic conductive materials, and are capable of providing a high oxygen flux while being chemically stable.

In this study, planar dual-phase membranes were made from the synthesized $LaCrO_3$ particles (LC5, phase-pure) and 10Sc1YSZ. 10Sc1YSZ was chosen as the ionic conductive phase in the membranes, because of its known good ionic conductivity and chemical stability [51].

3.2.1 Microstructure of dual-phase 10Sc1YSZ – $LaCrO_3$ membranes

The microstructure of the sintered 10Sc1YSZ – $LaCrO_3$ membrane is shown in **Fig. 6**. In general, the composite material was dense, and only some closed porosity could be observed (**Fig. 6a**). A statistic quantification of seven SEM images gave an average density of 88 vol %. Distinguishable by the contrast, the distribution of $LaCrO_3$ (light grey) and 10Sc1YSZ (dark grey) is presented in **Fig. 6b**. Both phases were evenly distributed assuring possible conduction paths for electrons and oxygen ions, which is important for an application as oxygen transport membrane. The average grain size of $LaCrO_3$ was 922 ± 125 nm, indicating that $LaCrO_3$ grew during the sintering process (for reference, the size of as-synthesized $LaCrO_3$ particles was 639 ± 47 nm).

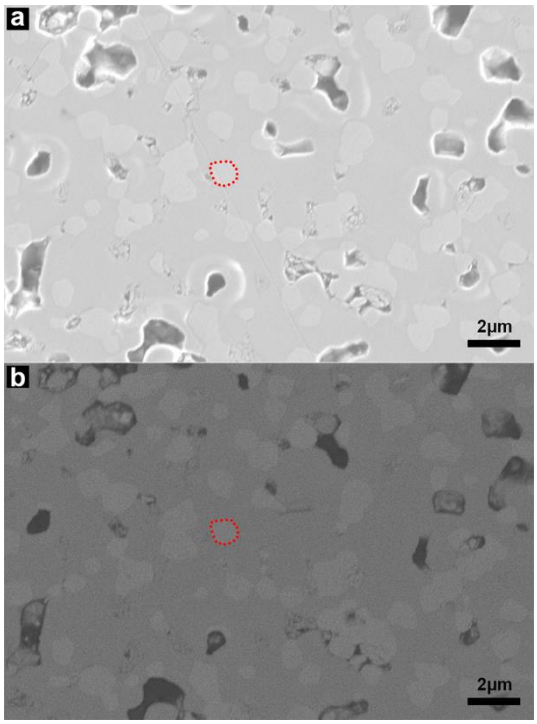

Figure 6. Microstructure of the sintered 10Sc1YSZ – $LaCrO_3$ membranes, presented by HE-SE2 (**a**) and ES-BSE (**b**); a $LaCrO_3$ grain is highlighted by red dashed lines.

3.2.2 Oxygen permeability

Oxygen permeation measurements were carried out on a 1-mm thick self-standing 10Sc1YSZ – $LaCrO_3$ (65 – 35 vol %) membrane. **Fig. 7** presents the microstructure of the polished cross section

of the symmetrical membrane with catalyst layers for oxygen permeation measurement. The screen-printed LSM – YSZ (50 – 50 vol %) layers after heat treatment at 980 °C were 13 µm and 14 µm thick respectively, and were well attached to the 10Sc1YSZ – $LaCrO_3$ (65 – 35 vol%, 960 µm).

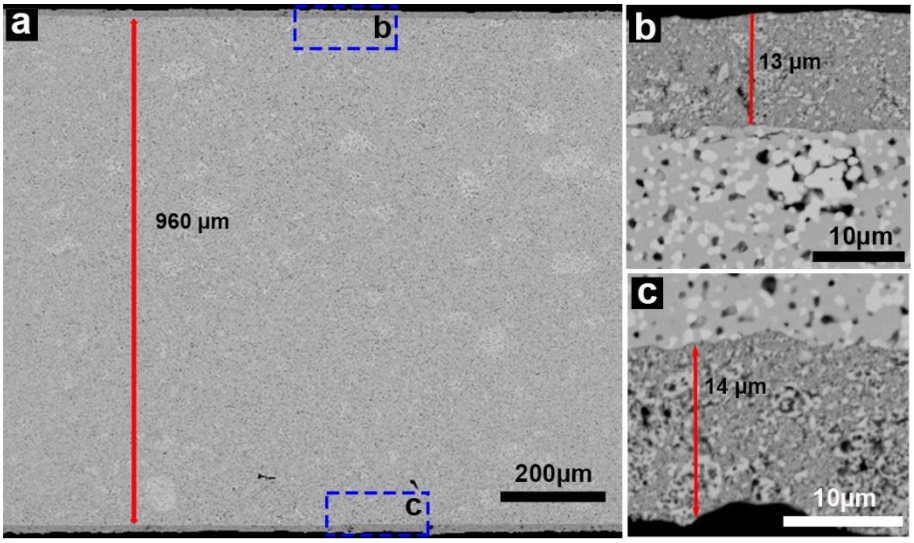

Figure 7. SE2 micrographs of the cross section of the sample for oxygen permeation measurement test.

Fig. 8 presents the oxygen permeation flux across the membrane as a function of log of the ratio between the oxygen partial pressures in the feed and permeate side gases (equivalent to the driving force). The flux across the membrane scaled proportionally with the driving force. Moreover, as the temperature increased, the flux increased for all oxygen partial pressure ratios. Among all measuring conditions, the highest flux corresponded to 0.066 $mL_N\ cm^{-2}\ s^{-1}$ or 4.9×10^{-8} mol $cm^{-2}\ s^{-1}$ (air/N_2, 900 °C).

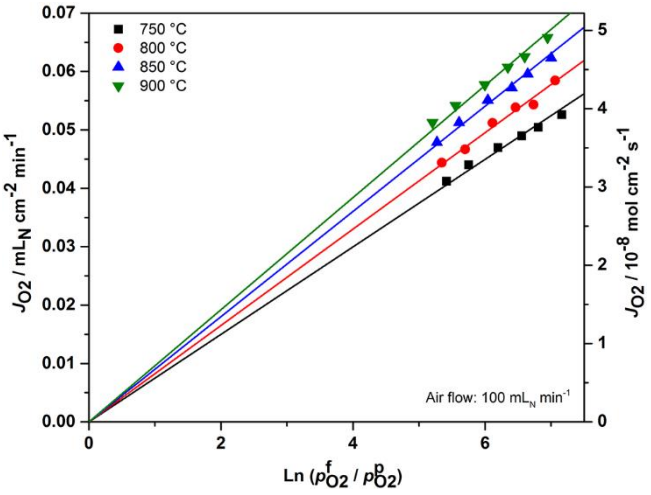

Figure 8. Oxygen permeation flux J_{O2} across a 1 mm-thick 10Sc1YSZ – $LaCrO_3$ (65 – 35 vol %) membrane as a function of the driving force, i.e. log of the ratio between oxygen partial pressures in the feed (p_{O2}^f) and permeate (p_{O2}^p) side gases. The flow rate of air at the feed side was constant at 100 mL_N min^{-1}, while N_2 of various flow rates (20, 30, 50, 75, 100 and 150 mL_N min^{-1}) was fed to the inlet of the permeate side.

A comparable performance ($J_{O2} = 5.7 \times 10^{-8}$ mol cm^{-2} s^{-1}) was reported for a dual-phase $Ce_{0.8}Sm_{0.2}O_{2-\delta}$ – $La_{0.8}Sr_{0.2}CrO_{3-\delta}$ membrane (60 – 40 vol %, 1-mm thick, air/He, 900 °C) [52]. However, it should be mentioned that $La_{0.8}Sr_{0.2}CrO_{3-\delta}$ has a much higher conductivity (6.3 – 7.9 S cm^{-1}, 800 – 1300 K, in air) than $LaCrO_3$ (0.1 – 0.3 S cm^{-1}, 800 – 1300 K, in air) [53], suggesting a promising performance of $LaCrO_3$ prepared by CHFS. In the case of dense self-supported membranes, the dominating rate-limiting process that governs the oxygen flux can either be the diffusion of oxygen ions or electrons within the bulk of membranes or the kinetics of oxygen redox reactions at surfaces of membranes. Here, the oxygen flux scaled in proportion to the driving force across the membrane, indicating that the main limiting factor of the oxygen permeation is the bulk diffusion. The diffusion-limited phenomenon is described by the *Wagner Equation* [12], showing that the electronic and ionic conductivities of a membrane have a direct impact on the oxygen permeation flux. Considering these, one can expect that further improvement of the oxygen permeability of the membranes can be achieved by doing the $LaCrO_3$ oxides to increase the electronic conductivity.

4. Conclusion

In summary, $LaCrO_3$ sub-micron particles (cube-shaped, 639 nm in edge size) were prepared by continuous hydrothermal flow synthesis (CHFS) in supercritical water. A continuous production of phase-pure $LaCrO_3$ particles was achieved for the first time, at 410 °C and 28 MPa with a reaction time as short as 23.2 s, which remarkably increases the throughput in comparison with conventional hydrothermal batch-type synthesis. The as-synthesized $LaCrO_3$ particles were further used to prepare 10Sc1YSZ – $LaCrO_3$ dual-phase oxygen transport membranes with ~90 vol % density after sintering at 1400 °C. Oxygen permeation fluxes of up to 4.9×10^{-8} mol cm^{-2} s^{-1} were obtained with a 1-mm thick membrane tested in air/N_2 at 900 °C. Given that CHFS is relatively easy to be up-scaled, a rapid, large-scale production of fine $LaCrO_3$ particles can be achieved by CHFS. Moreover, using doped $LaCrO_3$ (prepared by CHFS) with a higher electric conductivity compared to the un-doped material is expected to allow manufacturing of oxygen transport membranes with a higher oxygen flux. Further improvements will be reported in due course.

Supporting Information

1. BF-TEM images and EDS of the LC2 particles

Fig. S1 presents two BF-TEM images of the LC2 particles. Similar to the LC1 particles, the LC2 particles are composites of crystallized nanowires and amorphous irregular-shaped particles.

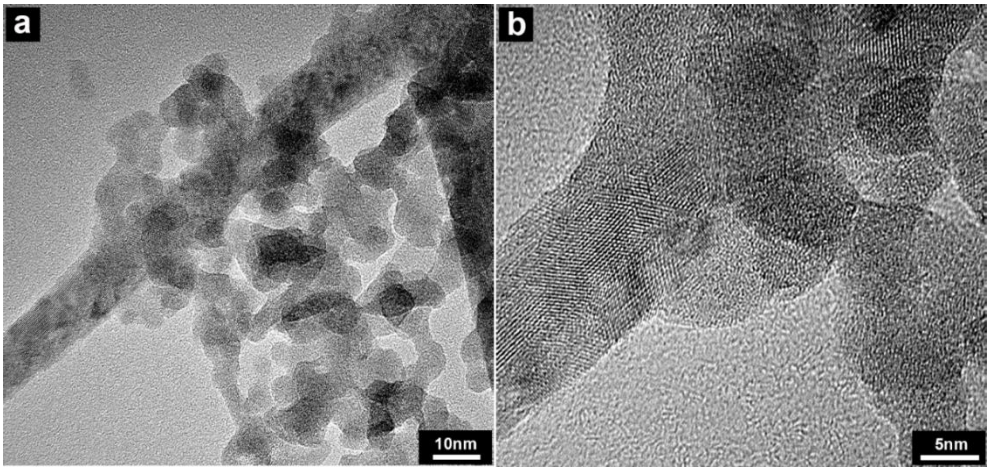

Figure S1. BF-TEM images of the LC2 particles.

For estimating the chemical composition, drought LC2 particles were loaded on a carbon tape, and a Hitachi Tabletop TM3000 microscope ('Analysis', 15 kV charge-reduction mode) equipped with a silicon drift EDS detector (SDD, energy resolution 0.154 keV) was used to do a standardless EDS quantification analysis. Quantax70 (Bruker) software was used to obtain the elemental composition from the spectra. Five areas were randomly selected. **Table S1** shows the results.

Table S1. Chemical composition (in atomic percent, at%) of the LC2 particles by EDS

	La / at%	**Cr / at%**
	51.0	49.0
	52.3	47.7
	51.7	48.3
	52.6	47.4
	51.6	48.4
Average	51.8	48.2

2. Rietveld refinements of the XRD patterns of the LC3 and LC4 particles, and refinement residuals

The refinement was conducted by using the FullProf Suite. In both cases, the structure of $LaCrO_3$ was refined in the *Pnma* space group, whereas the structure of $La(OH)_3$ was refined in the *P63/m*

space group. To simplify the estimation of phase compositions, the amorphous Cr-rich phase that was found in small amounts in the TEM characterization was not taken into account. The peak shape of both $LaCrO_3$ and $La(OH)_3$ was described by the Thompson-Cox-Hasting formulation of the pseudo-Voigt function. The scale factor, the zero point, and the unit cell parameters were refined. The peak broadening was assumed to arise purely from the particle size, whereas the strain contribution as well as the instrumental contribution were neglected. The XRD patterns of the LC3 and LC4 particles were refined in a 2θ range from 15° to 90° and 15° to 80°, respectively. The Rietveld refinement residuals are summarized in **Table S2** and **Table S3** (for LC3 and LC4 particles separately).

Table S2. Refinement residuals of the XRD pattern of the LC3 particles

Phase	$LaCrO_3$	$La(OH)_3$
Space group	Orthorhombic, Pnma	Hexagonal, P63/m
Number of Bragg peaks	107	45
Number of data points	11981	
Total number of parameters	20	
R_{Bragg}	4.35%	24.2%
R_F	5.76%	12.6%
Unit cell	a=5.4906Å, b=7.7804Å, c=5.5256Å	a=b=6.5359Å, c=3.8544Å
χ^2	1.16	

Table S3. Refinement residuals of the XRD pattern of the LC4 particles

Phase	$LaCrO_3$	$La(OH)_3$
Space group	Orthorhombic, Pnma	Hexagonal, P63/m
Number of Bragg peaks	75	30
Number of data points	11981	
Total number of parameters	20	
R_{Bragg}	9.79%	20.6%
R_F	10.9%	28.8%
Unit cell	a=5.4946Å, b=7.7846Å, c=5.5326Å	a=b=6.5359Å, c=3.8544Å
χ^2	1.34	

Fig. S2 presents the refined patterns in the EdPCR window of the FullProf Suite of the LC3 (**a**) and LC4 (**b**) particles.

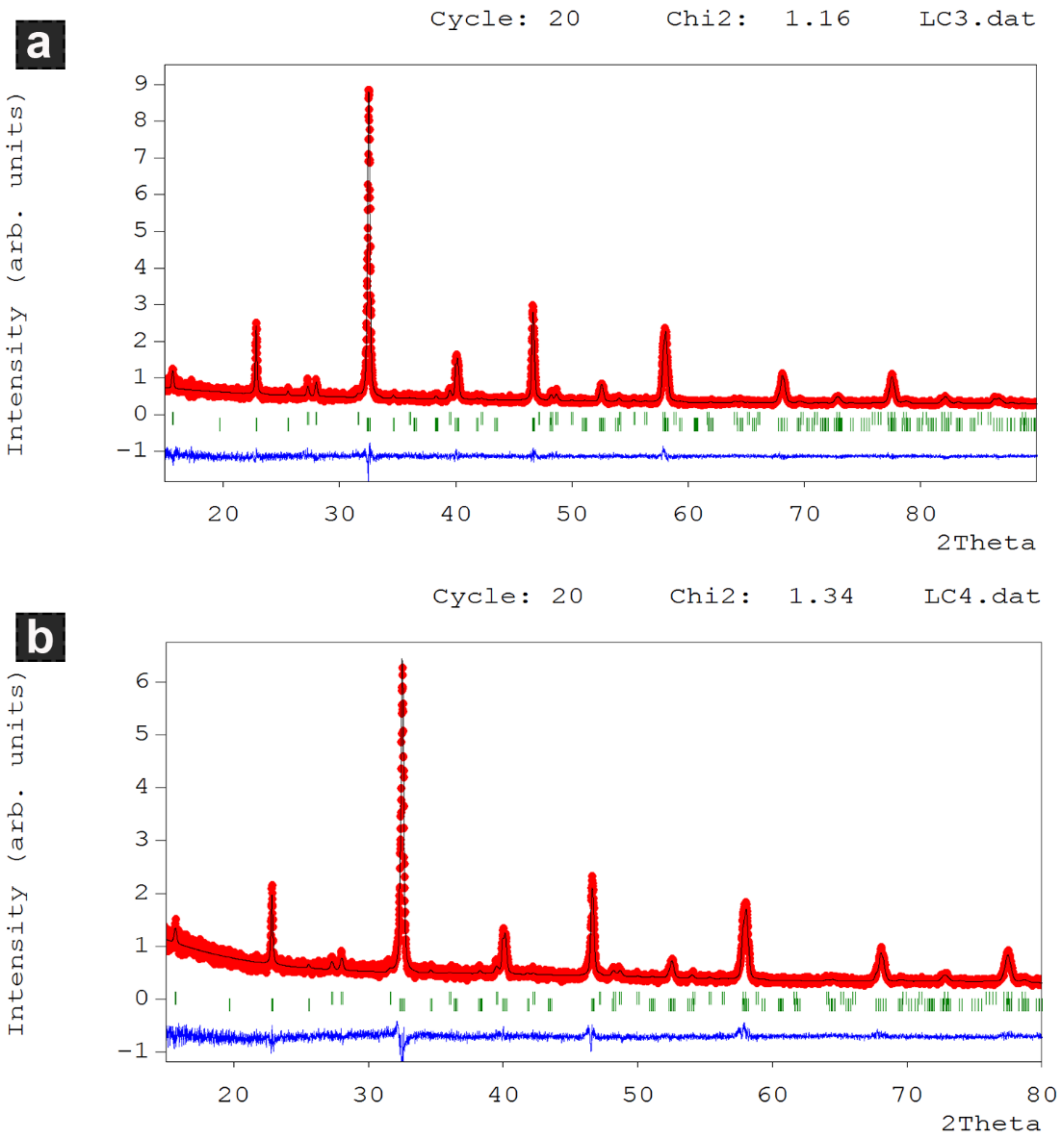

Figure S2. Refined patterns presented in the EdPCR window of the FullProf Suite of the LC3 (**a**) and LC4 (**b**) particles. The red circles present the observed patterns, the black lines are the calculated patterns, and the blue curves are the differential profiles; the green vertical bars in the first row indicate the Bragg positions of $La(OH)_3$ while those in the second row indicate the Bragg positions of $LaCrO_3$.

3. Rietveld refinement of the XRD patterns of the LC5 particles, and refinement residuals

The Rietveld refinement of the XRD pattern of the LC5 particles was conducted by using the FullProf Suite as well. The structure of the $LaCrO_3$ was refined in the *Pnma* space group. The peak shape of the $LaCrO_3$ was described by the Thompson-Cox-Hasting formulation of the pseudo-Voigt function. The scale factor, the zero point, and the unit cell parameters were refined. The peak broadening was

assumed to arise purely from the particle size, whereas the strain contribution as well as the instrumental contribution were neglected. The pattern was refined in 2θ range between 20° to 80°. The Rietveld refinement residuals are summarized in **Table S4**.

Table S4. Refinement residuals of the XRD pattern of the LC5 particles

Number of Bragg peaks	74
Number of data points	11981
Total number of parameters	16
R_{Bragg}	12.7%
R_F	13.6%
Unit cell	a=5.4984Å, b=7.7886Å, c=5.5266Å
χ^2	5.45

Fig. S3 presents a screenshot of the zoom-in of the experimental XRD pattern of the LC5 particles. The pattern was obtained by using a divergent slit size and the background was subtracted. The first three intense diffraction peaks of $La(OH)_3$ at 2θ 15.6°, 27.2° and 28.0° were not observed.

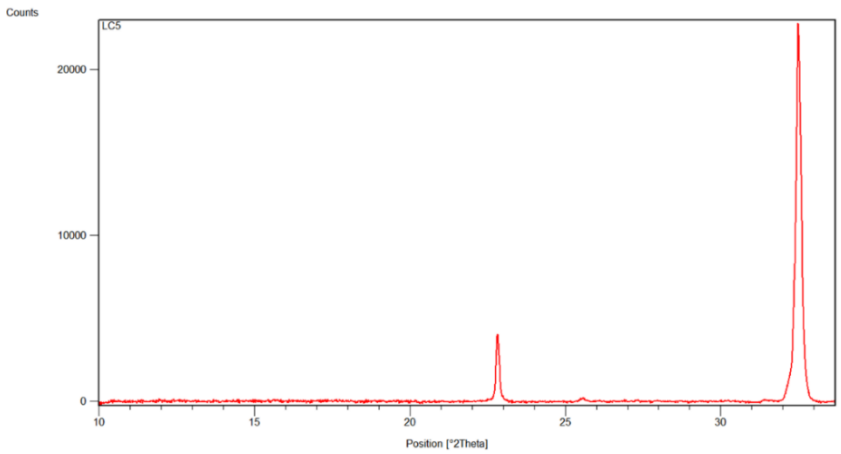

Figure S3. A screenshot of the zoom-in experimental XRD pattern of the LC5 particles.

4. Additional microscopy characterization results of the $LaCrO_3$ particles (LC5)

Fig. S4 presents an extra SEM image and a BF-TEM image of LC5 particles. They also show that the as-prepared particles display a cube-like morphology.

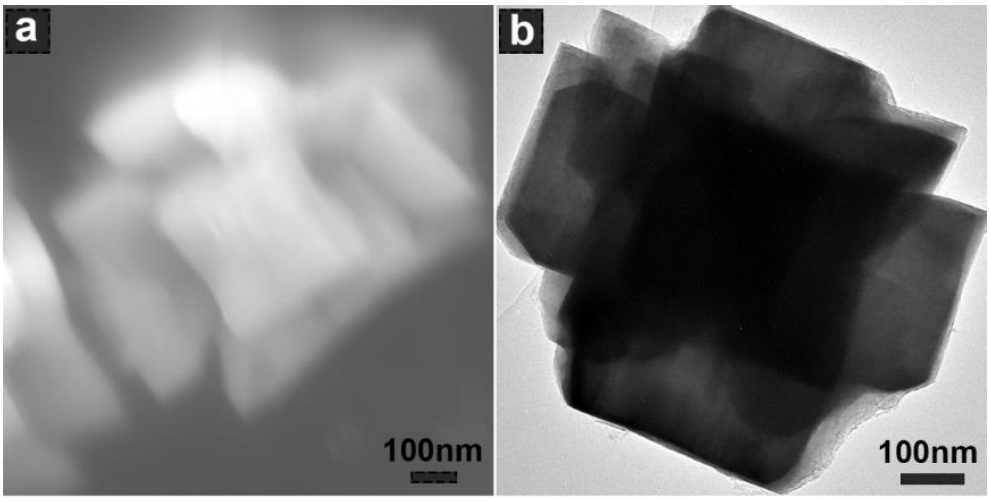

Figure S4. (**a**) A SEM image and (**b**) a BF-TEM image of $LaCrO_3$ particles (LC5).

Besides the element maps obtained by STEM-EDS, the element line distribution was also characterized (**Fig. S5**). The similar distribution of La and Cr indicates a homogeneous chemical composition.

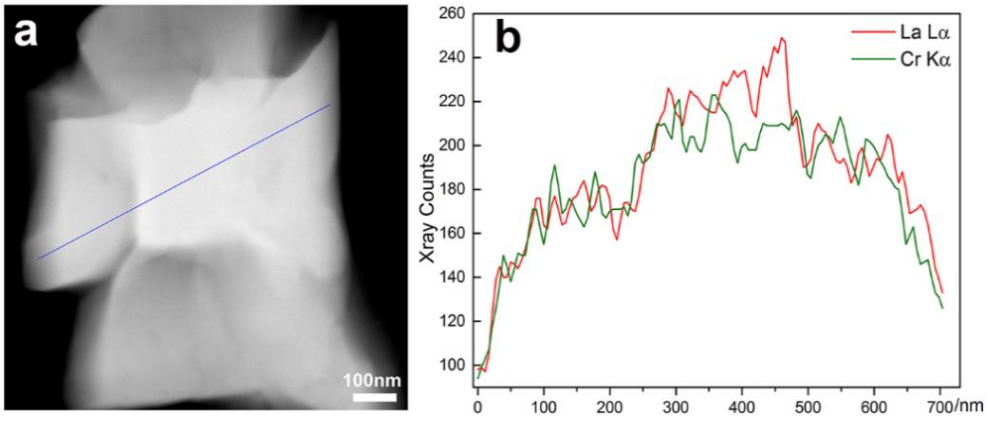

Figure S5. (**a**) A DF-STEM image of a $LaCrO_3$ particle (LC5); the blue line marks the trace of the electron probe; (**b**) element line distribution described by X-ray counts from La Lα and Cr Kα.

5. Mode assignment of the Raman spectrum of LC5 particles

Table S5. Band positions among the observed and the reported; assignment of the Raman modes and the main atomic motions

λ^{-1}/cm^{-1} Observed	λ^{-1}/cm^{-1} Ref. [46]	λ^{-1}/cm^{-1} Ref. [47]	λ^{-1}/cm^{-1} Ref. [48]	Mode	Main atomic motions
150	151	151.7	150	B_{2g} (B_{3g} [48])	A(x)
172	175	175.2	174	A_g	A(z) out-of-phase
258	256	255.3		A_g	BO_6 out-of-phase x rotations (O_1(x), A(−x) [40])
~350	350	351.4		B_{1g} (B_{2g} [46])	A(z), O_1(−z)
408	406	405.4		B_{2g}	BO_6 out-of-phase bendings
433	439	436.6	441	A_g	BO_6 bendings
550	590	586.8	590	B_{2g} (A_g [48])	O_2,O_1 antistretching
660			675		
703			719		

6. Details on the model to estimate the dehydration rate of $La(OH)_3$

The shrinking-core model was used to calculate the reaction rate constant (**Eq. S1**), assuming the $La(OH)_3$ are spherical particles [49]:

$$[1 - (1 - \alpha)^{1/3}]^2 = (2k / r^2)\, t \qquad (\mathbf{S1}),$$

where α is the degree of dehydration, k the reaction rate constant, r the particle radius, and t is the time.

The Arrhenius equation (**Eq. S2**) was used to describe the relationship between the temperature and the reaction rate constant:

$$\ln k = \ln A - E_A / (R\, T) \qquad (\mathbf{S2}),$$

where A is the Arrhenius constant, E_A the activation energy that for $La(OH)_3$ is 76 kJ mol^{-1} [49], R is the universal gas constant (8.314 J mol^{-1} K^{-1}) and T is the temperature.

Since the temperature was not constant throughout the reactive part of the reactor, the combined temperature composed of T_2 and T_3 was used to describe the temperature condition during the synthesis. To simplify the calculation, an average value was used. Therefore, for a same dehydration degree of $La(OH)_3$, the ratio of the required time t is given by **Eq. S3**:

$$\ln (t_1 / t_2) = \ln (k_2 / k_1) = (E_A / R) (1 / T_{a1} - 1 / T_{a2}) \quad (\mathbf{S3}),$$

where T_{a1} = (285 + 385) °C / 2 = 335 °C for the LC1 and LC2 synthesis, and T_{a2} = (325 + 410) °C / 2 = 368 °C for the LC3, LC4 and LC5 synthesis. The calculated value of (t_1 / t_2) was 2.17, showing that to reach a same degree of dehydration of $La(OH)_3$, nearly 2-fold long time was required at the temperature applied during the synthesis of LC1 and LC2 compared with that applied during the synthesis of LC3, LC4 and LC5.

7. Estimating the residence time

The residence time t [50] describes the period starting from the mixing until the end of re-heater. It can be calculated using **Eq. S4**:

$$t = V \rho_T / Q \quad (\mathbf{S4})$$

where V is the reactor volume (cm^3), Q is the total flow rate (g s^{-1}), ρ_T is the density of H_2O (g cm^{-3}) at T K.

In the current case, the hot reaction zone started from the first mixer where the precursor (premixture of the reactant solution and the KOH solution) was heated by the scH_2O, and ended after the re-heater. The volume of the zone V is 42.4 cm^3, Q is 65 mL min^{-1} (assuming densities of all supplied solutions were 1 g cm^{-3}, given the supplied solutions were diluted, then the Q equals to 1.08 g s^{-1}). At 30 MPa, the densities of H_2O at the reaction temperatures T_{a1} (335 °C or 608 K for LC1 and LC2) and T_{a2} (368 °C or 641 K for LC3, LC4 and LC5) were 677 × 10^{-3} g cm^{-3} and 591 × 10^{-3} g cm^{-3}

respectively (refer to W. Wagner, A. Pruß, *J. Phys. Chem. Ref. Data.* 31 (2002) 387–535. doi:10.1063/1.1461829). The calculations gave residence times of 26.6 s (LC1 and LC2) and 23.2 s (LC3, LC4 and LC5).

8. XRD analysis on the sintered 10Sc1YSZ – $LaCrO_3$ membranes

Fig. S6 presents the XRD pattern of the sintered 10Sc1YSZ – $LaCrO_3$ membranes. All diffraction peaks can be fitted to either the cubic ZrO_2 or the $LaCrO_3$. No extra peaks derived from a third phase could be detected, indicating that no new phase was formed.

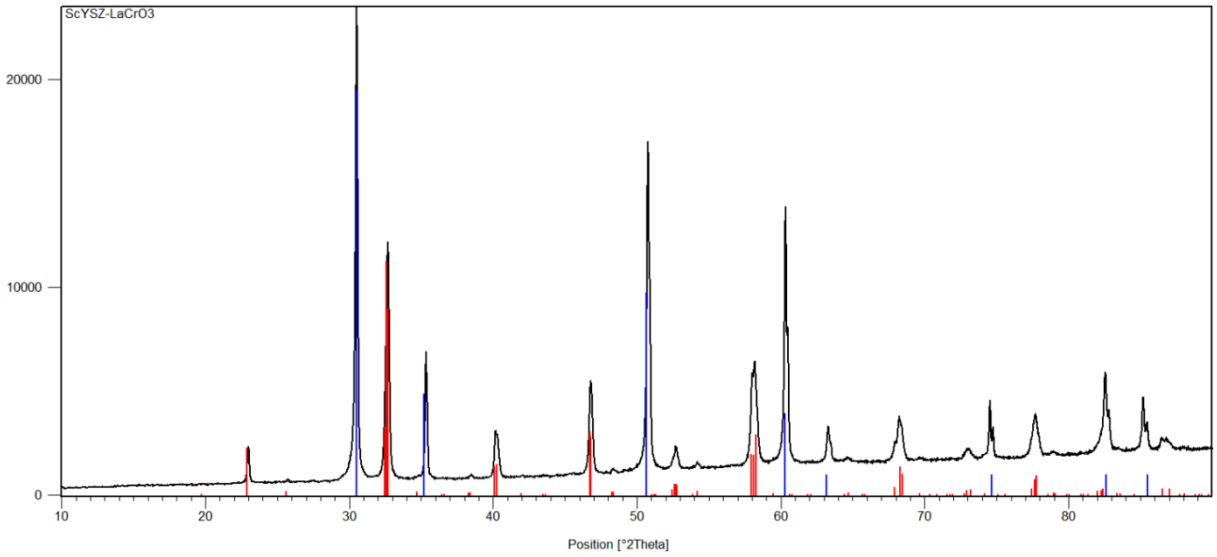

Figure S6. A screenshot of the XRD pattern of the sintered 10Sc1YSZ – $LaCrO_3$ membranes; reference patterns are peaks from $LaCrO_3$ (red, Pnma, *PDF* 01-089-8770 33-701, ICSD) and ZrO_2 (blue, Fm-3m, *PDF* 01-072-2742 49-1642, ICSD).

9. Additional HE-SE2 images of the cross section of the sintered 10Sc1YSZ – $LaCrO_3$ membranes

Fig. S7 presents two extra HE-SE2 images (**a**, **d**) of the polished cross section of the sintered 10Sc1YSZ – $LaCrO_3$ membranes. By the ThreshAlyzer software, pores could be outlined (**b**, **g**) within the images by setting an appropriate threshold of the grey intensity. In the segmented images (**c**, **f**) the pores are represented in black.

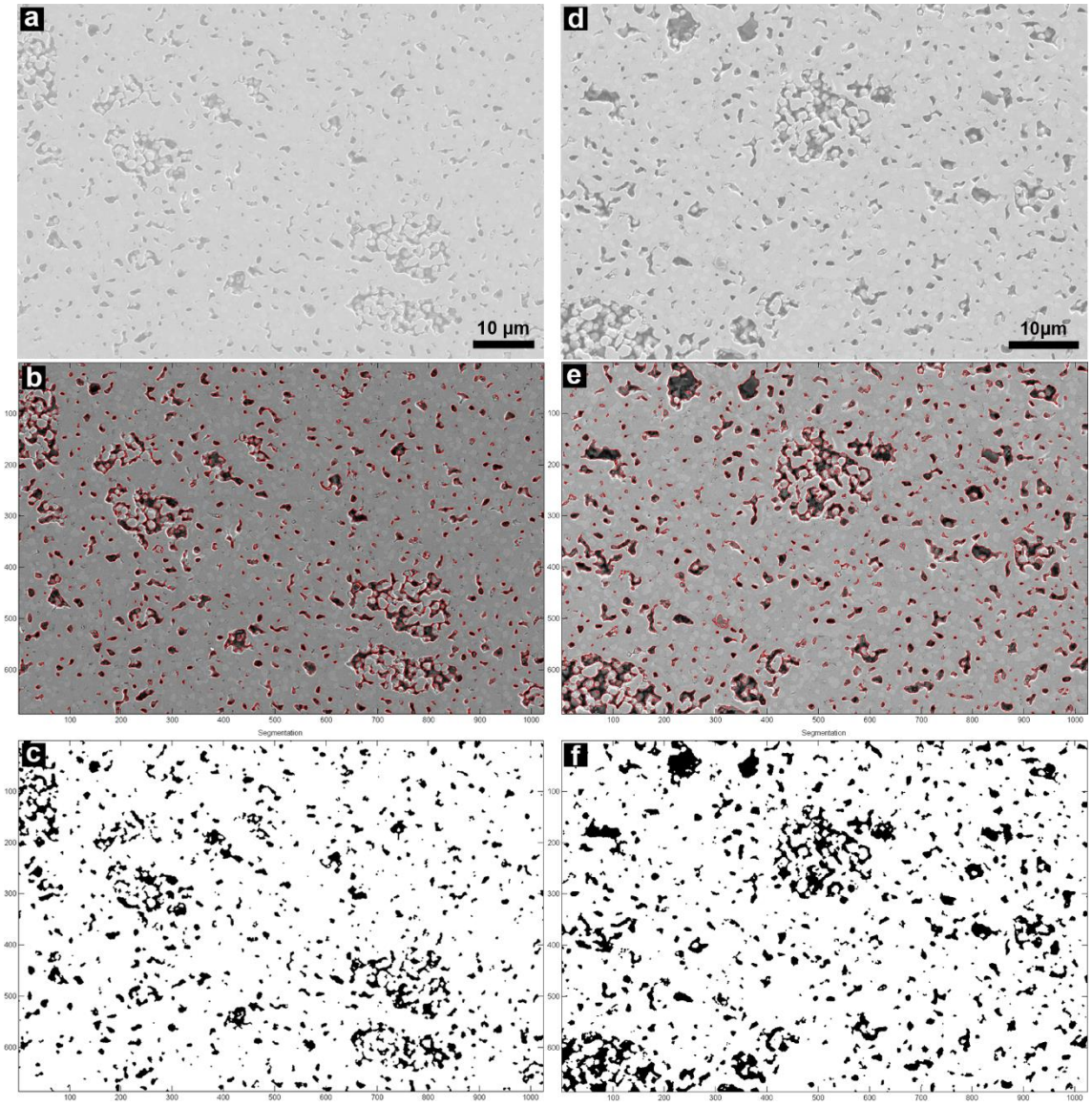

Figure S7. Two extra HE-SE2 images (**a**, **d**) of the polished cross section of the sintered 10Sc1YSZ – $LaCrO_3$ membranes; in **b** and **e**, the pores are outlined with red fringes; in **c** and **f**, the images are segmented with the pores shown in black.

The porosity was estimated by using the fraction of the black area representing the pores. In total, seven images (from different areas) were analyzed. The results are summarized in **Table S6**. The porosity on average was 12 vol%. In other words, the density of the sintered 10Sc1YSZ – $LaCrO_3$ was 88 vol%.

Table S6. Porosity of seven analyzed areas.

	Porosity / vol%	**Density / vol%**
	13	87
	9	91
	13	87
	11	89
	13	87
	12	88
	10	90
Average	12 (1)	88 (1)

Whenever available, the grain boundary of a $LaCrO_3$ grain in the 10Sc1YSZ – $LaCrO_3$ composite was outlined by using the ImageJ. An equivalent diameter was calculated from the area of the outlined grain, which was used to estimate the size of $LaCrO_3$ grain (**Fig. S8**).

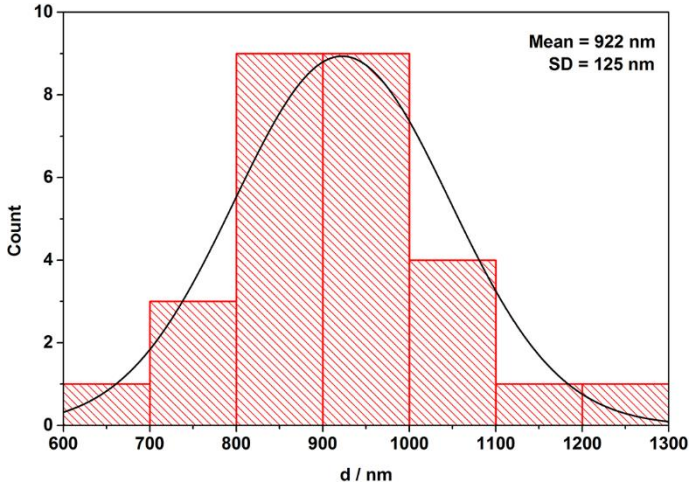

Figure S8. Size of $LaCrO_3$ grains in the 10Sc1YSZ – $LaCrO_3$ membranes.

References

[1] B. Tiwari, A. Dixit, R. Naik, G. Lawes, M.S. Ramachandra Rao, Dielectric and optical phonon anomalies near antiferromagnetic ordering in LaCrO3: A possible near room temperature magnetodielectric system, Appl. Phys. Lett. 103 (2013) 13–16. doi:10.1063/1.4824919.

[2] K. Ueda, H. Tabata, T. Kawai, Ferromagnetism in LaFeO3-LaCrO3 superlattices, Science. 280 (1998) 1064–1066. doi:10.1126/science.280.5366.1064.

[3] K.H.L. Zhang, Y. Du, A. Papadogianni, O. Bierwagen, S. Sallis, L.F.J. Piper, M.E. Bowden, V. Shutthanandan, P. V Sushko, S.A. Chambers, Perovskite Sr-doped LaCrO3 as a new p-type transparent conducting oxide, Adv. Mater. 27 (2015) 5191–5195. doi:10.1002/adma.201501959.

[4] K.P. Ong, P. Wu, L. Liu, S.P. Jiang, Optimization of electrical conductivity of LaCrO3 through doping: A combined study of molecular modeling and experiment, Appl. Phys. Lett. 90 (2007) 44109. doi:10.1063/1.2431780.

[5] S. Royer, D. Duprez, F. Can, X. Courtois, C. Batiot-Dupeyrat, S. Laassiri, H. Alamdari, Perovskites as substitutes of noble metals for heterogeneous catalysis: Dream or reality, Chem. Rev. 114 (2014) 10292–10368. doi:10.1021/cr500032a.

[6] B. de Collongue, E. Garbowski, M. Primet, Catalytic combustion of methane over bulk and supported LaCrO3 perovskites, J. Chem. Soc. Faraday Trans. 87 (1991) 2493. doi:10.1039/ft9918702493.

[7] K. Rida, A. Benabbas, F. Bouremmad, M.A. Peña, E. Sastre, A. Martínez-Arias, Effect of strontium and cerium doping on the structural characteristics and catalytic activity for C3H6 combustion of perovskite LaCrO3 prepared by sol-gel, Appl. Catal. B Environ. 84 (2008) 457–467. doi:10.1016/j.apcatb.2008.04.031.

[8] S.-W. Song, L.P. Martin, R.S. Glass, E.P. Murray, J.H. Visser, R.E. Soltis, R.F. Novak, D.J. Kubinski, Aging studies of Sr-doped LaCrO3/YSZ/Pt cells for an electrochemical NOx sensor, J. Electrochem. Soc. 153 (2006) H171–H180. doi:10.1149/1.2213367.

[9] M. Siemons, A. Leifert, U. Simon, Preparation and gas sensing characteristics of nanoparticulate p-type semiconducting LnFeO3 and LnCrO3 materials, Adv. Funct. Mater. 17 (2007) 2189–2197. doi:10.1002/adfm.200600454.

[10] S.P. Jiang, L. Liu, K.P. Ong, P. Wu, J. Li, J. Pu, Electrical conductivity and performance of doped LaCrO3 perovskite oxides for solid oxide fuel cells, J. Power Sources. 176 (2008) 82–89. doi:10.1016/j.jpowsour.2007.10.053.

[11] Y.P. Fu, H.C. Wang, C.S. Weng, S.H. Hu, Y.C. Liu, Characterizations of Fe doping on B-Site of (La0.8Ca0.2)(Cr0.9Co0.1)O3-δ interconnect materials for SOFCs, J. Am. Ceram. Soc. 98 (2015) 2561–

2569. doi:10.1111/jace.13669.

[12] S. Gupta, M.K. Mahapatra, P. Singh, Lanthanum chromite based perovskites for oxygen transport membrane, Mater. Sci. Eng. R Reports. 90 (2015) 1–36. doi:10.1016/j.mser.2015.01.001.

[13] Y. Luo, T. Liu, J. Gao, C. Chen, Zr0.84Y0.16O1.92 –La0.8Sr0.2Cr0.5Fe0.5O3−δ composite membrane for CO2 decomposition, Mater. Lett. 86 (2012) 5–8. doi:10.1016/j.matlet.2012.06.101.

[14] M. Puig-Arnavat, S. Soprani, M. Søgaard, K. Engelbrecht, J. Ahrenfeldt, U.B. Henriksen, P.V. Hendriksen, Integration of mixed conducting membranes in an oxygen–steam biomass gasification process, RSC Adv. 3 (2013) 20843–20854. doi:10.1039/c3ra44509g.

[15] V.G. Artemov, I.E. Kuritsyna, S.P. Lebedev, G.A. Komandin, P.O. Kapralov, I.E. Spektor, V. V. Kharton, S.I. Bredikhin, A.A. Volkov, Analysis of electric properties of ZrO2–Y2O3 single crystals using teraherz IR and impedance spectroscopy techniques, Russ. J. Electrochem. 50 (2014) 690–693. doi:10.1134/S1023193514070039.

[16] K. Azegami, M. Yoshinaka, K. Hirota, O. Yamaguchi, Formation and sintering of LaCrO3 prepared by the hydrazine method, Mater. Res. Bull. 33 (1998) 341–348.

[17] M. Yoshimura, S.T. Song, S. Sōmiya, Synthesis of LaCrO3 under hydrothermal conditions, in: S. Sōmiya (Ed.), Hydrothermal React. Mater. Sci. Eng. An Overv. Res. Japan, Springer Netherlands, Dordrecht, 1989: pp. 284–288. doi:10.1007/978-94-009-0743-0_47.

[18] W. Zheng, W. Pang, G. Meng, D. Peng, Hydrothermal synthesis and characterization of LaCrO3, J. Mater. Chem. (1999) 2833–2836. doi:10.1039/A904399C.

[19] S. Wang, K. Huang, C. Hou, L. Yuan, X. Wu, D. Lu, Low temperature hydrothermal synthesis, structure and magnetic properties of RECrO3 (RE = La, Pr, Nd, Sm), Dalt. Trans. 44 (2015) 17201–17208. doi:10.1039/C5DT02342D.

[20] L.P. Rivas-Vázquez, J.C. Rendón-Angeles, J.L. Rodríguez-Galicia, C.A. Gutiérrez-Chavarria, K.J. Zhu, K. Yanagisawa, Preparation of calcium doped LaCrO3 fine powders by hydrothermal method and its sintering, J. Eur. Ceram. Soc. 26 (2006) 81–88. doi:10.1016/j.jeurceramsoc.2004.10.023.

[21] K. Sardar, M.R. Lees, R.J. Kashtiban, J. Sloan, R.I. Walton, Direct hydrothermal synthesis and physical properties of rare-earth and yttrium orthochromite perovskites, Chem. Mater. 23 (2011) 48–56. doi:10.1021/cm102925z.

[22] H.-N. Girish, G.-Q. Shao, B. Basavalingu, Well-monocrystallized LaCrO3 particles from a LaCrO4 precursor by supercritical hydrothermal technique, RSC Adv. 6 (2016) 79763–79767. doi:10.1039/C6RA15354B.

[23] L.M. Daniels, M.C. Weber, M.R. Lees, M. Guennou, R.J. Kashtiban, J. Sloan, J. Kreisel, R.I. Walton, Structures and magnetism of the rare-earth orthochromite perovskite solid solution LaxSm1-xCrO3,

Inorg. Chem. 52 (2013) 12161–12169. doi:10.1021/ic402029u.

[24] T. Adschiri, K. Kanazawa, K. Arai, Rapid and continuous hydrothermal crystallization of metal oxide particles in supercritical water, J. Am. Ceram. Soc. 22 (1992) 1019–1022. doi:10.1111/j.1151-2916.1992.tb04179.x.

[25] T. Adschiri, Y. Hakuta, K. Arai, Hydrothermal synthesis of metal oxide fine particles at supercritical conditions, Ind. Eng. Chem. Res. 39 (2000) 4901–4907. doi:10.1021/ie0003279.

[26] A. Nugroho, J. Kim, Effect of KOH on the continuous synthesis of cobalt oxide and manganese oxide nanoparticles in supercritical water, J. Ind. Eng. Chem. 20 (2014) 4443–4446. doi:10.1016/j.jiec.2014.02.014.

[27] C. Slostowski, S. Marre, J.-M. Bassat, C. Aymonier, Synthesis of cerium oxide-based nanostructures in near- and supercritical fluids, J. Supercrit. Fluids. 84 (2013) 89–97. doi:10.1016/j.supflu.2013.09.014.

[28] Y. Shen, J.R. Eltzholtz, B.B. Iversen, Controlling size, crystallinity, and electrochemical performance of Li4Ti5O12 nanocrystals, Chem. Mater. 25 (2013) 5023–5030. doi:10.1021/cm402366y.

[29] S. Kubota, T. Morioka, M. Takesue, H. Hayashi, M. Watanabe, R.L. Jr. Smith, Continuous supercritical hydrothermal synthesis of dispersible zero-valent copper nanoparticles for ink applications in printed electronics, J. Supercrit. Fluids. 86 (2014) 33–40. doi:10.1016/j.supflu.2013.11.013.

[30] P.W. Dunne, C.L. Starkey, M. Gimeno-Fabra, E.H. Lester, The rapid size- and shape-controlled continuous hydrothermal synthesis of metal sulphide nanomaterials, Nanoscale. 6 (2014) 2406–2418. doi:10.1039/c3nr05749f.

[31] P.W. Dunne, E. Lester, R.I. Walton, Towards scalable and controlled synthesis of metal–organic framework materials using continuous flow reactors, React. Chem. Eng. 1 (2016) 352–360. doi:10.1039/C6RE00107F.

[32] T. Adschiri, Y.-W. Lee, M. Goto, S. Takami, Green materials synthesis with supercritical water, Green Chem. 13 (2011) 1380–1390. doi:10.1039/c1gc15158d.

[33] R.I. Gruar, C.J. Tighe, J.A. Darr, Scaling-up a confined jet reactor for the continuous hydrothermal manufacture of nanomaterials, Ind. Eng. Chem. Res. 52 (2013) 5270–5281. doi:10.1021/ie302567d.

[34] P. Zielke, Y. Xu, S.B. Simonsen, P. Norby, R. Kiebach, Simulation, design and proof-of-concept of a two-stage continuous hydrothermal flow synthesis reactor for synthesis of functionalized nano-sized inorganic composite materials, J. Supercrit. Fluids. 117 (2016) 1–12. doi:10.1016/j.supflu.2016.06.008.

[35] X. Weng, P. Boldrin, I. Abrahams, S.J. Skinner, J.A. Darr, Direct syntheses of mixed ion and electronic conductors La4Ni3O10 and La3Ni2O7 from nanosized coprecipitates, Chem. Mater. 19 (2007) 4382–4384. doi:10.1021/cm070134c.

[36] N.M. Islam, T. Noguchi, Y. Hakuta, H. Hayashi, Hydrothermal synthesis of strontium doped lanthanum

manganite nanoparticles by a supercritical flow reaction system, Nanosci. Nanotechnol. Lett. 3 (2011) 324–327. doi:10.1166/nnl.2011.1184.

[37] A.A. Galkin, B.G. Kostyuk, V. V Lunin, M. Poliakoff, Continuous reactions in supercritical water: a new route to La2CuO4 with a high surface area and enhanced oxygen mobility, Angew. Chemie Int. Ed. 39 (2000) 2738–2740. doi:10.1002/1521-3757(20000804)112:15<2850::AID-ANGE2850>3.0.CO;2-7.

[38] J. Rodríguez-Carvajal, Recent advances in magnetic structure determination by neutron powder diffraction, Phys. B Condens. Matter. 192 (1993) 55–69. doi:10.1016/0921-4526(93)90108-I.

[39] A.J. Samson, M. Søgaard, P.V. Hendriksen, (Ce,Gd)O2-δ-based dual phase membranes for oxygen separation, J. Memb. Sci. 470 (2014) 178–188. doi:10.1016/j.memsci.2014.07.028.

[40] K.A. Nielsen, M. Solvang, S.B.L. Nielsen, A.R. Dinesen, D. Beeaff, P.H. Larsen, Glass composite seals for SOFC application, J. Eur. Ceram. Soc. 27 (2007) 1817–1822. doi:10.1016/j.jeurceramsoc.2006.05.046.

[41] E.S. Stampler, W.C. Sheets, W. Prellier, T.J. Marks, K.R. Poeppelmeier, Hydrothermal synthesis of LnMnO3 (Ln = Ho–Lu and Y): exploiting amphoterism in late rare-earth oxides, J. Mater. Chem. 19 (2009) 4375–4381. doi:10.1039/b900370c.

[42] P. Fleming, R.A. Farrell, J.D. Holmes, M.A. Morris, The rapid formation of La(OH)3 from La2O3 powders on exposure to water vapor, J. Am. Ceram. Soc. 93 (2010) 1187–1194. doi:10.1111/j.1551-2916.2009.03564.x.

[43] E. Füglein, D. Walter, Thermal analysis of lanthanum hydroxide, J. Therm. Anal. Calorim. 110 (2012) 199–202. doi:10.1007/s10973-012-2298-2.

[44] J. Feng, X. Li, M. Wang, X. Zheng, J. Bai, L. Wang, Y. Peng, One-pot, template-free synthesis of hydrophobic single-crystalline La(OH)3 nanowires with tunable size and their d0 ferromagnetic properties, RSC Adv. 5 (2015) 16093–16100. doi:10.1039/C4RA14135K.

[45] P.L. Brown, C. Ekberg, First Transition Series Metals, in: P.L. Brown, C. Ekberg (Eds.), Hydrolys. Met. Ions, Wiley-VCH Verlag GmbH & Co. KGaA, Weinheim, Germany, 2016: pp. 499–716. doi:10.1002/9783527656189.ch11.

[46] M.N. Iliev, A.P. Litvinchuk, V.G. Hadjiev, Y.Q. Wang, J. Cmaidalka, R.L. Meng, Y.Y. Sun, N. Kolev, M. V. Abrashev, Raman spectroscopy of low-temperature (Pnma) and high-temperature (R-3c) phases of LaCrO3, Phys. Rev. B. 74 (2006) 214301 1-7. doi:10.1103/PhysRevB.74.214301.

[47] M.C. Weber, J. Kreisel, P.A. Thomas, M. Newton, K. Sardar, R.I. Walton, Phonon raman scattering of RCrO3 perovskites (R=Y, La, Pr, Sm, Gd, Dy, Ho, Yb, Lu), Phys. Rev. B. 85 (2012) 054303 1-9. doi:10.1103/PhysRevB.85.054303.

[48] G.A. Tompsett, N.M. Sammes, Characterisation of the SOFC material, LaCrO3, using vibrational

spectroscopy, J. Power Sources. 130 (2004) 1–7. doi:10.1016/j.jpowsour.2003.11.057.

[49] A. Neumann, D. Walter, The thermal transformation from lanthanum hydroxide to lanthanum hydroxide oxide, Thermochim. Acta. 445 (2006) 200–204. doi:10.1016/j.tca.2005.06.013.

[50] Y. Hakuta, H. Ura, H. Hayashi, K. Arai, Continuous production of BaTiO3 nanoparticles by hydrothermal synthesis, Ind. Eng. Chem. Res. 44 (2005) 840–846. doi:10.1021/ie049424i.

[51] S. Pirou, J. Gurauskis, V. Gil, M. Søgaard, P.V. Hendriksen, A. Kaiser, S. Ovtar, R. Kiebach, Oxygen permeation flux through 10Sc1YSZ-MnCo2O4 asymmetric membranes prepared by two-step sintering, Fuel Process. Technol. 152 (2016) 192–199. doi:10.1016/j.fuproc.2016.06.019.

[52] J. Yi, Y. Zuo, W. Liu, L. Winnubst, C. Chen, Oxygen permeation through a Ce0.8Sm0.2O2-δ-La0.8Sr 0.2CrO3-δ dual-phase composite membrane, J. Memb. Sci. 280 (2006) 849–855. doi:10.1016/j.memsci.2006.03.011.

[53] J.B. Webb, M. Sayer, A. Mansingh, Polaronic conduction in lanthanum strontium chromite, Can. J. Phys. 55 (1977) 1725–1731. doi:10.1139/p77-217.

Chapter VII. Continuous hydrothermal flow synthesis of $Co_{1-x}Ni_xFe_2O_4$ (x = 0 – 0.8) ferrite nanoparticles as catalysts for the CO oxidation and the oxygen evolution reaction

This chapter contains the manuscript 'Continuous Hydrothermal Flow Synthesis of $Co_{1-x}Ni_xFe_2O_4$ (x = 0 – 0.8) Ferrite Nanoparticles As Catalysts for the CO Oxidation and Oxygen Evolution Reaction' that is ready for submission.

Well crystallized $CoFe_2O_4$ and Ni-substituted $CoFe_2O_4$ ($Co_{1-x}Ni_xFe_2O_4$) nanoparticles were prepared by CHFS with a residence time of ~29 s. The activity of the synthesized $CoFe_2O_4$ nanoparticles in the catalytic CO oxidation process was evaluated. A conversion of 50% in CO was achieved at 223 °C and 100% at 310 °C when $CoFe_2O_4$ synthesized by CHFS was used as catalyst. Activity of the synthesized Ni-substituted $CoFe_2O_4$ nanoparticles with different Ni contents was evaluated in the oxygen evolution reaction. No schematic variation with Ni content in the catalytic activity of these materials was observed. However, a remarkable improvement of the activity was observed with $Co_{0.7}Ni_{0.3}Fe_2O_4$, where the overpotential (0.435 V) required for 10 mA cm^{-2} was comparable with that (0.443 V) of the commercial IrO_2 benchmark.

Continuous Hydrothermal Flow Synthesis of $Co_{1-x}Ni_xFe_2O_4$ (x = 0 - 0.8) Ferrite Nanoparticles: Catalysts in the CO Oxidation and in the Oxygen Evolution Reaction

Yu Xu [1,*], Fatih Özcan [2], Philipp Zielke [1], Stefanie Hoffmann [2], Manuel Heimann [2], Justus Heese [2], Kalapu Chakrapani [2], Malte Behrens [2], Søren Bredmose Simonsen [1], Poul Norby [1], Peter Vang Hendriksen [1], Ragnar Kiebach [1]

[1] Department of Energy Conversion and Storage, Technical University of Denmark (Risø campus), Frederiksborgvej 399, 4000 Roskilde, Denmark

[2] Faculty of Inorganic Chemistry and CENIDE, University of Duisburg-Essen, Universitätsstr. 7, 45141 Essen, Germany

* Correspondence: Y. Xu, Email: yuax@dtu.dk, Tel.: +45 93511148

Abstract

Well-crystallized $CoFe_2O_4$ and Ni-substituted $CoFe_2O_4$ nanoparticles were prepared by continuous hydrothermal flow synthesis (CHFS). Catalytic properties of the synthesized $Co_{1-x}Ni_xFe_2O_4$ nanoparticles in the i) catalytic oxidation of CO, and ii) electrochemical oxygen evolution reaction (OER) were studied. A conversion of 50% in CO was reached at 223 °C and 100% at 310 °C when $CoFe_2O_4$ synthesized by CHFS was loaded as catalyst. The effect of Ni substitution on the OER activity of as-synthesized $Co_{1-x}Ni_xFe_2O_4$ did not show a clear trend, however a remarkable improvement of the activity was observed with $Co_{0.7}Ni_{0.3}Fe_2O_4$.

Keywords: continuous flow synthesis; hydrothermal; cobalt ferrite; nanoparticle; CO oxidation; oxygen evolution reaction; water splitting

1. Introduction

Ferrite oxides, well known for their magnetic applications [1,2], are also attractive for their uses as catalysts in the oxygen evolution reaction [3,4] and organic decomposition processes [5]. The spinel-type structure (AB_2O_4, A and B are di- and trivalent metal cations) enables incorporating transition

metal elements in wide combinations, which provides versatile materials available to be tuned in composition, electronic structure and redox properties for specific catalytic applications. Moreover, the use of earth-abundant transition metal elements is appealing, due to the relatively low cost.

In general, heterogeneous catalysis is a surface reaction process, and the activity of a catalyst largely depends on the exposed surface area that determines the amount of the 'active sites' [6]. Therefore, the study on nanosized catalysts account for a large proportion in the efforts to searching for catalysts with high performance [4,7,8]. In addition, nanomaterials usually display different physicochemical properties in comparison with the bulk materials [9]. Examples of such 'size effect' have also be reported in heterogeneous catalysis [10,11].

Among all approaches available for synthesizing nanomaterials, continuous hydrothermal flow synthesis (CHFS) [12,13] in a flow-type apparatus (CHFS reactor) by using (near-) supercritical water (scH_2O, $T \geq 647$ K, $p \geq 22.1$ MPa) as the reaction medium is very attractive because of its relatively simple and scalable operation. It is usually realized by mixing a scH_2O flow and a precursor flow in a mixer within a CHFS reactor, and the synthesized materials are collected as slurries at the reactor outlet. The physicochemical properties of water, particularly its density and dielectric constant, significantly change at (near-) supercritical conditions, which affects the solvent power of water and the hydrothermal reaction rate [14]. As a result, a high degree of supersaturation is achieved and nucleation starts almost instantaneously upon mixing. To date, various types of nanomaterials prepared by CHFS have been reported, including oxides [15–17], metals [18], sulfides [19], and metal organic frameworks (MOFs) [20]. In addition, upscaled operations in an industrial level have been tested in a pilot plant [21], a commercial plant (Hanwha Chemical Corp., Republic of Korea) [22], and in the European FP7 project SHYMAN (www.shyman.eu). While hydrothermal synthesis is widely used in catalyst synthesis, CHFS is strongly underrepresented in this field, despite the facts that reproducibility and upscaling are serious issues in the synthesis of many heterogeneous catalysts.

Preparing ferrite ($MeFe_2O_4$, Me = divalent metal cations) nanoparticles by CHFS has also been reported [23–27]. Similar to other complex oxides, syntheses of spinel-type oxides by CHFS require a fine control of conditions especially when the solubilities of the composing metal cations are rather different with each other. For instance, efforts were made to tune the parameters of a CHFS process including the pH, residence time, reactor geometry and temperature to inhibit nucleation of Fe_2O_3 that would otherwise be present as a secondary phase besides ferrites since Fe based oxides have the lowest solubility compared with Ni-, Co-, Cu-, Zn- and Mg-based oxides [23,25–27].

$CoFe_2O_4$ was under focus in this work that uniform $CoFe_2O_4$ nanoparticles were prepared by CHFS. The activity of the as-synthesized $CoFe_2O_4$ nanoparticles was studied in oxygen evolution reaction in 1 mol L^{-1} KOH and in CO oxidation. Further, partial substitution of Co by Ni in $CoFe_2O_4$ nanoparticles with various compositions were prepared by CHFS, and the effect of chemical composition on the activity was studied with respect to their performance in the oxygen evolution reaction.

2. Experimental

2.1 Materials

$Co(NO_3)_2$•$6H_2O$ (98.0 – 102.0 %, ACS, Alfa Aesar) and $Fe(NO_3)_3$•$9H_2O$ (98.0 – 101.0 %, ACS, Alfa Aesar) were dissolved in deionized water (DI H_2O) with concentrations of 0.01 mol L^{-1} Co (II) and 0.02 mol L^{-1} Fe (III) as the reactant solutions for the syntheses of $CoFe_2O_4$. Solutions with concentrations of 0.02 mol L^{-1} [Co (II) + Ni (II)] and 0.04 mol L^{-1} Fe (III) were used for the syntheses of Ni-substituted $CoFe_2O_4$. NaOH pellets (≥98 %, Sigma Aldrich) were dissolved in DI H_2O with a concentration of 0.15 mol L^{-1} for the syntheses of $CoFe_2O_4$ and 0.3 mol L^{-1} for the syntheses of Ni-substituted $CoFe_2O_4$. IrO_2 (99.9 %, Sigma Aldrich) was used as the benchmark.

2.2 CHFS of ferrite nanoparticles in scH_2O

An in-house developed two-stage continuous flow-type apparatus (CHFS reactor) was used to conduct the syntheses, details of which were reported previously [28]. Briefly, two mixers (stages)

are integrated in series within the reactor. The first mixer with a co-flow pipe-in-pipe geometry was used to mix the scH_2O flow fed by a 1/16″ capillary with the precursor flow fed from two side arms of a 1/4″ encapsulating pipe. The precursor was a premixture of the Co (and Ni) and Fe nitrates solution (reactant solution) and the NaOH solution. Each solution was fed to the reactor by separate pumps, but they were mixed at a T-junction upstream of the first mixer. The outflow of the first mixer was fed subsequently to the second mixer with a counter-current geometry, and was mixed with an upward inlet flow at the room temperature that was DI H_2O here (to mitigate sedimentation), but could alternatively be another precursor of a second material [28]. The outflow of the second mixer passed subsequently through a re-heater. The outflow of the re-heater was rapidly cooled down to the room temperature by a water-cooled tube-in-tube heat exchanger. After passing an in-line filter (Swagelok, 90-µm pore size), the product flow was depressurized to atmospheric pressure by a backpressure regulator (Tescom, 26-1700 Series). Three thermocouples were inserted into the reactor, one to measure the temperature (T_1) of the fed scH_2O flow, one to measure the temperature (T_2) of the outflow of the second mixer and the third one to measure the temperature (T_3) of the outflow after the re-heater. During synthesis, T_1, T_2, and T_3 were maintained at 396 °C, 290 °C and 390 °C, respectively. The estimated residence time (*t)* was ~29 s (see definition of *t* in [26]). The synthesized particles were collected as colloidal slurries at the reactor outlet. A schematic description of the two-stage CHFS reactor is presented in **Fig. 1**.

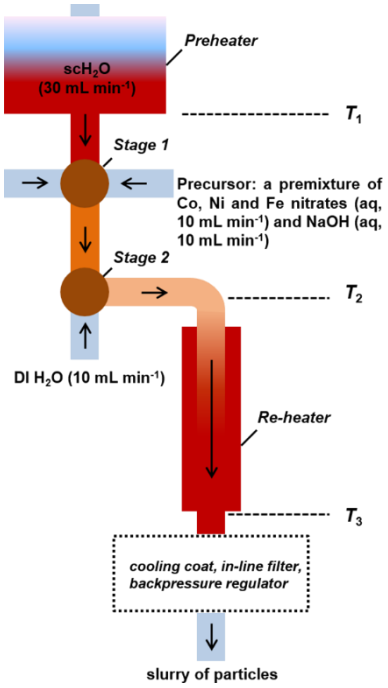

Figure 1. Schematic of the preparation of particles by CHFS. The total flow rate was 60 mL min^{-1} and the pressure was kept at 30 MPa.

2.3 Characterization of ferrite nanoparticles

Particles were separated from slurries by centrifugation, then cleaned with DI H_2O and dried at ambient conditions. Powder X-ray diffraction patterns were obtained from the particles on a Bruker Robot D8 diffractometer (Cu Kα radiation 0.154 nm, 10 – 90° using a stepsize of 0.01°). For TEM characterization, the particles were re-dispersed in ethanol by means of ultrasonic treatment and dropped onto a holey carbon film/Au grid. Bright field TEM (BF-TEM) and high-resolution TEM (HR-TEM) images were recorded with a JEOL 3000F microscope operating at 300 kV with a field emission gun. To analyze the elemental composition of the particles, they were loaded on carbon tapes and a Hitachi Tabletop TM3000 ('Analysis', 15 kV charge-reduction mode) equipped with a silicon drift detector (SDD, energy resolution 154 eV) was used to perform a standardless quantification EDS analysis.

The particles' specific surface area was measured by N_2 adsorption experiments performed at -196 °C (Brunauer–Emmett–Teller theory) by using a SA 3100 setup (Beckman Coulter, Inc.). The

samples were first degassed at 80 °C for 2 h in vacuum. BET surface area was calculated from p/p_0 data between 0.07 and 0.3.

2.4 CO oxidation

Temperature programmed CO oxidation experiments were conducted in a BELCAT-B (BEL Japan, Inc.) catalyst analyzer at a same linear heating rate (3 °C min^{-1}) for all samples between room temperature and 350 °C [29]. The later was maintained for 5 min before cooling down. The $CoFe_2O_4$ particles (by CHFS and reference) were first mildly pressed and a sieve fraction of the pressed particles ranging from 250 to 355 µm was used, and was mixed with SiC powders (>355 µm) in a weight ratio 1 to 2. Afterwards, samples (40 mg $CoFe_2O_4$ and 80 mg SiC) were placed on a fixed bed stabilized by quartz wool in a U-shaped cell. Prior to tests, samples were dried at 100 °C for 60 min in He (80 mL min^{-1}). During test, a flow of 3 vol% CO and 6 vol% O_2 in He at 80 mL min^{-1} was passed through the bed. The inlet gas flow was controlled by a mass flow controller while the outlet gas was analyzed by the equipped quadropole mass spectrometer (Pfeiffer Vacuum, Germany).

2.5 Electrochemical measurements for OER

The activity of the nanoparticles for the oxygen evolution reaction (OER) was evaluated using electrochemical measurements. All the measurements were conducted with a conventional three-electrode cell using an Autolab potentiostat/galvanostat (PGSTAT12, Eco Chemie, Utrecht, Netherlands) coupled to a Metrohm RDE rotator [4]. A disc glassy carbon electrode (diameter 0.3 cm, geometric area 0.07069 cm^2) modified with the catalyst inks was used as the working electrode, a silver / silver chloride electrode (Ag/AgCl, 3 mol L^{-1} KCl) as the reference electrode and a platinum foil as the counter electrode. The measured potentials were converted to the reversible hydrogen electrode (RHE) using the following equation $E_{RHE} = E_{Ag/AgCl} + 0.210\ V + 0.059\ pH$. The pH was determined using a pH meter and was 14 for 1 mol L^{-1} KOH.

The glassy carbon electrode was polished on a polishing cloth using alumina paste (0.05 µm) to obtain a mirror-like surface, followed by ultrasonic cleaning in DI H_2O. The catalyst suspension was

prepared by dispersing 2.5 mg nanoparticles in 498 µL mixture of ethanol and DI H_2O (1 to 1 in volume ratio) added with 2 µL Nafion 117 solution (Sigma Aldrich) and was sonicated for 20 min. The catalyst suspension of 3 µL was drop-coated onto the polished glassy carbon electrode with a mass loading of 0.21 mg cm^{-2} and was dried in air at room temperature. Before the OER measurements, the prepared electrode was subjected to continuous potential cycling in the potential window of 1 V to 1.45 V vs. RHE until reproducible cyclic voltammogram was obtained. Impedance spectroscopy was recorded in the frequency range from 50 kHz to 1 Hz at the corresponding open circuit potential of the electrode, using an AC perturbation of 10 mV. The resistance of the solution R_s was determined from the resulting Nyquist plot, and later was used for ohmic drop correction to the potential applied on the working electrode, according to the relation $E_c = E_m - i R_s$, where E_c and E_m are the corrected and applied potentials respectively and i is the current. For the OER test, measurements were performed by sweeping the potential from 0 V anodically to 0.8 V at 5 mV s^{-1} with the electrode rotating at 1600 rpm. Current densities were calculated using the geometric surface area of the glassy carbon electrode disk.

3. Results and Discussion

3.1 CHFS of $Co_{1-x}Ni_xFe_2O_4$

Cobalt ferrite particles without Ni (x = 0) were prepared by CHFS. **Fig. 2** presents the XRD pattern and BF-TEM image of the synthesized particles. All peaks in the experimental pattern (**Fig. 2a**) were well indexed to those deriving from $CoFe_2O_4$ with a cubic phase (Fd-3m, ICSD *PDF* 22-1086). Moreover, the pronounced peak broadening indicates that the synthesized particles had a nanoscale crystallite size that was estimated from the FWHM by the Scherrer equation to be 12 – 14 nm. The obtained $CoFe_2O_4$ nanoparticles were uniform in both size and morphology, as shown in **Fig. 2b**. Well-crystallized $CoFe_2O_4$ nanoparticles with an octahedron morphology were obtained that were observed as either a rhombohedral or a square projection. A fast Fourier transform (FFT) of the BF-TEM image is presented as an inset in **Fig. 2b**. It shows spotty ring patterns indicating that the

particles were randomly oriented. Moreover, determined by the radius, the rings were separately assigned to the three crystal planes (111), (220) and (311) of $CoFe_2O_4$ crystals.

In a CHFS process, the solubilities of metal cations in a solution under applied conditions significantly affect the conversion rates from metal cations to oxides [30]. Due to the relatively low solubility of Fe-hydrated intermediates, Fe (III) almost fully converts to Fe_2O_3 polymorphs even in an acidic condition [25]. The results presented here therefore show that the applied condition (*T*, pH and residence time) was suitable for forming supersaturations of both Fe and Co to a similar degree, as no Fe_2O_3 polymorphs, typical secondary phases reported previously [23,25,26], were found within the detection limit of XRD in the synthesized nanoparticles.

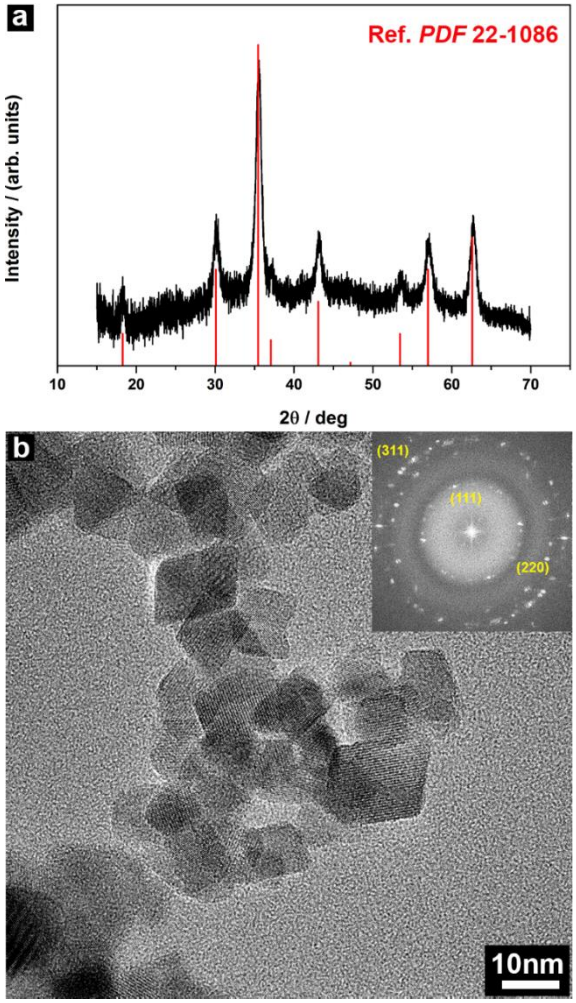

Figure 2. (**a**) XRD pattern of the $CoFe_2O_4$ particles; reference peaks are from $CoFe_2O_4$ (cubic, Fd-3m, ICSD *PDF* 22-1086); (**b**) BF-TEM image of the $CoFe_2O_4$ particles; the inset is a FFT of the image.

The same synthesis conditions (390 °C, molar ratio n[metal cations] : n[NaOH] = 0.2) were applied to prepare Ni-substituted $CoFe_2O_4$ with various Co:Ni ratios. Results are summarized in **Table 1**. For all synthesized particles, the elemental composition determined by standardless EDS quantification was in accordance with the nominal composition of the corresponding precursor solution, indicating that a similar conversion rate for Ni, Co and Fe was achieved during CHFS. XRD patterns of the particles with different Ni contents are presented in **Fig. 3**. All peaks in the diffraction pattern were assigned to $CoFe_2O_4$ with a cubic phase (Fd-3m, ICSD *PDF* 22-1086), which was independent on the Ni content (x). However, with increasing x, the diffraction peaks gradually shifted to higher 2θ positions, e.g., peaks deriving from (311) planes shown in **Fig. 3b**. This could be because of the contraction of unit cells as a result of Co (ionic radii: 4-coordinate 58 pm, 6-coordinate 75 pm) within the crystal lattice being replaced by Ni (ionic radii: 4-coordinate 55 pm, 6-coordinate 69 pm) [31]. No clear influence of Ni doping on the crystallite size nor BET surface area of particles prepared by CHFS were observed. In summary, CHFS is suitable for preparing homogeneous well-crystallized $Co_{1-x}Ni_xFe_2O_4$ nanoparticles with a controlled composition.

Table 1. $Co_{1-x}Ni_xFe_2O_4$ particles prepared by CHFS

Sample name	**Composition** [a] **Co : Ni : Fe**	**Crystallite size** [b] **/ nm**	**BET surface area / m^2 g^{-1}**
$CoFe_2O_4$	0.35 : 0 : 0.65	12 – 14	90
$Co_{0.9}Ni_{0.1}Fe_2O_4$	0.31 : 0.03 : 0.66	13 – 16	83
$Co_{0.7}Ni_{0.3}Fe_2O_4$	0.26 : 0.10 : 0.64	15 – 18	95
$Co_{0.6}Ni_{0.4}Fe_2O_4$	0.20 : 0.14 : 0.66	15 – 18	69
$Co_{0.5}Ni_{0.5}Fe_2O_4$	0.17 : 0.17 : 0.66	15 – 16	81
$Co_{0.4}Ni_{0.6}Fe_2O_4$	0.14 : 0.20 : 0.66	15 – 18	84
$Co_{0.2}Ni_{0.8}Fe_2O_4$	0.08 : 0.28 : 0.64	14 – 20	104

Notes: (1) a is the composition in atomic percent, which was obtained by standardless EDS quantification; the total amount of Ni, Co and Fe was normalized to 1. (2) b describes the crystallite size estimated by the Scherrer equation from the FWHMs of XRD peaks corresponding to (220), (311) and (400) planes.

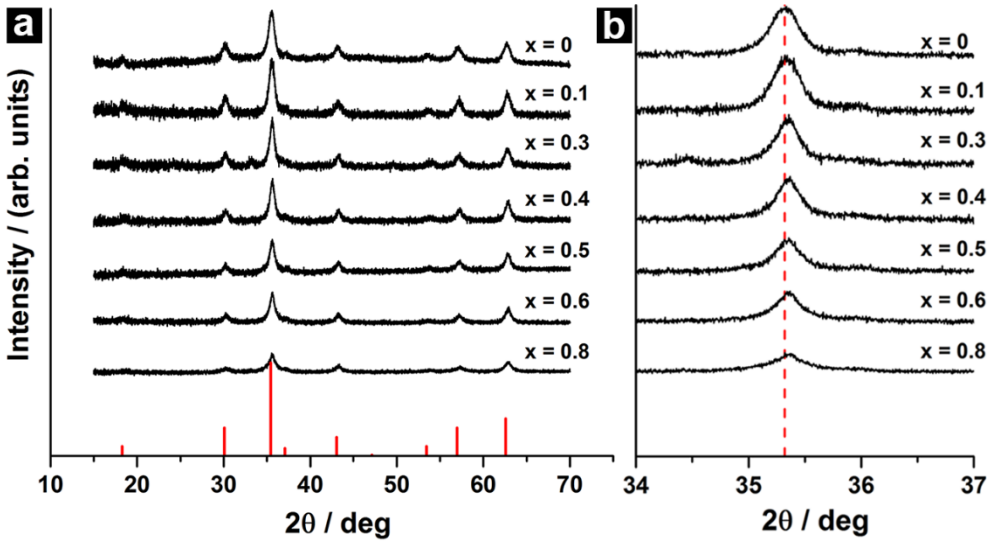

Figure 3. (**a**) XRD patterns of $Co_{1-x}Ni_xFe_2O_4$ particles; reference peaks are from $CoFe_2O_4$ (cubic, Fd-3m, ICSD *PDF* 22-1086); (**b**) zoom-in on peaks of the XRD patterns corresponding to (311) planes; the red dashed line shows the 2θ position of the peak in the reference pattern without Ni.

3.2 Catalytic CO oxidation by $CoFe_2O_4$

The catalytic properties of synthesized $CoFe_2O_4$ nanoparticles by CHFS was first evaluated in the catalytic CO oxidation reaction serving as a test reaction for the redox activity of the surface. The results are presented in **Fig. 4**, in which the CO conversion is plotted versus the temperature for experiments conducted at a linear heating rate.

The blank test without $CoFe_2O_4$ presented in the inset of **Fig. 4** shows that hardly any CO was oxidized throughout the measurement. In comparison, when synthesized $CoFe_2O_4$ nanoparticles were loaded as catalysts (**Fig. 4a**), CO started to be oxidized below 150 °C, and 50 % conversion was reached at T_{50} = 223 °C, and a full conversion was obtained at T_{100} = 310 °C. As a benchmark, the catalytic CO oxidation was also measured with another type of $CoFe_2O_4$ particles under identical conditions (**Fig. 4b**). This material was synthesized by pH-controlled (pH = 8.5) coprecipitation of a layered double hydroxide precursor followed by calcination at 600 °C for 3h in air yielding $CoFe_2O_4$ with a unique microstructure consisting of holey platelets. This material was recently shown to be a more active catalyst in the OER compared to commercial $CoFe_2O_4$ and more selective to propene

in the oxidative dehydration of 2-propanol [32]. It can been seen that at all temperatures the CO conversion rate was lower with this type of $CoFe_2O_4$ particles. The CO conversion reached 50 % at T_{50} = 325 °C, and no full conversion was achieved in the investigated temperature range up to 350°C. One possible explanation is that the $CoFe_2O_4$ nanoparticles prepared by CHFS had a smaller average particle size with more active sites exposed, as shown by the difference between BET specific surface areas (90 $m^2\ g^{-1}$ for $CoFe_2O_4$ by CHFS, and 33 $m^2\ g^{-1}$ for the benchmark $CoFe_2O_4$ by coprecipitation and calcination).

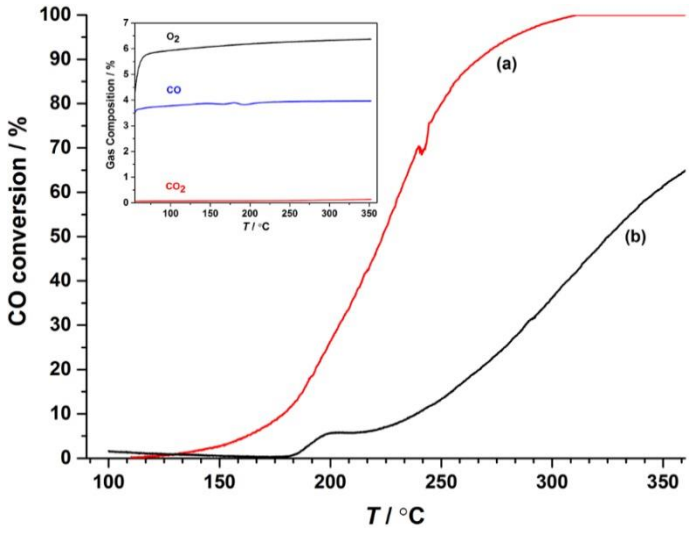

Figure 4. CO conversion rate as a function of temperature for synthesized $CoFe_2O_4$ nanoparticles by CHFS (**a**) and benchmark $CoFe_2O_4$ particles by coprecipitation and calcination (**b**); the inset shows the composition of the outlet gas flow in the blank test without catalyst.

3.3 Activity of $Co_{1-x}Ni_xFe_2O_4$ in electrochemical OER

The activity of as-synthesized $CoFe_2O_4$ (x = 0) and Ni-containing $Co_{1-x}Ni_xFe_2O_4$ (x = 0, 0.1, 0.3, 0.4, 0.5, 0.6, 0.8) nanoparticles in the OER process was evaluated electrochemically using a three-electrode electrochemical cell with a rotating disk configuration. **Fig. 5a** presents the linear sweep voltammetry curves of all synthesized nanoparticles in the OER process in 1 mol L^{-1} KOH solution. The onset potentials for an apparent anodic current of the OER for all samples were within 1.625 – 1.65 V (vs. RHE), with the exception that a much lower onset potential (< 1.60 V) was recorded for catalyst containing 30 at% Ni, i.e. $Co_{0.7}Ni_{0.3}Fe_2O_4$. The overpotential required for a current density of

10 mA cm^{-2}, a benchmark corresponding to a 10 % efficient solar-to-fuels conversion device [3], was used to compare the activity of the nanoparticles, as shown in **Fig. 5b**. For reference, the overpotential measured with a commercial IrO_2 benchmark at the same condition was 0.443 V. It seems that in most cases substituting Co by Ni into $CoFe_2O_4$ increased the overpotential (x = 0.1, 0.4, 0.5 and 0.6) by 4 – 21 mV, however no simple correlation between the Ni content and the overpotential could be observed. This is in contrast to a recent study on $Co_{1-x}Ni_xFe_2O_4$ colloidal nanoparticles, where the mixed oxides showed lower overpotential than pure $CoFe_2O_4$ or $NiFe_2O_4$ and a clear minimum was observed for $Co_{0.5}Ni_{0.5}FeO_4$, which was explained by lower binding energy differences between adsorbed O and OH [4]. However, $Co_{0.7}Ni_{0.3}Fe_2O_4$ with 30 at% Ni stands out, as the reduced overpotential of the partially Ni-substituted cobalt ferrite electrocatalyst was also confirmed in this study. It showed a remarkably lower overpotential (0.435 V) at a current density of 10 mA cm^{-2}, which is comparable to the value (0.443 V) obtained with IrO_2 benchmark at an identical condition.

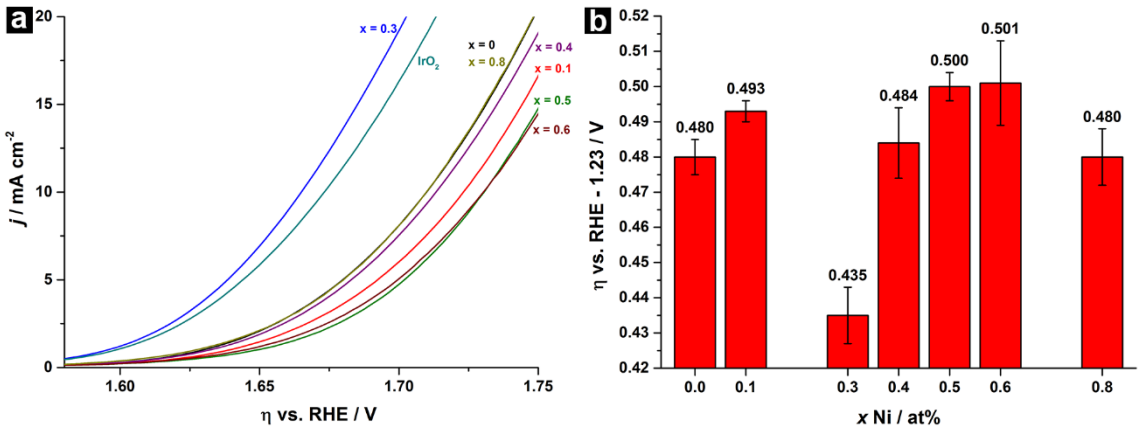

Figure 5. (**a**) Polarization curves of synthesized $Co_{1-x}Ni_xFe_2O_4$ nanoparticles by CHFS measured by linear sweep voltammetry showing activities towards OER in 1 mol L^{-1} KOH solution; scan rate 5 mV s^{-1}. (b) Overpotential η vs. RHE – 1.23 V at 10 mA cm^{-2}. The overpotential measured with IrO_2 benchmark at an identical condition is 0.443 V.

4. Conclusion

Well-crystallized $CoFe_2O_4$ and $Ni_xCo_{1-x}Fe_2O_4$ (x = 0.1, 0.3, 0.4, 0.5, 0.6 and 0.8) nanoparticles were synthesized by the continuous hydrothermal flow synthesis (CHFS) method with a short residence

time (~29 s). Catalytic properties of the synthesized $CoFe_2O_4$ nanoparticles in the catalytic CO oxidation and electrochemical oxygen evolution reaction (OER) were evaluated separately. CO was oxidized with a conversion of 50 % at 223 °C and a full conversion was achieved at 310 °C when $CoFe_2O_4$ prepared by CHFS was loaded as the catalyst. The effect of Ni dopant on the OER activity of as-synthesized $Co_{1-x}Ni_xFe_2O_4$ did not show clear trend however a remarkable improvement of the activity was observed with $Co_{0.7}Ni_{0.3}Fe_2O_4$ as the overpotential (0.435 V for 10 mA cm^{-2}) was comparable with that of the commercial IrO_2 benchmark (0.443 V).

References

[1] I.H. Gul, F. Amin, A.Z. Abbasi, M. Anis-ur-Rehman, A. Maqsood, Physical and magnetic characterization of co-precipitated nanosize Co-Ni ferrites, Scr. Mater. 56 (2007) 497–500. doi:10.1016/j.scriptamat.2006.11.020.

[2] D. Carta, M.F. Casula, A. Falqui, D. Loche, G. Mountjoy, C. Sangregorio, A. Corrias, A Structural and magnetic investigation of the inversion degree in ferrite nanocrystals MFe2O4 (M = Mn, Co, Ni), J. Phys. Chem. C. 113 (2009) 8606–8615. doi:10.1021/jp901077c.

[3] C.C.L. McCrory, S. Jung, J.C. Peters, T.F. Jaramillo, Benchmarking heterogeneous electrocatalysts for the oxygen evolution reaction, J. Am. Chem. Soc. 135 (2013) 16977–16987. doi:10.1021/ja407115p.

[4] K. Chakrapani, G. Bendt, H. Hajiyani, I. Schwarzrock, T. Lunkenbein, S. Salamon, J. Landers, H. Wende, R. Schlögl, R. Pentcheva, M. Behrens, S. Schulz, Role of composition and size of cobalt ferrite nanocrystals in the oxygen evolution reaction, ChemCatChem. (2017). doi:10.1002/cctc.201700376.

[5] A. Urdă, A. Herraïz, Á. Rédey, I.C. Marcu, Co and Ni ferrospinels as catalysts for propane total oxidation, Catal. Commun. 10 (2009) 1651–1655. doi:10.1016/j.catcom.2009.05.002.

[6] Y. Sun, S. Gao, F. Lei, Y. Xie, Atomically-thin two-dimensional sheets for understanding active sites in catalysis, Chem. Soc. Rev. 44 (2015) 623–636. doi:10.1039/C4CS00236A.

[7] Y. Dou, T. Liao, Z. Ma, D. Tian, Q. Liu, F. Xiao, Z. Sun, J. Ho Kim, S. Xue Dou, Graphene-like holey Co3O4 nanosheets as a highly efficient catalyst for oxygen evolution reaction, Nano Energy. 30 (2016) 267–275. doi:10.1016/j.nanoen.2016.10.020.

[8] C. Singh, A. Goyal, S. Singhal, Nickel-doped cobalt ferrite nanoparticles: efficient catalysts for the reduction of nitroaromatic compounds and photo-oxidative degradation of toxic dyes, Nanoscale. 6 (2014) 7959. doi:10.1039/c4nr01730g.

[9] E. Roduner, Size matters: why nanomaterials are different, Chem. Soc. Rev. 35 (2006) 583–592. doi:10.1039/b502142c.

[10] B.-Z. Zhan, M.A. White, T. Sham, J.A. Pincock, J. Doucet, K.V.R. Rao, K.N. Robertson, T.S. Cameron, Zeolite-confined nano-RuO2: a green, selective, and efficient catalyst for aerobic alcohol oxidation, J. Am. Chem. Soc. 125 (2003) 2195–2199. doi:10.1021/ja0282691.

[11] A.M. Molenbroek, S. Helveg, H. Topsøe, B.S. Clausen, Nano-particles in heterogeneous catalysis, Top. Catal. 52 (2009) 1303–1311. doi:10.1007/s11244-009-9314-1.

[12] T. Adschiri, K. Kanazawa, K. Arai, Rapid and continuous hydrothermal crystallization of metal oxide particles in supercritical water, J. Am. Ceram. Soc. 75 (1992) 1019–1022. doi:10.1111/j.1151-

2916.1992.tb04179.x.

[13] P.W. Dunne, A.S. Munn, C.L. Starkey, T.A. Huddle, E.H. Lester, Continuous-flow hydrothermal synthesis for the production of inorganic nanomaterials, Philos. Trans. A. 373 (2015) 20150015. doi:10.1098/rsta.2015.0015.

[14] T. Adschiri, Y. Hakuta, K. Arai, Hydrothermal synthesis of metal oxide fine particles at supercritical conditions, Ind. Eng. Chem. Res. 39 (2000) 4901–4907. doi:10.1021/ie0003279.

[15] A. Nugroho, J. Kim, Effect of KOH on the continuous synthesis of cobalt oxide and manganese oxide nanoparticles in supercritical water, J. Ind. Eng. Chem. 20 (2014) 4443–4446. doi:10.1016/j.jiec.2014.02.014.

[16] C. Slostowski, S. Marre, J.-M. Bassat, C. Aymonier, Synthesis of cerium oxide-based nanostructures in near- and supercritical fluids, J. Supercrit. Fluids. 84 (2013) 89–97. doi:10.1016/j.supflu.2013.09.014.

[17] Y. Shen, J.R. Eltzholtz, B.B. Iversen, Controlling size, crystallinity, and electrochemical performance of Li4Ti5O12 nanocrystals, Chem. Mater. 25 (2013) 5023–5030. doi:10.1021/cm402366y.

[18] S. Kubota, T. Morioka, M. Takesue, H. Hayashi, M. Watanabe, R.L. Jr. Smith, Continuous supercritical hydrothermal synthesis of dispersible zero-valent copper nanoparticles for ink applications in printed electronics, J. Supercrit. Fluids. 86 (2014) 33–40. doi:10.1016/j.supflu.2013.11.013.

[19] P.W. Dunne, C.L. Starkey, M. Gimeno-Fabra, E.H. Lester, The rapid size- and shape-controlled continuous hydrothermal synthesis of metal sulphide nanomaterials, Nanoscale. 6 (2014) 2406–2418. doi:10.1039/c3nr05749f.

[20] P.W. Dunne, E. Lester, R.I. Walton, Towards scalable and controlled synthesis of metal–organic framework materials using continuous flow reactors, React. Chem. Eng. 1 (2016) 352–360. doi:10.1039/C6RE00107F.

[21] R.I. Gruar, C.J. Tighe, J.A. Darr, Scaling-up a confined jet reactor for the continuous hydrothermal manufacture of nanomaterials, Ind. Eng. Chem. Res. 52 (2013) 5270–5281. doi:10.1021/ie302567d.

[22] T. Adschiri, Y.-W. Lee, M. Goto, S. Takami, Green materials synthesis with supercritical water, Green Chem. 13 (2011) 1380–1390. doi:10.1039/c1gc15158d.

[23] L.J. Cote, A.S. Teja, A.P. Wilkinson, Z.J. Zhang, Continuous hydrothermal synthesis of CoFe2O4 nanoparticles, Fluid Phase Equilib. 210 (2003) 307–317. doi:10.1016/S0378-3812(03)00168-7.

[24] N. Millot, B. Xin, C. Pighini, D. Aymes, Hydrothermal synthesis of nanostructured inorganic powders by a continuous process under supercritical conditions, J. Eur. Ceram. Soc. 25 (2005) 2013–2016. doi:10.1016/j.jeurceramsoc.2005.03.202.

[25] K. Sue, M. Aoki, T. Sato, D. Nishio-Hamane, S. Kawasaki, Y. Hakuta, Y. Takebayashi, S. Yoda, T. Furuya, T. Sato, T. Hiaki, Continuous hydrothermal synthesis of nickel ferrite nanoparticles using a

central collision-type micromixer: effects of temperature, residence time, metal salt molality, and NaOH addition on conversion, particle size, and crystal phase, Ind. Eng. Chem. Res. 50 (2011) 9625–9631. doi:10.1021/ie200036m.

[26] T. Sato, K. Sue, W. Suzuki, M. Suzuki, K. Matsui, Y. Hakuta, H. Hayashi, K. Arai, S. Kawasaki, A. Kawai-Nakamura, T. Hiaki, Rapid and continuous production of ferrite nanoparticles by hydrothermal synthesis at 673 K and 30 MPa, Ind. Eng. Chem. Res. 47 (2008) 1855–1860. doi:10.1021/ie071168x.

[27] T. Sasaki, S. Ohara, T. Naka, J. Vejpravova, V. Sechovsky, M. Umetsu, S. Takami, B. Jeyadevan, T. Adschiri, Continuous synthesis of fine MgFe2O4 nanoparticles by supercritical hydrothermal reaction, J. Supercrit. Fluids. 53 (2010) 92–94. doi:10.1016/j.supflu.2009.11.005.

[28] P. Zielke, Y. Xu, S.B. Simonsen, P. Norby, R. Kiebach, Simulation, design and proof-of-concept of a two-stage continuous hydrothermal flow synthesis reactor for synthesis of functionalized nano-sized inorganic composite materials, J. Supercrit. Fluids. 117 (2016) 1–12. doi:10.1016/j.supflu.2016.06.008.

[29] K.F. Ortega, D. Rein, C. Lüttmann, J. Heese, F. Özcan, M. Heidelmann, J. Folke, K. Kähler, R. Schlögl, M. Behrens, Ammonia decomposition and synthesis over multinary magnesioferrites: Promotional effect of Ga on Fe catalysts for the decomposition reaction, ChemCatChem. 9 (2017) 659–671. doi:10.1002/cctc.201601355.

[30] K. Sue, M. Suzuki, K. Arai, T. Ohashi, H. Ura, K. Matsui, Y. Hakuta, H. Hayashi, M. Watanabe, T. Hiaki, Size-controlled synthesis of metal oxide nanoparticles with a flow-through supercritical water method, Green Chem. 8 (2006) 634–638. doi:10.1039/b518291c.

[31] C. Singh, A. Goyal, S. Singhal, Nickel-doped cobalt ferrite nanoparticles: efficient catalysts for the reduction of nitroaromatic compounds and photo-oxidative degradation of toxic dyes, Nanoscale. 6 (2014) 7959–7970. doi:10.1039/c4nr01730g.

[32] K. Friedel Ortega, S. Anke, F. Özcan, S. Salamon, J. Heese, C. Andronescu, J. Landers, H. Wende, W. Schuhmann, M. Muhler, T. Lunkenbein, M. Behrens, Topotactic synthesis of porous cobalt ferrite platelets from a layered double hydroxide precursor and their application in oxidation catalysis, Chem. - A Eur. J. (2017). doi:10.1002/chem.201702248.

Chapter VIII. Summary

This thesis presents a study of continuous hydrothermal flow synthesis (CHFS) of functional oxide nanomaterials and their properties in applications. The thesis covers several activities, including modelling and constructing a two-stage CHFS reactor (Postdoc's work independent of the thesis), using the CHFS reactor to synthesize several types of oxide materials, characterization of synthesized materials, and testing them in specific applications.

To begin with, computational fluid dynamics simulations were employed to identify the most promising mixer geometries for a two-stage CHFS reactor. In addition, changes of the mixing behavior were evaluated on basis of variations in flow rates and geometry. With these inputs, a two-stage CHFS reactor was constructed. NiO and Y-doped ZrO_2 (YSZ) nanoparticles were synthesized separately using the newly built reactor working in a single-stage mode. Further, the two-stage mode of the CHFS reactor was tested with NiO and YSZ with respect to tailoring the morphology of the produced composite material.

A second fluorite-type oxide, Gd-doped CeO_2 (GDC), was then under focus. GDC nanoparticles were prepared by CHFS, of which the size, morphology and composition were tailored by varying the pH value. Particle sizes between 6 nm and 40 nm were obtained. The morphology was polyhedral (with flat surfaces or spherical-like) for small particles and octahedral for larger ones. A similar conversion of Ce and Gd, and consequently a stoichiometric composition, was achieved when alkaline conditions were applied. An up-scaled synthesis of $Gd_{0.2}Ce_{0.8}O_{2-\delta}$ nanoparticles was conducted afterwards, and inks made from the as-synthesized particles were formulated for inkjet printing. The inks showed good jetting behavior. GDC films were printed with the inks on green NiO-GDC substrates and on pre-sintered NiO-YSZ substrates, separately. For green NiO-GDC substrates, no dense films were formed, due to cracking of the printed films after drying (10- and 20-layered films) and after sintering (1- and 5-layered films). In comparison, dense continuous layers were observed in the sample with 10-layered films printed on pre-sintered NiO-YSZ substrates after firing at 1300 °C. The thin dense layer consisted of a YSZ layer (0.8 – 1 µm) covered by a GDC layer

(0.5 µm) decorated with GDC islands. Such a structure is expected to be attractive to solid oxide fuel cells. The dense thin layer fully covering the NiO-YSZ substrate could function as an electrolyte, which would reduce the Ohmic loss due to the significantly reduced thickness. Moreover, the disconnected GDC islands could provide a high number of active sites and a strong bonding to an applied cathode.

In addition to CHFS, the conventional hydrothermal synthesis route accommodated in an autoclave with a Teflon in-liner was used to prepare $(La_{0.6}Sr_{0.4})_{0.99}CoO_3$-$Gd_{0.2}Ce_{0.8}O_{2-\delta}$ particles with a core-shell structure (LSC-GDC) by precipitating $Gd_{0.2}Ce_{0.8}O_{2-\delta}$ nanoparticles on the surface of $(La_{0.6}Sr_{0.4})_{0.99}CoO_3$ particles. The integral shell, composed of ~6 nm large $Gd_{0.2}Ce_{0.8}O_{2-\delta}$ nanoparticles, was formed under a mild hydrothermal condition at 100 °C. The microstructural evolution of core-shell particles was investigated under two different sintering conditions (spark plasma sintering and conventional sintering). In both cases, nearly fully dense composites were obtained. A fine microstructure containing nanograins was obtained by spark plasma sintering, and the graded core-shell architecture was partially maintained. Phase transitions of $(La_{0.6}Sr_{0.4})_{0.99}CoO_3$ under the low oxygen partial pressure during spark plasma sintering resulted in the formation of $La_{2-x}SrCoO_4$, which, however, is not necessarily adverse for application in oxygen transport membranes or solid oxide cells. In comparison, the grain coarsening process was more pronounced when the core-shell particles were densified by conventional sintering. Coarse grains were found and the core-shell structure was lost in the final microstructure of the composite sintered conventionally.

The versatility of CHFS was later demonstrated in the preparation of $LaCrO_3$ with a perovskite-type structure. $LaCrO_3$ sub-micron particles (cube-shaped, 639 nm in edge size) were prepared by CHFS in supercritical water. A continuous production of phase-pure $LaCrO_3$ particles was achieved for the first time, at 410 °C and 28 MPa with a reaction time as short as 23 s. This remarkably increases the throughput in comparison with conventional hydrothermal batch-type synthesis. The synthesized $LaCrO_3$ particles were further used to prepare 10Sc1YSZ – $LaCrO_3$ dual-phase oxygen transport membranes with ~90 vol % density after sintering at 1400 °C. Oxygen permeation fluxes of up to 5

× 10^{-8} mol cm^{-2} s^{-1} were obtained with a 1-mm thick membrane tested in air/N_2 at 900 °C. Given that CHFS is relatively easy to scale up, a rapid, large-scale production of fine $LaCrO_3$ particles can be achieved. Moreover, using doped $LaCrO_3$ (prepared by CHFS) with a higher electric conductivity compared to the un-doped material is expected to allow manufacturing of oxygen transport membranes with a higher oxygen flux.

In the end, the scope was extended to the preparation of spinel-type ferrite oxides by the CHFS route. Well-crystallized $CoFe_2O_4$ and Ni-substituted $CoFe_2O_4$ ($Co_{1-x}Ni_xFe_2O_4$, x = 0.1, 0.3, 0.4, 0.5, 0.6 and 0.8) nanoparticles were synthesized. The catalytic properties of the synthesized $CoFe_2O_4$ nanoparticles for the CO oxidation and electrochemical oxygen evolution reaction (OER) were evaluated. A conversion of 50 % in CO was achieved at 223 °C and 100 % at 310 °C when $CoFe_2O_4$ was used as catalyst. The effect of Ni content in the substituted particles on the OER activity showed no simple trend, however a remarkable improvement of the activity was observed with $Co_{0.7}Ni_{0.3}Fe_2O_4$. The overpotential (0.435 V for 10 mA cm^{-2}) was comparable with that (0.443 V) of the commercial IrO_2 benchmark.

To summarize, the two-stage CHFS reactor working with the supercritical water showed its wide applicability to prepare nanomaterials ranging from simple oxides (NiO, YSZ and GDC) to complex oxides ($LaCrO_3$ and $Co_{1-x}Ni_xFe_2O_4$). The properties of the synthesized materials were evaluated in selected applications. Three ways of handling the particles were demonstrated: ‘all-wet’ processing of GDC nanoparticles into printable inks, conventional ceramic processing of $LaCrO_3$ particles, and use of as-synthesized $Co_{1-x}Ni_xFe_2O_4$ nanoparticles in their primary form in catalytic processes.

Chapter IX. Outlook

This chapter summarizes some of the primary learnings with CHFS, and then suggests future improvements on basis of these results.

Firstly, syntheses of oxides by CHFS where an oxidation step is required need to be optimized, in order to get phase-pure products. Secondly, two applications seem worthy to be continued: (1) a new design of cathodes in SOFC using composites of GDC and precursor of LSC, both synthesized by CHFS, (2) applying NiO and YSZ nanocomposites synthesized by CHFS for developing long-term stable SOFC anodes. Thirdly, some suggestions related to the practical operation of the CHFS reactor are made.

9.1 Syntheses of $La_{0.6}Sr_{0.4}CoO_{3-\delta}$

In solid oxide fuel cells (SOFCs), $La_{0.6}Sr_{0.4}CoO_{3-\delta}$ (LSC) is a very attractive cathode material with a mixed conductivity and a high activity for the oxygen reduction process [1]. The two-stage CHFS reactor (**Fig. 9.1**) was applied for synthesizing LSC, aiming at obtaining single-phase particles without post treatments. Synthesis conditions are summarized in **Table 9.1**.

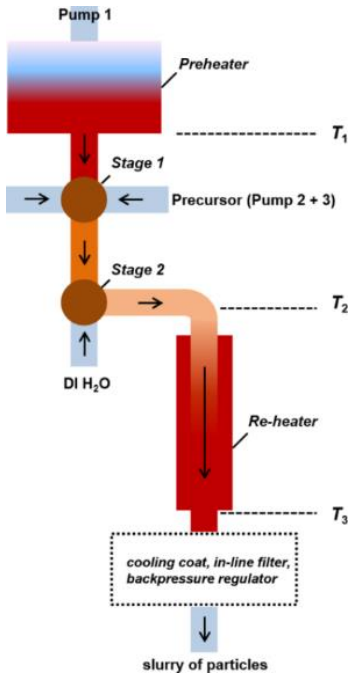

Figure 9.1 A schematic description of the CHFS reactor.

Table 9.1. Experimental conditions applied in the syntheses of $La_{0.6}Sr_{0.4}CoO_{3-\delta}$

	Pump 1	Precursor (Stage 1)		Temperature profiles		
		Pump 2	Pump 3	T_1 / °C	T_2 / °C	T_3 / °C
LSC1	DI H_2O	Me^{n+} (c, 0.05 M)	KOH (c, 0.5 M)	410	270	385
LSC2	KOH (c, 0.5 M)	Me^{n+} (c, 0.05 M)	DI H_2O	410	270	385
LSC3	KOH (c, 0.5 M)	Me^{n+} (c, 0.05 M); H_2O_2 (c, 0.5 M)	DI H_2O	410	336	410
LSC4	DI H_2O*	Me^{n+} (c, 0.05 M)	KOH (c, 6 M)	410	328	410

Notes: Me^{n+}: La^{3+}, Sr^{2+} and Co^{2+} from nitrate salts in molar ratio 0.6:0.4:1.0. Unit M means mol L^{-1}. Except in the synthesis of LSC4 where the flow rate of the pump 1 was 35 mL min^{-1}, the flow rates were kept at 30 mL min^{-1}, 10 mL min^{-1} and 10 mL min^{-1} for pump 1, pump 2 and pump 3 separately. DI H_2O (10 mL min^{-1}) was supplied through the inlet of the Stage 2 to mitigate sedimentation in all syntheses.

The work started from a relatively mild synthesis condition (LSC1) that was previously applied for synthesizing several simple oxides. However, only $La(OH)_3$, $SrCO_3$ and CoO were obtained (LSC1 in **Fig. 9.2, 9.3**). Subsequently, experimental conditions were modified by (1) heating KOH aqueous solutions to the supercritical state (LSC2, LSC3), (2) adding H_2O_2 in order to oxidize Co^{2+} (LSC3), and (3) using a KOH solution with a high concentration (LSC4). However, either LSC was not phase pure (**Fig. 9.2**) or was not present (**Fig. 9.3**) in the obtained particles. Nevertheless, some interesting changes in the phase composition were observed. Firstly, the introduction of H_2O_2 as oxidant was effective in oxidizing Co^{2+}, as Co_3O_4 and LSC was observed (LSC3, **Fig. 9.2**) in which Co is present in the valence state of +3. Secondly, the use of a highly concentrated KOH solution (6 mol L^{-1}) increased the amount of $SrCO_3$ in the obtained particles (LSC4, **Fig. 9.3**), which could be due to the enhanced dissolution of CO_2 from air in the concentrated KOH solution. This should be noticed in future work. Thirdly, one should be aware that the particles stuck in the filter might have phase deviations compared with the particles collected in the slurry, e.g. as was observed in the synthesis of LSC3 (**Fig. 9.2**).

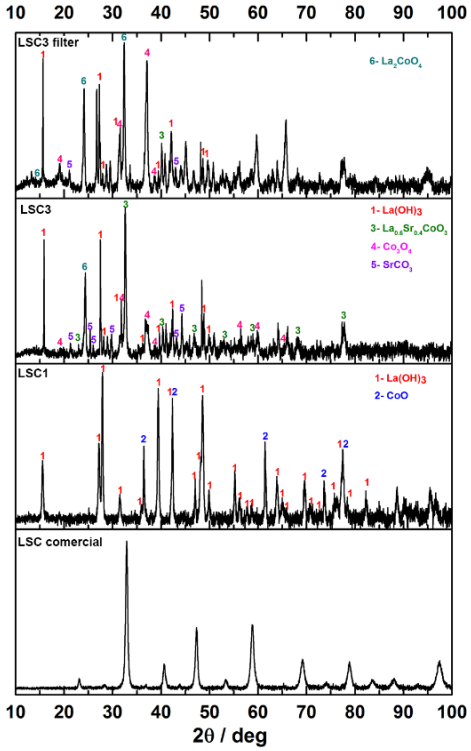

Figure 9.2 XRD patterns of LSC1, LSC3 and the commercial LSC powders. 'LSC3 filter' represents the particles stuck in the filter after the synthesis of LSC3.

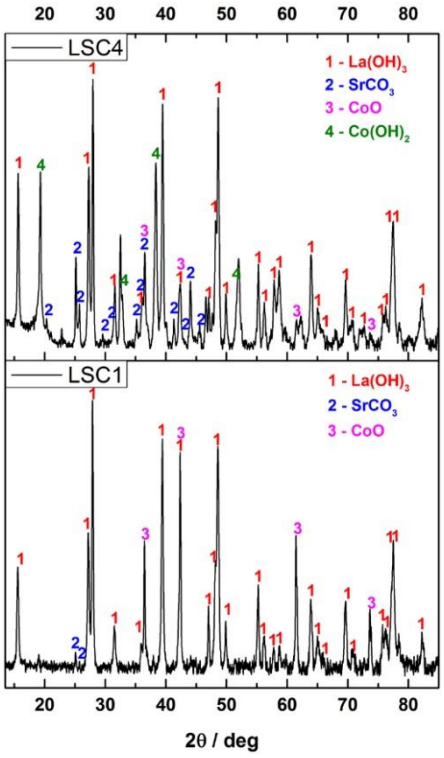

Figure 9.3 XRD patterns of LSC1 and LSC4.

On other hand, the fabrication of SOFCs usually requires sintering (typically > 1000 °C), during which these non-perovskite phases (hereafter called 'precursor of LSC') could be converted to the perovskite phase. Importantly, the precursor of LSC is nanosized (not shown here, e.g. $La(OH)_3$ nanorods viewed in TEM), which could reduce the sintering temperature because of the relatively high sinterability. In addition, all phases in the precursor of LSC are highly mixed in a nanoscale, which promises a homogeneous composition. Processing the precursor of LSC to make inks suitable for screen-printing of precursor cathodes has been conducted. The cell with the precursor cathode was sintered at 930 °C, a markedly low temperature compared to the sintering temperatures of the state-of-the-art cells. The latest cell test results show a very promising performance, compared to the standard cell at DTU with the cathode made from commercial LSC powders. The work is ongoing and more results will come soon.

9.2 Syntheses of α-MnO_2

Similar to other first row transition metal elements, Mn can present various valence states, and Mn_xO_y display in total 30 different polymorphs [2]. However, these polymorphs have different (catalytic) activities, e.g. in the catalytic water oxidation process [3] and in water pollution treatment [4]. Therefore, it is of great research interest to apply CHFS to prepare phase pure Mn_xO_y, facilitating a general understanding of the synthesis-structure-property relationship.

Table 9.2. Experimental conditions applied for syntheses of α-MnO_2

	Pump 1	Precursor (Stage 1)		Temperature profiles		
		Pump 2	Pump 3	T_1 / °C	T_2 / °C	T_3 / °C
MO1	H_2O_2 (c, 0.1 M)	Mn^{2+} (c, 0.05 M)	KOH (c, 0.1 M)	396	280	386
MO2	H_2O_2 (c, 0.3 M)	Mn^{2+} (c, 0.05 M)	KOH (c, 1.0 M)	398	275	390
MO3	H_2O_2 (c, 0.3 M)	Mn^{2+} (c, 0.05 M)	KOH (c, 0.5 M)	398	274	387
MO4	H_2O_2 (c, 1.0 M)	Mn^{2+} (c, 0.05 M)	KOH (c, 0.1 M)	398	276	394

Notes: Mn^{2+} from nitrate salts. Unit M means mol L^{-1}. The flow rates were kept at 30 mL min^{-1}, 10 mL min^{-1} and 10 mL min^{-1} for pump 1, pump 2 and pump 3 separately. DI H_2O (10 mL min^{-1}) was supplied through the inlet of the Stage 2 to mitigate sedimentation in all syntheses.

Syntheses of MnO_2 using $Mn(NO_3)_2$ as the precursor also required an oxidation step to increase the valence of Mn. Here, H_2O_2 solutions with different concentrations were used and were heated up to the supercritical state (**Table 9.2**). During this process, H_2O_2 decomposed to O_2, which then was available as an oxidant. XRD patterns of the synthesized particles are presented in **Fig. 9.4**. Phase-pure α-MnO_2 was not obtained. Nevertheless, some observations could be helpful for future work. Firstly, H_2O_2 is effective in oxidizing Mn^{2+}, as the oxidation state of Mn increased (from MO1 to MO4) with increased concentrations of H_2O_2. Secondly, when relatively high concentrations of alkali solutions were used (MO2 and MO3), it seems that δ-MnO_2 could be stabilized with K^+ insertions in the material and phase-pure δ-MnO_2 was obtained. Therefore, for further work, one may try to tune the pH as well as the temperature, particularly investigating acidic conditions and higher reaction temperatures, to obtain other MnO_2 polymorphs.

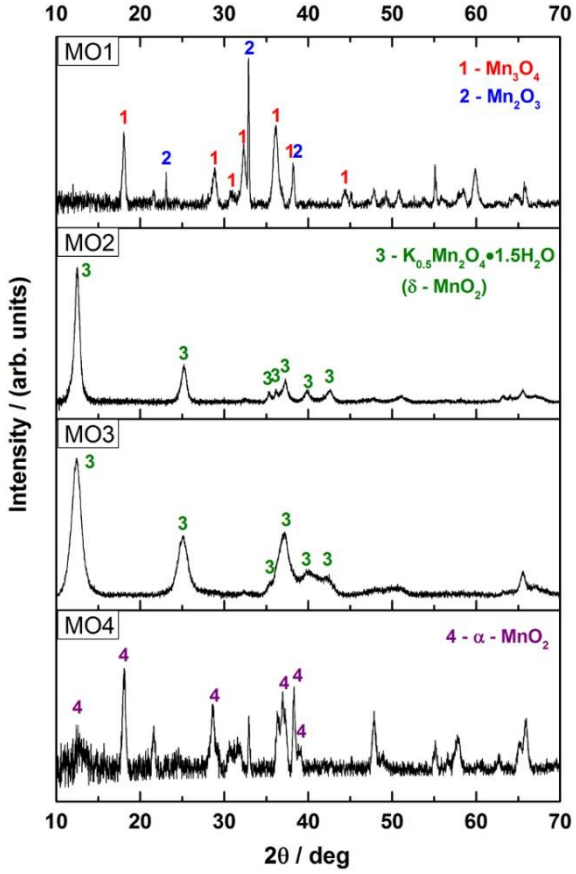

Figure 9.4 XRD patterns of the synthesized Mn_xO_y particles. The K^+ content in δ-MnO_2 was determined by EDS. The K : Mn ratio was 20.2 : 79.8 (in atomic percent), which is in accordance with the stoichiometry of the reference compound.

To summarize, for synthesizing oxides containing first transition metal elements and requiring oxidation steps, the process is complicated, due to the dynamic valence change of the transition metal elements and their high redox activity. Synthesis conditions particularly pH and temperature need to be finely controlled, which is challenging, in order to avoid the formation of secondary phases.

9.3 Nanocomposite particles of NiO and YSZ to advanced electrodes

Recently DTU has developed a microstructural-optimized Ni/YSZ electrode displaying a very good long-term stability for electrolysis at high current densities and high p_{H2O} inlets [5]. This was realized by (1) preparing NiO/YSZ precursor electrode as dense as possible, (2) reducing particle and pore size as much as possible, and (3) well matching the sizes of NiO, YSZ and pore phases that are meanwhile well dispersed. In **Chapter III**, CHFS has been proven viable for the production of composites of NiO and YSZ nanoparticles that are highly mixed in a nanoscale, of which the size and morphology could be tuned. Moreover, a Ni/YSZ cermet with ~96 % density made from nanocomposites of NiO and YSZ has been reported [6]. Given these findings, it is of interest to integrate the development of this type of advanced NiO/YSZ electrodes with CHFS of NiO and YSZ nanocomposites. Here some of the primary results are presented, which could be helpful for further future optimizations.

The synthesized NiO and YSZ composite nanoparticles (72.9 wt% and 27.1 wt%, respectively) were used to prepare slurries according to recipes developed at DTU suitable for tape casting. After casting and drying, the green tape was laminated with other tapes in three configurations. (1) On NiO-YSZ anode support; (2) on NiO-YSZ anode support then the other side of the green tape was laminated with YSZ electrolyte and GDC barrier layer (**Fig. 9.5**); (3) on NiO-YSZ electrode [5] on the anode support, then the other side of the green tape was laminated with YSZ electrolyte and GDC barrier layer. All samples were sintered at 1295 °C for 12 h.

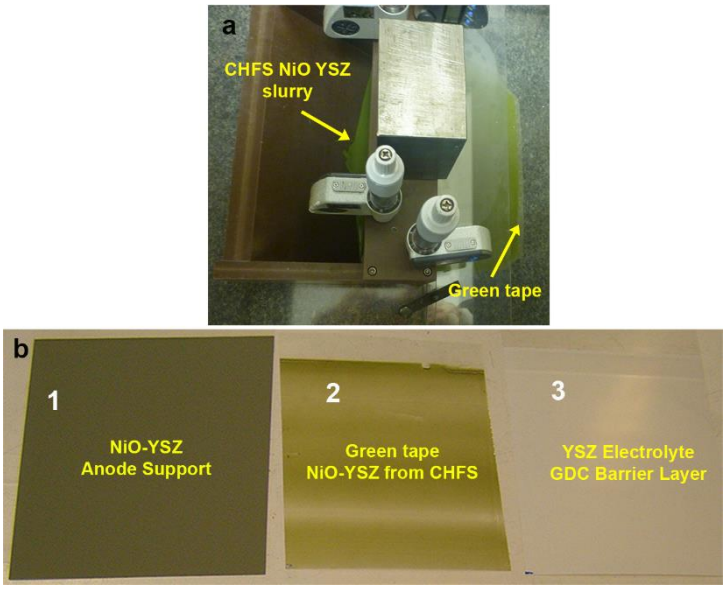

Figure 9.5 (**a**) Tape casting of the green tape with the slurry made from nanocomposites of NiO and YSZ prepared by CHFS. (**b**) Three green tapes that were laminated in sequence: 3 → 2 → 1.

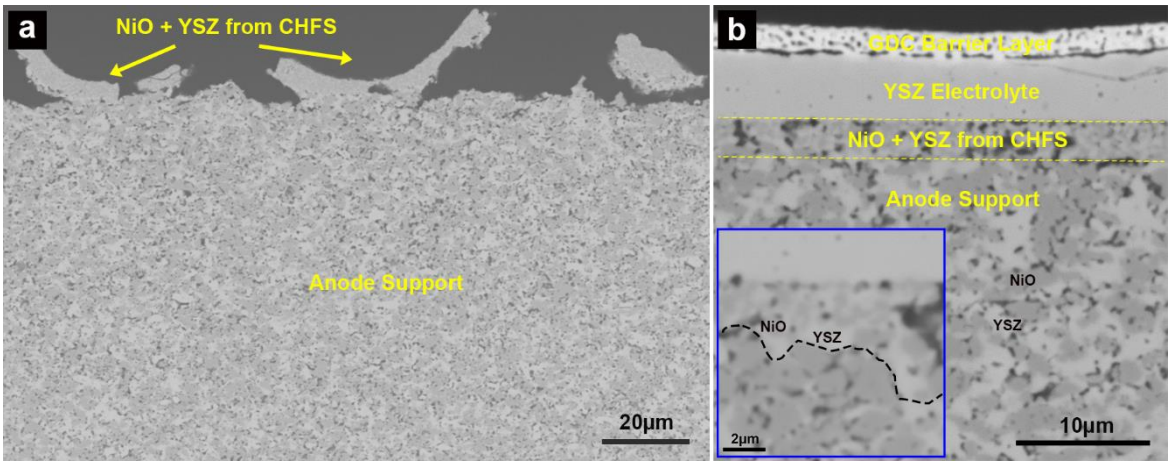

Figure 9.6 (**a**) NiO-YSZ green tape laminated on anode support after sintering; (**b**) NiO-YSZ green tape laminated on anode support and the other side laminated with YSZ electrolyte and GDC barrier layer, after sintering.

Fig. 9.6 presents micrographs of cross sections of the two samples after sintering. The NiO-YSZ tape laminated on the anode support de-laminated and cracked after sintering, possibly because of severe shrinkage (**Fig. 9.6a**). In comparison, thanks to the confinement of the YSZ electrolyte laminated on the other side, the NiO-YSZ tape laminated on the anode support in the other sample (**Fig. 9.6b**) was intact after sintering. Moreover, in the inset of **Fig. 9.6b** one may notice that the grains of both NiO (dark grey) and YSZ (white grey) in this part are much finer compared with those

in the anode support, and are well dispersed. This, according to the criteria suggested in [5], could be interesting for development of long-term stable NiO/YSZ electrodes. Further work could be as followings. (1) Laminating more than one NiO-YSZ tape to counterbalance the severe shrinkage after firing, which could also be achieved by adjusting the solvent/particles ratio in the slurry. (2) Sintering profiles could be optimized in order to get a denser microstructure. (3) The electrochemical performance of cells with the NiO-YSZ (by CHFS) electrode should be evaluated.

9.4 Suggestions for improving the CHFS reactor

As shown in **Fig. 9.1**, three thermocouples are used in the CHFS reactor to monitor the reaction temperature. However, the temperature of the outlet flow of the Stage 1 (the inlet flow of the Stage 2) is not known with the current configuration. Firstly, the temperature is the one for the solution after mixing scH_2O and the first precursor, and therefore gives information of the temperature condition for Stage 1. Secondly, the outflow of the Stage 1 is going to mix with and heat the inlet flow of the Stage 2. Therefore, the temperature is important particularly in cases when a second precursor or a surfactant is fed through the inlet of Stage 2. It is helpful to know the temperature condition in Stage 2. Adding a thermocouple between the outlet of the Stage 1 and the inlet of the Stage 2 could be an option to monitor better the reaction conditions.

For applications such as solid oxide fuel cells and oxygen transport membranes, usually relatively large amounts of particles (× 1 or × 10 g) are required to make bulk samples suitable for investigations. However, the current two-stage CHFS reactor was designed originally for synthesis of dual-phase nanomaterials with novel structures, which on the other hand limits its application for an up-scaled synthesis. If possible, it would be of interest to make a second CHFS reactor, with a higher production capacity (for up-scaled synthesis) and/or a simpler (e.g. single-stage/mixer) geometry.

References

[1] C. Sun, R. Hui, J. Roller, Cathode materials for solid oxide fuel cells: a review, J. Solid State Electrochem. 14 (2009) 1125–1144. doi:10.1007/s10008-009-0932-0.

[2] D.M. Robinson, Y.B. Go, M. Mui, G. Gardner, Z. Zhang, D. Mastrogiovanni, E. Garfunkel, J. Li, M. Greenblatt, G.C. Dismukes, Photochemical water oxidation by crystalline polymorphs of manganese oxides: structural requirements for catalysis, J. Am. Chem. Soc. 135 (2013) 3494–3501. doi:10.1021/ja310286h.

[3] V.B.R. Boppana, F. Jiao, Nanostructured MnO2: an efficient and robust water oxidation catalyst, Chem. Commun. 47 (2011) 8973–8975. doi:10.1039/c1cc12258d.

[4] Y. Liu, J. Wei, Y. Tian, S. Yan, The structure–property relationship of manganese oxides: highly efficient removal of methyl orange from aqueous solution, J. Mater. Chem. A. 3 (2015) 19000–19010. doi:10.1039/C5TA05507E.

[5] A. Hauch, K. Brodersen, M. Chen, M.B. Mogensen, Ni/YSZ electrodes structures optimized for increased electrolysis performance and durability, Solid State Ionics. 293 (2016) 27–36. doi:10.1016/j.ssi.2016.06.003.

[6] X. Weng, D. Brett, V. Yufit, P. Shearing, N. Brandon, M. Reece, H. Yan, C. Tighe, J.A. Darr, Highly conductive low nickel content nano-composite dense cermets from nano-powders made via a continuous hydrothermal synthesis route, Solid State Ionics. 181 (2010) 827–834. doi:10.1016/j.ssi.2010.04.014.

Chapter X. Appendix

This chapter documents some of the work agreed in the *Study Plan*.

File #1. Manual of the two-stage CHFS reactor

1. Pre-running checklist

This chapter describes the steps required to fill out the checklist that is part of the syntheses logbook page which can be found at the end of this manual.

- ✓ Ventilation working; Check indicators and valves (valves for the pumps, inlet and outlet flows)
- ✓ Log in to the lab computer

  User: ENRGKRI-D17453\ReactorUser
  PWD: Reactor123

- ✓ Software reading properly from PLC

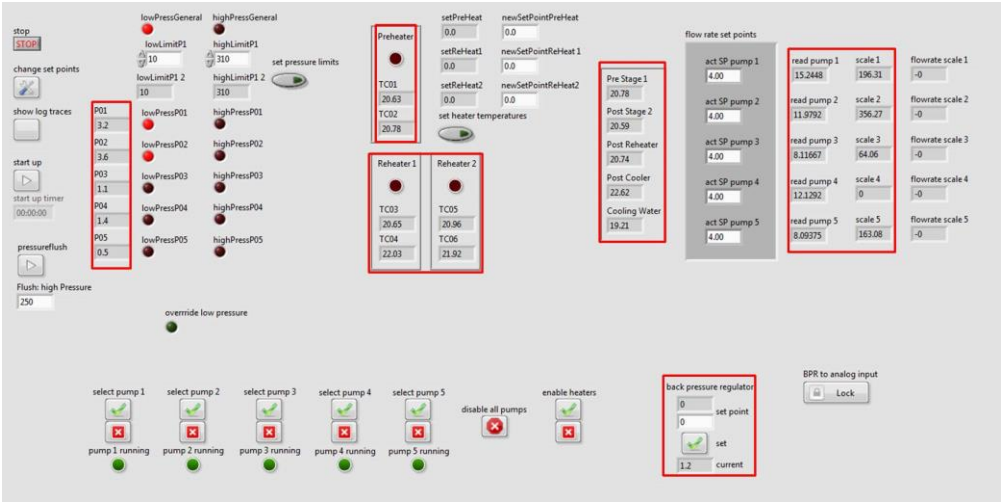

- ✓ System temperature < 50°C

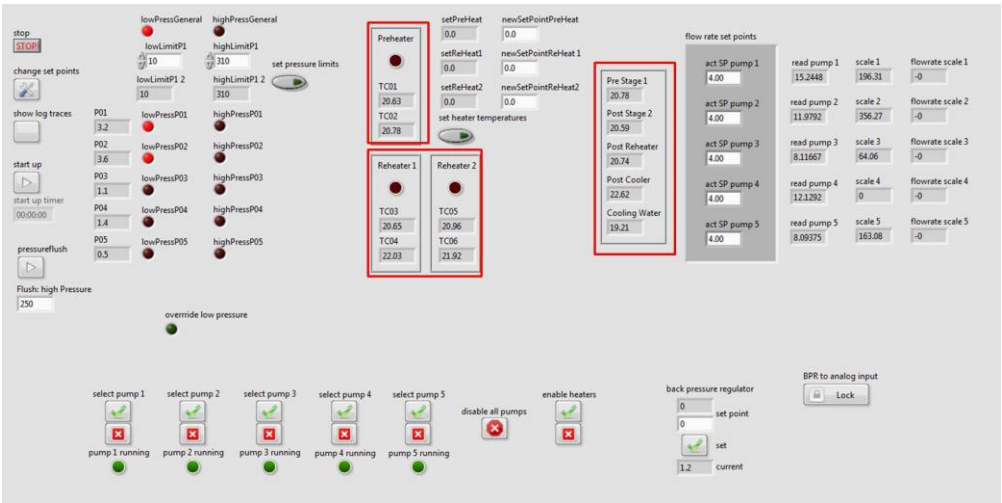

✓ System depressurized

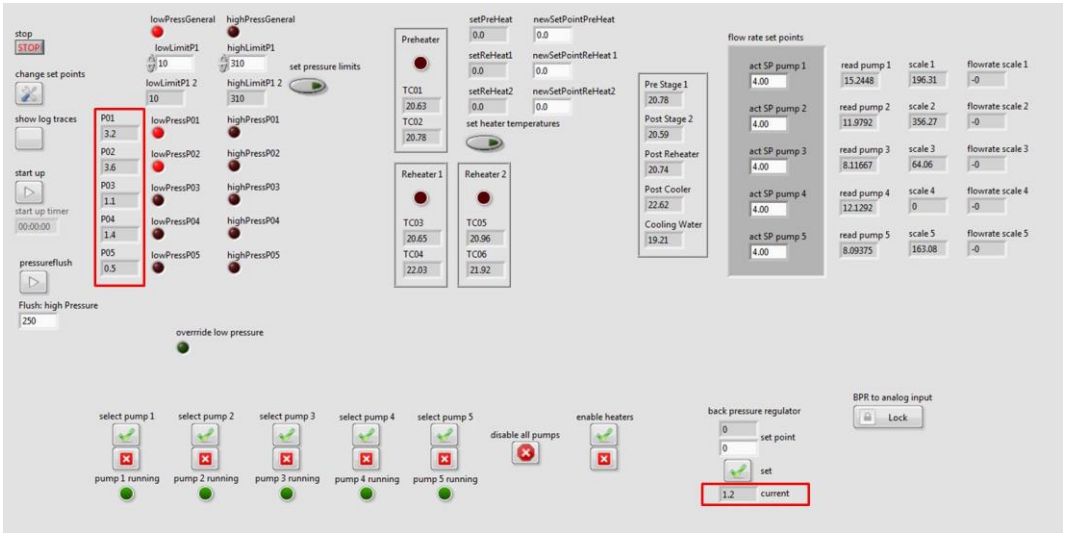

✓ Check the amount of DI water in PE flasks; add more DI water if it is not sufficient for the following heating and pressurizing processes. Check the PE flask for collecting outflows is empty.

✓ Make sure there are no bubbles in the PE tubes connected to the pumps

✓ Check working states of pumps, calibrate flow rate

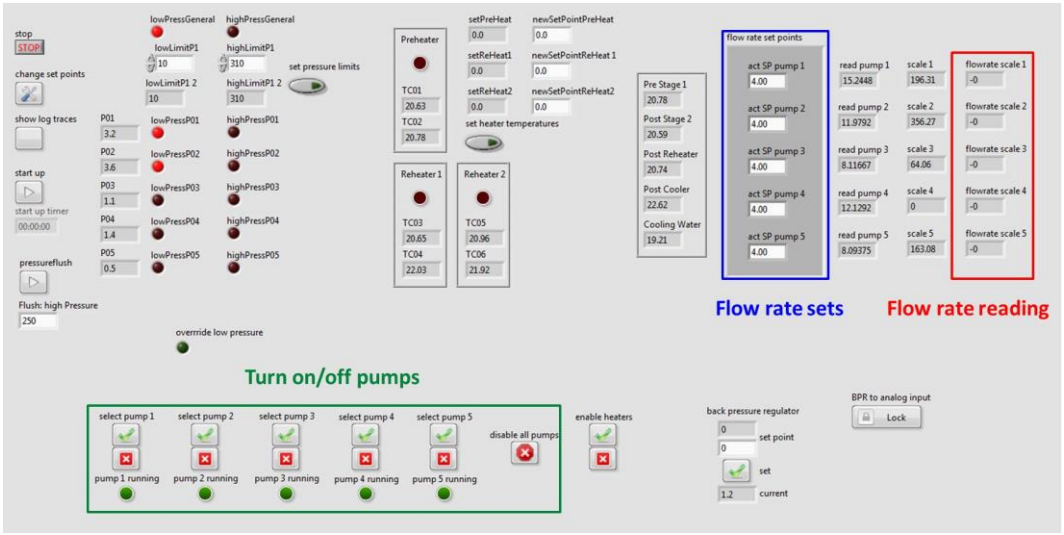

Notes: all pumps can also be turned on/off by buttons on the control box.

✓ Check back pressure regulator, pressure mechanical relief

Set the pressure to a value higher (e.g. 270bar, max. 300bar) than the targeted pressure (e.g. 240bar). The pressurization will cost for a while and simultaneously the current pressure can be read directly. After pressurization, adjust the pressure mechanical relief by a wrench until the current pressure reading drops to the targeted pressure 240bar (or slightly larger than 240bar). Reset the pressure to the targeted value 240bar. Ideally, the pressure readings

from pressure sensors should be equal to the current pressure reading whereas abnormal shifts can be used to determine the position where blockages might exist.

✓ Check supply of nitrogen for back pressure regulator

The gas bottle (outside) should at least have 20bar of nitrogen left.

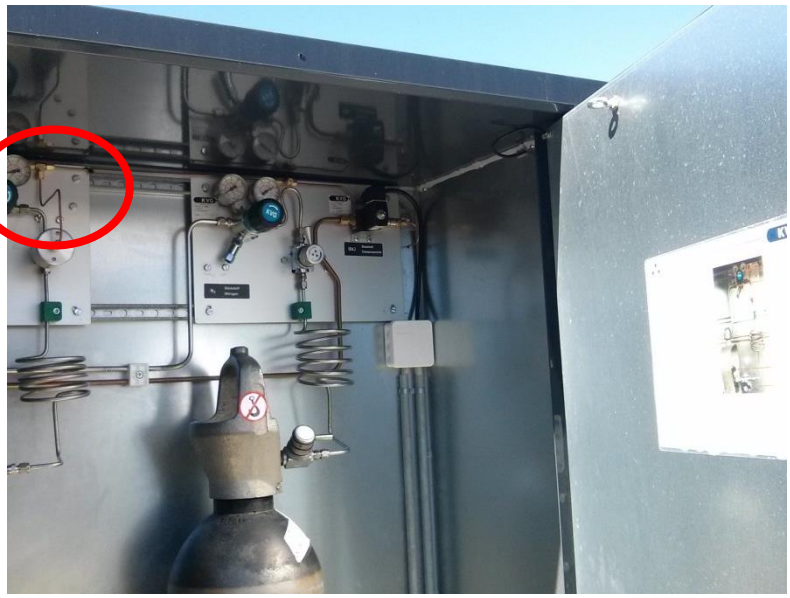

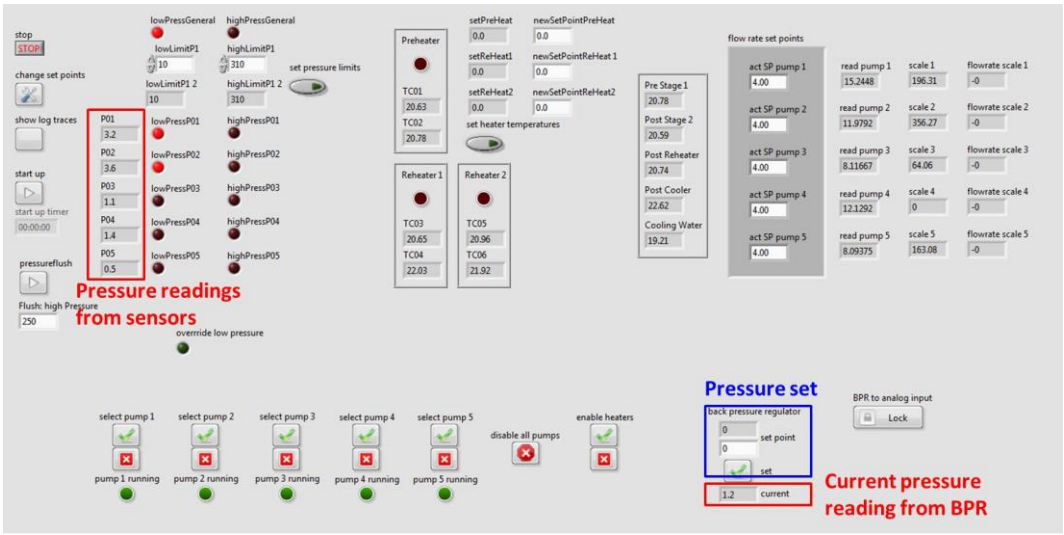

✓ Check the cooling system, preheater and reheaters

Check and start the cooling system. Set the temperatures (max. 450°C) separately for Preheater, Reheater 1 and 2. Press ‘enable heaters’ and then the heating process will start and instant temperature readings recorded by thermocouples will appear on the screen. For safety reason, each heater has a pair of thermocouple that independently monitors the temperature no higher than 450°C. Therefore, the temperature readings for TC01-06 should always stay smaller than 450°C. Simultaneously, the temperatures at several key points on

the flow path are also monitored and shown. The heating of DI water to its supercritical range will cost ca. 20min.

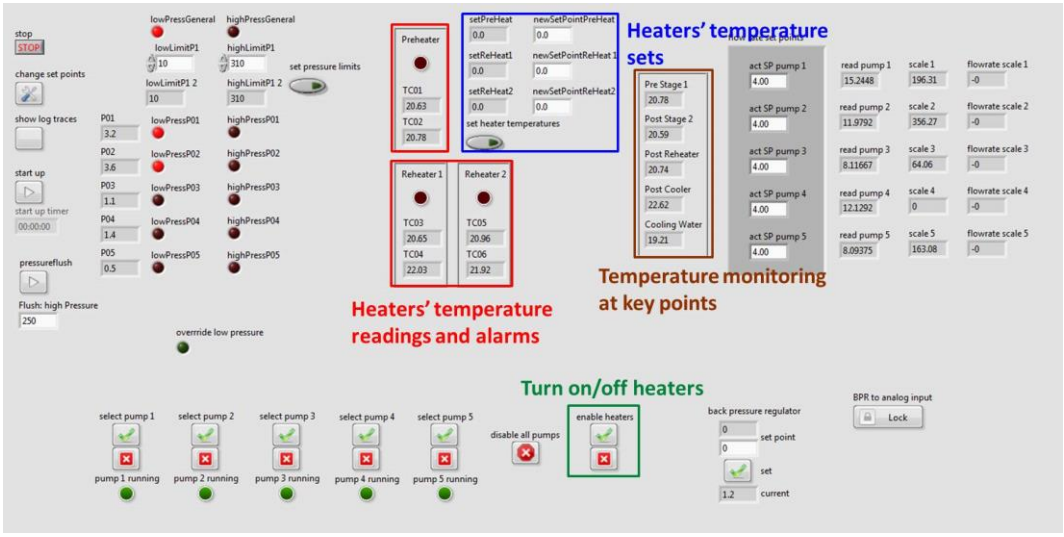

✓ After the temperatures at pre stage 1, post stage 2 and post reheater reach the desired values (near- or supercritical range), as well as the pressure and flow rates are stable, it is then regarded that the reactor is ready for the following nano particle synthesis.

2. Nano-oxide synthesis

(1) The metal salts that are going to be used for synthesizing nanoparticles should be ready before running the reactor.

(2) As designed, pump 1 is used for pumping DI water so during the synthesis there is no need to change the solution for pump 1. However, keep an eye on the amount of DI water in case it is running out which will result in bubbles being sucked into the pumps.

(3) For pump 2-5, the DI water used in the pre-running process should be exchanged with the metal salts solution. Before exchanging, the corresponding pump should be disabled.

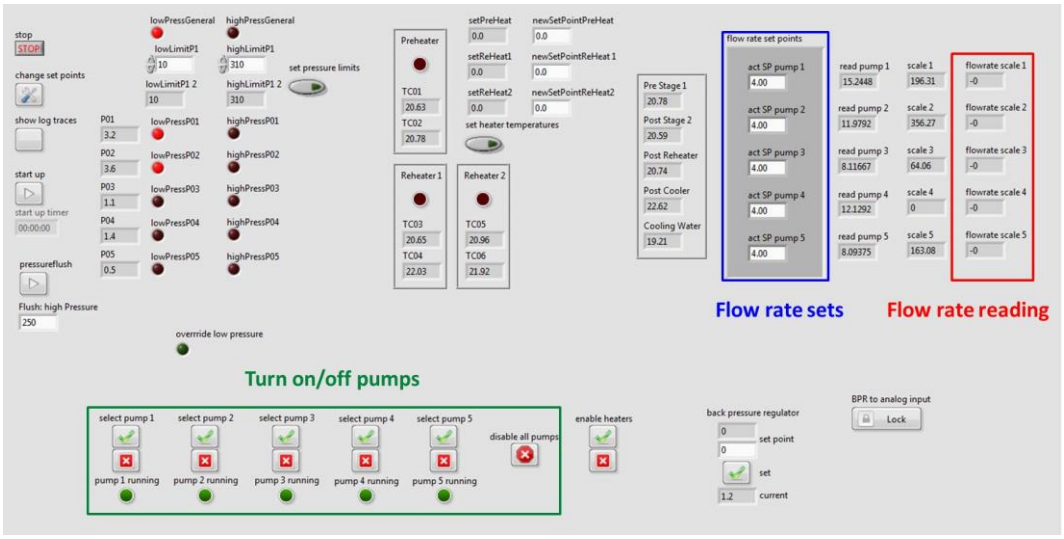

(4) After all metal salts solutions being pumped steadily into the reactor and no DI water left in the inlet tubes collected to pump 2-5 (normally this will cost ca. 5-10min), switch the outflow to a new PE flask by switching the outlet valve. Remember the outlet valve should always be kept open. This step makes sure that all nanoparticles collected are prepared in the same conditions (temperature, pressure, flow rates, metal salts concentration, residence time, etc.). Remember changing the PE flask when it is full.

(5) It is important to keep an eye on the instant readings of flow rates of all pumps, temperature (at the key points and at the three heaters) and pressure (at the backpressure regulator and at the pressure sensors). The trace of readings of all these parameters can also be monitored by pressing ‘show log traces’.

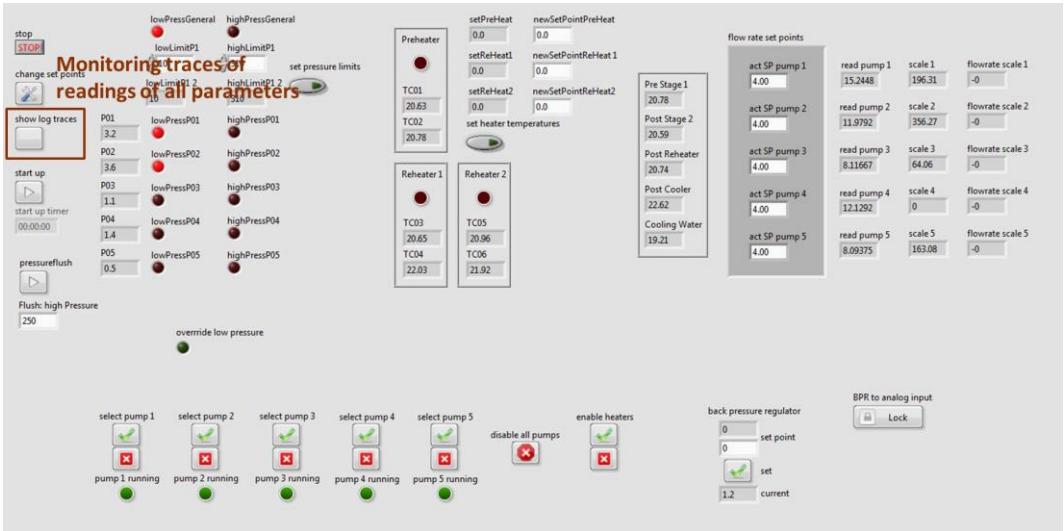

3. Post synthesis and close down

- ✓ After finishing the synthesis process, exchange the metal salts solutions with DI water for pump 2-5 following the similar procedure described before. Remember to disable the corresponding pump before changing the solutions.
- ✓ Disable the preheater and reheaters. The heating will be terminated.
- ✓ Wait the whole reactor to cool down.
- ✓ After the temperature drops to less than 50°C, the whole reactor can be depressurized by setting the backpressure regulator to 0.
- ✓ There is a 'pressure flush' shortcut to start the program to flush and clean the inline tubes of the reactor with DI water. Before starting the program, set the 'flush high pressure' that is the upper limit for the pressure that can reach in the flush process.

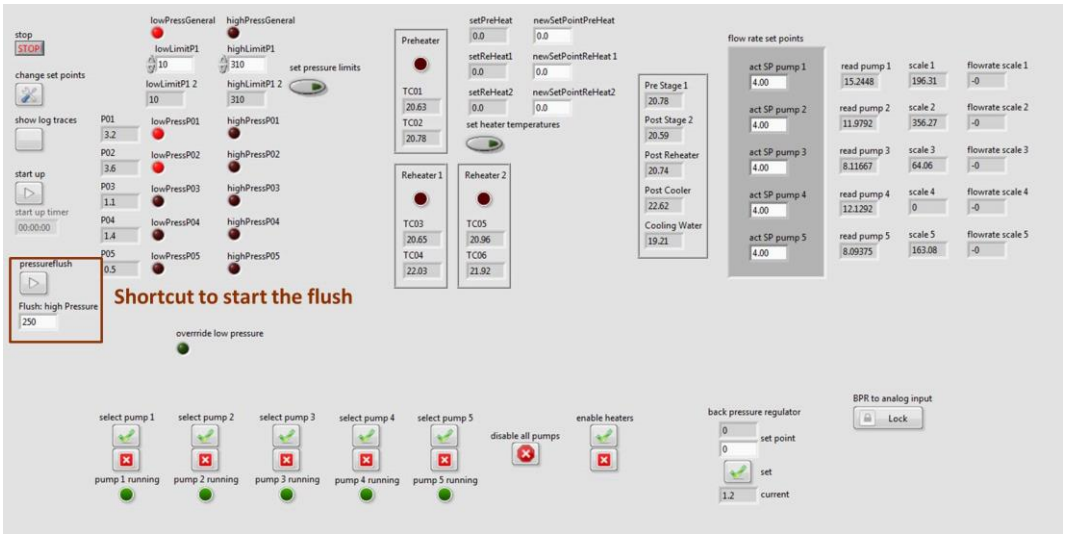

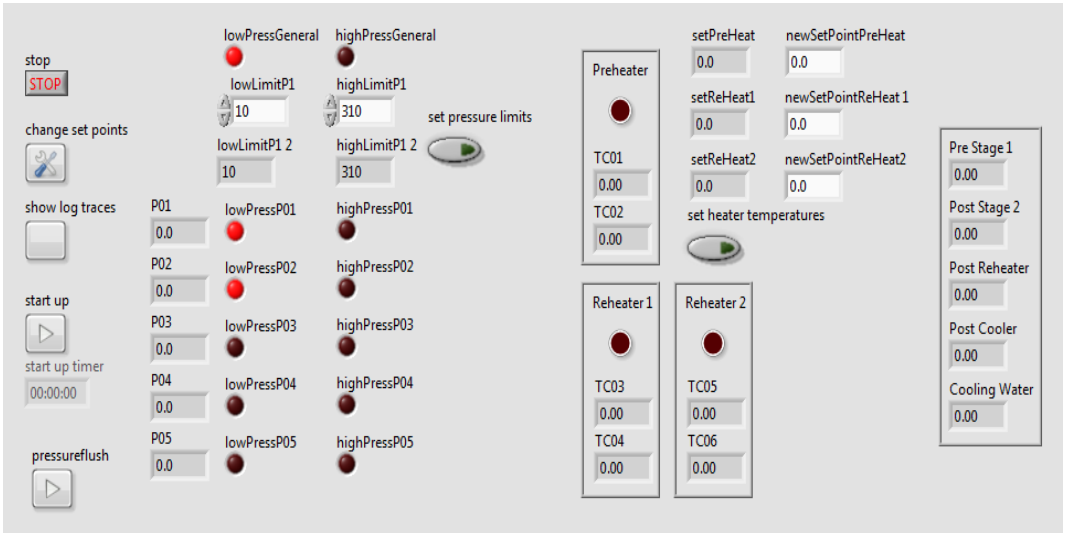

4. Possible failures and fix

(1) Software

End reactor control software

Open “services” (Start-> search Services -> open Services”)

Sort by Startup type

Go to NI (national instruments) services, Automatic (Delayed Start)

Top to bottom: right-click and restart (say yes, if asked)

Start rector control software

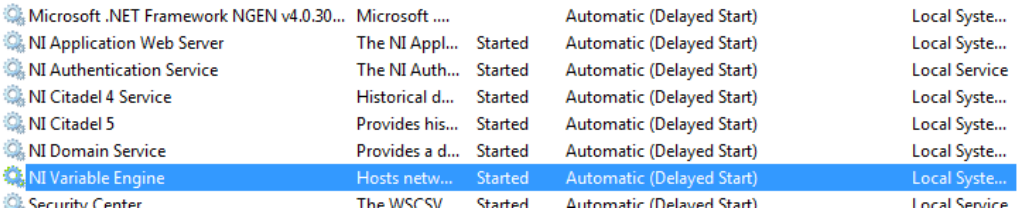

(2) Flow rate of pump drops to zero

Increase the actuator set point for that pump to 20mA. If the pump starts pumping again, lower the set point to the desired flowrate. The new set point might be higher than before and need adjustment over due to air in the pump head.

If the pump does not start pumping again, the system needs to be cooled down and depressurized.

(3) Pump doesn’t pump at all

If all valves are open, the system is depressurized but a pump is not pumping it is most likely that an internal check valve is stuck. In that case disconnect the in- and outlet-tube and unscrew the fittings that house the check valves. Make sure that the check valves are clean and the steel balls are moving freely.

(4) Negative flow rate if pump is switched off

Probably a not properly closing internal check valve. In that case disconnect the in- and outlet-tube and unscrew the fittings which house the check valves. Make sure that the check valves are clean and the steel balls are moving freely.

File #2. Logbook

Date (YY-MM-DD)		**Operator**	

A. Checklist							
1. ventilation working		2. software reading properly from PLC		3. temperature < 50 °C		4. system depressurized	
5. reservoirs for pumps filled with DI water		6. empty waste container placed at outflow		7. ball valves open (used pumps, BPR, outflow)		8. inlet valves open (scale cabinet)	
9. used pumps works, flow rate calibration		10. proportional relief valve set to **bar**		11. sufficient nitrogen for BPR (reading: **bar**)		12. back pressure regulator closes	
13. turn on chiller and check working states							

B. Chemicals registration and operation conditions

1. Chemicals (species + concentration)

Pump 1	Pump 2	Pump 3	Pump 4	Pump 5

2. Flow rates/(mL·min^{-1})

	Pump 1	Pump 2	Pump 3	Pump 4	Pump 5
Digit Set					
Reading					

3. Pressure [Set/Reading]/bar	

4. Temperature profile

Set point for preheater	Set point for reheater 1	Set point for reheater 2
Reading pre-stage 1	Reading post-stage 2	Reading post reheater
Reading post cooler	Reading cooling water	

C. Log

1. Fractions of collected outflow

Fraction No.	***Start (hh:mm)***	***End (hh:mm)***
Pre running (heating, pressurizing)		
Fraction 1		
Fraction 2		
Fraction 3		
Fraction 4		

Fraction 5		
Fraction 6		
2. Log of activities		
(*Format: time (hh:mm) + activities*)		
D. Failures and solutions		